

University of Alberta

**Stability of Cr₃C₂/Cr₂O₃ Based Porous Ceramics
in Supercritical Water**

by

Ziqiang Dong

A thesis submitted to the Faculty of Graduate Studies and Research
in partial fulfillment of the requirements for the degree of

Doctor of Philosophy

in

Materials Engineering

Department of Chemical and Materials Engineering

©Ziqiang Dong

Spring 2013

Edmonton, Alberta

Permission is hereby granted to the University of Alberta Libraries to reproduce single copies of this thesis and to lend or sell such copies for private, scholarly or scientific research purposes only. Where the thesis is converted to, or otherwise made available in digital form, the University of Alberta will advise potential users of the thesis of these terms.

The author reserves all other publication and other rights in association with the copyright in the thesis and, except as herein before provided, neither the thesis nor any substantial portion thereof may be printed or otherwise reproduced in any material form whatsoever without the author's prior written permission.

Dedicated to My Wife and My Daughter

Abstract

This research was aimed at developing porous ceramics as well as ceramic-metal composites that can be potentially used in Gen-IV supercritical water reactors (SCWR). The research mainly includes two parts: 1) fabricating and engineering the porous ceramics and porous ceramic-metal composite; 2) Evaluating the stability of the porous ceramics in SCW environments.

Reactive sintering in carbonaceous environments was used to fabricate porous $\text{Cr}_3\text{C}_2/\text{Cr}_2\text{O}_3$ -based ceramic. A new process consisting of freeze casting and reactive sintering has also been successfully developed to fabricate highly porous Cr_3C_2 ceramics with multiple interconnected pores. Various amounts of cobalt powders were mixed with ceramic oxides in order to modify the porous structure and property of the porous carbide obtained by reactive sintering. The hardness of the $\text{M}(\text{Cr},\text{Co})_7\text{C}_3$ -Co composite has been evaluated and rationalized based on the solid solution of cobalt in the ceramic phase, the composite effect of soft Co metal and the porous structure of the ceramic materials. Efforts have also been made in fabricating and evaluating interpenetrating Cr_3C_2 -Cu composites formed by infiltrating liquid copper into porous Cr_3C_2 .

The corrosion evaluation mainly focused on assessing the stability of porous Cr_3C_2 and Cr_2O_3 under various SCW conditions. The corrosion tests showed that the porous Cr_3C_2 is stable in SCW at temperatures below 425 °C. However, cracking and disintegrating of the porous Cr_3C_2 occurred when the SCW temperature increased above 425 °C. Mechanisms of the corrosion attack were

also investigated. The porous Cr_2O_3 obtained by oxidizing the porous Cr_3C_2 was exposed to various SCW environments. It was found that the stability of Cr_2O_3 was dependent on its morphology and the SCW testing conditions. Increasing SCW temperature increased the dissociation rate of the Cr_2O_3 . Adding proper amount of Y_2O_3 can increase the stability of the porous Cr_2O_3 in SCW. It was also concluded that decreasing dissolved oxygen in SCW can increase the stability of Cr_2O_3 ceramics in SCW. Various advanced analytic techniques including Scanning electron microscopy (SEM), Energy-dispersive X-ray spectroscopy (EDS), X-ray diffraction (XRD), X-ray photoelectron spectroscopy (XPS), and Mass spectroscopy (MS) have been used to characterize the materials involved in this research.

Acknowledgement

First and foremost, I would like to express my genuine gratitude to my supervisor, Dr. Weixing Chen, for the wise guidance, constant encouragement, and continuous support he has provided for my doctoral study. His diligence to work, enthusiasm to research, and curiosity to knowledge have inspired me to pursue the truth for the scientific research and will continue giving me the desire for lifelong learning.

I would like to thank the committee members, Dr. Reg. Eadie, Dr. Hao Zhang, Dr. Zihui Xia, and Dr. David Miltin for reviewing my dissertation and giving valuable comments. I also extend my thanks to Dr. Thomas Etsell and Dr. Samer Adeeb for serving as committee members in my candidacy exam and giving me encouragement and guidance.

I would like to express my sincere appreciation to Dr. Dave Guzonas and Dr. Wenyue Zheng for their patient review of my publications and providing assistance for this research program.

I would like to thank all my colleagues, Mr. Yashar Behnamian, Dr. Xinwei Cui, Dr. Yongwang Kang, Dr. Fengping Hu, Dr. Ming Li, Dr. Hao Li, Mr. Tianfei Wang, Ms. Renfei Wang for their kind help for my doctoral research.

I would like to give great appreciation to my wife Ms. Xi Han and my daughter Helen Dong who give me the strength to conquer every obstacle in my study.

Table of Contents

| | |
|--|-----------|
| Chapter 1 Introduction and Literature Review | 1 |
| 1.1 Introduction..... | 2 |
| 1.2 Literature Review | 3 |
| 1.2.1 Supercritical fluids | 3 |
| 1.2.2 Supercritical water and its properties | 5 |
| 1.2.3 Supercritical Water-cooled Reactor (SCWR) | 10 |
| 1.2.4 Insulation materials | 13 |
| 1.2.5 Fabrication of porous materials | 36 |
| 1.2.6 Corrosion in SCW environments..... | 47 |
| 1.3 Research Objectives..... | 60 |
| 1.4 Proposed Research..... | 61 |
| 1.5 Bibliography | 63 |
| | |
| Chapter 2 Experimental | 82 |
| 2.1 Preparation of Samples..... | 83 |
| 2.1.1 Preparation of porous Cr_3C_2 and $\text{M}(\text{Cr}, \text{Co})_7\text{C}_3\text{-Co}$ composite | 83 |
| 2.1.2 Preparation of porous Cr_2O_3 by oxidation | 87 |
| 2.1.3 Preparation of densified ceramic samples | 87 |
| 2.1.4 Preparation of $\text{Cu-Cr}_3\text{C}_2$ composite | 88 |
| 2.2 SCW Corrosion Tests..... | 88 |
| 2.2.1 Static supercritical water test | 88 |
| 2.2.2 Flowing supercritical water test | 90 |
| 2.3 Characterization Techniques..... | 90 |

| | |
|--|----|
| 2.3.1 Scanning electron microscopy (SEM) | 91 |
| 2.3.2 X-ray diffraction (XRD) | 91 |
| 2.3.3 Mass spectrum (MS) test | 91 |
| 2.3.4 X-ray photoelectron spectroscopy (XPS) | 91 |
| 2.4 Bibliography | 92 |

Chapter 3 Preparation of Highly Porous Cr₃C₂..... 93

| | |
|---|-----|
| 3.1 Introduction..... | 94 |
| 3.2 Experimental..... | 97 |
| 3.2.1 Materials | 97 |
| 3.2.2 Fabrication procedures | 97 |
| 3.2.3 Characterization..... | 99 |
| 3.3 Results | 99 |
| 3.3.1 Microstructure of porous bodies..... | 99 |
| 3.3.2 Porous samples with different solid loading content | 100 |
| 3.3.3 Porous structure obtained at different freeze temperatures | 102 |
| 3.4 Discussion..... | 103 |
| 3.4.1 Large pore channels formed by the sublimation of freezing vehicle | 103 |
| 3.4.2 Small pores formed by reactive sintering | 108 |
| 3.4.3 The formation of the high porous structure with multiple pore sizes | 113 |
| 3.5 Concluding Remarks..... | 115 |
| 3.6 Bibliography | 117 |

Chapter 4 Preparation of Porous M(Cr, Co)₇C₃-Co Composites

..... **121**

| | |
|---|-----|
| 4.1 Introduction..... | 122 |
| 4.2 Experimental..... | 123 |
| 4.3 Results and Discussion..... | 124 |
| 4.3.1 Porous carbide foam obtained by carburization | 125 |
| 4.3.2 Porous $M(\text{Cr, Co})_7\text{C}_3$ -Co Composites..... | 126 |
| 4.3.3 Hardness characterization of the porous cermets | 137 |
| 4.4 Concluding Remarks..... | 145 |
| 4.5 Bibliography | 146 |

Chapter 5 Corrosion Behavior of Porous Chromium Carbide in Supercritical Water 149

| | |
|---|-----|
| 5.1 Introduction..... | 150 |
| 5.2 Experimental..... | 152 |
| 5.3 Results | 154 |
| 5.3.1 Porous chromium carbide ceramic | 154 |
| 5.3.2 Stability of porous chromium carbide in SCW | 155 |
| 5.4 Discussion..... | 160 |
| 5.4.1 Exposure of porous chromium carbide in air | 161 |
| 5.4.2 Corrosion of chromium carbide in SCW..... | 162 |
| 5.4.3 Formation of cracks in SCW environments..... | 167 |
| 5.5 Concluding Remarks..... | 168 |
| 5.6 Bibliography | 170 |

Chapter 6 Effect of Yttria Addition on the Stability of Porous Chromium Oxide Ceramics in Supercritical Water 172

| | |
|--|-----|
| 6.1 Introduction..... | 173 |
| 6.2 Experimental..... | 176 |
| 6.3 Results and Discussion..... | 178 |
| 6.3.1 Porous chromium oxide based ceramics | 178 |
| 6.3.2 SCW testing of the porous Cr ₂ O ₃ -based ceramics | 183 |
| 6.4 Concluding Remarks..... | 201 |
| 6.5 Reference..... | 202 |

Chapter 7 Stability of Cr₂O₃ in Various SCW Environments... 205

| | |
|---|-----|
| 7.1 Introduction..... | 206 |
| 7.2 Experimental..... | 209 |
| 7.2.1 Preparation of Cr ₂ O ₃ based ceramics | 209 |
| 7.2.2 SCW test facilities | 210 |
| 7.2.3 Characterization..... | 211 |
| 7.3 Results | 212 |
| 7.3.1 Morphology of the samples prior to SCW exposures | 212 |
| 7.3.2 Corrosion tests in static SCW environments..... | 214 |
| 7.3.3 Corrosion tests in flowing SCW..... | 221 |
| 7.4 Discussion..... | 226 |
| 7.4.1 Corrosion of Cr ₂ O ₃ in SCW environments | 226 |
| 7.4.2 Comparison of the static autoclave and loop tests | 233 |
| 7.5 Concluding Remarks..... | 235 |
| 7.6 Bibliography | 237 |

Chapter 8 Infiltration of Porous Cr₃C₂ with Molten Cu..... 241

| | |
|---|-----|
| 8.1 Introduction..... | 242 |
| 8.2 Experimental..... | 244 |
| 8.2.1 Preparation of carbide foam..... | 244 |
| 8.2.2 Preparation of composite..... | 245 |
| 8.2.3 Sample characterization..... | 245 |
| 8.3 Results and Discussion..... | 246 |
| 8.3.1 Porous chromium carbide foam prepared [22]..... | 246 |
| 8.3.2 Cu-Cr ₃ C ₂ composite fabricated by infiltration..... | 247 |
| 8.4 Concluding Remarks..... | 260 |
| 8.5 Bibliography..... | 262 |

Chapter 9 Concluding Remarks and Future Work 266

| | |
|--|-----|
| 9.1 Concluding Remarks..... | 267 |
| 9.1.1 Fabrication of ceramics and composites..... | 267 |
| 9.1.2 Evaluation in SCW environments..... | 268 |
| 9.2 Future Work..... | 270 |
| 9.2.1 Evaluation of the performance of composite materials in SCW..... | 270 |
| 9.2.2 Engineering the surface of Cr ₃ C ₂ to improve its stability in SCW..... | 270 |
| 9.2.3 The stability of other reactive element/oxides -Cr ₂ O ₃ systems..... | 271 |

List of Tables

| | |
|--|-----|
| Table 1-1. Critical temperature and pressure for various solvents [6]. | 4 |
| Table 1-2. Comparison of the values of thermophysical properties of water for the conditions of CANDU-SCWR, CANDU-6 and PWR [8, 44]. | 12 |
| Table 1-3. Thermal conductivity of some ceramics [45, 46]. | 15 |
| Table 1-4. Thermal spraying of various ceramics [52]. | 16 |
| Table 1-5. TBC materials and their characteristics [55]. | 17 |
| Table 1-6. Physic-properties of Cr_3C_2 [125]. | 31 |
| Table 1-7. Comparison of the fracture toughness of various carbides potentially applicable in the SCWR. | 31 |
| Table 1-8. Comparison of processing methods used for fabricating macroporous materials [161]. | 40 |
| Table 2-1. Isobaric properties for water at 25 MPa [1]. | 89 |
| Table 3-1. Comparison of porosity with other reported results. | 115 |
| Table 4-1. EDS tests for samples added with various amounts of cobalt. | 134 |
| Table 4-2. Porosity and hardness of the samples added with various amounts of cobalt. | 138 |
| Table 5-1. Weight changes of ceramic coupons after exposure to SCW for 25 hours at different temperatures. | 156 |
| Table 5-2. Weight changes of ceramic coupons exposed to SCW for 25 hours at different pressures | 160 |
| Table 6-1. Porosity of chromium carbide and chromium oxide | 180 |
| Table 7-1. Chromium oxide based ceramics prepared for SCW test. | 209 |
| Table 8-1. Comparison of the J factor: Cr_3C_2 -carbide foam for this study, P=63%. Al_2O_3 -1: Porous polycrystalline aggregates, P≤30% [43, 44]; Al_2O_3 -2: porous, P≤40% [43, 45]; | |

MgO: aggregates, $P \leq 40\%$ [43, 46] ; SiC: aggregates, $P \leq 42\%$ [43]; MgAl₂O₄: aggregates
[43, 47]..... 258

List of Figures

| | |
|---|----|
| Figure 1- 1. Phase diagram of water and the supercritical domain [6]. | 5 |
| Figure 1- 2. Phase diagram of water and schematic course of density versus pressure and temperature (P - Pressure, ρ – Density, T – Temperature, SC – Supercritical region) [15]. | 6 |
| Figure 1- 3. Drop of physical properties of high-temperature water at different pressure [15]. | 7 |
| Figure 1- 4. Specific heat of water [35, 36]. | 9 |
| Figure 1- 5. An insulated pressure tube design of the CANDU-SCWR fuel channel [44]. | 13 |
| Figure 1- 6. A schematic diagram showing the formation of oxide film on zirconium and the reactions during oxidation [71]. | 21 |
| Figure 1- 7. Theoretical solubility of Al_2O_3 in sub-critical and supercritical water at 25 MPa under neutral conditions [73]. | 24 |
| Figure 1- 8. (a) Schematical course of the electrochemical potential for the formation of soluble chromate in acidic and alkaline solutions; (b) Stability islands of chromium and nickel [15]. | 30 |
| Figure 1- 9. Erosion-oxidation wastage of Ni20Cr, Cr_3C_2 25Ni20Cr and WC 20Cr7Ni [139]. | 33 |
| Figure 1- 10. Total mass gain for Ni-25wt.%Cr alloys with various oxide dispersions added at a nominal level of 0.1 cation% after 100h at 1000 °C [152]. | 36 |
| Figure 1- 11. Change of the physical property with different porosity [163]. | 38 |
| Figure 1- 12. Typical porosity and average pore size achieved via the replica, sacrificial templating, and direct foaming processing routes [161]. | 41 |

Figure 1- 13. Top: plot of grain size versus sintered density typically observed in ceramics. (1) Random close packing of ceramic particles. (2) Intermediate stage sintering where interconnected pore channels limit grain growth. (3) 92-95% where pore channels close off to form isolated pores at triple points and grain boundaries. (4) Final stage densification where pores shrink and grain growth rate accelerates due to decreasing pore drag. (5) Colorized scanning electron micrograph of a dense ceramic [185].42

Figure 1- 14. SEM micrographs of pure Cr₂O₃ samples after carburizing at different temperatures in reducing atmosphere (2% CH₄ + 98% H₂) for 10 Hrs respectively: a)1000 °C; b) 1100 °C; c) 1200 °C; d) 1300 °C [205].44

Figure 1- 15. Typical microstructures obtained by freeze-casting (a) porous alumina using a hypoeutectic amorphous/naphthalene as a solvent [206, 216]. (b) porous alumina using water as a solvent [206, 214] (c) porous silicon carbide using polycarbosilane as a precursor and camphene as a solvent [206, 217] and (d) porous alumina using camphene as a solvent [162, 206].46

Figure 1- 16. Cross-section EBSD scanning maps of SCW-exposed samples (a) 500 °C, 25 ppb dissolved oxygen, 505 h and (b) 500 °C, 2000 ppb dissolved oxygen, 505 h, where base metal, spinel, magnetite, and hematite are highlighted in red, blue, yellow, and magenta, respectively [114].49

Figure 1- 17. Dissolution model and expected reactions: (1) assuming protective corrosion layer of SiO₂ is produced; (2) assuming non-protective reaction product is produced. (Symbol A and B represent reaction occurring at the interface) [142].53

Figure 1- 18. SEM micrographs of surfaces for (a) as-received CVD SiC; (b) after a 21-day exposure [143].54

Figure 1- 19. EBSD analysis of the cross-section surface (28 ×28 μm) of the sample exposed to the SCW with ~10 ppb oxygen for 333 h [240].55

| | |
|---|-----|
| Figure 1- 20. Grain boundary attack on the surface of Mg-PSZ (HCl, 50 h, 390 °C/27 MPa) [241]. | 56 |
| Figure 1- 21. Appearances of the Y-TZP sample hydrothermally treated at 300 °C for 24 h [242]. | 57 |
| Figure 1- 22. Transient response of chromium effluent concentration following changes in reactor inlet oxygen concentration at 400 °C and 238 atm [79]. | 58 |
| Figure 2- 1. Schematic illustration of the reactive sintering process | 84 |
| Figure 2- 2. Schematic illustration of the process incorporated reactive sintering with freeze casting. | 86 |
| Figure 2- 3. A sketch of freeze casting experimental setup. | 86 |
| Figure 2- 4. Schematic illustration of the process for fabricating porous Cr ₂ O ₃ . | 87 |
| Figure 2- 5. A sketch of the experimental setup for the fabrication of Cr ₃ C ₂ -Cu composite. | 88 |
| Figure 2- 6. Schematic illustration of the static SCW test autoclave adopted in the current study. | 89 |
| Figure 2- 7. Schematic illustration of the dynamic SCW fluid loop adopted in the current study. | 90 |
| Figure 3- 1. Schematic illustration of the fabrication procedure. | 98 |
| Figure 3- 2. A sketch of freeze casting experimental set up. | 98 |
| Figure 3- 3. SEM micrographs of sintered samples casted at 25 °C with a solid loading of 10 vol. %: (a) surface, (b) Cross-section, (c)(d) high magnification images on struts. | 100 |
| Figure 3- 4. SEM micrographs of porous samples obtained which were freeze casted at 25 °C with solid loading content of (a)(d) 10 vol. %; (b)(e) 20 vol. %; (c)(f) 30 vol. %; (d)(e)(f) are images in high magnification. | 101 |
| Figure 3- 5. Correlation of porosity with the content of solid loading at the casting temperature of 25 °C. | 102 |

| | |
|---|-----|
| Figure 3- 6. Porous morphologies of samples casted at (a) 0 °C; (b) 15 °C; (c) 25 °C; with a same solid loading content of 10 vol. %..... | 103 |
| Figure 3- 7. Optical images of solidification structure of a dilute slurry. | 107 |
| Figure 3- 8. Porous morphologies of freeze casted YSZ sample and Cr ₃ C ₂ sample: both of those two samples were freeze casted under the same condition, YSZ sample was sintered in air for 2 hours, (c)(d) were images in high magnification. | 108 |
| Figure 3- 9. SEM micrographs of 100% Cr ₂ O ₃ green disk before sintering (a) and after sintering at 1100 °C in reducing atmosphere (2% CH ₄ +98% H ₂) for 10 hours (b) surface, (c) cross-section and (d) equilibrium dihedral angle between grain boundary and solid/vapor interfaces [34]. | 110 |
| Figure 4- 1. SEM micrographs of 100% Cr ₂ O ₃ green disk before sintering (a) and after sintering at 1100 °C in reducing atmosphere (2% CH ₄ +98% H ₂) for 10 hours (b) surface and (c) cross-section [14]. | 125 |
| Figure 4- 2. SEM micrographs of chromium oxide sample added with various amount of cobalt after carburization at 1100 °C for 10Hrs: (a) 5 wt. % Co (b) 10 wt. % Co (c) 15 wt. % Co (d) 20 wt. % Co (e) 35 wt. % Co (f) 45 wt. % Co..... | 127 |
| Figure 4- 3. The change of porosity with the cobalt content. | 128 |
| Figure 4- 4. XRD patterns of carburized samples added with various amount of cobalt. | 129 |
| Figure 4- 5. XRD patterns of (a) mixing sample (24.4 wt. % Co + 75.59 wt. % Cr ₇ C ₃); (b) carburized sample with 20 wt. % Co. | 130 |
| Figure 4- 6. EDS mapping results for carburized sample added with 10 wt. % cobalt... | 131 |
| Figure 4- 7. EDS mapping results for carburized samples added with various amounts of cobalt..... | 132 |

| | |
|--|-----|
| Figure 4- 8. XPS analysis for the cobalt added samples: A(1-3) - Co 2p _{3/2} peaks; B(1-3) - Cr 2p _{3/2} peaks; C(1-3) - C 1s peaks; 1, 2, 3 denote the samples added with cobalt of 5, 20, and 50 wt. % respectively. | 136 |
| Figure 4- 9. Measured hardness values of cobalt added samples and calculated hardness values based on MSA model..... | 139 |
| Figure 4- 10. Relative changes of the hardness derived by using the measured average value minus the theoretical value. | 143 |
| Figure 4-11. The dissolved cobalt content in M ₇ C ₃ phase plotted against the cobalt content being added..... | 144 |
| Figure 5- 1. Supercritical water test facility. | 153 |
| Figure 5- 2. SEM micrographs of 100% Cr ₂ O ₃ green disk before sintering (a) and after sintering at 1100 °C under a reducing atmosphere (2%CH ₄ +98%H ₂) for 10 hours (b) surface and (c) cross-section [13]. | 155 |
| Figure 5- 3. Surface morphologies of porous carbide coupons after SCW tests at (a) 375 °C, (b) 425 °C and (d) 450 °C; (d) (e) (f) are magnified images. | 157 |
| Figure 5- 4. XRD patterns of coupons after SCW tests at different temperatures: (a) 375 °C; (b) 425 °C; (c) 450 °C; (d) 625 °C. | 158 |
| Figure 5- 5. Surface morphologies of porous chromium carbide after SCW tests at 415 °C under different pressures: (a) 12~15 MPa; (b) 25~28 MPa; (c) 33~35 MPa; (d) 47~50 MPa..... | 159 |
| Figure 5- 6. Surface morphologies of the porous chromium carbide after exposure in air at different temperatures (a) 425 °C, (b) 800 °C. | 162 |
| Figure 5- 7. Surface of chromium carbide sample prepared by HIPping: (a) before SCW test; (b) and (c) after SCW test at 500 °C/25MPa for 25h; (d) Cross-section of HiPping sample after SCW exposure test..... | 163 |
| Figure 5- 8. Predicted corrosion products in equilibrium between Cr ₃ C ₂ and H ₂ O..... | 165 |

| | |
|--|-----|
| Figure 5- 9. FT-IR spectra (transmission) of (a) porous Cr_3C_2 ; (b) porous Cr_3C_2 exposed in air at 425 °C; (c) porous Cr_3C_2 exposed in SCW at 400 °C; (d) porous Cr_3C_2 exposed in SCW at 450 °C. | 166 |
| Figure 5- 10. Proposed mechanism for cracks induced by decomposition of CrOOH ; the crystal structure of CrOOH was adapted from reference [18]. | 169 |
| Figure 6- 1. An insulated pressure tube design of the CANDU-SCWR fuel channel [4] | 174 |
| Figure 6- 2. Supercritical Water Test Facility. | 178 |
| Figure 6- 3. Morphologies of (a) as-compressed Cr_2O_3 sample, (b) porous Cr_3C_2 sample, (c) porous Cr_2O_3 sample. | 180 |
| Figure 6- 4. Morphologies of porous chromium oxide obtained by oxidizing different porous chromium carbide ceramics at 850 °C for 50 hours in air; the carbide ceramics were obtained by carburizing chromium oxide at: (a) 1000 °C; (b) 1100 °C; (c) 1200 °C; (d) 1300 °C for 15 hours. | 181 |
| Figure 6- 5. Morphologies of the porous Cr_2O_3 added with (a) 5 wt. % Y_2O_3 , (b) 10 wt. % Y_2O_3 , (c) 20 wt. % Y_2O_3 , (d) Back scattered electron image of porous Cr_2O_3 with 20 wt. % Y_2O_3 | 182 |
| Figure 6- 6. X-ray diffraction patterns of chromium oxides added with various amounts of yttria at 5 wt. %, 10 wt. % and 20 wt. % | 182 |
| Figure 6- 7. Weight changes of porous Cr_2O_3 after exposure at different temperatures for 100 hours under a pressure of 25-30 MPa in supercritical water. | 184 |
| Figure 6- 8. Partial disintegration of porous chromium oxide after exposure at 625 °C for 100 hours in SCW: (a) Powders collected from the SCW capsule reactor and un-disintegrated sample remain (inset); SEM image of Cr_2O_3 sample after SCW test: (b) at low magnification; (c) Zoom in on the surface; (d) at high magnification. | 185 |

| | |
|---|-----|
| Figure 6- 9. Pourbaix diagram for Cr-H ₂ O system under different conditions: (a) 25 °C/1 MPa; (b) 625 °C/25 MPa..... | 188 |
| Figure 6- 10. Spectra of Cr2p _{3/2} from the high resolution XPS analysis of water after SCW test at 600 °C for 25 hours using hydrogen peroxide solution (30 wt. %)...... | 189 |
| Figure 6- 11. Weight changes of chromium oxide based ceramics with yttria addition after being exposed to SCW at 625 °C under a constant pressure of around 25-30 MPa..... | 193 |
| Figure 6- 12. Surface morphologies of yttria added porous chromium oxide after SCW tests at 625 °C for 600 hours: (a) 5 wt. % yttria added, (b) 10 wt. % yttria added, (c) 20 wt. % yttria added. | 194 |
| Figure 6- 13. Y and Cr concentration analyzed by mass spectra for the water liquid after SCW tests at 625 °C for 100 hours; (0Y ₂ O ₃ - Pressed pure Cr ₂ O ₃ sample, 5Y ₂ O ₃ , 10Y ₂ O ₃ , 20Y ₂ O ₃ - Porous Cr ₂ O ₃ ceramics added with yttria at 5 wt. %, 10 wt. %, 20 wt. %, respectively). | 195 |
| Figure 6- 14. XRD patterns recorded for samples added with various amounts of yttria before and after SCW tests at 625 °C for 600 hours. | 197 |
| Figure 6- 15. Comparison of Cr concentration measured in the water samples from three capsule reactors after exposure at 600 °C for 100 hours. The capsule reactor was either not loaded or loaded with a pure chromium oxide coupon and a 5Y ₂ O ₃ -Chromium oxide coupon, respectively (wppm-in weight). | 199 |
| Figure 7- 1. Schematic illustration of the static SCW test autoclave adopted in the current study. | 212 |
| Figure 7- 2. Schematic illustration of the dynamic SCW fluid loop adopted in the current study. | 212 |
| Figure 7- 3. Morphology of the as-sintered samples (a) Sample A1; (b) Sample A2; (c) Sample A3; (d) Sample B1; (e) Sample B2; (f) Sample B3; (g) Sample C1. | 213 |

| | |
|---|-----|
| Figure 7- 4. Weight changes of Cr ₂ O ₃ samples after exposure in SCW with different levels of oxygen at 625 °C/25 MPa: I-deionized water utilized to conduct the test; II-hydrogen peroxide solution (30 wt. % H ₂ O ₂) utilized to conduct the test. | 216 |
| Figure 7- 5. Disintegration of porous chromium oxide sample (A2) in SCW at 625 °C/25 MPa: (a) Powders from the disintegration; (b) Magnified image of powder particles; (c) Remained part of the sample after SCW exposure; (d) Magnified image on the surface of remained part (inset: magnified image to show the cracks formed). | 216 |
| Figure 7- 6. The concentration of chromium ion present in the water liquid after the static SCW tests. ([O ₂]-calculated oxygen concentration present in SCW; 8 ppm, 40 ppm-the oxygen concentration of the deionized water used; H ₂ O ₂ - 30 wt.% H ₂ O ₂ solution was used.)..... | 219 |
| Figure 7- 7. The concentration of chromium ion present in the water solution after an exposure of Sample A1 in SCW 650 °C/25 MPa for different times. Deionized water with 8 ppm oxygen concentration was used to conduct the tests with no purge procedure. | 219 |
| Figure 7- 8. Weight changes of sample B(1~3) and C(1~3) after static SCW tests for 500 hours. Deionized water with 8 ppm oxygen was used to conduct the tests with no nitrogen purge. | 221 |
| Figure 7- 9. Weight changes of Cr ₂ O ₃ based ceramics after exposing to flowing SCW at 625 °C/25 MPa. Each sample was sequentially exposed to flowing SCW with different levels of oxygen: 8 ppb (using deionized water as the feeding liquid), 8 ppm (using deionized water with oxygen concentration of 8 ppm as the feeding liquid), H ₂ O ₂ (4 vol. %)(using hydrogen peroxide solution containing 4 vol. % H ₂ O ₂ as the feeding liquid)..... | 223 |
| Figure 7- 10. Surface morphologies of Samples A2 after SCW loop test for 700 hours: (a) low magnification; (b) high magnification. | 224 |

| | |
|--|-----|
| Figure 7- 11. Surface morphologies of Samples B1 (a) and B2 (b) after SCW loop test for 700 hours (insets: cracks observed). | 225 |
| Figure 7- 12. Surface morphologies of Samples C1: (a) low mag. (d) high mag., C2: (b) low mag. (e) high mag. and C3: (c) low mag. (f) high mag. after SCW loop test for 700 hours..... | 226 |
| Figure 7- 13. Spectra of Cr2p _{3/2} from the high resolution XPS analysis of water after SCW test at 600 °C for 25 hours using hydrogen peroxide solution (30 wt. %). | 229 |
| Figure 7- 14. EDS mapping of chromium oxide based ceramics after exposure at 625 °C in SCW with high oxygen level (30 % H ₂ O ₂ solution was used) for 100 hours: (a) Secondary electron image; (b) EDS mapping for Mo. | 230 |
| Figure 7- 15. Illustration of the roughness, grain size and grain boundaries with the stability of Cr ₂ O ₃ ceramics in SCW environments..... | 232 |
| Figure 7- 16. EDS mapping of cross-section of Samples C2 and C3 after SCW loop tests. | 235 |
| Figure 7- 17. Illustration showing the transportation of chromium species from Samples C2 and C3 during SCW loop exposure. | 235 |
| Figure 8- 1. SEM micrographs of 100% Cr ₂ O ₃ green disk before sintering (a) and after sintering at 1100 °C in reducing atmosphere (2% CH ₄ +98% H ₂) for 10 hours (b) surface and (c) cross-section [22]. | 246 |
| Figure 8- 2. (a) and (c): SE and BE SEM images of obtained composite; (b): Interface between the composite and copper; (d): magnified microstructure image of composite. (A: closed pore; B, C: voids and gaps formed may be due to the shrinkage of copper during solidification). | 248 |
| Figure 8- 3. XRD patterns of the composite obtained. | 248 |
| Figure 8- 4. Fracture surface of the composite at different magnification. | 249 |

| | |
|--|-----|
| Figure 8- 5. Comparison of hardness values of pure copper, composite, “lower bound” and “upper bound” determined by the “rule of mixture” and calculated value according “GRM” model. | 255 |
| Figure 8- 6. (a) diagram representing the extreme case ($\rho=0$) for porous structure that the pores totally surround solid particles; (b) Part of the indentation after the hardness test for the composite. | 256 |
| Figure 8- 7. Comparison of Young’s modulus values of composite with calculated values predicted: “lower bound” and “upper bound” determined by the “rule of mixture” and calculated value according “GRM” model and “Tuchinskii” model (lower bound). | 260 |
| Figure 9- 1. Surface (a) and cross-section (b) of the porous chromium carbide after being electroplated with nickel; (c) Inner porous matrix. | 271 |

Chapter 1 Introduction and Literature Review

1.1 Introduction

Because of the severe climate change caused by the increase of the CO₂ emission, CO₂-free nuclear power has become more and more attractive in recent years [1]. However, most of the current nuclear plants are run with generation II and III reactors, which have been operated for many years, with many concerns for their safety, efficiency and operating cost. To overcome the aforementioned deficiencies, new generation nuclear reactor concepts termed as the fourth generation nuclear reactors have been proposed by the Generation IV International Forum (GIF) [2]. Supercritical Water-Cooled reactor (SCWR) is one of the most promising nuclear reactor concepts proposed by the GIF.

The SCWR has also been proposed to be the next generation nuclear power plant for Canada's nuclear industry, as developing the SCWR can take the advantage of the current Canada's nuclear infrastructures [3, 4]. As stated by the Canadian National Program on Generation IV Energy Technologies Research and Development priorities, the identification of appropriate materials for in-core and out-of-core components will be one of the major challenges for the development of the supercritical water reactor (SCWR) since no single material has currently received enough study to ensure its performance in an SCWR [4].

This research project aims to identify and to test new porous insulation and coating materials for the potential use in the Canadian Gen-IV SCWR. The research focuses on the development of bulk porous ceramic carbides and oxides as well as bulk ceramic-metal composites that entail high corrosion resistance and

chemical stability and at the same time provide good insulation and corrosion protection desirable for their application in the SCWR. This research will explore new materials that have not been considered for this application before. It is believed that this research will generate new knowledge/technology key to the future development of Canada's nuclear industry.

1.2 Literature Review

1.2.1 Supercritical fluids

When a compound is above its critical point ($P > P_c$, $T > T_c$), this compound goes into its supercritical phase state that is different from normal gas, liquid, or solid phases, which is called the supercritical phase [5]. It has been determined that every stable compound has its critical point and Table 1-1 lists the critical temperatures and pressures for a variety of commonly used supercritical fluid (SCF) chemicals [5, 6]. As shown in Table 1-1, different chemical compounds have much different critical temperature and pressure. Water and carbon dioxide are probably the most widely used SCF compounds that have been extensively used in various industries, including power generation, chemical extraction, waste treatment, food production, and chemical synthesis [5, 7-10].

Table 1- 1. Critical temperature and pressure for various solvents [6].

| Solvents | Critical Temp. (°C) | Critical Pressure (MPa) |
|------------------------|----------------------|-------------------------|
| Carbon dioxide | 31.1 | 7.38 |
| Water | 374.2 | 22.05 |
| Ethane | 32.2 | 4.88 |
| Propane | 96.7 | 4.25 |
| Propylene | 91.6 | 4.62 |
| Cyclohexane | 280.3 | 4.07 |
| Isopropanol | 235.2 | 4.76 |
| Benzene | 289.0 | 4.89 |
| Toluene | 318.6 | 4.11 |
| p-Xylene | 343.1 | 3.52 |
| Chlorotrifluoromethane | 28.9 | 3.92 |
| Trichlorofluoromethane | 198.1 | 4.41 |
| Ammonia | 132.5 | 11.28 |
| Ethylene | 9.3 | 5.04 |

Supercritical fluid can be considered as a dense gas with both liquid-like and gas-like characteristics, as it usually exhibits a liquid-like density but with gas-like transport properties [11]. A supercritical fluid can be treated as a homogeneous single phase due to the disappearance of the gas-liquid interface, however, it also exhibits an inhomogeneous microscopic structure that consists of clusters of

solvent molecules and free spaces [12]. SCFs have tunable physicochemical properties, such as density, viscosity and diffusivity, that can be continuously adjusted by varying the pressure and temperature [13, 14]. This tunable properties enable SCFs to find some specific applications, such as the solvents for highly specific separations or reactions [12].

1.2.2 Supercritical water and its properties

When the temperature and pressure exceed the critical temperature ($T_c = 374.2 \text{ }^\circ\text{C}$) and pressure ($P_c = 22.05 \text{ MPa}$) of water, the interface between the gas and liquid phase disappears and water goes into its fourth phase state called Supercritical Water (SCW) [6] [7, 14]. Figure 1-1 shows the supercritical domain for water.

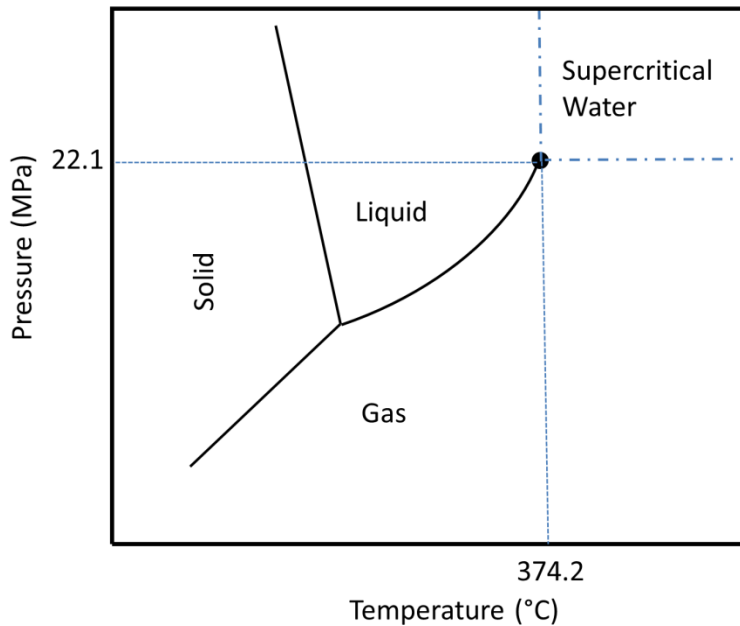


Figure 1- 1. Phase diagram of water and the supercritical domain [6].

Like other SCFs, SCW also exhibits variable properties, such as tunable pressure and volume in its supercritical domain. Under supercritical conditions, the density of water can be tuned continuously from low (gas-like) values to high (liquid-like) values without phase transition by varying the pressure and temperature [7]. Figure 1-2 shows the change of water density when temperature or pressure are crossing the critical values [15]. As shown in the isothermal diagram, the density of water increases significantly when the pressure of water approaches the critical pressure. When increasing the temperature, the density of water decreases and an evident drop can be observed at a certain temperature as shown in the isobaric diagram. The ionic product of water decreases drastically when water goes into its supercritical region as shown in Figure 1-3 [15].

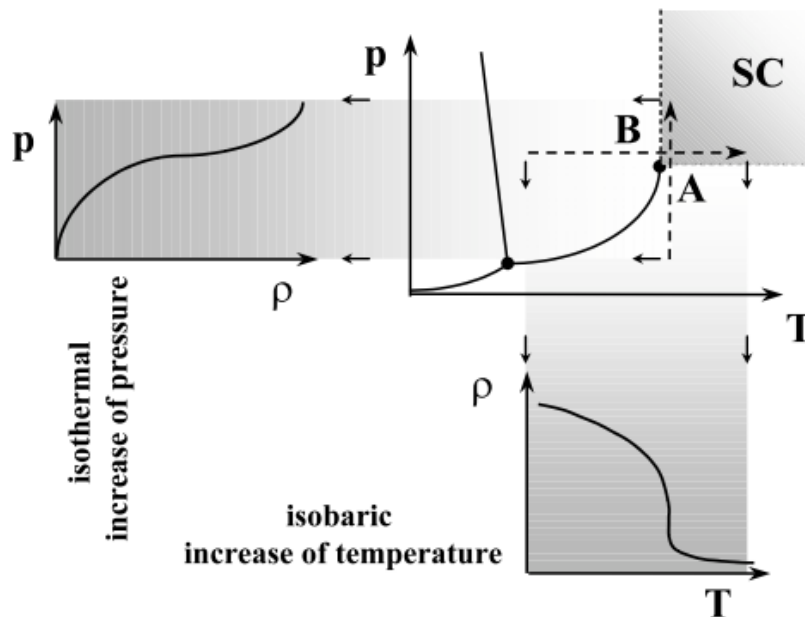


Figure 1- 2. Phase diagram of water and schematic course of density versus pressure and temperature (P - Pressure, ρ – Density, T – Temperature, SC – Supercritical region) [15].

From a microscopic view, the SCW consists of water molecular clusters (high density area) and free space cavities (low density area) between those clusters [16]. The clusters appeared in SCW have been analyzed in detail by Yoshii et al. [17-20]. Those clusters were described as bulky, fractal, containing a lot of open spaces. It has been found that larger clusters, which usually have longer lifetime than smaller clusters, are easily observed in the SCW with higher density [19, 20].

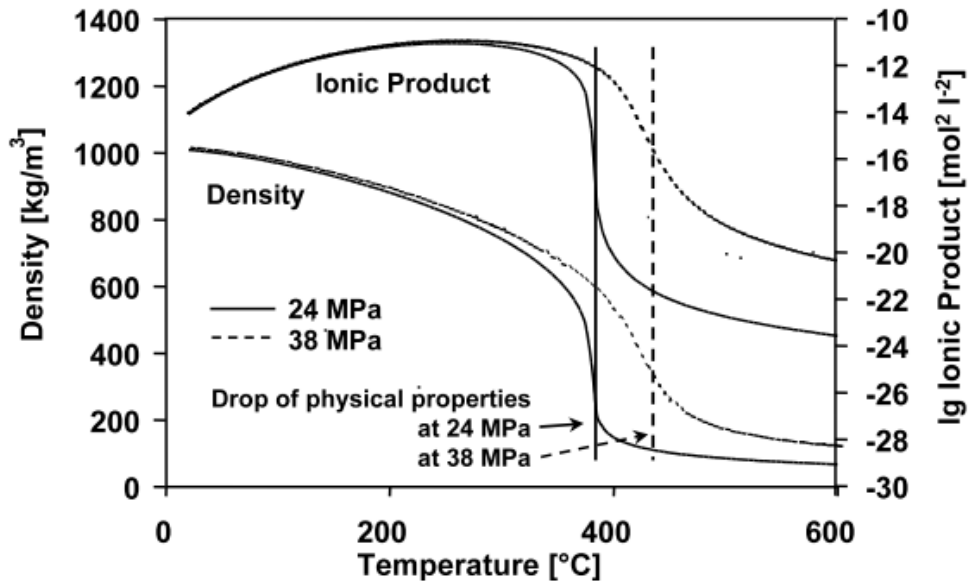


Figure 1- 3. Drop of physical properties of high-temperature water at different pressure [15].

The properties of SCW are quite different from that of the normal water liquid or atmospheric steam. One significant difference is the change of the solubility for some substances. It was found that ionic compounds, such as salts, which are usually soluble in normal water liquid, become almost insoluble in low-density

SCW [21]. Sodium chloride can only be slightly dissolved with a solubility value of 100 ppm and sodium sulfate can slightly be dissolved with a solubility value of 1 ppm [22]. However, the SCW can completely dissolve gases (such as oxygen (O_2), nitrogen (N_2), carbon dioxide (CO_2) and methane (CH_4)) and organic compounds (i. e., miscible in all proportions) [9, 23]. The change of the solubility behaviour of water is intimately related to the variation of the dielectric constant of water under different conditions. The dielectric constant (k) is a measure of the degree of molecular association [24]. Under ambient condition, water has a dielectric constant value of 80 [25]. With increasing temperature and decreasing density, the dielectric constant value of water decreases significantly to about 5 at the critical point [26]. The decrease of the dielectric constant is mainly caused by the change of hydrogen bonding when the density of water is decreasing, as it has been found that hydrogen bonds get attenuated with the amount significantly reduced under SCW condition [16, 27, 28].

Another important property of SCW is the heat-transporting property. The early investigation of the heat transfer at supercritical pressures was conducted by Schmidt et al. in 1930s, who studied the free convection heat transfer in fluids at the near-critical point [29, 30]. Their studies show that SCW fluid has a high free convection heat transfer coefficient (HTC) at the near-critical state. Later, the heat transfer of SCW attracted more attention and was studied by many researchers because of its potential application in steam power plant and nuclear reactor [31-33]. The heat transfer characterized by the thermal-physical properties (specific

heat) changes significantly near the critical and pseudo-critical regions [34]. Figure 1-4 shows the specific heat of water correlated with temperature and pressure [35, 36]. As shown in this figure, the specific heat is high in the pseudo-critical regions and a maximum value was achieved at around the critical point ($P = 22.1 \text{ MPa}$, $T = 374 \text{ }^\circ\text{C}$).

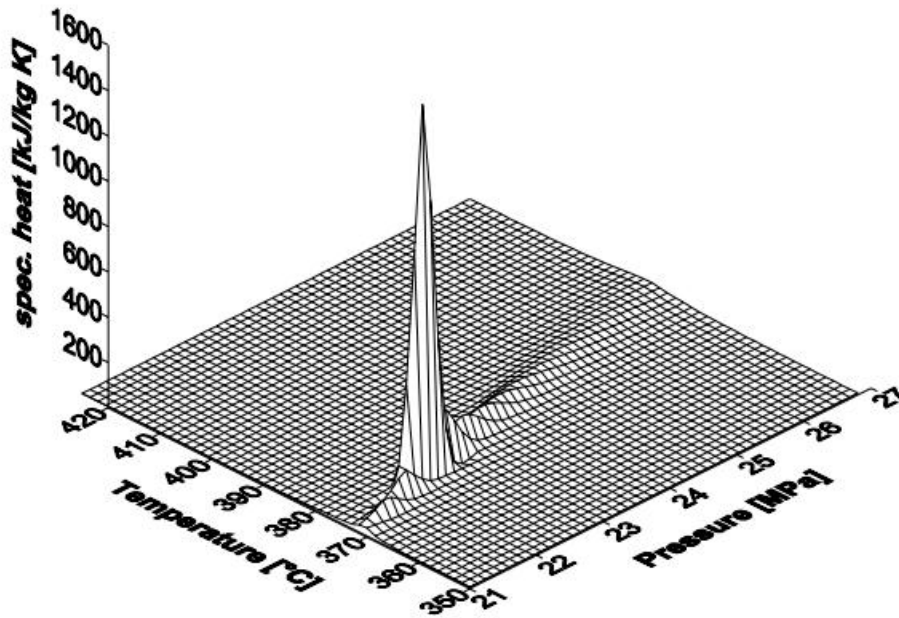


Figure 1- 4. Specific heat of water [35, 36].

Swenson et al. [32] and Yamagata et al. [33] investigated the heat transfer behavior of SCW flowing in different tubes. Both of their results show that the heat transfer coefficient of water in the pseudo-critical region was dependent on the heat flux. The high heat flux usually lead to lower heat transfer coefficient and the heat transfer deteriorates under low heat flux condition which may be related to the mass velocity of the water flow [33].

1.2.3 Supercritical Water-cooled Reactor (SCWR)

SCW has been considered to be used in nuclear reactors as early as 1950s [8, 37]. The early concepts for supercritical water-cooled reactor had been developed during the 1950s and 1960s mainly conducted by US and Japan [8, 38, 39]. Two types nuclear reactors that use SCW as the coolant have been proposed, one is called Supercritical Light Water Reactor (SCLWR-H) [40], and the other one is called Supercritical Water-cooled Fast Reactor (Superfast Reactor) [41]. Currently, a number of SCWR concepts are being under development worldwide and SCWR has also been proposed as one of the most promising next generation (Gen-IV) nuclear reactors by the Generation IV International Forum [2]. The advantages offered by SCWRs are listed below [37, 42, 43]:

- (1) The thermal efficiency of reactor can increase from about 30-35% of current generation water-cooled reactors to about 45-50 %.
- (2) The heat transport system is simplified by elimination of the steam generators, steam dryers, and steam separators, as the coolant remains one single phase from the core inlet to the high pressure turbine.
- (3) Reduced size of reactor components and containment buildings because of the decrease of the coolant mass flow rate by using the coolant with a high enthalpy.
- (4) No risks of coolant boiling or dry out, since the coolant keeps on one phase state under the operation condition.
- (5) Improved safety and reduced risks because of the simplified thermal cycle design.

- (6) Decreased electrical energy cost because of the increased thermal efficiency and reduced capital costs.

One most important conceptual design for SCWRs is the Canadian SCWR design (CANDU[®] -SCWR) which uses light water as the coolant operated at a fixed pressure of 25 MPa, with an inlet temperature of 350 °C and an outlet temperature of up to 625 °C. The thermophysical properties of water for the CANDU[®]-SCWR, the current CANDU[®]-6 and the Pressurized Water Reactor (PWR) are shown in Table 1-2 [43, 44]. The pressure tube design in the current light water reactor cannot be used for the SCWR because of the increased operation temperature and pressure. Therefore, a new pressure tube design, called the “High Efficiency Channel” (HEC), has been proposed, which is shown in Figure 1-5 [44]. This design uses a pressure tube (usually made of Zr-alloy) that contacts directly with the moderator. The heavy water will be used as the moderator which operates at an average temperature of about 80 °C. An insulator will be placed between the fuel bundle and the pressure tube which can thermally insulate the pressure tube from the hot SCW coolant. A perforated metal liner may also be used to protect the insulator from erosion by the coolant flow and from being damaged by the fuel bundles. The pressure of SCW coolant is applied to the pressure tube through the perforated metal liner and small openings in the insulator [44].

Table 1- 2. Comparison of the values of thermophysical properties of water for the conditions of CANDU-SCWR, CANDU-6 and PWR [8, 44].

| Parameter | Unit | CANDU[®]- SCWR | CANDU[®]-6 | PWR |
|------------------------------------|-------------------|--|--|--|
| Pressure | MPa | 25 | 10.5 | 15 |
| Temperature Inlet-Outlet | °C | 350 - 625 | 265-310 | 290-325 |
| ΔT from inlet to outlet | °C | 275 | 45 | 35 |
| Density | kg/m ³ | 625.5- 67.58 | 782.9-692.4 | 745.4-664.9 |
| Enthalpy | kJ/kg | 1624-3567 | 1159-1401 | 1285-1486 |
| Increase in enthalpy | kJ/kg | 1943 | 242 | 201 |
| Specific heat | J/kg ·K | 6978-2880 | 4956-6038 | 52576460 |
| Expansivity | 1/K | 5.17 ·10 ⁻³ - 1.74 ·10 ⁻³ | 2.09 ·10 ⁻³ - 3.71 ·10 ⁻³ | 2.54 ⁻³ - 4.36 ·10 ⁻³ |
| Thermal conductivity | W/m ·K | 0.481-0.107 | 0.611-0.530 | 0.580-0.508 |

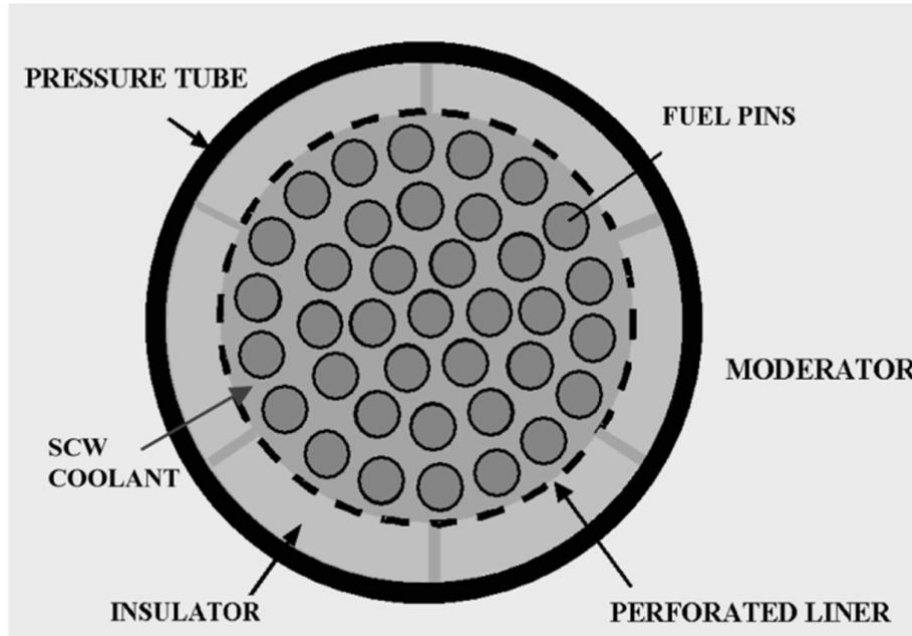


Figure 1- 5. An insulated pressure tube design of the CANDU-SCWR fuel channel [44].

1.2.4 Insulation materials

This research will focus on the development of the porous ceramic as well as ceramic-metal composite materials which can be used as insulators in the SCWR. The general requirements for the insulation material include [44]: 1. High corrosion resistance in SCW; 2. Effective thermal insulation with good stability that will withstand thermal stresses and cycling; 3. Enough strength to bear the load of the fuel bundles; 4. Resistance to irradiation damage.

1.2.4.1 Material selection

Generally, the thermal energy carriers in solid materials for heat transfer mainly include phonons (lattice vibration), free electrons, and thermal radiation [45, 46].

The total thermal conductivity can be represented as [46]:

$$k_{th} = (const)(N_{th}\lambda_{th}v_{th}) \quad 2-1$$

Where k_{th} represents the thermal conductivity, N_{th} represents the number of thermal energy carriers (free electrons, phonons), v_{th} represents the average velocity of thermal energy carriers, λ_{th} is referred to as the mean free path represent the average distance that the disturbance caused by the application of heat travels before being scattered.

In solid materials, especially in metals, free electrons are the major thermal energy carrier which are more efficient to transfer heat because of its high velocities and long free paths [47, 48]. Because of the presence of relatively large numbers of free electrons, metallic materials usually have very good thermal conductivity. The values of the thermal conductivity of most metals generally range between about 20 to 400 W/m·K [49].

Compared to metals, most of ceramic materials usually have much lower thermal conductivity because of the lack of large numbers of free electrons. Phonons are the principle thermal energy carriers in ceramic materials. Phonons usually have much shorter free paths and their transfer can be significantly disturbed by defects, grain boundaries, and other internal imperfections [45, 47]. Therefore, ceramics usually have low thermal conductivities and can be used as thermal insulation

materials. The thermal conductivity values of most ceramics are usually between 2 and 50 W/m·K [46]. Table 2-3 lists the thermal conductivity values for a number of commonly used ceramic materials [45, 46]. It can be noted that some ceramics, such as SiC, BeO, and AlN, have much higher thermal conductivity values than other ceramics. This is because the scattering of phonon is reduced by their highly ordered structures composed of same mass/size atoms or ions. [46, 50, 51].

In addition to the low thermal conductivity, ceramics possess some unique properties, such as high melting point, high hardness and Young's modulus, high chemical inertness, high corrosion and wear resistance, which make them suitable for use as coating or insulation materials in some harsh environments. Table 1-4 lists a variety of ceramic materials commonly used for coating deposition by thermal spraying technique [52].

Table 1- 3. Thermal conductivity of some ceramics [45, 46].

| Materials | k (W/m·K) | Materials | k (W/m·K) |
|--------------------------------|-----------------|-------------------------------------|--------------|
| Al ₂ O ₃ | 39 | Ti ₃ SiC ₂ | 43 |
| MgO | 37.7 | Cordierite (Mg- aluminosilicate) | 4 |
| SiO ₂ | 1.4 | Glasses | 0.6-1.5 |
| BeO | 63.0- 216.0 | Forsterite | 3 |
| PSZ | 2 | SiAlON | 21 |
| SiC | 84.0-93.0 | Borosilicate (Pyrex) glass | 1.4 |
| Si ₃ N ₄ | 25 | Cr ₃ C ₂ | 19 |
| TiB ₂ | 40 | Cr ₂ O ₃ | 10 |
| Spinel | 12 | cemented carbides | 14.3-119 |
| Soda-lime silicate glass | 1.7 | Fully stabilized ZrO ₂ | 1.7 |
| AlN | 200.0- 280.0 | Mullite | 5.2 |

One of the most important applications of ceramics by virtue of the low thermal conductivity is thermal barrier coatings (TBCs), which are usually used on turbine parts in aerospace industry [53-57]. The commonly used ceramic materials for TBCs have been reviewed by Cao et al. [55], which are listed in Table 2-5. The selection of the insulation materials for the SCWR can take the advantage of the existing knowledge on TBC materials because of some similar application requirements, such as low thermal conductivity and chemical inertness.

Table 1- 4. Thermal spraying of various ceramics [52].

| Property | Examples | Details |
|-----------------------------------|--|---|
| Wear/abrasion resistance | Al ₂ O ₃ , WC-Co, Cr ₂ C ₃ -Ni-Cr, TiO ₂ , Al ₂ O ₃ -TiO ₂ , TiC, Mo, ZrO ₂ , SiC | Resistance to abrasion, erosion, fretting, friction, sliding wear |
| Thermal barrier coatings | MCrAlY (M=Fe, Co, Ni), ZrO ₂ , Al ₂ O ₃ , YSZ | Oxidation, thermal insulation |
| Electrical insulation | Al ₂ O ₃ , Al ₂ O ₃ + TiO ₂ , | Insulating property |
| electronic | TaN, In ₂ O ₃ , WN ₂ , TiN, WSi ₂ , YSZ, Co-fired ceramics (HTCC, LTCC) | Conductive ceramics |
| Biocompatibility | TiO ₂ , hydroxyapatite (HA) coatings, porcelain | Tissue growth propensivity |
| Aesthetics | TiN, Al ₂ O ₃ | Jewelry, tiles, coatings, gemstones |
| Oxidation/corrosion resistance | Ti ₃ SiC ₂ , Al ₂ O ₃ , ZrO ₂ , SiO ₂ , MgO, Cr ₂ O ₃ | Resistance against oxidation/corrosion |
| Ultra-high-temperature resistance | W, W-Re, HfC, Al ₂ O ₃ , TaC | Resistance to ultra-high-temperature softening and wear |

Table 1- 5. TBC materials and their characteristics [55].

| Materials | Characteristics | |
|--|--|--|
| 7-8 YSZ | (1) High thermal expansion coefficient (2) Low thermal conductivity (3) High thermal shock resistance | (4) Sintering above 1473 K (5) Phase transformation (1443 K) (6) Corrosion (7) Oxygen-transparent |
| Mullite | (1) High corrosion-resistance (2) Low thermal conductivity (3) Good thermal-shock resistance below 1273k (4) Not oxygen-transparent | (5) Crystallization (1023-1273 K) (6) Very low thermal expansion coefficient |
| Alumina | (1) High corrosion-resistance (2) High hardness (3) Not oxygen-transparent | (4) Phase transformation (1273 K) (5) High thermal conductivity (6) Very low thermal expansion coefficient |
| YSZ+CeO ₂ | (1) High thermal expansion coefficient (2) Low thermal conductivity (3) High corrosion-resistance (4) Less phase transformation between m and t than YSZ (5) High thermal-shock resistance | (6) Increased sintering rate (7) CeO ₂ precipitation (> 1373 K) (8) CeO ₂ - loss during spraying |
| La ₂ Zr ₂ O ₇ | (1) Very high thermal stability (2) Low thermal conductivity (3) Low sintering (4) Not oxygen-transparent | (5) Relatively low thermal expansion coefficient |
| Silicates | (1) cheap, readily available (2) High corrosion-resistance | (3) Decomposition into ZrO ₂ and SiO ₂ during thermal sparying (4) Very low thermal expansion coefficient |

1.2.4.2 Oxide ceramics

1.2.4.2.1 Yttria-stabilized Zirconium oxide (YSZ)

Zirconium oxide (ZrO_2) is an extremely refractory material, which exists in three crystal phases: the fluorite cubic structure at temperatures higher than 2370 °C, the tetragonal structure between 1150 and 2370 °C, and the monoclinic structure below 1150 °C [58]. With decreasing temperature, ZrO_2 usually undergoes phase transitions from a cubic to tetragonal ($c \rightarrow t$) at around 2300 °C and a tetragonal to monoclinic ($t \rightarrow m$) at around 1000 °C. Because of the difference in the density, volume expansion occurs when ZrO_2 transforms from cubic to tetragonal to monoclinic, which can induce large stresses and cracking because of the induced stress [58, 59]. The transition from tetragonal to monoclinic is characterized by a martensitic phase transition accompanied by a relatively large volume increase (3~5 %), generating large shear and volume elastic strains in the monoclinic phase, which may lead to the catastrophic cracking failure of the ceramics [60]. However, it has been found that the volume expansion of $t \rightarrow m$ transformation induced by the controlled stress in the area of crack front can increase the fracture toughness of the ZrO_2 ceramics [61-64]. Partially stabilized zirconia (PSZ) ceramics, which are usually fabricated by adding small amounts of oxides such as CaO, MgO, and Y_2O_3 to stabilize the metastable tetragonal phase, are the most widely used mechanically superior zirconia-based ceramics [65-67].

Yttria-stabilized Zirconia (YSZ), which is the most extensively studied and used TBC material, has been proposed as one of the candidate insulation materials considered for the SCWR fuel channel [44]. YSZ possesses a very low thermal

conductivity (around 2.7 W/m · K), attributed to the existence of high concentration of point defects, including oxygen vacancies and substitutional solute atoms, which can effectively scatter heat-conducting phonons [68]. YSZ exhibits high corrosion resistance in most ambient and high temperature corrosive environments [56]. YSZ possesses a high hardness (about 14 GPa), which makes it highly resistant to erosion [69]. YSZ also has a low neutron cross-section and is exceptionally resistant to irradiation damage from fast neutron and energetic ions [70].

Chow et al. has calculated the wall thickness of the porous YSZ insulator (Porosity: 70%) by using the following rough upper-bound estimation, which was around 7 mm to keep the heat lost at around 1.5% of the thermal power [44].

$$k_e = v_1 k_1 + v_2 k_2 \quad 2-2$$

Where k_e is the effective thermal conductivity, k_i is the thermal conductivity and v_i is the volume fraction of the i^{th} component.

Although YSZ shows advantages over many other ceramics for use in the SCWR, there is a concern about the high oxygen ion conductivity of YSZ that can potentially cause the corrosion of the Zr-alloy pressure tube that is in direct contact with the YSZ. The formation of Zr oxides on the surface of Zr-alloy exposed to a SCW environment can be illustrated in Figure 1-6 [71]. As shown in

this figure, the corrosion of Zr-alloy occurs through the reaction between the zirconium metal and the negative oxygen ions dissociated from water. The corrosion rate of Zr alloy was determined by the transfer of the negative oxygen ions diffused toward the metal side as well as the opposite transfer of the free electrons from the ionization of zirconium. The studies conducted by Howlader et al. has demonstrated that the slow-diffusing negative oxygen ions may control the oxidation process of zircalloys [71]. The high oxygen ion conductivity of YSZ may lead to the corrosion of the pressure tube alloy if YSZ was used as the insulation material. This issue has been confirmed by Guzonas et al. in the SCW corrosion tests of zirconia films deposited on carbon steel and stainless steel surfaces using a zirconia colloid [72]. Their corrosion testing results show that although zirconia films can improve the corrosion resistance of carbon steel in relatively short duration (200-300 hours) time in a SCW autoclave, an increased corrosion rate was observed for the coated stainless steel samples. They also found that a chromium-rich oxide layer formed under the zirconia film by SIMS characterization, indicating that the film may not be preventing the transport of species to or from the metal surface [72]. Hui et al. evaluated the performance of a crack-free ZrO_2 coating applied on Zr-2.5Nb substrates exposed to SCW environment [73]. Their results show that the coated Zr-2.5Nb samples exhibited better corrosion resistance than the coating-free samples when tested in static SCW, but identical weight changes were observed for both samples when tested in a flowing system.

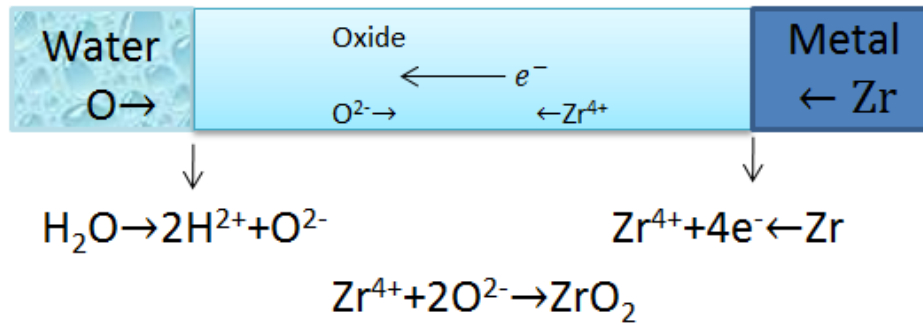


Figure 1- 6. A schematic diagram showing the formation of oxide film on zirconium and the reactions during oxidation [71].

In addition to the above potential problems, the corrosion of Zr oxide in SCW has not been well defined. Sato et al. investigated the phase and the microstructure changes of yttria-doped tetragonal ZrO_2 polycrystals annealed in water at temperatures from 65° to 120°C [74]. Their results show that the annealing treatment accelerated the phase transformation of ZrO_2 from tetragonal to monoclinic which caused appearance of micro-cracks on the surface. Hirano et al. studied the transformation of the crystalline phase and microstructure of Y-TZP, (Y, Ce)-TZP, Y-TZP- Al_2O_3 and (Y, Ce)-TZP- Al_2O_3 composites under hydrothermal conditions at 180°C and 1 MPa and they also found that the tetragonal phase of ZrO_2 could easily transform to monoclinic phase by ageing under the hydrothermal condition accompanied by the formation of micro-cracks [75]. The t→m low temperature (150° to 400°C) water vapor aging phenomenon has also been confirmed by Lange et al. [76] who examined the detrimental water aging phenomenon in $\text{ZrO}_2\text{-Y}_2\text{O}_3$ materials in hydrothermal environments. They

suggested that the reaction between water and yttrium may play an important role in the phase transformation of ZrO_2 observed, based on the observation of clusters of small (20 to 50 nm) crystallites of α - $Y(OH)_3$ by TEM examination.

1.2.4.2.2 Aluminum oxide (Al_2O_3)

Boukis et al. [77] have conducted screen corrosion tests for various commercial ceramics in SCW containing 0.44 mol kg^{-1} oxygen and 0.05 mol kg^{-1} hydrochloric acid at a temperature of $465 \text{ }^\circ\text{C}$ and a pressure of 25 MPa. Their results show that monolithic Al_2O_3 exhibited better corrosion resistance than Al_2O_3 mixed with other additives. The addition of non-oxide hard particles (20 vol % TiC/TiN) reduced the corrosion resistance of Al_2O_3 . Schacht et al. [78] systematically examined the corrosion resistance of alumina ceramics and zirconia toughened alumina (ZTA) ceramics in aqueous acidic solutions (HCl , H_2SO_4 , H_3PO_4) containing 0.1 mol/kg H_2SO_4 , H_3PO_4 or HCl at $T=240 \text{ }^\circ\text{C}$ - $500 \text{ }^\circ\text{C}$ and $P=27 \text{ MPa}$. Their results indicated that intergranular corrosion was the dominant corrosion mechanism for Al_2O_3 exposed to the SCW environment and the grain boundary phases formed by the segregation of impurities, such as SiO_2 , CaO and MgO , were more susceptible to corrosion. Accordingly, high purity alumina (99.7% Al_2O_3) generally shows the highest resistance against intergranular corrosion in SCW. Hui et al. have evaluated the performance of Al_2O_3 coatings in deaerated supercritical water at $650 \text{ }^\circ\text{C}$ and 25 MPa [73]. They applied a dense Al_2O_3 coating on P91 alloy and found that the weight gain of the coated sample was

significantly reduced about nine times less than that of uncoated sample after SCW exposures for 400 hours.

Although high-purity Al_2O_3 exhibits much better stability in SCW than other ceramics, one problem for using Al_2O_3 as an insulation material is its high thermal conductivity, which may require thicker component or higher volumes of pores to achieve a low thermal conductivity for the use in the SCWR. Another concern for the use of Al_2O_3 in the SCWR is the high solubility of Al_2O_3 in sub-critical water. Figure 1-7 shows the theoretical solubility of Al_2O_3 in sub-critical and supercritical water at 25 MP under neutral conditions [73]. It can be seen that alumina has a much higher solubility in subcritical water than in supercritical water. The results from the corrosion tests conducted by Schacht et al. [78] show high dissolution rates of Al_2O_3 and its corresponding corrosion products in acidic aqueous solution at temperatures of $240^\circ - 290^\circ \text{C}$. They also found that the corrosion rate of Al_2O_3 was still high in the sub-critical water ($340^\circ \text{C} - 500^\circ \text{C}$), although the solubility of the corrosion products decreases and a non-protecting corrosion layer was formed. In the work conducted by Hui et al. [73], the results show that Al_2O_3 coatings appeared to be quite soluble in sub-critical water. Therefore, the high solubility of Al_2O_3 in subcritical water should be a concern if it was used in the SCWR and exposed to the sub-critical water during start-up and shut-down operations.

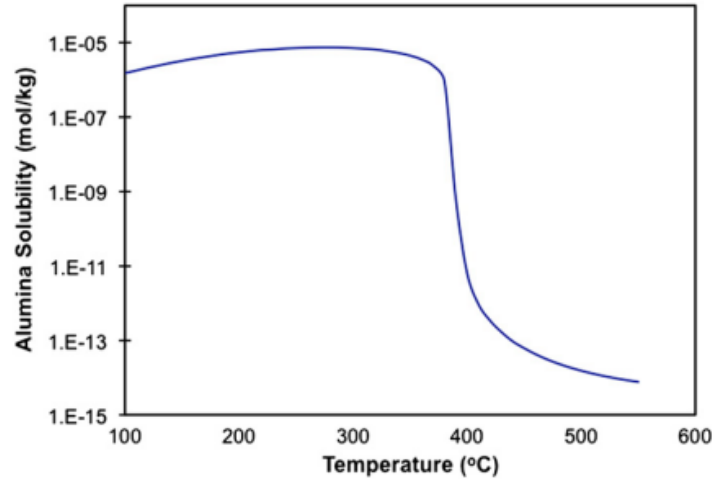
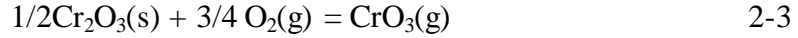


Figure 1- 7. Theoretical solubility of Al_2O_3 in sub-critical and supercritical water at 25 MPa under neutral conditions [73].

1.2.4.2.3 Chromium oxide (Cr_2O_3)

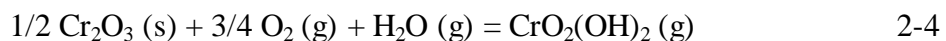
Chromium oxide (Cr_2O_3) has been widely used in various industry areas including corrosion protection, wear resistance, electronics, and optics [79-82]. Cr_2O_3 coatings exhibit high chemical inertness, high mechanical strength, high hardness, high corrosion and wear resistance, and unique electronic properties [81-87]. Cr_2O_3 is also a commonly used refractory or insulation material by virtue of its high melting temperature and low thermal conductivity [88]. It was reported that the thermal conductivity of an as-pressed chromium oxide powder disk with an apparent density of 2.35 g/cm^3 is only $0.45 \text{ W/m} \cdot \text{K}$ at $20 \text{ }^\circ\text{C}$ [89]. The thermal conductivity of a chromium oxide block with an open porosity of 12-18% is around $3.1 \text{ W/m} \cdot \text{K}$ at $1200 \text{ }^\circ\text{C}$ which is comparable with a zirconium oxide block with an open porosity of 8% [88].

The stability of Cr_2O_3 under various oxidizing conditions has been extensively studied. Cr_2O_3 is an important coating material and also an important oxide which plays an important role in protecting steels from corrosion. A protective Cr_2O_3 layer usually forms when alloys containing chromium above a certain threshold concentration are exposed to oxidizing environments. Numerous reports can be found regarding the stability of Cr_2O_3 in various oxidizing environments. Caplan et al. [90] examined the weight loss of Cr_2O_3 at 1000 – 1200 °C in various oxidizing atmospheres. Their results show that more volatilization was observed when the Cr_2O_3 was exposed to wet oxygen than to dry oxygen. However, no volatilization was observed in argon or wet argon, which indicates that the volatilization of Cr_2O_3 observed was related to the presence of oxygen. Brewer suggested that the presence of Cr-species such as $\text{CrO}(\text{g})$, $\text{Cr}(\text{g})$, $\text{Cr}_x\text{O}_2(\text{g})$ and $\text{Cr}_x\text{O}_3(\text{g})$ may contribute to the vaporization of Cr_2O_3 in oxidizing environments [91]. Later research showed that the predominant gaseous species, which was responsible for the volatilization of Cr_2O_3 in a dry oxidizing environment at temperatures higher than 1000 °C, is $\text{CrO}_3(\text{g})$ [92-94]. Grimley et al. identified the presence of CrO_3 during the vaporization of Cr_2O_3 by mass spectrometry [92]. Graham et al. examined the oxidation/vaporization kinetics of Cr_2O_3 in oxidizing environments with different oxygen partial pressure ($P_{\text{O}_2} = 1$ to 10^{-3} atm) at 1200 °C [95] and their results revealed that the correspondence between the volatilization rate of Cr_2O_3 and the experimental determined O_2 partial pressure followed this reaction:



They also suggested that the vaporization rate of Cr_2O_3 was controlled by the mass transport through a gaseous boundary layer close to the surface of Cr_2O_3 .

The evaporation rate of Cr_2O_3 is insignificant at temperatures below 1000 °C, but it has been reported that the evaporation rate increased in the environments containing both O_2 and H_2O [90, 96-98]. Much attention has been attracted to the accelerated evaporation of Cr_2O_3 in wet oxidation atmospheres, since it was believed that the promoted oxidation of Fe-Cr alloys and stainless steels exposed to this environment was related to this evaporation [99-102]. In the investigation conducted by Caplan et al. [90], it was found that the weight loss of Cr_2O_3 in wet oxygen is higher than that in dry oxygen, although the reason for the promoted volatilization in wet oxygen was not clarified. Yamauchi et al. [96] examined the evaporation behaviour of Cr_2O_3 in $\text{N}_2\text{-O}_2\text{-H}_2\text{O}$ atmospheres at temperatures ranging from 900 °C to 1200 °C and found that the evaporation rate of Cr_2O_3 was higher in an $\text{N}_2\text{-O}_2\text{-H}_2\text{O}$ atmosphere than that in $\text{N}_2\text{-O}_2$ and $\text{N}_2\text{-H}_2\text{O}$ atmospheres. They suggested that the enhanced volatilization of Cr_2O_3 was related to the following reaction based on their experimental results:



Asteman et al. [97] studied the influence of water vapour and flow rate on the high-temperature oxidation of 304L alloy at temperature of 600 °C, and their results show that 304L suffered four to five times more corrosion in the atmosphere containing water vapor than that in dry O₂ according to the weight gain observed after 168 hours exposure. They suggested that a non-protective iron-rich oxide was formed instead of a protective oxide film which may be due to the evaporation of CrO₂(OH)₂(g) in the environment containing the high concentrations of water vapour. Graham and Davis [95] examined the oxidation/vaporization kinetics of Cr₂O₃ in oxygen at temperature of 1200 °C, and their results show that adding small amount (2.5 vol.%) of H₂O(g) can result in an evident increase (50% more) of the evaporation rate of Cr₂O₃. They suggested that this might be due to the formation of CrO₂OH(g) according to the following reaction:



The volatile species CrO₃, CrO₂(OH)₂ and CrO₂(OH) have all been proposed or experimentally identified to be responsible for the volatilization of Cr₂O₃ in oxidizing environment with the presence of water [90, 92, 95, 103, 104]. Ebbinghaus [105] evaluated the volatilities of three gaseous chromium oxides and twelve gaseous chromium oxyhydroxides based on equilibrium calculations and concluded that CrO₂(OH)₂(g) is the dominant vapour species for Cr-containing materials exposed to oxygen-water vapour environments across a wide range of

temperatures. Recently, Opila et al. [106] employed both experimental and theoretical calculation methods to identify the volatile species in the Cr-O-H system. Their results also demonstrated that $\text{CrO}_2(\text{OH})_2(\text{g})$ is the primary vapour species for the volatilization of Cr_2O_3 in oxygen - water vapour mixtures at temperatures ranging from 600 °C to 900 °C. They also proved that both $\text{CrO}_3(\text{g})$ and $\text{CrO}_2\text{OH}(\text{g})$ species contribute to the degradation of Cr_2O_3 when exposed to environments containing $\text{O}_2(\text{g})$ and $\text{H}_2\text{O}(\text{g})$ at temperatures higher than 900 °C.

Although the degradation or vaporization of Cr_2O_3 in dry or wet oxidizing environments have been extensively investigated, evaluation of the performance of Cr_2O_3 in SCW especially under the condition close to that in the SCWR is still very limited. However, some potential candidates of Cr-containing alloys for the use in SCWRs have been studied [15, 107-117] and more details can be found in a recent review given by Kritzer [15]. As indicated by Kritzer, the stability of Cr-containing alloys depends on the pH and electrochemical potential of the SCWR environments, while both the pH and electrochemical potential are strongly influenced by the operating condition of SCW, as illustrated in Figure 1-8(a) [15].

As shown in Figure 1-8(b), there exists a stable region for Cr_2O_3 [15]. In the passive region, chromium oxides (Cr(III)) is insoluble and perfectly protects the alloy. Adschiri et al. used a revised Helgeson-Kirkham-Flowers (HKF) model to estimate the solubility of different metal oxides under SCW conditions [118]. Their results show that the solubility of chromium oxide (Cr_2O_3) in SCW is lower

than that of iron and nickel oxides. It has been determined that different thermodynamically stable Cr(III) species (Cr(OH)_3 ; CrOOH ; Cr_2O_3) are favored at different temperatures which can protect Cr-containing alloys from degradation [117, 119]. However, when the potential is out of the stable region, unstable compound such as Cr(II) and Cr(VI) species can form, in which case a protective layer cannot be formed. At high temperatures, the transpassive transformation of chromium and Cr(III) to soluble Cr(VI) compounds becomes easier due to the decrease of the electrochemical potential and therefore Cr-containing alloys are easier to corrode [15, 120]. Nevertheless, It has been proved that Cr is a key alloying element which can improve the resistance against acidic and oxidizing water media and reduce pitting corrosion [15, 98, 102]. Therefore, the stability of Cr_2O_3 will largely depend on the chemical composition and operating conditions of SCW.

Besides the temperature and pressure, the oxygen dissolved in SCW also significantly affects the corrosion of Cr-containing alloys occurring in SCW. Watanabe et al. investigated the effects of oxygen concentration on the corrosion behaviour of alloys, including stainless steels and Ni-base alloys, in SCW containing 0.01 mol/kg H_2SO_4 at 400 °C/30 MPa and 400 °C /60 MPa [121]. Their results show corrosion was promoted for the Ni-based alloy exposed to the SCW with a high oxygen concentration (800 ppm), but the corrosion resistance of iron-based alloys was enhanced in SCW at the high oxygen level. They also

determined that the corrosion resistance of those alloys was dependent on the Cr content [121].

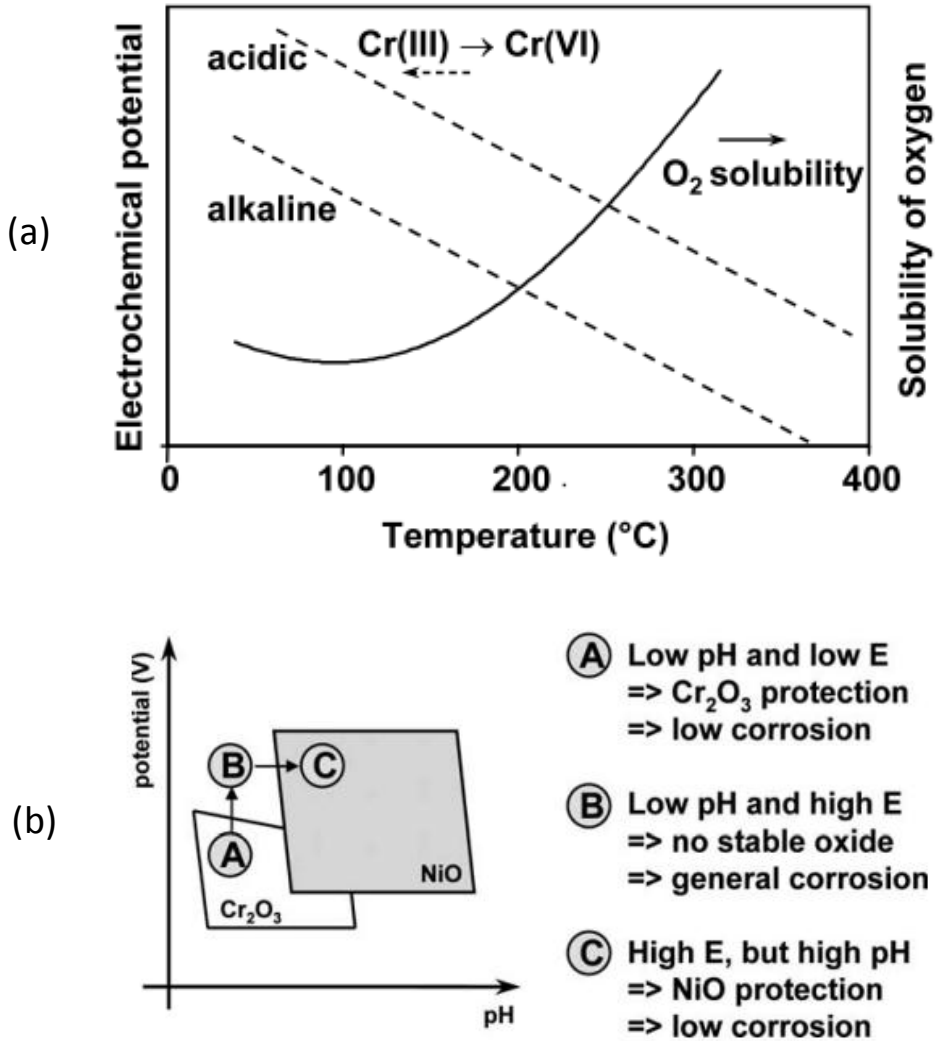


Figure 1- 8. (a) Schematic course of the electrochemical potential for the formation of soluble chromate in acidic and alkaline solutions; (b) Stability islands of chromium and nickel [15].

1.2.4.3 Carbide ceramics

1.2.4.3.1 Chromium carbide (Cr₃C₂)

Cr₃C₂ possesses some unique properties, such as high hardness, high Young's modulus, medium fracture toughness, excellent high-temperature erosion and wear resistance, high-temperature and chemical stability [122-124]. Table 1-6 shows some physical properties of Cr₃C₂ [125]. It was also reported that Cr₃C₂ exhibited the highest oxidation resistance at high temperatures among all metal carbides, and was also highly resistant to acids and alkalies [125]. Among various carbides potentially applicable in the Gen-IV SCWR, Cr₃C₂ has much better fracture toughness, as listed in Table 1-7. Moreover, it has been found that Cr₃C₂ coating showed high stability under the irradiation of neutron flux and was qualified for the use in liquid-metal-cooled nuclear reactors [126].

Table 1- 6. Physical properties of Cr₃C₂ [125].

| Formula | Crystal structure | Density (g/cm ³) | Melting point (°C) | Hardness (GPa) | Young's modulus (GPa) | Fracture toughness (MPa·m ^{1/2}) |
|--------------------------------|-------------------|------------------------------|--------------------|----------------|-----------------------|--|
| Cr ₃ C ₂ | Orthorhombic | 6.68 | 1895 | 27 | 380 | 5.5 |

Table 1- 7. Comparison of the fracture toughness of various carbides potentially applicable in the SCWR.

| Carbides | Cr ₃ C ₂ [127] | TiC[128] | SiC[129] | ZrC[130] |
|--|--------------------------------------|----------|----------|----------|
| Fracture toughness, MPa·m ^{1/2} | 5.5 | 1.7-3.5 | 3.1-3.3 | 4 |

Cr_3C_2 has been extensively used as a thermal spray material for protecting the underlying metal surface, such as coatings of bearings, orifices, valve seals, and also used as an additive added into other sintered ceramics to increase their resistance to corrosion and wear [123, 131-133]. The thermal expansion coefficient of Cr_3C_2 is almost equal to that of steel, which can reduce the stress buildup at the boundary between Cr_3C_2 coating and the surface of steel [134].

Although no direct experiments have been conducted so far to evaluate the performance of Cr_3C_2 in the SCWR environment, Cr_3C_2 has received extensive studies as a coating material under various harsh conditions. The most widely used Cr_3C_2 coating is chromium carbide (Cr_3C_2)/nickel-chrome coatings usually deposited by detonation or plasma spraying techniques, which have proved to be very useful for protecting against corrosion and wear at high temperatures in various industries, such as automobile, aircraft, nuclear, and power [135, 136]. Kosolapova et al. have conducted initial work on the stability of Cr_3C_2 in oxidizing environments at high temperatures and determined that the initial oxidation temperature of Cr_3C_2 was 700 °C [137]. The result was later confirmed by Bhushan, who conducted systematic tests on large number of carbides in oxidizing atmosphere up to 650 °C for 300 hours and Cr_3C_2 survived this screening evaluation [138]. Kuniوشي et al. have studied the erosion-oxidation behavior of thermal sprayed cermet and alloy coatings, including Cr_3C_2 Ni20Cr, Ni20Cr, and WC-20Cr7Ni, at temperatures up to 850 °C (Figure 1-9) [139]. They found that the erosion of substrate (coating) was dominant in the erosion-

oxidation regime at temperatures below 600 °C for both Cr₃C₂Ni₂₀Cr and WC₂₀Cr₇Ni coatings. At temperatures above 600 °C, WC₂₀Cr₇Ni has shown substantial increases of material wastage due to oxidation, while Cr₃C₂Ni₂₀Cr showed little changes in weight loss up to the highest testing temperature of 850 °C. This indicates substantial stability of Cr₃C₂ and a protective role of Cr₃C₂ in highly oxidizing conditions. Mann et al. reported the evaluation of chromium carbide coated valve spindles for the application in steam turbine and their results showed that the chromium carbide coating can give excellent performance which was in agreement with the field performance of this carbide coated component [135].

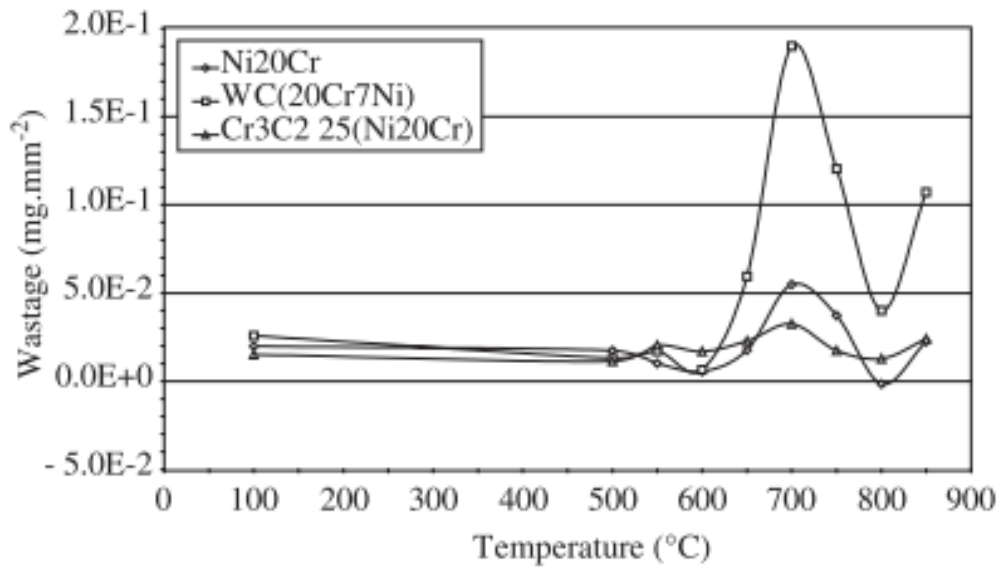


Figure 1- 9. Erosion-oxidation wastage of Ni₂₀Cr, Cr₃C₂25(Ni₂₀Cr) and WC₂₀Cr₇Ni [139].

1.2.4.3.2 Silicon carbide

Several carbides have been assessed under different hydrothermal conditions because of their potential application in nuclear reactors. SiC has been proposed as a candidate cladding material for advanced nuclear fuels by virtue of its excellent high-temperature mechanical properties, and high stability under neutron irradiation [140, 141]. The results obtained by Hirayama et al. [142] show that SiC can be corroded in water at 290 °C, especially at grain boundaries. In the screening corrosion tests conducted by Boukis et al. [77], the SiC exhibited higher corrosion resistance than silicon nitride. Barringer et al. [143] examined the stability of CVD SiC in SCW and the results show that the corrosion rate was lower than that reported for reaction-bonded SiC. More details on the corrosion of SiC in SCW environment can be found in Section 1.2.6.2.1.

1.2.4.4 Reactive elements/oxides

The discovery that addition of rare earth elements can improve the oxidation resistance of alloys can be dated to a very early time [144, 145]. Later, the “reactive element effect” of elements, such as Y, Ce, La, Ti, Zr, Hf ..., has been extensively studied and applied for improving high temperature oxidation resistance of alloys [144, 146, 147]. The beneficial effects of adding reactive elements and the mechanisms have been reviewed by many researchers [144, 146-151]. A comprehensive review has been given by Whittle and Stringer regarding the reactive element effect [147]. In 2001, Pint [152] published another review paper for the understanding of the reactive element effect based on the most recent experimental findings at the time.

The beneficial effects of the addition of reactive elements mainly include:

- (1) REs can promote the selective oxidation of the protective scale-forming element (Cr or Al). Therefore, the required content of Cr or Al for the formation of a protective Cr_2O_3 or Al_2O_3 layer can be reduced [144, 153]. The REs can be oxidized to REOs at the early stage of oxidation process, which promotes the preferential oxidation of Cr/Al because of the nucleation effect [147, 148, 152].
- (2) REs can reduce the growth rate of Cr_2O_3 or Al_2O_3 scales because of the segregation of reactive element ions in the oxide scale grain boundaries which can retard the outward cation transport [154, 155].
- (3) REs can change the growth mechanism for the oxide scales. Since the outward transport of cations can be reduced because of the segregation of reactive element ions, therefore, the inward transport of oxygen becomes the dominant steps for the oxidation process [144, 155, 156].
- (4) REs can inhibit the void formation at the alloy-oxide interface and hence reduce the spallation of the oxide scales, as it was found that the oxide dispersions can act as vacancy sinks. Because the voids at the alloy-oxide interface are suppressed, the adherence of the oxide scale to the alloy substrate is improved [144, 153, 155, 156].
- (5) REs can increase oxide scale plasticity. The increased scale plasticity is attributed to small grain sizes in the scale, since the segregation of RE ions or REO particles inhibit the motion of grain boundaries and the growth of the scale oxides were retarded [155, 157]

(6) REs can reduce the detrimental effect of sulfur in oxidation of alloys. It was found that the scale spallation may be related to the segregation of S at the metal-scale interface[158]. REs, such as Y, can react with S to form a very stable sulfide, which suppresses the segregation of S at the metal scale interface and hence improves the oxidation resistance, especially the cyclic oxidation resistance of alloys [146, 154].

Pint investigated the oxidation of Ni-25wt. %Cr with the addition of different oxides and their results indicated that the RE effects are also related to the size of RE cations as shown in Figure 1-10 [152]. It can be seen that the addition of RE with larger cations is more efficient to increase the oxidation resistance of alloys.

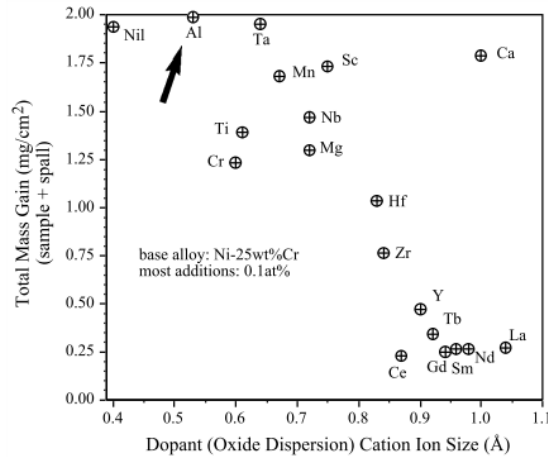


Figure 1- 10. Total mass gain for Ni-25wt.%Cr alloys with various oxide dispersions added at a nominal level of 0.1 cation% after 100h at 1000 °C [152].

1.2.5 Fabrication of porous materials

1.2.5.1 Properties of porous ceramics

Although the presence of pores are usually viewed to be problematic and should be avoided in the fabrication of ceramics, introducing pores into ceramics enable them to obtain some specific properties, such as low thermal mass, low thermal conductivity, controlled permeability, high surface area, low density, controllable strength-to-density and stiffness-to-density ratios, and low dielectric constant [159, 160]. Those unique properties combined with the intrinsic features of ceramics, such as high melting point, tailored electronic properties, high chemical inertness, high corrosion, and wear resistance, enable porous ceramics to be used in many industrial fields, such as for catalysis supports, gas distributors, liquid or gas filters, high-temperature thermal insulators, particulate filters, molten metal filters, preforms for metal-impregnated ceramic-metal composites, and implantable bone scaffolds [159, 161, 162].

The variation of the porosity significantly influences the physical properties of materials as shown in Figure 1-11 [163]. The amount of porosity, pore size, pore shape and distribution and the types of pores (open or close) are highly dependent on the manufacturing process [159]. The properties of material can be optimized by introducing proper amounts of pores through specific processing methods. As shown in Figure 1-11, the thermal conductivity is reduced by increasing the porosity of materials since the heat transfer across pores is inefficient. For the porous insulator material used in the SCWR, the pores will be filled with SCW that has an extremely low thermal conductivity (approximately $0.1 \text{ W/m}\cdot\text{K}$ at $400 \text{ }^\circ\text{C}$) [44]. Therefore, increasing the pore volume can significantly decrease the

thermal conductivity of the insulation material in the SCW environment. Besides that, it was reported that adding pores into ceramics improves the thermal-shock-tolerance, especially when continuous small pores were formed [46]. Russell [164] has discussed the effect of pore size on the thermal conductivity of porous materials at different temperatures. He suggested that small pores were preferred to achieve a low thermal conductivity, since the heat transfer by radiation becomes more effective with large pores at high temperatures.

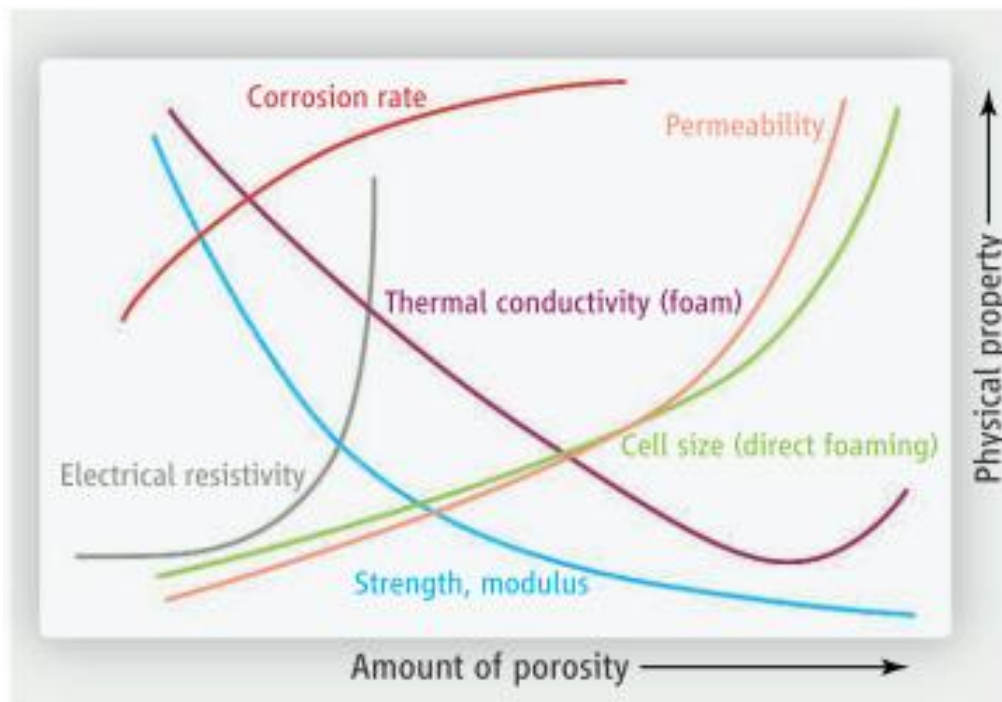


Figure 1- 11. Change of the physical property with different porosity [163].

1.2.5.2 Processing methods

Porous materials are generally classified into three categories based on the size of pores, which include microporous (pore diameters are less than 2 nm),

mesoporous (pore diameters are between 2 nm and 50 nm), and macroporous (pore diameters are larger than 50 nm) [165]. Microporous and mesoporous materials are primarily used for ion exchange and gas sorption by virtue of their huge surface areas, tuneable molecular-size pores, and active sites [166, 167] [168-170]. Those porous materials have been extensively studied because of their numerous applications in catalysis, separation, adsorption and many other fields. Zeolites are the most successfully used microporous materials, which have been widely used in various industries, including catalysts for oil refining, petrochemistry, and organic synthesis in the production of fine and speciality chemicals [171].

The microporous and mesoporous ceramics are not considered for the use as insulation materials in SCWR as severe corrosion may occur due to the huge surface area. The macro-porous ceramics are considered for the use as insulator materials. Many processing techniques have been developed to fabricate a variety of macroporous ceramics [172-176]. More details can be found in a recent review given by Studart et al. [161]. They have classified the techniques for the synthesis of macroporous ceramics into three categories: replica, sacrificial template and direct foaming. The major features of these methods are summarized in Table 1-8. The ranges of porosity and pore size achieved by different methods are shown in Figure 1-12 [161]. It can be seen that reliable methods are still lacking that can fabricate macroporous ceramics with high density pores with the small micro-pore sizes, such as ranging from 500 nm to 5 μm , as shown in Figure 1-12.

Table 1- 8. Comparison of processing methods used for fabricating macroporous materials [161].

| Processing methods | | Pore density/pore sizes | Major features |
|-------------------------------|-------------|---|---|
| Replica: synthetic templates | | 40-95 %/200 μm -3 mm | <ul style="list-style-type: none"> ● Poor mechanical properties ● Open cellular structures for high through-put filtration ● Easy and well-established |
| Replica: natural templates | | 25-95 %/10 μm -300 μm | <ul style="list-style-type: none"> ● Filtration of liquids and gases ● Mechanically anisotropic ● Time consuming process/high costs |
| Sacrificial template | | 20-90 %/1-700 μm | <ul style="list-style-type: none"> ● Long processing time and extensive gaseous by-products ● Feasible for any materials dispersible in an aqueous suspension ● Flexible in pore size, distribution and morphology ● Better mechanical properties than replica method ● Predominantly open pores |
| Direct stabilized surfactants | foaming: by | 40-97 %/35 μm -1.2 mm | <ul style="list-style-type: none"> ● Remarkable mechanical properties ● Easy, cheap and fast |
| Direct Stabilized particles | foaming: by | 40-93 %/10 μm -300 μm | <ul style="list-style-type: none"> ● Simple, cheap, and environmentally friendly ● Mechanical properties considerably better than the replica methods |

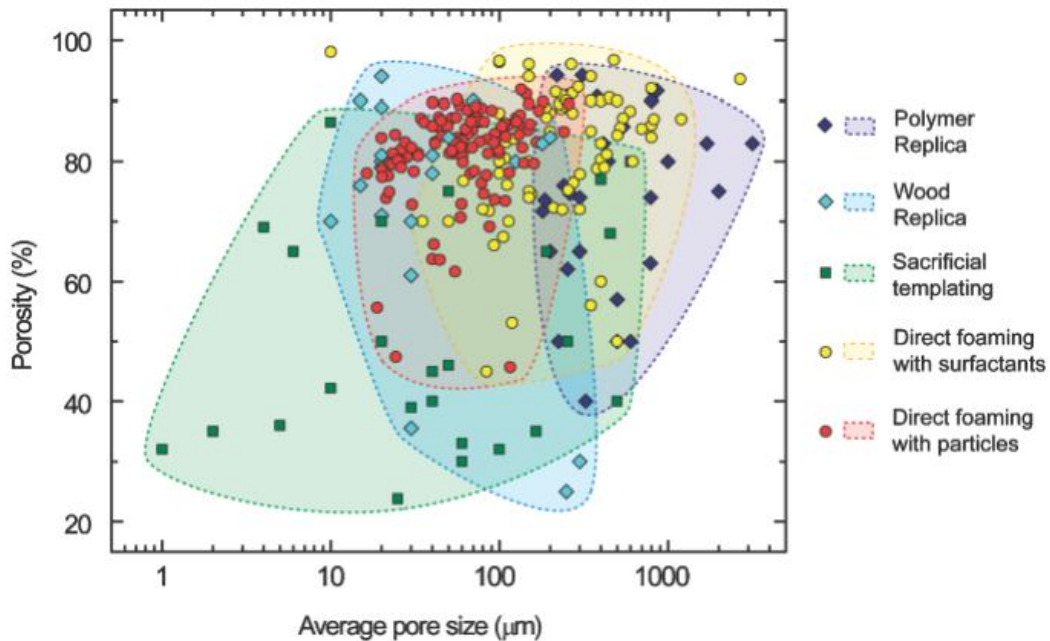


Figure 1- 12. Typical porosity and average pore size achieved via the replica, sacrificial templating, and direct foaming processing routes [161].

1.2.5.3 Fabrication of porous structure by reactive sintering

1.2.5.3.1 Sintering of ceramics

The sintering of ceramics usually proceeds with the evolution of pores during the solid sintering process. The sintering of ceramics has been extensively studied [177-183]. Coble defined solid state sintering process to three different stages [178, 184]: The first stage is featured with the formation of interface between intact particles accompanied with neck growth; In the second stage, evident shrinkage and densification can be observed because of the occurrence of grain growth. Evolution of pores also happens in this stage, in which a continuous and interconnected pore channels evolves to isolated pores at the end of this stage because of the densification of ceramic; The third stage is featured with the

significant grain growth, although the density increase slightly. Isolated pores are produced which are mainly located at grain boundaries, linear or point junctures of grains, or inside grains. Figure 1-13 illustrates the sintering process of a densified ceramic [185].

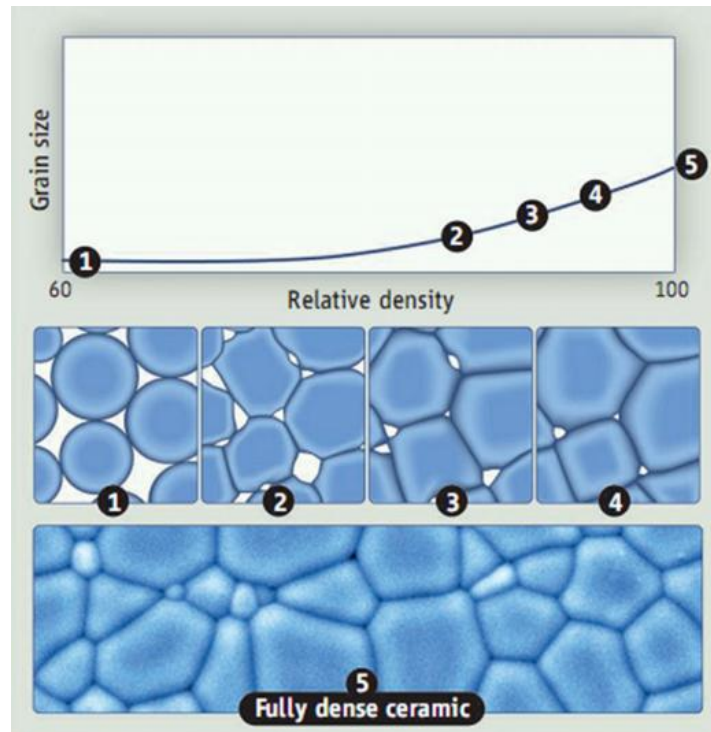


Figure 1- 13. Top: plot of grain size versus sintered density typically observed in ceramics. (1) Random close packing of ceramic particles. (2) Intermediate stage sintering where interconnected pore channels limit grain growth. (3) 92-95% where pore channels close off to form isolated pores at triple points and grain boundaries. (4) Final stage densification where pores shrink and grain growth rate accelerates due to decreasing pore drag. (5) Colorized scanning electron micrograph of a dense ceramic [185].

Therefore, a porous ceramic may be obtained by partial sintering of an initially porous powder compacts. However, the porosity generated by this method is relative low and usually is smaller than 60 vol. % [161].

1.2.5.3.2 Reaction (reactive) sintering method

A reaction sintering process usually involves one or several reactions during the sintering process, and both the reactions and sintering processes affect the final structure of ceramics obtained [186]. Many novel materials have been fabricated using reaction sintering process [187-200]. Claussen [194] reported the fabrication of homogeneous $\text{Al}_2\text{O}_3/\text{Me}_x\text{Al}_y$ composites with interpenetrating networks by reaction sintering of compacted $\text{Al}/\text{Me}_a\text{O}_b$ powder mixtures. Chen et al. [201] prepared mullite ceramics by reaction sintering of kaolinite and alumina at a temperature above 1000 °C. Hong et al. [189] reported the reaction sintering process of a $\text{ZnO}-\text{Al}_2\text{O}_3$ powder mixture. Liou et al. [202] reported the fabrication of stoichiometric PFN ceramics of 100% perovskite phase by reaction sintering of a powder mixture containing PbO , Nb_2O_5 , and $\text{Fe}(\text{NO}_3)_3$ at 1120 and 1210 °C for 2 and 4 hours.

Porous ceramics can be prepared by using reaction sintering method. Eom et al. [203] reported the synthesis of porous silicon carbide (SiC) ceramics with pore size ranging from 0.003 to 30 μm by carbothermal reduction and subsequent sintering process. Their results show that the porosity of porous SiC obtained was affected by the sintering temperature and decreased from 55% at 1800 °C to 40%

at 1950 °C. Yang et al. [204] reported the synthesis of high porous (porosity at about 65-71%) β - Si_3N_4 ceramics with a unique fibrous interlocking microstructure by carbothermal nitridation (CT/N) of SiO_2 .

Recent research has formed a method to fabricate full size porous structure chromium carbide (Cr_3C_2) by a reaction sintering process in a carbonaceous atmosphere [205]. This fabrication technique involves first a low-pressure packing at room temperature to desired geometries, then a medium-high temperature reaction sintering in controlled environments at atmospheric pressure. Figure 1-14 shows the porous chromium carbide obtained by reaction sintering at different temperatures.

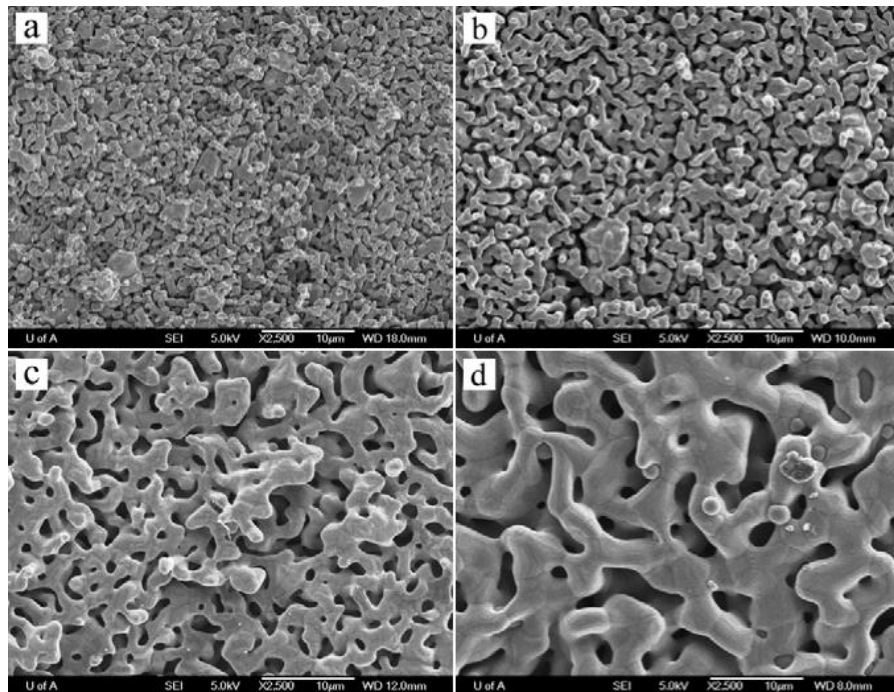


Figure 1- 14. SEM micrographs of pure Cr_2O_3 samples after carburizing at different temperatures in reducing atmosphere (2% CH_4 + 98% H_2) for 10Hrs respectively: a) 1000 °C; b) 1100 °C; c) 1200 °C; d) 1300 °C [205].

The porosity of the porous carbide could reach about 77% at sintering temperatures of 1000 °C and 1100 °C and the pores could be tuned from 0.5 μm at 1000°C to 2.5 μm at 1300 °C. It was suggested that the porous feature was produced due to the volume changes associated with phase transformation during the reaction sintering process [205]. This kind of porous ceramics can be considered for usage as the insulation material in the SCWR because of the high porosity and the inter-connected macro-pores.

1.2.5.4 Fabrication porous materials by freeze casting methods

A freeze casting technique has been used to fabricate ceramic objects for a long time and has attracted considerable attention in fabricating porous ceramics in the last few years [206]. This technique usually uses a wetting agent, such as water [207, 208], silica sol [209], camphene [210], tert-butyl alcohol [211], as the pore forming agent, which is mixed with ceramic powders to form a liquid suspension. Then a casting process is conducted to freeze the liquid suspension in a mold at a temperature below the melting point of wetting agent, which forms a solid cast sample. The pore forming agent will be sublimed out from the cast sample by a sublimation process which is usually conducted under reduced pressure. After the sublimation, a porous structure is therefore obtained, in which the pores are formed as a replica of the solvent crystals. Usually, a following calcination process is required to consolidate and densify the struts [206].

Some studies have been published to report a variety of interesting and highly porous materials fabricated by using freeze casting technique. Figure 1-15 shows

the typical microstructures obtained by different freeze casting methods [206]. Fukasawa et al. reported the synthesis of porous alumina ceramics with a complex porous structure by using a water based freeze casting method [212]. Munch et al. reported the fabrication of tough, bio-inspired hybrid ceramic-based materials obtained by impregnating polymethyl methacrylate into ice-templated lamellar porous aluminum oxide scaffolds [213]. It has determined the porous structures obtained by freeze casting are dependent on the different freezing vehicles used as shown in Figure 1-15 [206, 214, 215].

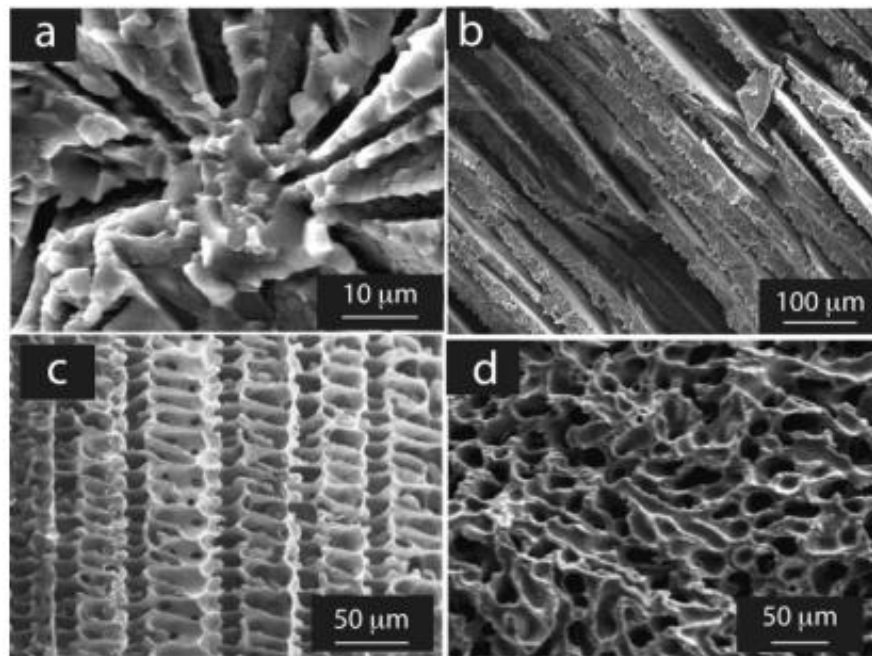


Figure 1- 15. Typical microstructures obtained by freeze-casting (a) porous alumina using a hypoeutectic amorphous/naphthalene as a solvent [206, 216]. (b) porous alumina using water as a solvent [206, 214] (c) porous silicon carbide using polycarbosilane as a precursor and camphene as a solvent [206, 217] and (d) porous alumina using camphene as a solvent [162, 206].

Araki et al. developed a novel freeze casting technique by employing camphene as a freezing vehicle, which produced a porous structure with interconnected pore channels [162]. Recently, more attention has been attracted to this camphene-based freezing casting technique, since sublimation of camphene can be easily conducted at ambient temperature and unique porous structure can be obtained by this method. It is believed that some attractive properties, such as high compressive strength, high permeability and ease to be further engineered, can be obtained by using different freeze casting methods.

1.2.6 Corrosion in SCW environments

The corrosion of materials in SCW is different from that in ordinary water or water solutions, since the chemical-physical properties change significantly when water goes into the supercritical region. Both metals and ceramics have been found to suffer severe degradation in SCW, which is quite different from the corrosion occurred under normal conditions [73, 108, 109]. Some work has been done to investigate the corrosion in various SCW environments. More details can be found in the recent reviews given by Was et al. [110] (SCWR environments) and Kritzer et al. [15] (SCWO environments).

1.2.6.1 Corrosion of metallic materials in SCW

Extensive investigations have been conducted to evaluate a wide range of candidate alloys for the use in an SCWR, including nickel-based alloys (Alloy 625, etc.) [218, 219], iron-based alloys (ferritic-martensitic steels [108, 113, 116],

austenitic stainless steels [111] and ODS steels [107, 220]), zirconium-based alloys [110, 221] and titanium-based alloys [110].

Ferritic-martensitic (FM) and austenitic stainless steels, as well as numerous oxide dispersion strengthened steels, have been extensively evaluated in various SCW environments [108, 110, 115, 222, 223]. Tan et al. evaluated the oxidation behavior of ferritic/martensitic steel HCM12A in SCW at 500 °C, 25 MPa with two levels of dissolved oxygen concentrations of 25 ppb and 2 ppm [114]. Their results show that the growth behavior of oxide scales was affected by the dissolved oxygen concentrations as a parabolic growth behavior was observed under the low oxygen condition while the oxide growth followed a cubic law at the high-oxygen level. Yi et al. investigated the corrosion of 9Cr steel in SCW at temperatures from 370 °C to 500 °C with a pressure of 25 MPa [224]. Their results show that oxidation on the surface was the principle corrosion mechanism for the steel in the high temperature SCW and a bi-layer oxide scale was observed after the SCW exposure. It was also found that bi-oxide layers were formed on the surface of the steel under SCW condition. The bi- or tri oxide scales growth in SCW environments have been observed by other researchers. Gao et al. investigated the oxide film growth on 316L stainless steel exposed to H₂O₂ - containing SCW and they found a duplex-layer consisting of Fe enriched outside layer and Cr, Fe enriched inside layer [225]. In the investigation conducted by Yin [108], a bi-oxide layer (Figure 1-16(a)), which was composed of the outside magnetite (Fe₃O₄) layer and inside spinel ((Fe, Cr)₃O₄) layer, was observed for the

steel sample after exposure in SCW with a low oxygen level. A tri-oxide layer (Figure 1-16(b)) composed of a thin outside hematite (Fe_2O_3) layer, middle magnetite (Fe_3O_4) layer and inside spinel ($(\text{Fe}, \text{Cr})_3\text{O}_4$) layer was formed after exposure in SCW with high oxygen level. Same as the Ferritic-martensitic (FM), it was also found that austenitic stainless steels also formed the bi- or tri- layer structure scales which consist of magnetite, spinel or hematite. [226, 227].

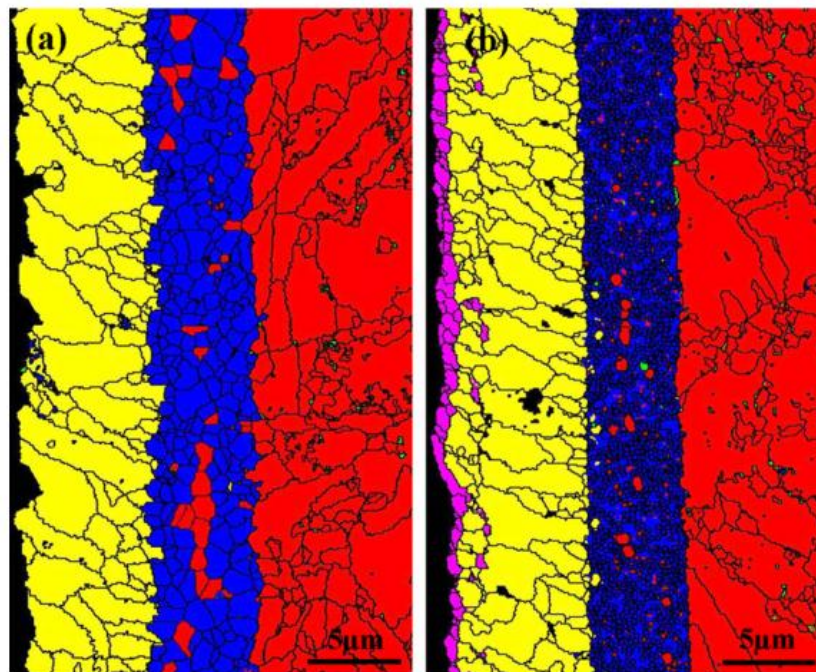


Figure 1- 16. Cross-section EBSD scanning maps of SCW-exposed samples (a) 500 °C, 25 ppb dissolved oxygen, 505 h and (b) 500 °C, 2000 ppb dissolved oxygen, 505 h, where base metal, spinel, magnetite, and hematite are highlighted in red, blue, yellow, and magenta, respectively [114].

The ODS steels were found to show higher oxidation resistance than other conventional steels [223, 228, 229]. Chen et al. examined the oxide layers formed

on a 9Cr oxide dispersion strengthened (ODS) ferritic steel after exposure in supercritical water at 500 °C with a 25 ppb dissolved oxygen concentration [230]. Their results indicated that the improved overall corrosion resistance of 9Cr ODS steel can be attributed to the reactive element effect and that yttrium acts as a barrier for cation diffusion along oxide/metal grain boundaries.

Nickel-based alloys have also been extensively studied because of their high corrosion resistance under SCW conditions. It has been found that the weight gain observed for alloy 625 in SCW is much smaller than that of steel exposed to same environment [112, 231]. Ren et al. examined the corrosion behavior of Ni-based alloys (Inconel 617, 625, and 718) in SCW at 500 °C and 600 °C for up to 1,026 hours [112]. Their results show that the nickel-based alloys mainly suffered surface oxidation and pitting under this SCW condition and alloy 625 exhibited the better corrosion resistance than alloy 718, which may be due to the higher chromium content in alloy 625.

Zr-base, and Ti-base alloys have also been investigated in SCW because of their potential application in SCWR [232, 233]. Motta et al. have investigated the corrosion behavior of a series of model Zr-based alloys exposed to SCW at 500 °C for up to 400 days [234]. Their results show that Zr alloys with added Fe and Cr exhibited higher corrosion resistance than those alloys with other element (Mo, Nb, Cu) additions. The alloys with the compositions of Zr_{0.4}Fe_{0.2}Cr and

Zr1.0Cr0.2Fe showed the highest corrosion resistance and the corrosion rate was up to a factor of two lower than that of the best F-M alloys.

1.2.6.2 Corrosion of ceramics in SCW

Ceramics have received fewer investigations than metallic materials due to their brittle nature which severely limits their use as reactor or structural materials. However, ceramics are considered to be used as coating or insulation materials by virtue of their unique properties and understanding the corrosion behavior of ceramics under SCW condition is essential for the development of the SCWR.

1.2.6.2.1 Non-oxide ceramics

Boukris et al. have evaluated a number of high-performance ceramics in a SCWO environment containing 0.44 mol kg^{-1} oxygen and 0.05 mol kg^{-1} hydrochloric acid at $465 \text{ }^{\circ}\text{C}$ and 25 MPa [77]. Their results revealed that non-oxide ceramics, including Si_3N_4 , SiC , $\text{Si}_3\text{N}_4\text{-TiC/TiN}$, AlN , B_4C , BN , TiB_2 , suffered more severe degradation than oxide ceramics and some of them, such as B_4C , BN , TiB_2 , disintegrated after the exposure.

Silicon carbide (SiC) is probably the most studied ceramic in hydrothermal environment because of its potential application in a fusion reactor [235-237]. Kim et al. have investigated the corrosion behavior of CVD SiC and reaction-bonded SiC (RBSC) in water at $360 \text{ }^{\circ}\text{C}$ [238, 239]. Their results show that CVD SiC exhibited better corrosion resistance than reaction-bonded SiC under SCW

condition and the corrosion kinetics of SiC followed a parabolic law. They also suggested that some residual-free silicon in reaction-bonded SiC could be preferentially corroded during the exposure and the pH value of SCW may also affect the corrosion process. Barringer et al. investigated the corrosion behavior of CVD SiC in SCW at 500 °C and found that the corrosion rate of the CVD SiC was lower than that previously reported [143]. Their results also indicated that hydrated silica species might be produced during the corrosion of the high-purity SiC, which were rapidly dissolved into the supercritical water since no measurable oxide scale was observed on the surface of SiC. In the screening corrosion tests conducted by Boukis et al. [77], the silicon carbide exhibited more corrosion resistance than silicon nitride under the given experimental conditions, although the carbide sample showed a white, brittle layer on the surface and also a higher weight loss compared to oxide ceramics.

Hirayama et al. [142] have investigated the corrosion behavior of SiC in 290 °C water solutions with different pH and dissolved-oxygen concentrations. Their results showed that the corrosion of SiC samples occurred preferentially through intergranular attack, which increased with increasing dissolved-oxygen concentration and was accelerated by increasing pH value. Two dissolution models were proposed by Hirayama et al. which are shown in Figure 1-17 [142]. The first model, as shown in Figure 1-17(1), hypothesized that a protective silica film was formed on the surface and corrosion proceeded through the diffusion and reaction at the interface. However, this model was not well supported by the

experimental results as no SiO₂ surface scale could be detected through SEM, X-ray, or AES examinations and a larger weight loss was observed in oxygenated water. Therefore, the corrosion of SiC under the hydrothermal condition probably occurred according to the second model (Figure 1-17(2)), in which a SiO₂ layer does not produce or does not play an important role in the high-temperature water corrosion. The results obtained by Barringer et al. [143] confirmed that SiC was preferentially attacked at the grain boundaries, as shown in Figure 1-18, and also indicated that no measurable oxide scale formed during the test.

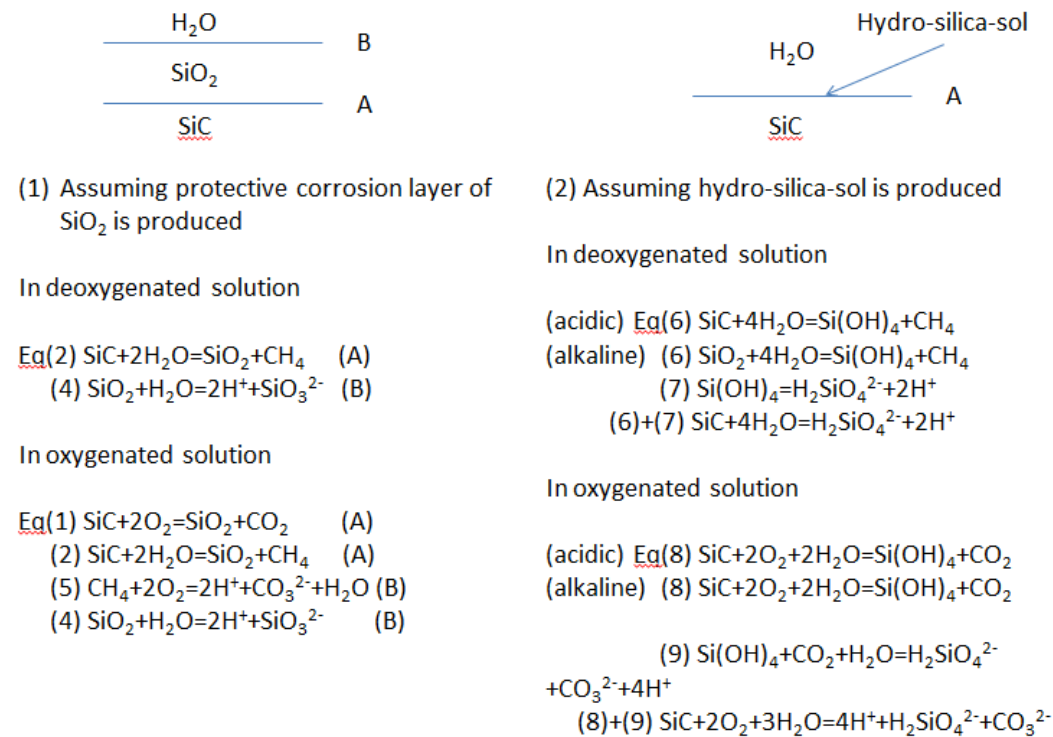


Figure 1- 17. Dissolution model and expected reactions: (1) assuming protective corrosion layer of SiO₂ is produced; (2) assuming non-protective reaction product is produced. (Symbol A and B represent reaction occurring at the interface) [142]

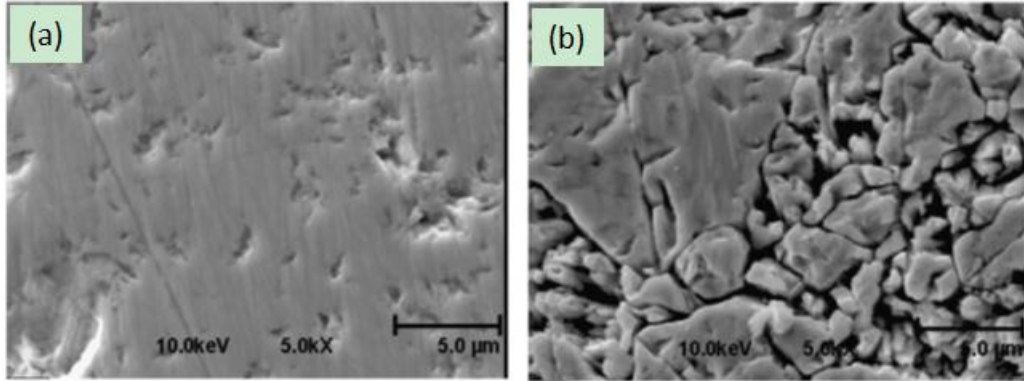


Figure 1- 18. SEM micrographs of surfaces for (a) as-received CVD SiC; (b) after a 21-day exposure [143].

Later Tan et al. [240] investigated the effect of residual strain, grain size, grain boundary types, and surface orientations on the corrosion of CVD SiC exposed to SCW at 500 °C and 25 MPa. Their results show that the corrosion primarily occurred at regions with high intensity of strains. Those strains were believed to be related to the large amounts of grain boundaries in these small-grain regions as shown in Figure 1-19. Tan et al. suggested that the dissolution and diffusion kinetics could be increased in this region due to lattice dilation associated with the stress. Their results also indicated that the degree of attack on the grain boundaries is dependent on the relative grain boundary energies as the boundaries with higher grain boundary energy suffered higher corrosion. The transgranular corrosion occurred on the large grains was found to be related to the surface energy and surfaces with lower surface energies showed higher corrosion resistance.

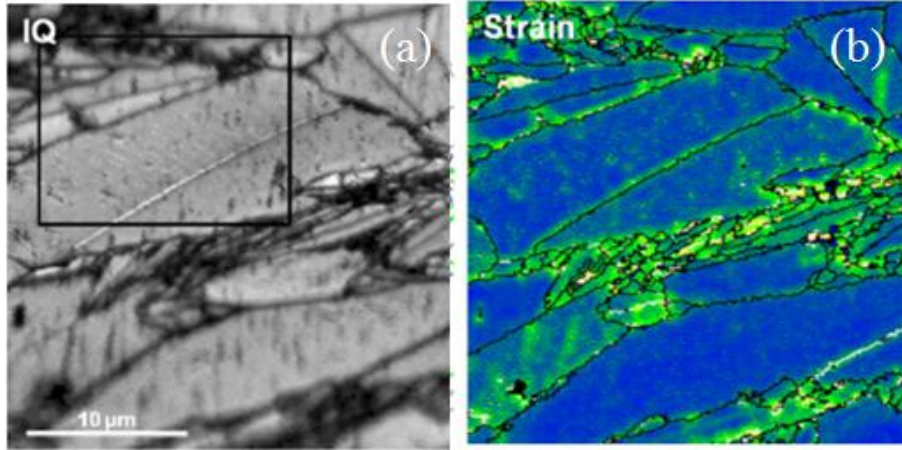


Figure 1- 19. EBSD analysis of the cross-section surface ($28 \times 28 \mu\text{m}$) of the sample exposed to the SCW with ~ 10 ppb oxygen for 333 h (a) SEM image; (b) Strains existed at different regions [240].

1.2.6.2.2 Oxide ceramics

Zirconia ceramics are the most interesting ceramic materials that have been evaluated in various SCW environments. Schacht et al. [241] have assessed the stability of ceria stabilized tetragonal zirconia polycrystals (Ce-TZP), magnesia and yttria partially stabilized zirconia (Mg, Y-PSZ), and magnesia partially stabilized zirconia (Mg-PSZ) in SCW at $390 \text{ }^\circ\text{C}$ and 27 MPa containing 0.1 mol kg^{-1} HCl, H_2SO_4 or H_3PO_4 . Their results show that Mg-PSZ and Ce-TZP is more susceptible to corrosion attack in SCW containing acidic species and a transformation from tetragonal to monoclinic was observed at the surface with the appearance of intercrystalline microrackings (Figure 1-20), which may be caused by the dissolution of Mg or Ce in the SCW environment. Kojima et al. [242] studied the disintegration process of yttria-stabilized tetragonal zirconia polycrystalline (Y-TZP) in a hydrothermal environment at $400 \text{ }^\circ\text{C}$ and 30 MPa .

They found that Y-TZP sintered bodies (sintered at 1550 °C and 1600 °C for 2 hours) disintegrated into small fragments after the hydrothermal treatment as shown in Figure 1-21. The transformation from tetragonal to monoclinic phase was observed for all specimens after the SCW exposure. Lange et al. [243] examined the detrimental aging phenomenon of ZrO_2 - Y_2O_3 ceramics exposed to water vapor at 250 °C by transmission electron microscopy. Their results show that the water vapor reacted with yttrium in the ZrO_2 to produce clusters of small (20 to 50 nm) crystallites of α - $Y(OH)_3$. Therefore, they suggested that this reaction might produce Y_2O_3 depleted spots which act as nuclei inducing the phase transformation (tetragonal to monoclinic). Micro-cracks could be produced due the phase transformation, which may result in catastrophic degradation the ceramic samples.

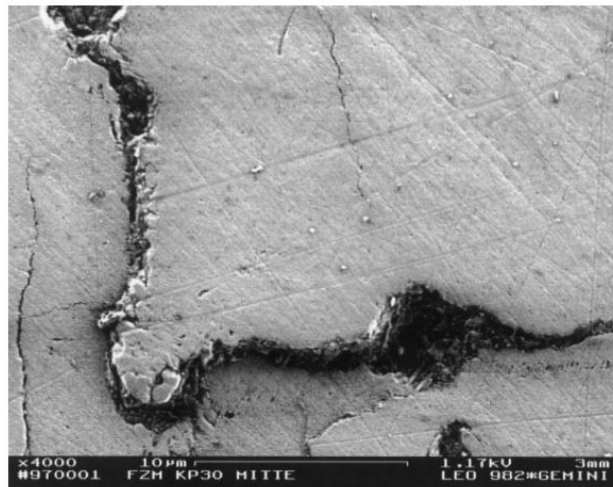


Figure 1- 20. Grain boundary attack on the surface of Mg-PSZ (HCl, 50 h, 390 °C/27 MPa) [241].

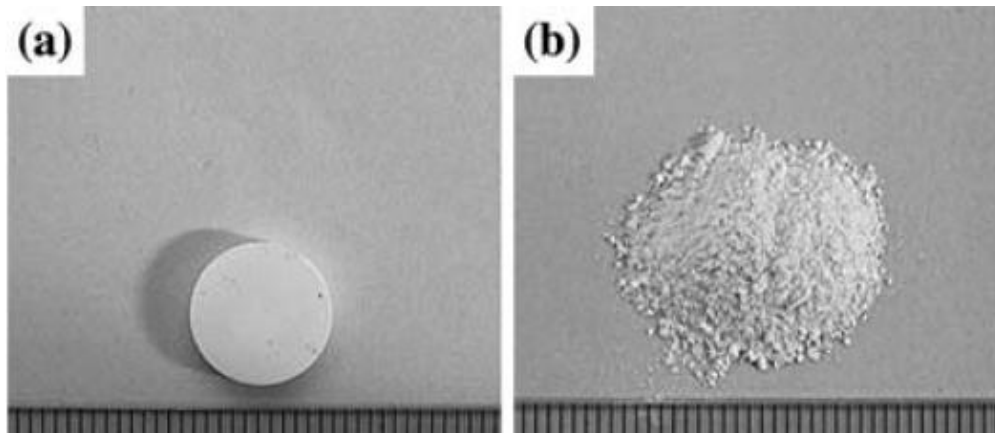


Figure 1- 21. Appearances of the Y-TZP sample hydrothermally treated at 300 °C for 24 h [242].

Few reports can be found on the stability of bulk porous Cr_2O_3 in SCW environments, although, a lot of studies have been undertaken to investigate the evaporation of chromia scale in SCW. Cr-containing alloys have been proposed as candidate alloys for use in the SCWR. Aki et al. [79] investigated the stability of chromium oxide catalyst under SCWO condition at temperatures ranging from 390 °C to 420 °C and pressure of 238 atm. Their results show that the concentration of chromium species present in the reactor effluent, identified as chromic acid (H_2CrO_4), was affected by the dissolved oxygen concentration, as shown in Figure 1-22. When oxygen was not present in the feed, the concentration of chromium in the effluent dropped below the detectability limit of approximately 0.05 ppm. Besides the dissolved oxygen concentration, their results also indicated that the rate of Cr_2O_3 depletion was related to the temperature, water concentration, and flow rate.

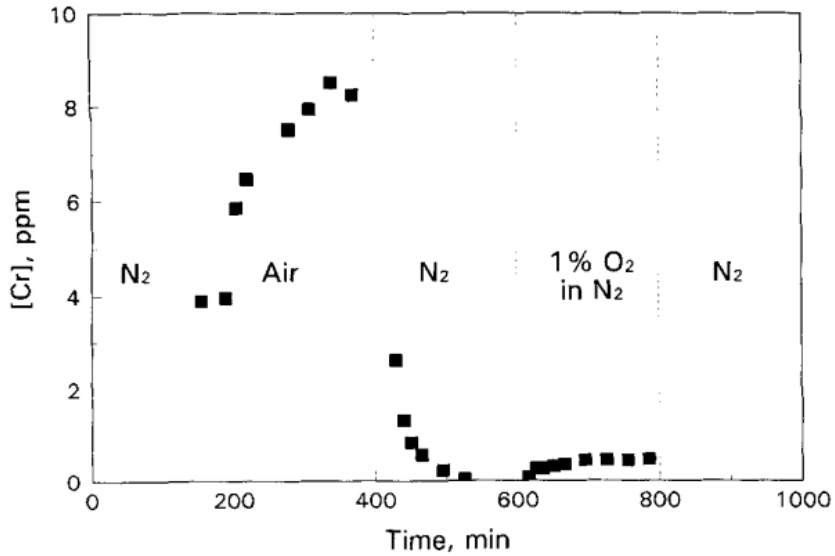


Figure 1- 22. Transient response of chromium effluent concentration following changes in reactor inlet oxygen concentration at 400 °C and 238 atm [79].

The reactive-evaporation rates of Cr_2O_3 in flowing air-water vapor has been studied by Holcomb [244, 245] and Young et al. [246]. A mass-transfer calculation model has been proposed by Young to predict the volatilization of Cr_2O_3 during oxidation based on the very recent thermodynamic data for $\text{CrO}_2(\text{OH})_2$, which shows an accurate prediction for the evaporation rate of Cr_2O_3 (Figure 1-22) [247]. The gas transport theory in the viscous flow regime [248] was used to calculate the mass-transfer rates in the flowing gas mixture. The molar flux, J , of a species is given by

$$J = \frac{k_m}{RT} (p^{(i)} - p^{(o)}) \quad 2-6$$

Where p is the partial pressure of the gas species, the superscripts (i) and (o) represent the values at the solid surface and the the bulk-gas, respectively, k_m is the mass-transfer coefficient which was given as

$$k_m = 0.664 \left(\frac{D_{AB}^4}{\nu} \right)^{1/6} (V/l)^{1/2} \quad 2-7$$

where D_{AB} is the binary gas diffusion coefficient and V is the bulk-gas linear velocity and l is the sample length. D_{AB} is calculated from the following Chapman-Enskog expression:

$$D_{AB} = \frac{1.858 \times 10^{-3} \sqrt{T^3 (1/M_A + 1/M_B)}}{P \sigma_{AB}^2 \Omega_{D,AB}} \text{ (cm}^2 \text{ s}^{-1}\text{)} \quad 2-8$$

Where M_i denotes molecular weight, P is the total pressure and Ω is a “collision integral”,

Figure 1-22 shows the comparison of the measured Cr loss with the values predicted by the proposed model and a good agreement can be observed.

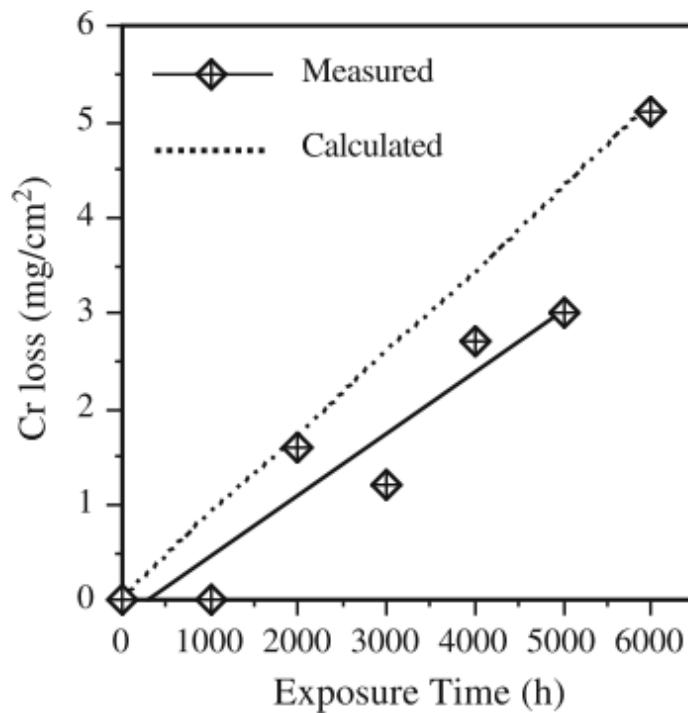


Figure 1-22. Comparison of the calculated and measured Cr loss by evaporation from alloy 709 foils exposed to humid air at 800 °C [246].

1.3 Research Objectives

This project mainly focuses on developing new porous materials that can be used as thermal insulator in the “High Efficiency Channel” (HEC). This porous material should have high corrosion resistance and chemical stability and at the same time provide good thermal insulation desirable for the service in the SCWR. The specific objectives of the project include:

1. Fabricate full-size porous ceramic as well as porous ceramic-metallic composite materials with sufficient mechanical integrity for use in the SCWR.
2. Engineering the composition, surface and pores to improve the corrosion resistance, chemical stability and thermal insulation.

3. Evaluation of the performance of the porous materials in various SCW conditions, and expansion of the SCWR database with information of new insulation materials for selection, which would fulfill Canada's obligations under the Generation IV International Forum (GIF) agreement.

1.4 Proposed Research

As discussed in the literature review, Cr_3C_2 may have the potential to be used in the SCWR. This research will first focus on the fabrication and engineering of Cr_3C_2 -based porous structures for SCWR application. The stability of the porous Cr_3C_2 will be evaluated in SCW environments. Cobalt was added to engineer the porous Cr_3C_2 to optimize the porous structure as well as mechanical properties since cobalt has an excellent wettability with carbides and slight dissolution in the solid carbide. It was also proposed that the porous Cr_3C_2 can be partly immersed into liquid metals to form a solid structure at the surface for enhanced mechanical properties, while the inside still retains its porous structure that can provide thermal insulation as required. Molten Copper was used for the immersion liquid since copper was reported to have a small contact angle with Cr_3C_2 and the reaction between copper and Cr_3C_2 can hardly occur [249]. Efforts will be made to investigate the structures and mechanical properties of the ceramics after the various modifications mentioned.

The performance of Cr_2O_3 will be largely dependent on the operation conditions of the SCWR, such as temperature, pressure or oxygen dissolved, as stated in the literature review. The oxygen content present in a SCWR will be much less than

that in a SCWO environment and it can be further controlled by adding oxygen scavenger into the coolant. However, high concentrations of oxidizing species may be possible in a SCWR core if water radiolysis cannot be controlled [250]. As many Cr-containing alloys have proposed to be the candidate structure materials for the SCWR, the investigation of the stability of Cr_2O_3 will benefit the selection of those alloys since the corrosion resistance of those alloys relies on the stability of oxide scales formed. Ytria was added to improve the corrosion resistance of porous oxide ceramics in the SCW.

1.5 Bibliography

- [1] M.I. Hoffert, K. Caldeira, G. Benford, D.R. Criswell, C. Green, H. Herzog, A.K. Jain, H.S. Kheshgi, K.S. Lackner, J.S. Lewis, H.D. Lightfoot, W. Manheimer, J.C. Mankins, M.E. Mauel, L.J. Perkins, M.E. Schlesinger, T. Volk, T.M.L. Wigley, *Science*, 298 (2002) 981-987.
- [2] GIF-002-00, 2002 December.
- [3] D. Torgerson, B.A. Shalaby, S. Pang, *Nuclear engineering and design*, 236 (2006) 1565-1572.
- [4] S. Baindur, *Bulletin of the Canadian Nuclear Society*, 29 (2008) 32-38.
- [5] R. Noyori, *Chemical reviews*, 99 (1999) 353-354.
- [6] M.A. McHugh, V.J. Krukonis, Elsevier, 1994, pp. 10.
- [7] E.U. Franck, *Supercritical water and other fluids - A historical perspective*, in: E. Kiran, P.G. Debenedetti, C.J. Peters (Eds.) *Supercritical Fluids - Fundamentals and Applications*, Springer, Dordrecht, 2000, pp. 307-322.
- [8] R.B. Duffey, I.L. Pioro, *Supercritical Water-Cooled Nuclear Reactors: Review and Status*, EOLSS Publishers, Oxford, UK, 2005.
- [9] H. Weingärtner, E.U. Franck, *Angewandte Chemie International Edition*, 44 (2005) 2672-2692.
- [10] H. Peker, M. Srinivasan, J. Smith, B.J. McCoy, *AIChE Journal*, 38 (1992) 761-770.
- [11] G.M. Schneider, *Angewandte Chemie International Edition in English*, 17 (1978) 716-727.
- [12] Y.P. Sun, *Supercritical fluid technology in materials science and engineering: syntheses, properties, and applications*, CRC, 2002.

- [13] F. Cansell, C. Aymonier, A. Loppinet-Serani, *Current Opinion in Solid State and Materials Science*, 7 (2003) 331-340.
- [14] D. Broell, C. Kaul, A. Kraemer, P. Krammer, T. Richter, M. Jung, H. Vogel, P. Zehner, *Angewandte Chemie International Edition*, 38 (1999) 2998-3014.
- [15] P. Kritzer, *The Journal of Supercritical Fluids*, 29 (2004) 1-29.
- [16] A.G. Kalinichev, *Reviews in Mineralogy and Geochemistry*, 42 (2001) 83-129.
- [17] N. Yoshii, S. Miura, S. Okazaki, *Chemical Physics Letters*, 345 (2001) 195-200.
- [18] N. Yoshii, R. Miyauchi, S. Miura, S. Okazaki, *Chemical Physics Letters*, 317 (2000) 414-420.
- [19] N. Yoshii, S. Miura, S. Okazaki, *Bulletin of the Chemical Society of Japan*, 72 (1999) 151-162.
- [20] N. Yoshii, H. Yoshie, S. Miura, S. Okazaki, *The Journal of Chemical Physics*, 109 (1998) 4873.
- [21] M. Hodes, P.A. Marrone, G.T. Hong, K.A. Smith, J.W. Tester, *The Journal of Supercritical Fluids*, 29 (2004) 265-288.
- [22] O.I. Martynova, *Solubility of inorganic compounds in subcritical and supercritical water*, NACE National Association of Corrosion Engineers, Houston, TX, 1976.
- [23] A.E. Mather, E.U. Franck, *The Journal of Physical Chemistry*, 96 (1992) 6-8.
- [24] K. Kimura, R. Fujishiro, *Bulletin of the Chemical Society of Japan*, 35 (1962) 85-89.

- [25] M. Uematsu, E. Franck, Static dielectric constant of water and steam, American Chemical Society and the American Institute of Physics for the National Bureau of Standards, 1981.
- [26] R.L. Holliday, J.W. King, G.R. List, Industrial & engineering chemistry research, 36 (1997) 932-935.
- [27] M.M. Hoffmann, M.S. Conradi, Journal of the American Chemical Society, 119 (1997) 3811-3817.
- [28] T.I. Mizan, P.E. Savage, R.M. Ziff, The Journal of Physical Chemistry, 100 (1996) 403-408.
- [29] I.L. Piro, R.B. Duffey, Nuclear Engineering and Design, 235 (2005) 2407-2430.
- [30] E. Schmidt, E. Eckert, U. Grigull, AFF Translation, (1946).
- [31] N. Dickinson, C. Welch, Trans. Am. Soc. Mech. Engrs., 80 (1958).
- [32] H.S. Swenson, J.R. Carver, C.R. Kakarala, Journal of Heat Transfer, 87 (1965) 477-483.
- [33] K. Yamagata, K. Nishikawa, S. Hasegawa, T. Fujii, S. Yoshida, International Journal of Heat and Mass Transfer, 15 (1972) 2575-2593.
- [34] H. Swenson, J. Carver, C. Kakarala, Journal of Heat Transfer, 87 (1965) 477.
- [35] W. Wagner, A. Kruse, Properties of Water and Steam, (1997).
- [36] X. Cheng, T. Schulenberg, Heat Transfer at Supercritical Pressures: Literature Review and Application to an HPLWR, FZKA, 2001.
- [37] Y. Oka, ICAPP'02: 2002 International Congress on Advances in Nuclear Power Plants, Hollywood, FL (United States), 2002.

- [38] C. deGanahl, H. Woodsum, H. Garabedian, Pratt and Whitney Aircraft Div., United Aircraft Corp., Hartford, Conn., 1954.
- [39] J. Chastain, J. Long, R. Redmond, R. Grimble, R. Dayton, Battelle Memorial Inst., Columbus, Ohio, 1953.
- [40] K. Dobashi, A. Kimura, Y. Oka, S. Koshizuka, *Annals of Nuclear Energy*, 25 (1998) 487-505.
- [41] L. Cao, Y. Oka, Y. Ishiwatari, Z. Shang, *Journal of Nuclear Science and Technology*, 45 (2008) 138-148.
- [42] R. Duffey, Australian Nuclear Association, 2006, pp. 181.
- [43] R.B. Duffey and I. L. Piro, *Supercritical Water-cooled Nuclear Reactors: Review and Status*, EOLSS Publishers, Oxford, UK, 2005.
- [44] C.K. Chow, H.F. Khartabil, *Nuclear Engineering and Technology*, 40 (2007) 139.
- [45] W.D. Callister Jr, *Materials Science and Engineering an Introduction*, John Wiley& Sons, 1994.
- [46] M.W. Barsoum, *Fundamentals of Ceramics*, Taylor & Francis, 2003.
- [47] C. Kittel, P. McEuen, *Introduction to Solid State Physics*, Wiley New York, 1996.
- [48] E.H. Sondheimer, *Advances in Physics*, 50 (2001) 499-537.
- [49] C. WD Jr, John Wiley & Sons. Inc. New York, USA, 2007.
- [50] G.A. Slack, R.A. Tanzilli, R.O. Pohl, J.W. Vandersande, *Journal of Physics and Chemistry of Solids*, 48 (1987) 641-647.
- [51] G.A. Slack, *Journal of Physics and Chemistry of Solids*, 34 (1973) 321-335.

- [52] B. Basu, K. Balani, *Advanced Structural Ceramics*, Wiley Online Library, 2011.
- [53] A. Feuerstein, J. Knapp, T. Taylor, A. Ashary, A. Bolcavage, N. Hitchman, *Journal of Thermal Spray Technology*, 17 (2008) 199-213.
- [54] D.R. Clarke, S.R. Phillpot, *Materials Today*, 8 (2005) 22-29.
- [55] X. Cao, R. Vassen, D. Stoeber, *Journal of the European Ceramic Society*, 24 (2004) 1-10.
- [56] N.P. Padture, M. Gell, E.H. Jordan, *Science*, 296 (2002) 280-284.
- [57] R.A. Miller, *Surface and Coatings Technology*, 30 (1987) 1-11.
- [58] K. Negita, *Acta Metallurgica*, 37 (1989) 313-317.
- [59] R. Garvie, R. Hannink, R. Pascoe, *Nature*, 258 (1975) 703-704.
- [60] G.M. Wolten, *Journal of the American Ceramic Society*, 46 (1963) 418-422.
- [61] B. Basu, *International materials reviews*, 50 (2005) 239-256.
- [62] J. Wang, R. Stevens, *Journal of Materials Science*, 24 (1989) 3421-3440.
- [63] R.C. Garvie, R.H. Hannink, R.T. Pascoe, *Nature*, 258 (1975) 703-704.
- [64] D.L. Porter, A.H. Heuer, *Journal of the American Ceramic Society*, 60 (1977) 183-184.
- [65] D. Porter, A. Heuer, *Journal of the American Ceramic Society*, 62 (2005) 298-305.
- [66] R.C. Garvie, P.S. Nicholson, *Journal of the American Ceramic Society*, 55 (1972) 152-157.
- [67] T. MASAKI, *Journal of the American Ceramic Society*, 69 (1986) 519-522.

- [68] K.W. Schlichting, N.P. Padture, P.G. Klemens, *Journal of Materials Science*, 36 (2001) 3003-3010.
- [69] V. Srinivasan, *JOM Journal of the Minerals, Metals and Materials Society*, 46 (1994) 34-34.
- [70] B. Savoini, D. Caceres, I. Vergara, R. Gonzalez, J.E.M. Santiuste, *Journal of Nuclear Materials*, 277 (2000) 199-203.
- [71] M.R. Howlader, K. Shiiyama, C. Kinoshita, M. Kutsuwada, M. Inagaki, *Journal of Nuclear Materials*, 253 (1998) 149-155.
- [72] D.A. Guzonas, J.S. Wills, G.A. McRae, e. al., in: T.R. Allen, P.J. King, L. Nelson (Eds.) *Proc. of the 12th Int. Conf. on Environ. Degrad. of Maters in Nuclear Power System-Water Reactors*, TMS, 2005.
- [73] R. Hui, W. Cook, C. Sun, Y. Xie, P. Yao, J. Miles, R. Olive, J. Li, W. Zheng, L. Zhang, *Surface and Coatings Technology*, 205 3512-3519.
- [74] T. Sato, M. Shimada, *Journal of the American Ceramic Society*, 68 (1985) 356-356.
- [75] M. Hirano, H. Inada, *Journal of Materials Science*, 26 (1991) 5047-5052.
- [76] F.F. Lange, G.L. Dunlop, B.I. Davis, *Journal of the American Ceramic Society*, 69 (1986) 237-240.
- [77] N. Boukis, N. Claussen, K. Ebert, R. Janssen, M. Schacht, *Journal of the European Ceramic Society*, 17 (1997) 71-76.
- [78] M. Schacht, N. Boukis, E. Dinjus, *Journal of Materials Science*, 35 (2000) 6251-6258.

- [79] S.N.V.K. Aki, Z.-Y. Ding, M.A. Abraham, *AIChE Journal*, 42 (1996) 1995-2004.
- [80] S. Hashimoto, A. Yamaguchi, *Journal of the American Ceramic Society*, 79 (1996) 2503-2505.
- [81] J. Wei, Q. Xue, *Wear*, 162 (1993) 229-233.
- [82] A. Abass, E. Jaboori, *physica status solidi (a)*, 116 (1989) K111-K114.
- [83] X. Pang, K. Gao, F. Luo, Y. Emirov, A.A. Levin, A.A. Volinsky, *Thin Solid Films*, 517 (2009) 1922-1927.
- [84] H.C. Barshilia, N. Selvakumar, K. Rajam, A. Biswas, *Journal of Applied Physics*, 103 (2008) 023507-023507-023511.
- [85] J.C. Nable, S.L. Suib, F.S. Galasso, *Surface and Coatings Technology*, 186 (2004) 423-430.
- [86] A. Nyaiesh, E. Garwin, F. King, R. Kirby, *Journal of Vacuum Science & Technology A: Vacuum, Surfaces, and Films*, 4 (1986) 2356-2363.
- [87] S. Tao, Z. Yin, X. Zhou, C. Ding, *Tribology international*, 43 69-75.
- [88] P.P. Krivoruchko, V.P. Kravchenko, B.G. Alapin, D.M. Shakhtin, E.V. Degtyareva, Y.I. Kolesov, *Refractories*, 22 (1981) 228-233.
- [89] T. Averbukh, P. Pavlov, *Khimiya, Moscow*, (1967).
- [90] D. Caplan, M. Cohen, *J. Electrochem. Soc.*, 107 (1960) C182-C182.
- [91] L. Brewer, *Chemical Reviews*, 52 (1953) 1-75.
- [92] R.T. Grimley, R.P. Burns, M.G. Inghram, *The Journal of Chemical Physics*, 34 (1961) 664-667.

- [93] C.A. Stearns, F.J. Kohl, G.C. Fryburg, J. Electrochem. Soc., 121 (1974) 945-951.
- [94] J.E. Croll, G.R. Wallwork, Oxidation of Metals, 4 (1972) 121-140.
- [95] H.C. Graham, H.H. Davis, Journal of the American Ceramic Society, 54 (1971) 89-93.
- [96] A. Yamauchi, K. Kurokawa, H. Takahashi, Oxidation of metals, 59 (2003) 517-527.
- [97] H. Asteman, J.E. Svensson, M. Norell, L.G. Johansson, Oxidation of metals, 54 (2000) 11-26.
- [98] R. Peraldi, B.A. Pint, Oxidation of metals, 61 (2004) 463-483.
- [99] S. Henry, A. Galerie, L. Antoni, Materials science forum, Trans Tech Publ, 2001, pp. 353-360.
- [100] H. Asteman, J.E. Svensson, L.G. Johansson, J. Electrochem. Soc., 151 (2004) B141-B150.
- [101] M. Halvarsson, J.E. Tang, H. Asteman, J.E. Svensson, L.G. Johansson, Corrosion science, 48 (2006) 2014-2035.
- [102] A. Galerie, S. Henry, Y. Wouters, M. Mermoux, J.P. Petit, L. Antoni, Materials at High Temperatures, 22 (2005) 1-2.
- [103] Y. Kim, G. Belton, Metallurgical and Materials Transactions B, 5 (1974) 1811-1816.
- [104] G.C. Fryburg, R.A. Miller, F.J. Kohl, C.A. Stearns, J. Electrochem. Soc., 124 (1977) 1738.
- [105] B.B. Ebbinghaus, Combustion and Flame, 93 (1993) 119-137.

- [106] E.J. Opila, D.L. Myers, N.S. Jacobson, I.M.B. Nielsen, D.F. Johnson, J.K. Olminky, M.D. Allendorf, *Journal of Physical Chemistry A*, 111 (2007) 1971-1980.
- [107] J. Isselin, R. Kasada, A. Kimura, *Corrosion Science*, 52 (2010) 3266-3270.
- [108] K. Yin, S. Qiu, R. Tang, Q. Zhang, L. Zhang, *The Journal of Supercritical Fluids*, 50 (2009) 235-239.
- [109] P.A. Marrone, G.T. Hong, *The Journal of Supercritical Fluids*, 51 (2009) 83-103.
- [110] G. Was, P. Ampornrat, G. Gupta, S. Teysseyre, E. West, T. Allen, K. Sridharan, L. Tan, Y. Chen, X. Ren, *Journal of Nuclear Materials*, 371 (2007) 176-201.
- [111] Y. Chen, K. Sridharan, T. Allen, *CORROSION 2007*, NACE International, Nashville, Tennessee, USA, 2007, pp. 14.
- [112] X. Ren, K. Sridharan, T. Allen, *Corrosion*, 63 (2007) 603-612.
- [113] X. Ren, K. Sridharan, T. Allen, *Journal of nuclear materials*, 358 (2006) 227-234.
- [114] L. Tan, Y. Yang, T.R. Allen, *Corrosion Science*, 48 (2006) 3123-3138.
- [115] X. Ren, K. Sridharan, T. Allen, *Journal of Nuclear Materials*, 358 (2006) 227-234.
- [116] P. Ampornrat, C.B. Bahn, G.S. Was, in: T.R. Allen, P.J. King, L. Nelson (Eds.) *12th Int. Conf. on Environmental Degradation of Materials in Nuclear Power Systems-Water Reactors*, 2005, pp. 1387-1396.
- [117] S. Iimura, M. Miyasaka, H. Yakuwa, *CORROSION 2002*, (2002).

- [118] T. Adschiri, K. Sue, K. Arai, Y. Watanabe, CORROSION 2001, (2001).
- [119] P. Kritzer, N. Boukis, E. Dinjus, Corrosion, 54 (1998).
- [120] C. Chen, K. Aral, G. Theus, Handbook of Diagrams, EPRI NP-3137-vol, 2 (1983).
- [121] Y. Watanabe, T. Adschiri, K. Shoji, CORROSION 2002, (2002).
- [122] K. Juhani, J. Pirso, M. Viljus, S. Letunovits, Mater. Sci.-Medzg., 14 (2008) 341-344.
- [123] D.-Y. Wang, K.-W. Weng, C.-L. Chang, W.-Y. Ho, Surface and Coatings Technology, 120-121 (1999) 622-628.
- [124] E. Yun, S. Lee, Materials Science and Engineering: A, 405 (2005) 163-172.
- [125] R.J. Lewis, Recherche, 67 (2001) 02.
- [126] R. Johnson, S. Schrock, G. Whitlow, Journal of Vacuum Science and Technology, 11 (1974) 759-764.
- [127] K. Hirano, J. Mater. Sci. Lett., 13 (1994) 1219-1221.
- [128] N. Nomura, K. Yoshimi, T. Konno, S. Hanada, J. Mater. Sci. Lett., 19 (2000) 1879-1881.
- [129] K.G. Budinski, M.K. budinski, Engineering Materials, Pearson Prentice Hall, 2005.
- [130] E. Min-Haga, W.D. Scott, J. Mater. Sci. Lett., (1988) 2865-2870.
- [131] B.H. Kim, D.S. Suhr, Materials transactions-JIM, 41 (2000) 1657-1662.
- [132] Y. Wang, Y. Jin, S. Wen, Wear, 128 (1988) 265-276.
- [133] G. Sundararajan, K.U.M. Prasad, D. Rao, S. Joshi, Journal of materials engineering and performance, 7 (1998) 343-351.

- [134] L. Pawlowski, The science and engineering of thermal spray coatings, Wiley, 2008.
- [135] B. Mann, B. Prakash, Wear, 240 (2000) 223-230.
- [136] R. Tucker, Journal of Vacuum Science and Technology, 11 (1974) 725-734.
- [137] T.Y. Kosolapova, G.V. Samsonov, Journal Name: Zhur. Fiz. Khim.; Journal Volume: Vol: 35; Other Information: Orig. Receipt Date: 31-DEC-61, (1961) Medium: X; Size: Pages: 363-366.
- [138] B. Bhushan, S. Gray, Thin Solid Films, 53 (1978) 313-331.
- [139] C. Kunioshi, O. Correa, L. Ramanathan, Surface Engineering, 22 (2006) 121-127.
- [140] E.E. Bloom, Journal of Nuclear Materials, 258 (1998) 7-17.
- [141] D. Senior, G. Youngblood, C. Moore, D. Trimble, J. Woods, Knolls Atomic Power Lab., Schenectady, NY (United States), 1997.
- [142] H. Hirayama, T. Kawakubo, A. Goto, T. Kaneko, Journal of the American Ceramic Society, 72 (1989) 2049-2053.
- [143] E. Barringer, Z. Faiztompkins, H. Feinroth, T. Allen, M. Lance, H. Meyer, L. Walker, E. Lara-Curzio, Journal of the American Ceramic Society, 90 (2007) 315-318.
- [144] J. Stringer, Mater. Sci. Eng. A-Struct. Mater. Prop. Microstruct. Process., 120 (1989) 129-137.
- [145] L. Pfeil, UK patent, 1937.
- [146] A.W. Funkenbusch, J.G. Smeggil, N.S. Bornstein, Metallurgical Transactions a-Physical Metallurgy and Materials Science, 16 (1985) 1164-1166.

- [147] D.P. Whittle, J. Stringer, Philos. Trans. R. Soc. Lond. Ser. A-Math. Phys. Eng. Sci., 295 (1980) 309-329.
- [148] D.G. Lees, Oxidation of Metals, 27 (1987) 75-81.
- [149] B. Pint, Proceedings of the John Stringer Symposium. Edited by PF Tortorelli and PY Hou. ASM, Materials Park, OH, Citeseer, 2001.
- [150] J. Quadakkers, L. Singheiser, Materials science forum, Trans Tech Publ, 2001, pp. 77-92.
- [151] D. Whittle, J. Stringer, Philosophical Transactions of the Royal Society of London. Series A, Mathematical and Physical Sciences, 295 (1980) 309-329.
- [152] B. Pint, Proceedings of the John Stringer Symposium, 2001.
- [153] P. Hou, J. Stringer, Materials Science and Engineering: A, 202 (1995) 1-10.
- [154] B. Pint, Oxidation of metals, 45 (1996) 1-37.
- [155] D. Moon, Materials Science and Technology, 5 (1989) 754-764.
- [156] B.A. Pint, Oxidation of Metals, 45 (1996) 1-37.
- [157] E. Polman, T. Fransen, P. Gellings, Journal of Physics: Condensed Matter, 1 (1999) 4497.
- [158] H. Grabke, D. Wiemer, H. Viefhaus, Applied surface science, 47 (1991) 243-250.
- [159] P. Colombo, Science, 322 (2008) 381-383.
- [160] P. Colombo, Philosophical Transactions of the Royal Society A: Mathematical, Physical and Engineering Sciences, 364 (2006) 109-124.
- [161] A.R. Studart, U.T. Gonzenbach, E. Tervoort, L.J. Gauckler, Journal of the American Ceramic Society, 89 (2006) 1771-1789.

- [162] K. Araki, J.W. Halloran, *Journal of the American Ceramic Society*, 88 (2005) 1108-1114.
- [163] L.J. Gibson, M.F. Ashby, *Cellular solids: structure and properties*, Cambridge Univ Pr, 1999.
- [164] H. Russell, *Journal of the American Ceramic Society*, 18 (1935) 1-5.
- [165] O. Pure, *Pure and Applied Chemistry*, 66 (1994) 1739-1758.
- [166] G. Li, F.F. Lu, L. Zhang, Z. Sun, X. Song, B. Ding, Z. Yang, *Advances in Synthesis, Processing, and Applications of Nanostructures: Ceramic Transactions*, 238 (2012) 141.
- [167] S.T. Wilson, B.M. Lok, C.A. Messina, T.R. Cannan, E.M. Flanigen, *Journal of the American Chemical Society*, 104 (1982) 1146-1147.
- [168] A. Taguchi, F. Schuth, *Microporous and mesoporous materials*, 77 (2005) 1-45.
- [169] R.H.P.R. Poladi, C.C. Landry, *Journal of Solid State Chemistry*, 167 (2002) 363-369.
- [170] F. Schüth, W. Schmidt, *Advanced Engineering Materials*, 4 (2002) 269-279.
- [171] A. Corma, *Chemical Reviews*, 97 (1997) 2373-2420.
- [172] A. Imhof, D.J. Pine, *Advanced Materials*, 10 (1998) 697-700.
- [173] H. Schmidt, D. Koch, G. Grathwohl, P. Colombo, *Journal of the American Ceramic Society*, 84 (2001) 2252-2255.
- [174] U.T. Gonzenbach, A.R. Studart, E. Tervoort, L.J. Gauckler, *Journal of the American Ceramic Society*, 90 (2006) 16-22.

- [175] N.W. Androff, L.F. Francis, B.V. Velamakanni, *AIChE journal*, 43 (2004) 2878-2888.
- [176] U. Vogt, L. Györfy, A. Herzog, T. Graule, G. Plesch, *Journal of Physics and Chemistry of Solids*, 68 (2007) 1234-1238.
- [177] T. Gupta, R. Coble, *Journal of the American Ceramic Society*, 51 (1968) 525-528.
- [178] R. Coble, *Journal of Applied Physics*, 32 (1961) 787-792.
- [179] R.L. Coble, *Journal of the American Ceramic Society*, 41 (1958) 55-62.
- [180] T. Gupta, R. Coble, *Journal of the American Ceramic Society*, 51 (1968) 521-525.
- [181] A. Paladino, R. Coble, *Journal of the American Ceramic Society*, 46 (2006) 133-136.
- [182] C. Hsueh, A. Evans, R. Coble, *Acta Metallurgica*, 30 (1982) 1269-1279.
- [183] R. Coble, J. Burke, *Progress in ceramic science*, 3 (1963) 24.
- [184] R. Coble, *Journal of Applied Physics*, 32 (1961) 793-799.
- [185] G.L. Messing, A.J. Stevenson, *Science*, 322 (2008) 383-384.
- [186] K. Morsi, *Materials Science and Engineering: A*, 299 (2001) 1-15.
- [187] J.W. McCauley, N.D. Corbin, *Journal of the American Ceramic Society*, 62 (2006) 476-479.
- [188] Y.C. Liou, C.T. Wu, K.H. Tseng, T.C. Chung, *Materials research bulletin*, 40 (2005) 1483-1489.
- [189] W.S. Hong, L.C. Jonghe, X. Yang, M.N. Rahaman, *Journal of the American Ceramic Society*, 78 (2005) 3217-3224.

- [190] H. Orthner, R. Tomasi, W. Botta F, *Materials Science and Engineering: A*, 336 (2002) 202-208.
- [191] M. Bartsch, B. Saruhan, M. Schmuecker, H. Schneider, *Journal of the American Ceramic Society*, 82 (1999) 1388-1392.
- [192] M. Kobayashi, K. Funami, S. Suzuki, C. Ouchi, *Materials Science and Engineering: A*, 243 (1998) 279-284.
- [193] J. Lis, R. Pampuch, T. Rudnik, Z. Wegrzyn, *Solid State Ionics*, 101 (1997) 59-64.
- [194] N. Claussen, D. Garcia, R. Janssen, *Journal of Materials Research*, 11 (1996) 2884-2888.
- [195] V. Buscaglia, P. Nanni, G. Battilana, G. Aliprandi, C. Carry, *Journal of the European Ceramic Society*, 13 (1994) 411-417.
- [196] H. Thomas, R. Stevens, E. Gilbert, *Journal of Materials Science*, 26 (1991) 3613-3616.
- [197] P. Pena, P. Miranzo, J.S. Moya, S. De Aza, *Journal of Materials Science*, 20 (1985) 2011-2022.
- [198] S. Yangyun, R. Brook, *SCI. SINTERING Sci. Sintering*, 17 (1985) 35.
- [199] P. Miranzo, P. Pena, J.S. Moya, S. Aza, *Journal of Materials Science*, 20 (1985) 2702-2710.
- [200] M. Mitomo, N. Kuramoto, Y. Inomata, *Journal of Materials Science*, 14 (1979) 2309-2316.
- [201] C.Y. Chen, G.S. Lan, W.H. Tuan, *Journal of the European Ceramic Society*, 20 (2000) 2519-2525.

- [202] Y.C. Liou, K.H. Tseng, *Materials research bulletin*, 38 (2003) 1351-1357.
- [203] J.-H. Eom, Y.-W. Kim, I.-H. Song, H.-D. Kim, *Materials Science and Engineering: A*, 464 (2007) 129-134.
- [204] J.F. Yang, S.Y. Shan, R. Janssen, G. Schneider, T. Ohji, S. Kanzaki, *Acta materialia*, 53 (2005) 2981-2990.
- [205] T. Xing, X. Cui, W. Chen, R. Yang, *Materials Chemistry and Physics*, 128 (2011) 181-186.
- [206] S. Deville, *Advanced Engineering Materials*, 10 (2008) 155-169.
- [207] T. Fukasawa, Z.Y. Deng, M. Ando, T. Ohji, Y. Goto, *Journal of materials science*, 36 (2001) 2523-2527.
- [208] H. Zhang, A.I. Cooper, *Advanced materials*, 19 (2007) 1529-1533.
- [209] D. Koch, L. Andresen, T. Schmedders, G. Grathwohl, *Journal of sol-gel science and technology*, 26 (2003) 149-152.
- [210] K. Araki, J.W. Halloran, *Journal of the American Ceramic Society*, 87 (2004) 1859-1863.
- [211] R. Chen, C.A. Wang, Y. Huang, L. Ma, W. Lin, *Journal of the American Ceramic Society*, 90 (2007) 3478-3484.
- [212] T. Fukasawa, M. Ando, T. Ohji, S. Kanzaki, *Journal of the American Ceramic Society*, 84 (2004) 230-232.
- [213] M.E. Launey, E. Munch, D.H. Alsem, H.B. Barth, E. Saiz, A.P. Tomsia, R.O. Ritchie, *Acta Materialia*, 57 (2009) 2919-2932.
- [214] S. Deville, E. Saiz, A.P. Tomsia, *Acta Materialia*, 55 (2007) 1965-1974.

- [215] Y.-H. Koh, E.-J. Lee, B.-H. Yoon, J.-H. Song, H.-E. Kim, H.-W. Kim, *Journal of the American Ceramic Society*, 89 (2006) 3646-3653.
- [216] K. Araki, J.W. Halloran, *Journal of the American Ceramic Society*, 87 (2004) 2014-2019.
- [217] B.H. Yoon, E.J. Lee, H.E. Kim, Y.H. Koh, *Journal of the American Ceramic Society*, 90 (2007) 1753-1759.
- [218] N. Boukis, W. Habicht, G. Franz, E. Dinjus, *Materials and Corrosion*, 54 (2003) 326-330.
- [219] J. Konys, A. Ruck, J. Novotny, J. Hausselt, *CORROSION* 2001, (2001).
- [220] J.H. Lee, R. Kasada, A. Kimura, T. Okuda, M. Inoue, S. Ukai, S. Ohnuki, T. Fujisawa, F. Abe, *Journal of nuclear materials*, 417 (2011) 1225-1228.
- [221] Y. Jeong, J. Park, H. Kim, J. Busby, E. Gartner, M. Atzmon, G. Was, R. Comstock, M.G. da Silva, A. Motta, in: T.R. Allen, P.J. King, L. Nelson (Eds.) *12th International conference on environmental Degradation of Materials in Nuclear Power System-Water reactors*, TMS, 2005, pp. 1,369-361,377.
- [222] P. Ampornrat, G.S. Was, *Journal of Nuclear Materials*, 371 (2007) 1-17.
- [223] J. Isselin, R. Kasada, A. Kimura, *Corrosion Science*, 52 (2010) 3266-3270.
- [224] Y. Yi, B. Lee, S. Kim, J. Jang, *Materials Science and Engineering: A*, 429 (2006) 161-168.
- [225] X. Gao, X. Wu, Z. Zhang, H. Guan, E.-h. Han, *The Journal of Supercritical Fluids*, 42 (2007) 157-163.
- [226] M. da Cunha Belo, M. Walls, N. Hakiki, J. Corset, E. Picquenard, G. Sagon, D. Noel, *Corrosion Science*, 40 (1998) 447-463.

- [227] L. Tan, K. Sridharan, T.R. Allen, *Journal of Nuclear Materials*, 348 (2006) 263-271.
- [228] Y. De Carlan, J.L. Bechade, P. Dubuisson, J.L. Seran, P. Billot, A. Bougault, T. Cozzika, S. Doriot, D. Hamon, J. Henry, *Journal of Nuclear Materials*, 386 (2009) 430-432.
- [229] H.S. Cho, A. Kimura, S. Ukai, M. Fujiwara, *Journal of nuclear materials*, 329 (2004) 387-391.
- [230] Y. Chen, K. Sridharan, S. Ukai, T.R. Allen, *Journal of Nuclear Materials*, 371 (2007) 118-128.
- [231] D.B. Mitton, J.H. Yoon, J.A. Cline, H.S. Kim, N. Eliaz, R.M. Latanision, *Industrial & Engineering Chemistry Research*, 39 (2000) 4689-4696.
- [232] A.T. Motta, A. Yilmazbayhan, M.J.G. da Silva, R.J. Comstock, G.S. Was, J.T. Busby, E. Gartner, Q. Peng, Y.H. Jeong, J.Y. Park, *Journal of Nuclear Materials*, 371 (2007) 61-75.
- [233] N. Boukis, C. Friedrich, E. Dinjus, *CORROSION* 98, (1998).
- [234] A.T. Motta, A. Yilmazbayhan, M.J.G. da Silva, R.J. Comstock, G.S. Was, J.T. Busby, E. Gartner, Q. Peng, Y.H. Jeong, J.Y. Park, *Journal of Nuclear Materials*, 371 (2007) 61-75.
- [235] D. Godfrey, *Metals Mater*, 2 (1968) 305-311.
- [236] J. Chin, T. Ohkawa, *Nuclear Technology*, 32 (1977) 115-124.
- [237] Y. Hirohata, M. Kobayashi, S. Maeda, K. Nakamura, M. Mohri, K. Watanabe, T. Yamashina, *Thin Solid Films*, 63 (1979) 237-242.

- [238] W.-J. Kim, H.S. Hwang, J. Y. Park, W.-S. Ryu, *Journal of Materials Science Letters*, 22 (2003) 581-584.
- [239] W.-J. Kim, H.S. Hwang, J.Y. Park, *Journal of Materials Science Letters*, 21 (2002) 733-735.
- [240] L. Tan, T.R. Allen, E. Barringer, *Journal of Nuclear Materials*, 394 (2009) 95-101.
- [241] M. Schacht, N. Boukis, E. Dinjus, K. Ebert, R. Janssen, F. Meschke, N. Claussen, *Journal of the European Ceramic Society*, 18 (1998) 2373-2376.
- [242] T. Kojima, Y. Mori, M. Kamiya, R. Sasai, H. Itoh, *Journal of Materials Science*, 42 (2007) 6056-6061.
- [243] F.F. Lange, G.L. Dunlop, B.I. Davis, *Journal of the American Ceramic Society*, 69 (1986) 237-240.
- [244] G. Holcomb, *Oxidation of Metals*, 69 (2008) 163-180.
- [245] G.R. Holcomb, *J. Electrochem. Soc.*, 156 (2009) C292-C297.
- [246] D. Young, B. Pint, *Oxidation of Metals*, 66 (2006) 137-153.
- [247] E.J. Opila, D.L. Myers, N.S. Jacobson, I.M.B. Nielsen, D.F. Johnson, J.K. Olminky, M.D. Allendorf, *The Journal of Physical Chemistry A*, 111 (2007) 1971-1980.
- [248] D.R. Gaskell, *An introduction to transport phenomena in materials engineering*, Macmillan Publishing Company, 1992.
- [249] A.R. Kennedy, J.D. Wood, B.M. Weager, *Journal of Materials Science*, 35 (2000) 2909-2912.
- [250] D. Guzonas, F. Brosseau, P. Tremaine, J. Meesungnoen, J.-P. Jay-Gerin, *Nucl. Technol.*, 179 (2012) 205.

Chapter 2 Experimental

2.1 Preparation of Samples

2.1.1 Preparation of porous Cr_3C_2 and $\text{M}(\text{Cr}, \text{Co})_7\text{C}_3$ -Co composite

2.1.1.1 Reactive sintering

Figure 2-1 shows the reactive sintering process employed to prepare the porous Cr_3C_2 ceramics and porous $\text{M}(\text{Cr}, \text{Co})_7\text{C}_3$ composite. Chromium (III) oxide powder (Alfa Aesar, USA, average particle size P_s of $\sim 2 \mu\text{m}$, purity of 99%) was used as the starting material. The oxide powder was uniaxially compressed in a cylindrical mold under a pressure of 80 MPa to form disk-shaped samples with a diameter of 16 mm and thickness of 2 mm. The disk shaped samples were put into a tube furnace (GSL1600X, MTI Corporation) and heated to 1100 °C, in a reducing gas mixture (2% CH_4 +98% H_2 , Praxair Canada) at a flow rate of 140 ml/min for 15 hours. For the purpose of engineering the porous carbide, different amounts of cobalt (Inframat Advanced Materials, USA, average particle size P_s of $\sim 1.5 \mu\text{m}$, purity of 99.95 %) ranging from 5 wt. % to 50 wt. % were added into the starting powder. Ball milling was engaged to mix the powder mixture using high purity alumina balls (13 mm in diameter) and ethanol for 10 hours. The mass ratio of ball to powder was 8:1.

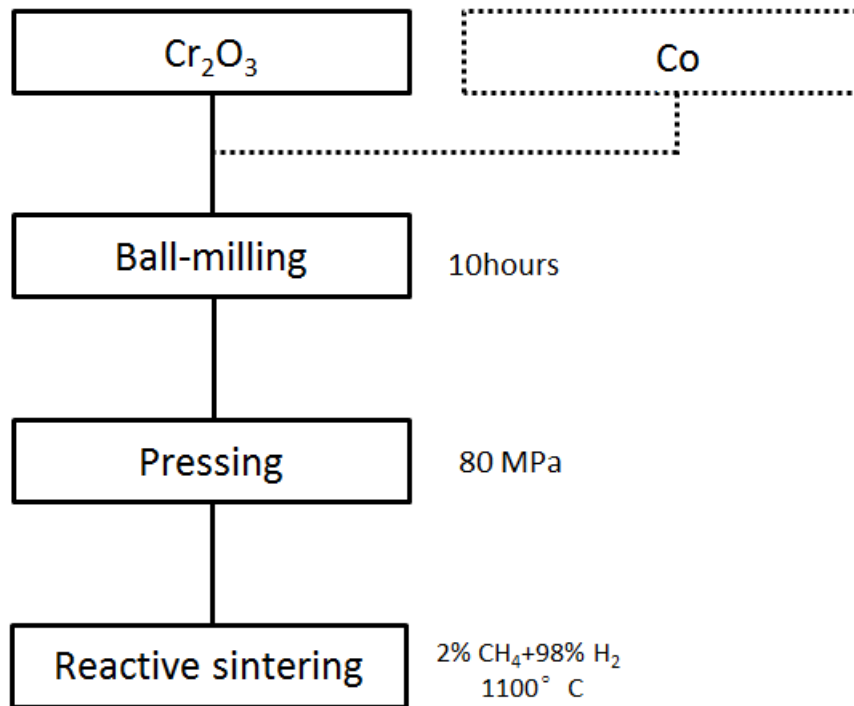


Figure 2- 1. Schematic illustration of the reactive sintering process

2.1.1.2 Freeze casting

A novel processing technique that incorporates a camphene-based freeze casting technique with the reactive sintering process was invented aiming to adjust the porosity as well as the porous architecture of the porous carbide. Figure 2-2 schematically presents the procedures for this technique. Chromium (III) oxide powder (Inframat Advanced Materials, USA, average particle size P_s of 0.7~1 μm , purity of 99.7%) was used as a starting ceramic material. Camphene ($\text{C}_{10}\text{H}_{16}$, CAS5794-03-6, Sigma-Aldrich, US, purity > 95%) was used as the sublimable vehicle. Anoligomeric polyester (Hypermer KD-4; UniQema, Everburg, Belgium) was used as a dispersant. Controlled amounts of Cr_2O_3 powder, dispersant, and

camphene were sealed inside a polyethylene bottle. The mixtures were mixed through a ball milling process at a temperature of 60 °C in a water bath using Al₂O₃ milling media to produce uniform dispersed slurries. The initial solid loading content of Cr₂O₃ powder varied from 10 to 30 vol. %. The dispersant content was always controlled at around 1 wt. % of Cr₂O₃ powder. The mixed slurries were then poured into a cylindrical polyurethane mold for freezing. The mold was 40 mm in internal diameter and 20 mm in height. The bottom of the mold was a cooling finger made of a copper plate that was immersed into a coolant with the temperature controlled by a refrigerator. This freezing setup is further sketched in Figure 2-3. After casting, the slurry solidified to a solid green body. The solidification time depends on the cooling temperature but was usually within 5 minutes. The solidified green body was moved out of the mold and placed in an ambient atmosphere to sublime the frozen camphene from the green body. The sublimation process usually took around 24 hours to complete, according to the weight change of the sample. After the sublimation, the disc-shaped green sample became very fragile. The sample was carefully moved into a tube furnace (GSL1600X, MTI Corporation) and sintered at 1100 °C (ramping rate of 5 °C/min), in a carbonaceous gas mixture (2% CH₄+98% H₂, Praxair Canada) with a gas flow rate of 140 ml/min for 15 hours.

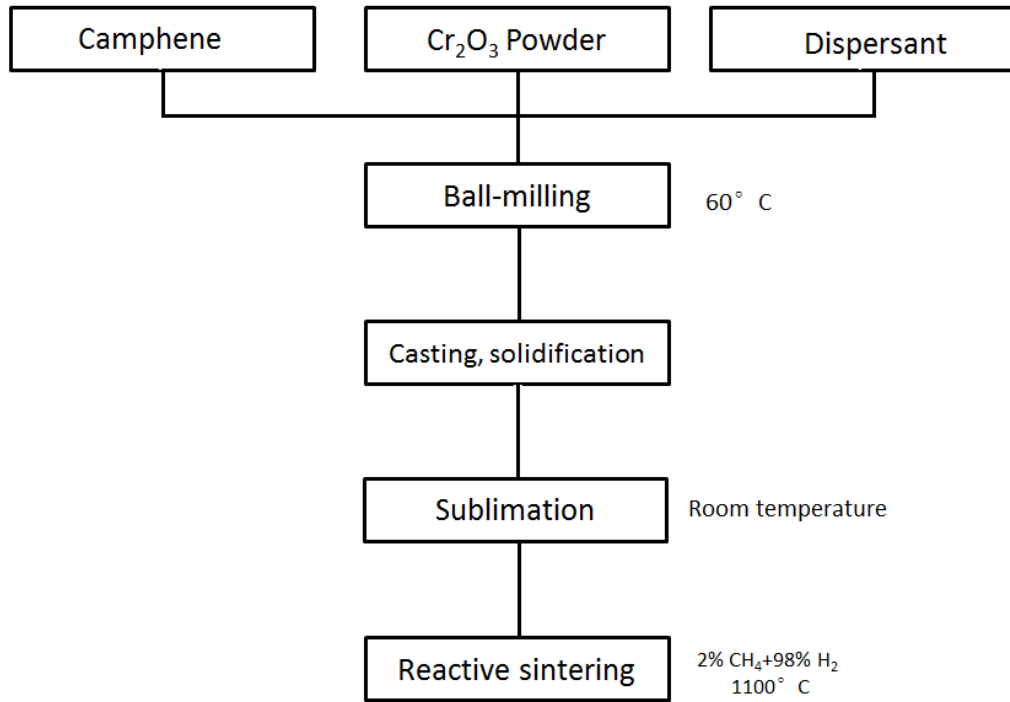


Figure 2- 2. Schematic illustration of the process incorporated reactive sintering with freeze casting.

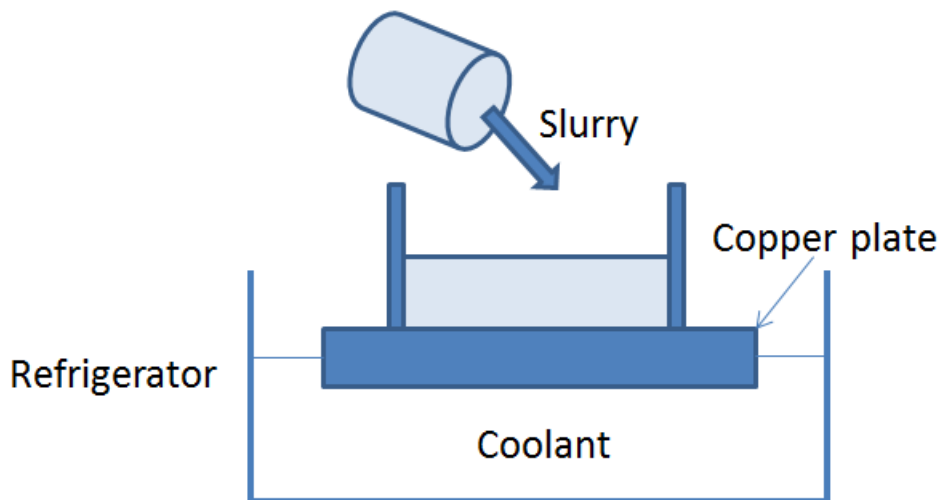


Figure 2- 3. A sketch of freeze casting experimental setup.

2.1.2 Preparation of porous Cr₂O₃ by oxidation

The porous Cr₂O₃ samples were prepared by oxidizing the porous chromium carbide at 850 °C for 50 hours in air. Yttria was added to the starting chromium oxide powder with different mass ratios of 5 %, 10 % and 20 %. The powder mixtures were mixed through ball milling for 10 hours. Figure 2-4 shows the process for preparing the porous Cr₂O₃ samples.

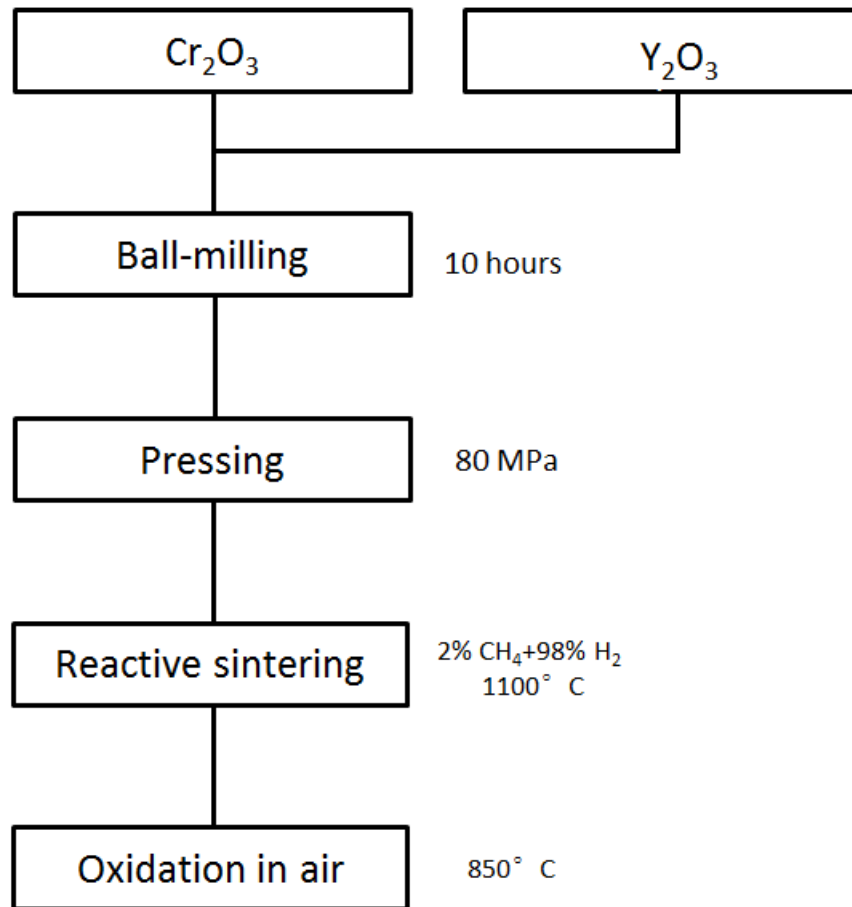


Figure 2- 4. Schematic illustration of the process for fabricating porous Cr₂O₃.

2.1.3 Preparation of densified ceramic samples

To comprehensively investigate the corrosion behavior in SCW, densified ceramic samples were also prepared through a hot isostatic pressing (HIPping) process which was conducted at 1650 °C at a pressure of 17.24 MPa.

2.1.4 Preparation of Cu-Cr₃C₂ composite

Figure 2-5 illustrates the experimental setup for the infiltration of copper into porous carbide foam. The porous carbide was prepared by the reactive sintering as described in section 2.1.1.1. The carbide foam was put into an alumina crucible with a bulk copper placed on it. The crucible was covered with an alumina plate and was then heated in a tube furnace. The tube furnace had flown hydrogen gas to form a protective environment that prevented the oxidation of copper metal. The temperature of the furnace increased from ambient temperature to 1250 °C with a heating speed at 5 °C/min and was kept at 1250 °C for 10 hours, then cooled down at a cooling rate also at 5 °C/min.

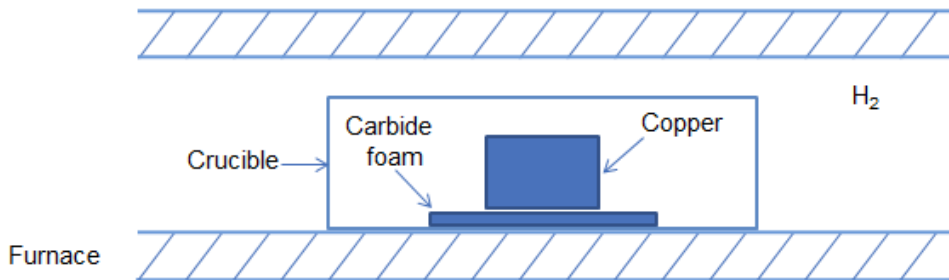


Figure 2- 5. A sketch of the experimental setup for the fabrication of Cr₃C₂-Cu composite.

2.2 SCW Corrosion Tests

2.2.1 Static supercritical water test

An autoclave, shown in Figure 2-6, was built for static SCW tests. The static autoclave was made of Alloy 625 tubing, with an outside diameter of 9.525 mm and a wall thickness of 1.651 mm. The ceramic coupons were cut from ceramic disk samples with a size of 10 mm×4mm×2mm and cleaned by using ethanol in

an ultrasonic cleaner. The ceramic coupons were then sealed separately in the capsule. Only one coupon was placed in the capsule in each test. Air-saturated neutral pH deionized water with an oxygen concentration of 8 ppm was used in the static SCW tests. In some cases, H₂O₂ solution (30 wt. % H₂O₂) was used instead of the deionized water to increase the concentration of dissolved oxygen in SCW. The filling ratios of water in static reactors were determined based on the isobaric data for water at 25 MPa listed in Table 2-1 based on the NIST database [1].

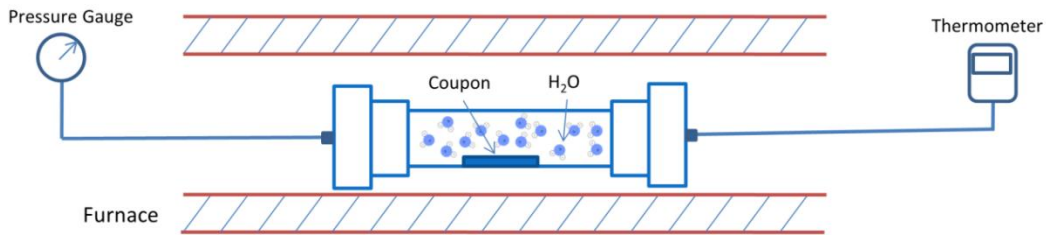


Figure 2- 6. Schematic illustration of the static SCW test autoclave adopted in the current study.

Table 2- 1. Isobaric properties for water at 25 MPa [1].

| Temperature(°C) | Pressure(MPa) | Density(g/ml) | Volume(ml/g) |
|------------------|---------------|---------------|--------------|
| 500 | 25 | 0.089744 | 11.143 |
| 550 | 25 | 0.078517 | 12.736 |
| 600 | 25 | 0.070720 | 14.140 |
| 625 | 25 | 0.067584 | 14.796 |
| 650 | 25 | 0.064810 | 15.430 |
| 700 | 25 | 0.060084 | 16.643 |

2.2.2 Flowing supercritical water test

Figure 2-7 shows the schematic drawing of the SCW loop facility, which was used to evaluate the stability of the ceramics obtained in a dynamic SCW environment. The oxygen concentration in the SCW loop facility was controlled by using water liquids with different oxygen levels.

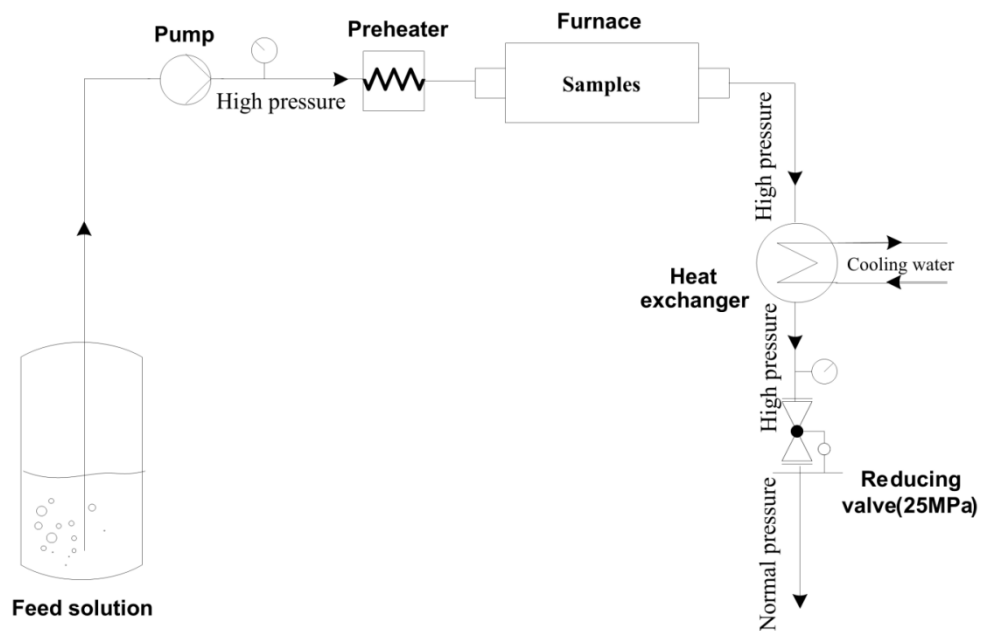


Figure 2- 7. Schematic illustration of the dynamic SCW fluid loop adopted in the current study.

2.3 Characterization Techniques

Various characterization techniques have been used in this study. The main analysis methods used are:

2.3.1 Scanning electron microscopy (SEM)

The surface morphology and chemical composition were examined by scanning electron microscopy equipped with an energy-dispersive X-ray (EDX) spectroscope. Two SEM facilities, JEOL (JSM-6301FXV) field emission high-resolution SEM and ZEISS (EVO –MA15) SEM, were employed.

2.3.2 X-ray diffraction (XRD)

X-ray diffraction analysis was conducted to obtain the information of the phases existing in the ceramics by using a Rigaku Geigerflex 2173 X-ray diffraction equipment with Cu K_α radiation, using a scanning rate of 3 degree/min from 10 to 110 degree.

2.3.3 Mass spectrum (MS) test

The concentration of elements in the water liquid after SCW tests was measured using an inductively coupled plasma mass spectrometer (ICP-MS) Perkin Elmer Elan 6000.

2.3.4 X-ray photoelectron spectroscopy (XPS)

XPS was conducted to determine the chemical states of elements in the samples. Kratos Axis 165 X-ray Photoelectron Spectrometer was used to conduct the XPS tests. The spectrums obtained were analyzed using CasaXPS software. C 1s (286.4 eV) was selected as the standard reference to eliminate the effect of peak shift.

2.4 Bibliography

[1] E.W. Lemmon, M.O. McLinden, D.G. Friend, NIST Chemistry WebBook, NIST Standard Reference Database Number 69, Eds. P.J. Linstrom and W.G. Mallard, National Institute of Standards and Technology, Gaithersburg MD, 20899, <http://webbook.nist.gov>.

Chapter 3 Preparation of Highly Porous Cr₃C₂

3.1 Introduction

Although porosity was viewed to be problematic in fabrication of ceramic materials, specific properties, such as low thermal conductivity, high surface area, controlled permeability, and high specific strength, can be obtained from cellular architectures when tailored pores are introduced into ceramics [1, 2]. Those features combined with the intrinsic properties of ceramics, such as high melting point, high corrosion and wear resistance, high chemical inertness, enable their many industrial applications, such as catalysis supports, gas distributors, liquid or gas filters, high-temperature thermal insulators, particulate filters, molten metal filters, preforms for metal-impregnated ceramic-metal composites, and implantable bone scaffolds [2, 3]. On the other hand, those applications also require that the porous materials are fabricated with controllable porous properties, including pore types (open or closed pores), specific pore size, certain pore volume fraction, and kinds of pore morphology, which usually can be achieved by using proper starting materials and well-controlled processing conditions.

Many efforts have been made to develop different processing techniques to fabricate porous ceramics with various porous morphologies to fulfill the requirements for different applications. Studart et al. have reviewed the main processing methods for the fabrication of macro-porous ceramics and divided them into three main categories: replica technique, sacrificial template method and direct foaming method, with each, porous structure with specific range of pore size and porosity can be obtained [2]. However, most of the conventional methods can only produce porous structures with a narrow range of porous

characteristics. Some processes also suffer from the difficulty of removing pore forming agent during processing.

Recently, more attention has been attracted to a novel processing method called freeze casting, by virtue of the various porous structures produced and new freezing vehicles found recently. Numerous investigations have been published on the fabrication of various kinds of porous ceramics through the freeze casting technique by employing different freezing vehicles, such as water, camphene, silicon sol, tert-butyl alcohol [3-12]. Many efforts have been made to optimize freeze casting process to modify the porous microstructure obtained, for example, increasing the open porosity, changing the pore size and shape, in the purpose of varying the specific property of ceramics obtained, such as permeability or relative density.

The freeze casting techniques usually use a wetting agent, such as water, silica sol, camphene, or tert-butyl alcohol, as the pore forming agent, which is mixed with ceramic powders to form a liquid suspension [13], which will be then frozen in a mold at a temperature below melting point of the wetting agent. A subsequent sublimation process will be conducted usually under reduced pressure to sublime the pore forming agent phase from solid to gas state. A porous structure is therefore obtained when the pore forming agent is vaporized out of the sample whereas pores are formed as a replica of the solvent crystals. Usually, a

calcination process is subsequently required to consolidate and to densify the struts.

A variety of interesting porous materials fabricated using freeze casting technique has been reported. Fukasawa et al. synthesized porous alumina ceramics with a complex porous structure by using a water-based freeze casting method [14]. Munch et al. reported the fabrication of tough, bio-inspired hybrid ceramic-based materials obtained by impregnating polymethyl methacrylate into ice-templated lamellar porous aluminum oxide scaffolds [15]. Araki et al. introduced a freeze casting technique by employing camphene as a freezing vehicle, which produced a porous structure with interconnected pore channels [3]. Recently, more attention has been attracted to this camphene-based freezing casting technique since sublimation of camphene can be easily conducted at ambient temperature, and some unique porous structures can be obtained which are believed to bring about more attractive properties, such as high permeability, higher compressive strength, and ease of further structure re-engineering.

In this chapter, a novel processing technique that incorporates a camphene-based freeze casting technique with a reactive sintering process has been developed. This method enables us to fabricate highly porous chromium carbide foams featured with complex inter-connected porous structure with well-defined multi-sized pores. To our knowledge, no published research can be found in publications that report the fabrication of the porous ceramics with similar porous

architecture. This highly porous ceramics can be potentially used to make components requiring high thermal insulation properties. The formation mechanism of the porous structure was also be discussed in this study.

3.2 Experimental

3.2.1 Materials

Chromium (III) oxide powder (Inframat Advanced Materials, USA, average particle size P_s of 0.7~1 μm , purity of 99.7%) was used as a starting ceramic material. Camphene ($\text{C}_{10}\text{H}_{16}$, CAS5794-03-6, Sigma-Aldrich, US, purity > 95%) was used as the sublimable vehicle. An oligomeric polyester (Hypermer KD-4; UniQema, Everburg, Belgium) was used as a dispersant.

3.2.2 Fabrication procedures

Figure 3-1 illustrates the fabrication procedure employed in this research. Controlled amounts of Cr_2O_3 powder, dispersant, camphene and Al_2O_3 balls were sealed inside a polyethylene bottle. The mixtures were mixed through a ball milling process at a temperature of 60 $^\circ\text{C}$ in a water bath using Al_2O_3 milling media to produce uniform dispersed slurries. The initial solid loading content of Cr_2O_3 powder varied from 10 to 30 vol. %. The dispersant content was always controlled at around 1 wt. % of Cr_2O_3 powder. The mixed slurries were then poured into a cylindrical polyurethane mold for freezing. The mold was 40 mm in internal diameter and 20 mm in height. The bottom of the mold was a cooling finger made of a copper plate that was immersed into a coolant with the

temperature controlled by a refrigerator. This freezing setup is further sketched in Figure 3-2. After casting, the slurry solidified to a solid green body. The solidification time depends on the cooling temperature but was usually within 5 minutes. The solidified green body was moved out of the mold and placed in an ambient atmosphere to sublime the frozen camphene from the green body. The sublimation process usually took around 24 hours to complete, according to the weight change of the sample. After the sublimation, the disc-shaped green sample became very fragile. The sample was carefully moved into a tube furnace (GSL1600X, MTI Corporation) and sintered at 1100 °C (ramping rate of 5 °C/min), in a carbonaceous gas mixture (2% CH₄+98% H₂, Praxair Canada) with a gas flow rate of 140 ml/min for 15 hours.

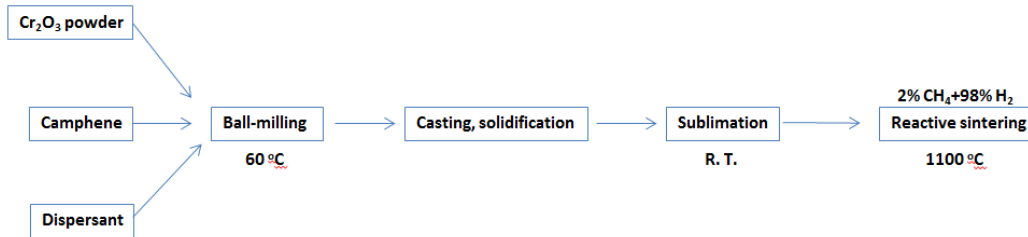


Figure 3- 1. Schematic illustration of the fabrication procedure.

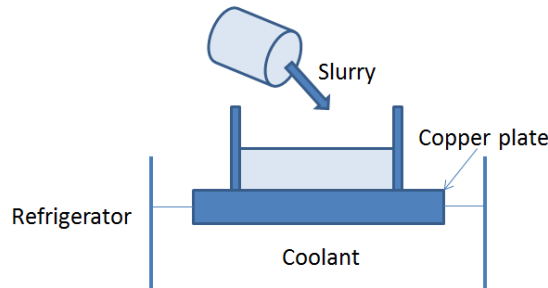


Figure 3- 2. A sketch of freeze casting experimental set up.

3.2.3 Characterization

The samples fabricated were examined by JEOL (JSM-6301FXV) field emission scanning electron microscope and ZEISS (EVO –MA15) SEM to characterize the porous structure. The porosity was calculated based on the mass and volume of the sample. X-ray diffraction (XRD) analysis was carried out by using a Rigaku Geigerflex 2173 X-ray diffraction equipment.

3.3 Results

3.3.1 Microstructure of porous bodies

Figure 3-3 shows the porous morphology of the sample obtained after sintering a freeze-cast Cr_2O_3 green sample at 1100 °C for 15 hours in a carbonaceous atmosphere (2% CH_4 +98% H_2). The freeze-casting procedure was conducted at a room temperature (around 25 °C) with a powder loading content of 10 vol. %. As shown in Figure 3-3, a unique porous structure consisting of inter-connected multi-size pores has been produced after the sintering. Compared with other conventional porous materials, this porous carbide foam exhibited a well-defined multiple porous structure. Three-dimensional large pore channels (Figure 3-3(a) and 3-3(b)) with a pore size of 10~30 μm appeared throughout the sintered body, whereas the interconnected struts possessed a finer porous structure with a pore size of 1~2 μm as shown in Figure 3-3(c) and 3-3(d). The porosity of the porous carbide sample obtained was determined to be around 90 % based on its mass and volumetric values.

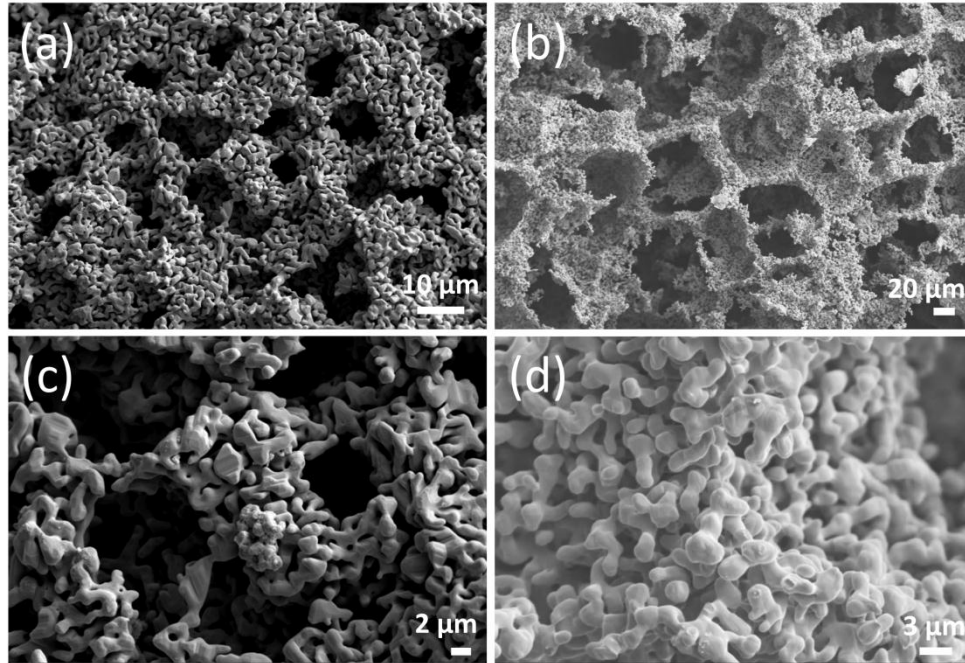


Figure 3- 3. SEM micrographs of sintered samples cast at 25 °C with a solid loading of 10 vol. %: (a) surface, (b) cross-section, (c)(d) high magnification images on struts.

3.3.2 Porous samples with different solid loading content

Figure 3-4 shows the pore morphologies obtained with different solid loading contents varying from 10 to 30 vol. %. Like the morphologies shown in Figure 3-3, the porous ceramics in Figure 3-4 also features a bimodal pore structure. It can be seen that lower solid loading content resulted in more and larger pores with sizes above 10 μm in the porous structure. With increased loading content, the size of the large pores was reduced and the micro-meter level pores become predominant, as shown in Figure 3-4(c). The latter is also seen to be quite consistent regardless of the variation of the loading content as shown in Figure 3-4 (d)-(f). The correlation of the porosity with the loading content is shown in

Figure 3-5. It shows that a super porous structure with a pore volume fraction of about 90 % can be achieved at the solid loading of 10 vol. %. With increasing the loading content, the porosity decreased, which is about 80 vol. % when the solid loading content increased to 30 vol. %.

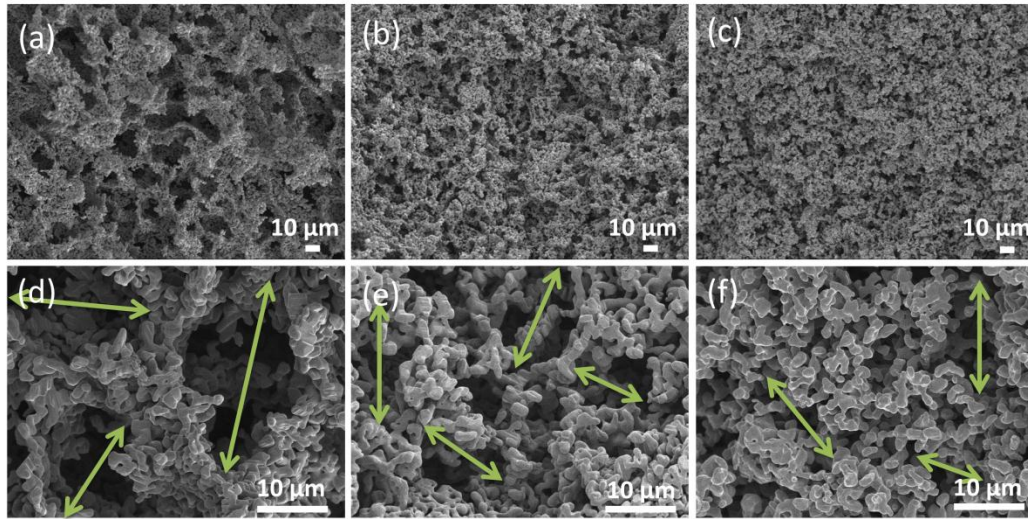


Figure 3- 4. SEM micrographs of porous samples obtained which were freeze casted at 25 °C with solid loading content of (a)(d) 10 vol. %; (b)(e) 20 vol. %; (c)(f) 30 vol. %; (d)(e)(f) are images in high magnification.

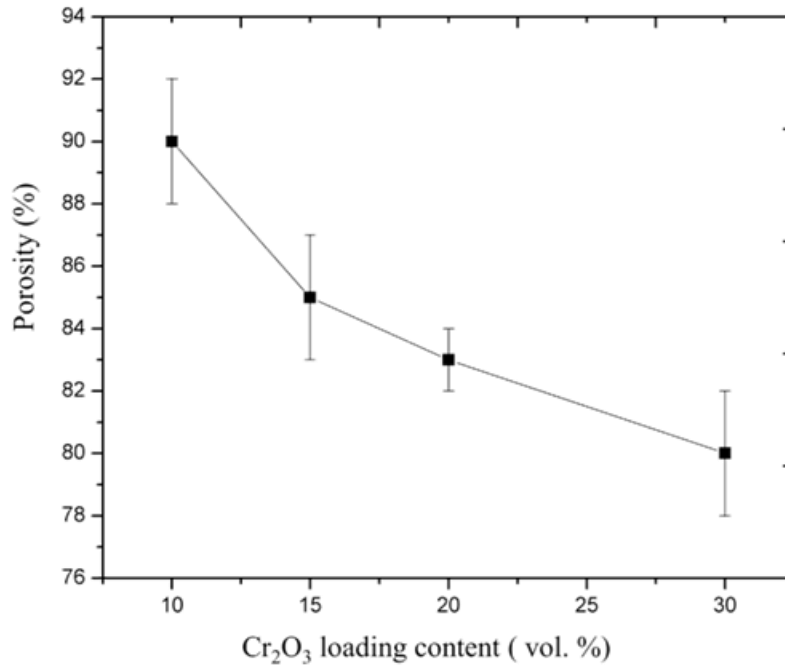


Figure 3- 5. Correlation of porosity with the content of solid loading at the casting temperature of 25 °C

3.3.3 Porous structure obtained at different freeze temperatures

The freezing temperatures was changed from 0 °C to 25 °C to examine the effect of freezing temperature on the porous structure obtained. The obtained porous morphologies at different temperatures with the same solid loading content (10 vol. %) are shown in Figure 3-6. It can be seen that the porous morphology was affected by the freezing temperature. The surface of the sample cast at higher temperature (25 °C) appeared rougher compared with the samples cast at lower temperatures. Bigger size of large pores was observed for the sample cast at high temperature (25 °C). With decrease in the casting temperature, the size of large pores decreased as shown in Figure 3-6(a) and (b). However, the fine porous

structure that constructed the struts showed no changes with the variation of casting temperatures.

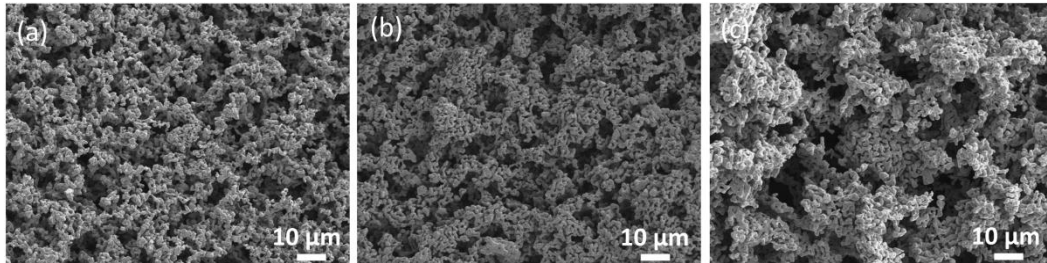


Figure 3- 6. Porous morphologies of samples casted at (a) 0 °C; (b) 15 °C; (c) 25 °C; with a same solid loading content of 10 vol. %.

3.4 Discussion

3.4.1 Large pore channels formed by the sublimation of freezing vehicle

It has been found that different pore morphologies can be produced by using different freezing vehicles: water-lamellar structure, camphene-dendritic channels, tertbutyl alcohol-prismatic channels [3, 15, 16]. Camphene has attracted considerable attention because of the following features [3, 13]: (1) interconnected open pores obtained by the replication of dendritic structure; (2) ease of control of operation condition associated with the moderate solidification temperature range (T_S : 44-48 °C [17]); (3) Environmental friendliness and non-toxicity. On the other hand, solidified camphene can be sublimed at ambient temperature and pressure which is different from the ice-cast sample that should be freeze-dried in vacuum, in which case collapse of the ice-casted sample may occur, especially when solid loading is low. Therefore, using camphene as the

freezing vehicle is believed to be more suitable to fabricate porous ceramics with ultra-high porosity and good permeability [18].

The solidification behaviour of camphene has been well studied, which was found to resemble that of metals, especially on the mechanism of dendritic growth [19-21]. The crystal structure of camphene was reported to be a face centered cubic structure [22] and subsequent study [23] indicated a probable tetragonal symmetry crystal structure. Unlike other nonmetallic materials which usually grow with faceted morphologies, camphene exhibited a non-faceted dendritic solidification behavior that was believed to be related to its small entropy of melting. The solidification behavior of materials was dependent on its own crystallographic factor (defined as Jackson factor α), the temperature gradient, and impurities present. Metallic materials, which usually have small α values ($\alpha < 1$), solidify through random atom deposition on atomically rough crystal interface [22]. The atomically rough solid interface moves into the liquid phase in a planar mode under a positive temperature gradient across the liquid-solid interface. Cellular or dendritic growth may occur if negative temperature gradient is maintained or impurities are present under certain solidification conditions. Non-metallic materials, such as ceramics or polymers, usually have a large α factor and tend to grow in a faceted interface with atomically flat crystallographic interface. As an exception, several organic compounds, such as camphene, also have small entropies of melting and hence low α factors, exhibiting solidification behavior similar to that of metals. Therefore, dendrite growth can easily be observed when

camphene is solidified under appropriate cooling and compositional conditions [23].

Non-planar solidification behavior (dendritic structure for camphene) is just one of the requirements to produce pores in ceramics. The other requirement is that the ceramic particles must be added to the camphene and could be rejected out from the camphene solvent during the solidification process to construct the solid sturts [24]. The rejection of the suspended inert particles in the advancing solidification front of a slurry suspension has been documented either in various systems or in terms of different model simulation [25-27]. A simple thermodynamic criterion has been suggested [13] for the rejection of a foreign particle by the solidification front is that the total energy associated with surfaces ($\Delta\sigma$) defined below, if the particle is engulfed by the solid, is bigger than zero, that is,

$$\Delta\sigma = \sigma_{sp} - (\sigma_{lp} + \sigma_{sl}) > 0 , \quad 3-1$$

where σ_{sp} , σ_{lp} and σ_{sl} are the interfacial free energies with the solid-particle, liquid-particle and solid-liquid, respectively [28, 29].

To understand the mechanism of the formation of the porous structure obtained, the solidification of droplets of dilute camphene - 5 vol.% Cr_2O_3 slurry was investigated and examined under optical microscopy. The slurry was dropped on

to a pre-warmed slide glass and then covered with another pre-warmed slide glass to allow the solidification to occur at room temperature. Although the freezing on a glass plate was considered to be a two dimensional solidification that might be different from the solidification in a freezing mold, it can still be used to manifest the solidification behavior of camphene slurry in a freezing mold [3, 12]. Figure 3-7 shows some typical solidified structures of the dilute camphene - 5 vol.% Cr₂O₃ slurry observed. Dendritic structure was observed as shown in the inset image of Figure 3-7(a). Interestingly, cellular morphology (Figure 3-7(a)) was observed in some specific areas, indicating the transition from planar growth to dendritic growth. The planar growth proceeded in a direction against the direction of heat flow, which is vertical to the surface of the glass plates. It can be clearly seen that solute (foreign particles: Cr₂O₃) rejected from the solidifying liquid and segregated into the cell walls during the growth as shown in Figure 3-7(a). However, cellular microstructures are only stable within a certain range of temperature gradients, and dendritic structures formed preferably in most of the solidified parts as shown in Figure 3-7(b), in which Cr₂O₃ particles were expelled into the inter-spaces of dendrites. The large pore channels observed in Figure 3-3 were believed to be the replication of the camphene dendrites formed during the freeze cast.

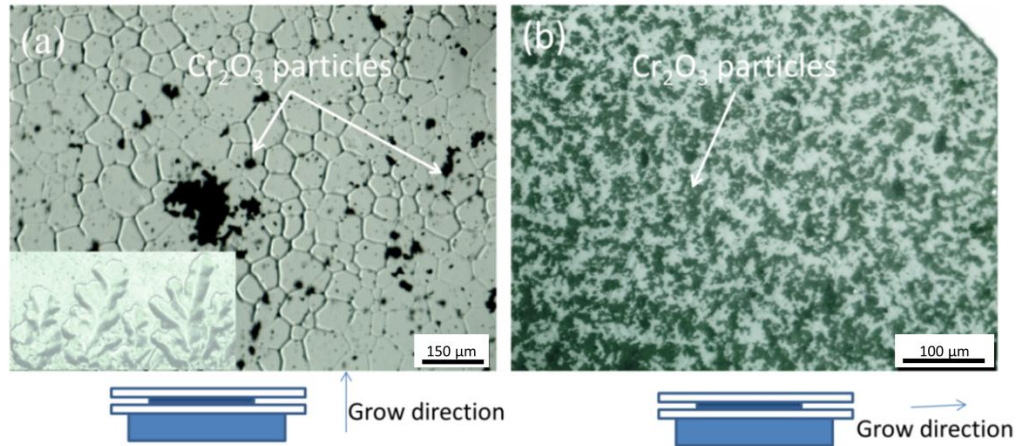


Figure 3- 7. Optical images of solidification structure of a dilute slurry (a) Cellular structures formed, inset: dendritic structure formed; (b) Dendritic structure with Cr₂O₃ particles dispersed between dendrites. .

For the purpose of comparison, yttria-stabilized Zirconia (YSZ) powder was used instead of Cr₂O₃ powder to produce a porous sample through the same freeze casting procedure and then sintered at 1400°C in air for 2 hours. The porous structure of YSZ sample is shown in Figure 3-8(a). Comparing to the porous Cr₃C₂ sample shown in Figure 3-8(b), an evident difference in porous morphology is that the strut walls of porous YSZ sample are denser and free of fine interconnected porous structure as shown in Figure 3-8(b). It can be seen that the morphology of the large size pores in both the YSZ and Cr₃C₂ samples are almost the same with pore sizes around 10~20 μm. The size of the large pores is consistent with that of the porous ceramics reported by others who also used camphene as the freezing vehicle [3, 12, 30-32]. It should also be noted that although typical dendrites were observed in the carbide sample as shown in Figure 3-8(b), the orientation of the dendrites formed throughout the sample is

completely random, since the slurry was partially quenched and initial freezing was not steady when the slurry was poured over the cold finger that was maintained at a constant and negative temperature (also as the situation shown in Figure 3-7(b)). As addressed by Deville et al. [29], homogeneous freezing with long order structure can be achieved by cooling the fingers at a constant rate from a starting temperature at which the slurry was a liquid.

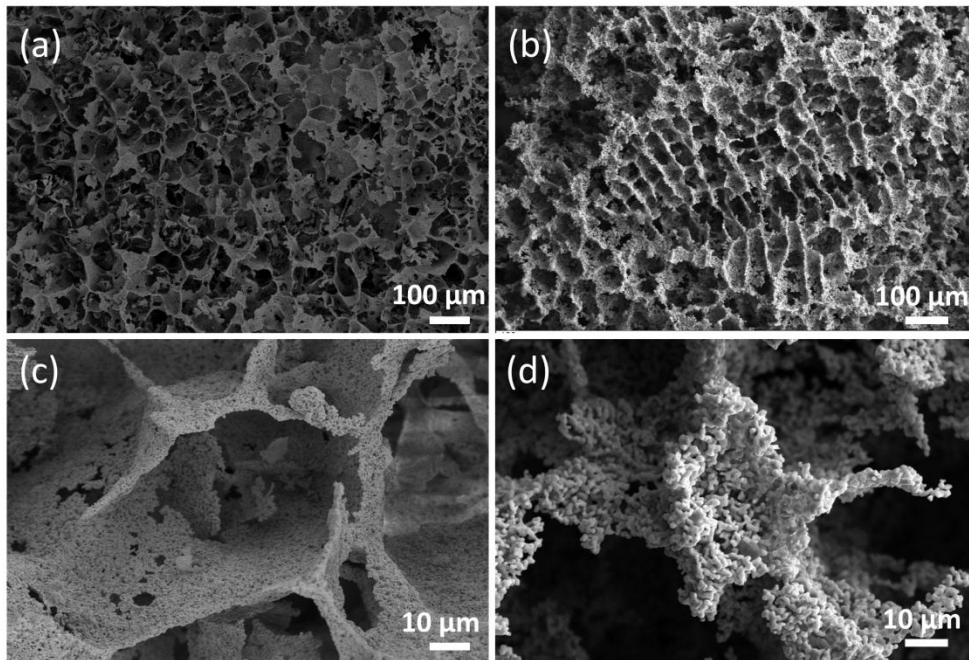


Figure 3- 8. Porous morphologies of freeze cast YSZ sample and Cr₃C₂ sample: both of those two samples were freeze cast under the same condition, (a)(c) YSZ sample was sintered in air for 2 hours, (b)(d) porous Cr₃C₂ produced in this study.

3.4.2 Small pores formed by reactive sintering

It can be noted that the struts of the porous carbide obtained exhibited a well-defined inter-connected porous structure with much finer pores at a size about 1-2

μ m. These specific porous struts were believed to be the result of the reactive sintering. Araki et al. investigated the fabrication of dense [33] and porous [3] Al_2O_3 samples by the freeze casting technique using camphene as the freezing vehicle. Their results indicated that the concentration of the particles in the remaining slurry in interdendritic spaces which finally sintered to the struts was at least more than 50 vol. %. The powder compact in such a density was close to that of an as-pressed green sample. Figure 3-9 compares the morphology of the as-pressed Cr_2O_3 green sample pressed under the pressure of 80 MPa with that of the same sample after reactive sintering. It can be seen that the micrometer size Cr_2O_3 particles were compacted together and the volume fraction of pores was calculated to be around 50~60 vol. %. Figure 3-9 (b) and (c) show SEM micrographs of the surface and cross-section of the sample after reactive sintering which exhibits a remarkably homogeneous porous morphology with a smooth three-dimensional network structure that appears in morphology similar to the fine porous structure observed on the struts of the freeze cast sample after sintering. The as-pressed sample after reactive sintering was identified to be Cr_3C_2 by X-ray diffraction analysis. The porosity of the carbide was determined to be about 77 % with an average pore size of 1~2 μm [35].

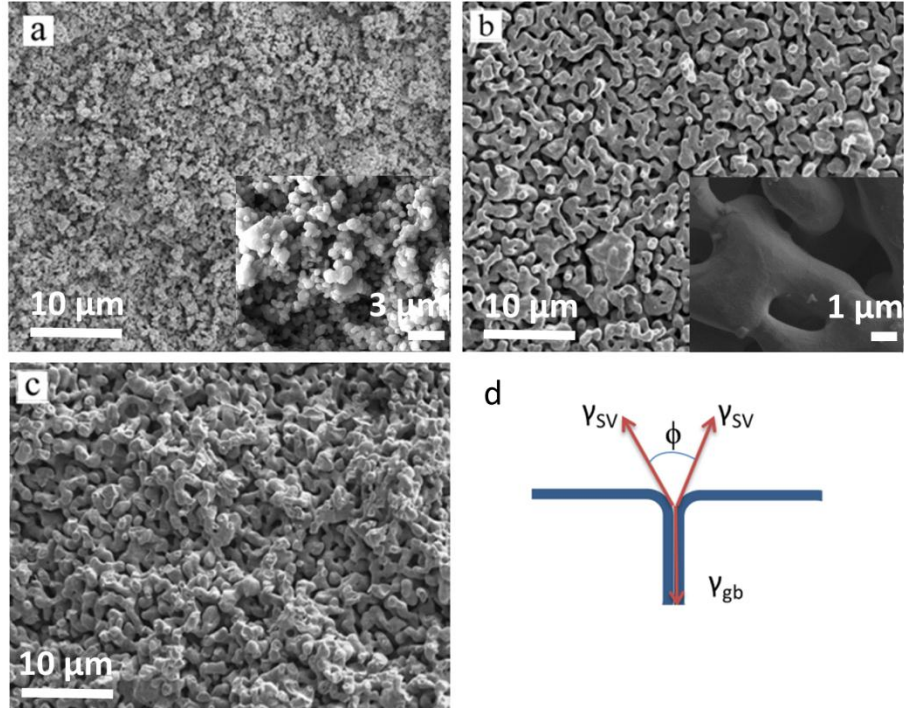
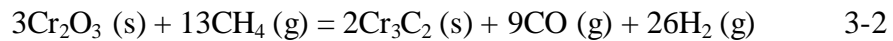


Figure 3- 9. SEM micrographs of 100% Cr_2O_3 green disk before sintering (a) and after sintering at 1100 °C in reducing atmosphere (2% CH_4 +98% H_2) for 10 hours (b) surface, (c) cross-section and (d) equilibrium dihedral angle between grain boundary and solid/vapor interfaces [34][35].

The formation of the porous Cr_3C_2 with inter-connected open pores through the reactive sintering in the carbonaceous atmosphere has been previously reported by our group [35]. Hashimoto et al. also reported the fabrication of porous Cr_3C_2 grains by heating a powder mixture of MgCr_2O_4 and graphite at temperatures from 1450 °C to 1650 °C [36]. The mechanism of Cr_2O_3 reduction by methane-hydrogen gas has been investigated by some researchers using different methods. Read et al. concluded that the role of methane was to supply carbon, and carbon diffuses into the oxide, which based on the observation leads to nonisothermal

reduction of chromium oxide by solid carbon in the hydrogen atmosphere [37]. Anacleto et al. suggested the adsorbed carbon is firstly consumed by the carburization reaction [38]. After completion of this reaction, adsorbed carbon is not consumed and forms solid carbon. All studies are unanimous that the carburization of Cr_2O_3 takes place according to the following equation.



However, the detailed reason for the formation of the inter-connected porous structure is still unclear. The following hypotheses were proposed based on the experimental results obtained in this investigation and in the available literature. The chemical reaction is accompanied with the phase transformation from Cr_2O_3 to Cr_3C_2 . There is a reduction in volume when Cr_2O_3 is carburized to Cr_3C_2 since Cr_3C_2 ($6.68\text{g}/\text{cm}^3$) has a higher density than Cr_2O_3 ($5.22\text{g}/\text{cm}^3$). This volume reduction can introduce extra pore volume into the sample since no obvious changes in sample dimension were measured after sintering. Interestingly, struts of porous carbides were seen to be quite smooth, that is, no particulate shape of the Cr_2O_3 remained in the struts of the porous carbide. Therefore, there should be two processes occurring simultaneously: the volume shrinkage of the solid volume due to the phase transformation and the coalescence of $\text{Cr}_2\text{O}_3/\text{Cr}_3\text{C}_2$ particles into a joint network of struts.

The shrinkage of Cr_2O_3 when exposed to an environment with a low oxygen partial pressure, which leads to the densification of Cr_2O_3 samples, has been observed by many researchers [39-41]. Ownby et al. determined that the maximum density of a Cr_2O_3 sample can be obtained when Cr_2O_3 powder sample is sintered at 1600 °C for 1 hour in the environment with $P_{\text{O}_2} = 2 \times 10^{-12}$ atm. This is an equilibrium partial pressure that would enable the reaction below to occur at 1600°C:



The density decreased when P_{O_2} was higher or lower than 2×10^{-12} atm, because of volatilization of Cr oxide species ($P_{\text{O}_2} > 2 \times 10^{-12}$ atm) or Cr-metal formation ($P_{\text{O}_2} < 2 \times 10^{-12}$ atm). Yamaguchi has observed evident densification of Cr_2O_3 samples when it was heated in carbon powder [39]. Since the oxygen partial pressure in his investigation was less than the equilibrium P_{O_2} necessary for Reaction 3) to occur. Yamaguchi therefore suggested that a film of Cr, Cr_3O_4 or off-stoichiometry oxide appeared to be formed on the surface of Cr_2O_3 particles. This thin film acts as a liquid phase during the sintering and therefore enhances the densification of the Cr_2O_3 samples. In this study, the carbon activity of the gas mixture was calculated to be around 3.1 and the oxygen partial pressure P_{O_2} is less than the equilibrium P_{O_2} for Reaction 3) to occur. It was reasonable that a thin film containing metallic Cr appeared. A necessary condition for densification to occur is that the grain boundary energy γ_{gb} be less than twice of the solid/vapor

surface energy γ_{sv} , as shown in Figure 3-9(d), in which γ_{gb} and γ_{sv} are related through Young's equation [34]:

$$\gamma_{gb} = 2\gamma_{sv}\cos\frac{\phi}{2} \quad 3-4$$

Where ϕ is the dihedral angle.

Metallic systems usually have the smaller ratio of γ_{gb}/γ_{sv} that is between 0.25 and 0.5, in contrast to ceramic systems, such as many oxide systems with the ratio of γ_{gb}/γ_{sv} which is around 1.0 and densification occurs more easily in metallic systems than ceramic systems [34]. Therefore, the smooth surface of the struts as shown in the inset image in Figure 3-9 (b) could be attributed to the possible existence of a thin film containing metallic Cr, or even that the film was liquid-like during the sintering process that led to the densification of the struts. It is therefore reasonable to conclude that the densification and phase transformation of Cr_2O_3 in this low oxygen partial pressure environment may involve the formation of liquid-like film and the solidification of the liquid film, which might facilitate the process of sintering of the particulate Cr_2O_3 phase into a continuous Cr_3C_2 phase.

3.4.3 The formation of the high porous structure with multiple pore sizes

Based on the above discussion, it is evident that the formation of the porous carbides with multi-level pore sizes resulted from both the freeze casting and the reactive sintering. The freeze casting introduces large sizes of pore channels that

replicate the dendrites of camphene which can be removed through sublimation. The reactive sintering induces additional pores into the structure due to the phase transformation and at the same time provides some chemical reactions that produce intermediate phases and phase transformations enabling the sintering.

The changes in porous morphologies with the variation of casting temperatures (Figure 3-6) should be correlated to the different dendrites solidified under the different cooling conditions. It has been found that primary dendrite arm spacing (λ_1), secondary dendrite arm spacing (λ_2), dendrite tip radius (R) and mushy zone depth (d) decreased with increasing of the imposed negative temperature gradient (G), growth rate (V) and cooling rate (GV) [42]. Therefore, finer dendrites were obtained at the lower freezing temperature that hence produced smaller pore channels as shown in Figure 3-6(a). With an increase of the freezing temperature, large pore channels appeared due to the formation of the coarser dendrites. It has also been suggested that there existed a critical solidification velocity (v_c), at which the transportation of the freezing vehicle is restricted and encapsulated by the solid, therefore the growth of dendrites were inhibited leading to the reduction in the size of dendrites formed [24, 43].

Compared with the porous ceramics reported by other researchers using freeze casting techniques, the porous carbide fabricated in this study showed higher porosity due to the reactive sintering process. Table 3-1 is a comparison of the porosity of the ceramics prepared by the current method with that of other

ceramics reported obtained through freeze casting technique. It can be seen that higher porosity can be achieved by using this method under the same solid loading. Therefore, this current method is suitable to the fabrication of some ultra-high porous ceramics. Another feature of the current technique is that the sintering process can be conducted at temperatures (1100°C) that are much lower than that required for sintering ceramics (usually above 1500°C).

Table 3- 1. Comparison of porosity with other reported results.

| Solid load (vol. %) | 5 | 10 | 15 | 20 | 25 | 30 |
|------------------------|----|------|------|-----------|----|----|
| Current work | | 90 | 85 | 83 | | 80 |
| Arki[3] | | | | around 60 | | |
| Han[12] | | 81.5 | 74.4 | 65.5 | | |
| Koh[18] | 89 | 81 | 73 | 65 | 57 | 49 |

3.5 Concluding Remarks

Highly porous chromium carbide (Cr_3C_2) foams have been fabricated by sintering freeze-cast chromium oxide (Cr_2O_3) green samples in a carbonaceous atmosphere. The porous Cr_3C_2 exhibited a unique multiple porous architectures with large pore channels throughout the sample and small pores in the network of struts. The large pore channels were formed from the replication of camphene dendrites in

the freeze casting, while the small pores were produced from the reactive sintering. It was also found that the size of large pores decreased with decrease in the freezing temperature as well as increased in the solid loading content, as dictated by the solidification behaviour of camphene. Compared to the porous ceramics prepared by conventional methods, this process is advantageous because of much higher porosity obtained and significantly lower temperature required for sintering.

3.6 Bibliography

- [1] P. Colombo, *Science*, 322 (2008) 381-383.
- [2] A.R. Studart, U.T. Gonzenbach, E. Tervoort, L.J. Gauckler, *Journal of the American Ceramic Society*, 89 (2006) 1771-1789.
- [3] K. Araki, J.W. Halloran, *Journal of the American Ceramic Society*, 88 (2005) 1108-1114.
- [4] T. Waschkes, R. Oberacker, M.J. Hoffmann, *J. Am. Ceram. Soc.*, 92 (2009) S79-S84.
- [5] Q. Fu, M.N. Rahaman, F. Dogan, B.S. Bal, *Journal of Biomedical Materials Research Part B: Applied Biomaterials*, 86 (2008) 125-135.
- [6] S.W. Sofie, *J. Am. Ceram. Soc.*, 90 (2007) 2024-2031.
- [7] S. Deville, E. Saiz, A.P. Tomsia, *Biomaterials*, 27 (2006) 5480-5489.
- [8] K. Lu, C.S. Kessler, R.M. Davis, *J. Am. Ceram. Soc.*, 89 (2006) 2459-2465.
- [9] T. Moritz, H.J. Richter, *J. Am. Ceram. Soc.*, 89 (2006) 2394-2398.
- [10] D. Koch, L. Andresen, T. Schmedders, G. Grathwohl, *Journal of sol-gel science and technology*, 26 (2003) 149-152.
- [11] S.W. Sofie, F. Dogan, *J. Am. Ceram. Soc.*, 84 (2001) 1459-1464.
- [12] J. Han, C. Hong, X. Zhang, J. Du, W. Zhang, *Journal of the European Ceramic Society*, 30 53-60.
- [13] S. Deville, *Advanced Engineering Materials*, 10 (2008) 155-169.
- [14] T. Fukasawa, M. Ando, T. Ohji, S. Kanzaki, *Journal of the American Ceramic Society*, 84 (2004) 230-232.
- [15] M.E. Launey, E. Munch, D.H. Alsem, H.B. Barth, E. Saiz, A.P. Tomsia, R.O. Ritchie, *Acta Materialia*, 57 (2009) 2919-2932.

- [16] R. Chen, C.A. Wang, Y. Huang, L. Ma, W. Lin, *Journal of the American Ceramic Society*, 90 (2007) 3478-3484.
- [17] T.E. Daubert, R.P. Danner, *Physical and thermodynamic properties of pure chemicals: Data compilation*, Hemisphere Pub. Corporation, 1989.
- [18] Y.-H. Koh, J.-H. Song, E.-J. Lee, H.-E. Kim, *Journal of the American Ceramic Society*, 89 (2006) 3089-3093.
- [19] D. Jones, University of Cambridge Department of Engineering, *Research in the Materials Group*, (1979) 11.
- [20] G. Swallowe, J. Field, C. Rees, A. Duckworth, *Acta Metallurgica*, 37 (1989) 961-967.
- [21] H. Dean, B. Meredith, D. Milner, *Solidification Technology in the Foundry and Cast House*, (1980) 161-170.
- [22] J. Jacksonand, *Acta Metallurgica*, 13 (1965) 1212-1215.
- [23] E. Rubinstein, M. Glicksman, *Journal of crystal growth*, 112 (1991) 97-110.
- [24] S. Deville, *Advanced Engineering Materials*, 10 (2008) 155-169.
- [25] N.O. Shanti, K. Araki, J.W. Halloran, *Journal of the American Ceramic Society*, 89 (2006) 2444-2447.
- [26] M. Worster, J. Wettlaufer, *The Journal of Physical Chemistry B*, 101 (1997) 6132-6136.
- [27] S.A. Barr, E. Luijten, *Acta Materialia*, 58 709-715.
- [28] R. Asthana, S. Tewari, *Journal of materials science*, 28 (1993) 5414-5425.
- [29] S. Deville, E. Saiz, A.P. Tomsia, *Acta Materialia*, 55 (2007) 1965-1974.

- [30] Y.-H. Koh, E.-J. Lee, B.-H. Yoon, J.-H. Song, H.-E. Kim, H.-W. Kim, *Journal of the American Ceramic Society*, 89 (2006) 3646-3653.
- [31] T. Waschkes, R. Oberacker, M.J. Hoffmann, *Journal of the American Ceramic Society*, 92 (2009) S79-S84.
- [32] L. Hu, C.-A. Wang, Y. Huang, C. Sun, S. Lu, Z. Hu, *Journal of the European Ceramic Society*, 30 (2010) 3389-3396.
- [33] K. Araki, J.W. Halloran, *J. Am. Ceram. Soc.*, 87 (2004) 1859-1863.
- [34] M.W. Barsoum, *Fundamentals of ceramics*, Taylor & Francis, 2002.
- [35] T. Xing, X. Cui, W. Chen, R. Yang, *Materials Chemistry and Physics*, 128 (2011) 181-186.
- [36] S. Hashimoto, A. Yamaguchi, *Journal of the American Ceramic Society*, 79 (1996) 2503-2505.
- [37] P.J. Read, D.A. Reeve, J.H. Walsh, J.E. Rehder, *Can. Metall. Q.*, 13 (1974) 587-595.
- [38] N. Anacleto, O. Ostrovski, *Metallurgical and Materials Transactions B*, 35 (2004) 609-615.
- [39] A. Yamaguchi, *J. Am. Ceram. Soc.*, 64 (1981) 67-68.
- [40] P. Ownby, G. Jungquist, *Journal of the American Ceramic Society*, 55 (1972) 433-436.
- [41] J.W. HALLORAN, H.U. ANDERSON, *J. Am. Ceram. Soc.*, 57 (1974) 150-150.
- [42] E. Çadırlı, N. Maraslı, B. Bayender, M. Gündüz, *Materials Research Bulletin*, 35 (2000) 985-995.

[43] H.F. Zhang, I. Hussain, M. Brust, M.F. Butler, S.P. Rannard, A.I. Cooper,
Nat. Mater., 4 (2005) 787-793.

Chapter 4 Preparation of Porous $M(\text{Cr, Co})_7\text{C}_3\text{-Co}$ Composites

4.1 Introduction

Porous materials are used in many applications both in our daily life and in modern industry owing to their specific features and properties attained by introducing tailored porosity into materials [1]. Compared to porous metals and polymers, porous ceramics find their extraordinary applications where service conditions are harsh, such as high temperature thermal insulation, catalyst support in corrosive environments, and filtration of hot corrosive fluids and molten metals. Those applications can be attributed to the specific properties of ceramics, such as high melting point, high chemical inertness, high wear and corrosive resistance, and also the unique features associated with the presence of pores in the material. The latter may include controlled permeability, low thermal conductivity, large surface area and controlled strength to density ratio [2-4]. All the features can be adjusted by tuning the pore properties in the structure.

Cobalt could be used as an additive for engineering carbide ceramics because of its excellent wettability with carbides and slight dissolution in the solid carbide. No study has been published on the formation of porous $M(\text{Cr}, \text{Co})_7\text{C}_3$ phase through reactive sintering in a carbonaceous atmosphere. However, Carbide-Co systems, especially WC-Co system, have been extensively investigated due to their wide applications in industries, such as for the fabrication of extremely hard and wear-resistant tool materials or turbine blade [5-7]. The Cr-Co-C system has also attracted considerable attention because of its wide use in the hard material industry [8-11]. The first investigation on the ternary system Cr-Co-C was reported by Koster and Sperner in 1955 who had examined more than 60 different

C-Co-Cr compositions at 1073 K [8]. The subsequent work on Cr-Co-C system was conducted by Thompson [9], Sahm[10] and Kusoffsky [11], most of which involved in the fabrication of cobalt based cermet materials. The determination of the maximum solubility of cobalt in Cr_7C_3 phase is also one key interest for the fabrication of Co-Cr-C hard material as the $\text{M}(\text{Cr}, \text{Co})_7\text{C}_3$ phase was found to be precipitated during cooling for the quaternary system C-Co-Cr-W [12, 13].

This chapter review the study of the synthesis of porous $\text{M}(\text{Cr}, \text{Co})_7\text{C}_3$ and $\text{M}(\text{Cr}, \text{Co})_7\text{C}_3$ -Co composites by a reactive sintering process. The effect of cobalt content on the porous structure was investigated. The dissolution of cobalt in the carbide phase was also examined. The results obtained were compared with the published data to reveal the fast process of Co dissolution in porous carbides during reactive sintering as well as the variation of hardness of the $\text{M}(\text{Cr}, \text{Co})_7\text{C}_3$ phase with the solubility of cobalt.

4.2 Experimental

Chromium (III) oxide powder (Alfa Aesar, USA, average particle size P_s of $\sim 2 \mu\text{m}$, purity of 99%) and Cobalt powder (Inframat Advanced Materials, USA, average particle size P_s of $\sim 1.5 \mu\text{m}$, purity of 99.95 %) were used as the starting materials. Chromium oxide powder was added with various amounts of cobalt ranging from 5 wt. % to 50 wt. %. Ball milling was engaged to mix the powder mixture using high purity alumina balls (13 mm in diameter) in ethanol for 10 hours. The mass ratio of ball to powder was at 8:1. Powders were uniaxially

pressed in a cylindrical mould at a pressure of 80 MPa to obtain disc-shaped green samples with a diameter of 16 mm and thickness of 2 mm. The disc samples were then heated in a tube furnace (GSL1600X, MTI Corporation, USA) at 1100 °C with a flowing carbonaceous reducing gas mixture (2% CH₄+98% H₂, Praxair Canada) at a flow rate of 140 ml/min. Both the heating and cooling ramp-rates were kept at 5 °C/min and argon purging was conducted during the ramping stages.

Morphologies of the resulting samples were examined by field emission scanning electron microscope (JSM-6301FXV, JEOL, Japan) and (EVO –MA15, ZEISS, Germany). X-ray diffraction (XRD) analysis was carried out using a Rigaku Geigerflex 2173 X-ray diffraction instrument. The porous properties of the as-carburized samples were characterized by mercury intrusion porosimeter (AutoPore IV 9510) and the Archimedes method. X-ray Photoelectron Spectroscopy (XPS) test was conducted using a Kratos Axis 165 X-ray Photoelectron Spectrometer. Hardness was measured by a micro indentation hardness tester (Buehler, USA, IndentaMet 1100 Series). The load for the hardness tests was 1 kg with a dwell time of 20 seconds. Indentations with diagonal lengths ranging from 100 µm to 400 µm were observed for the cobalt-added porous samples. The indentation sizes were much larger than the pore size and are believed to represent the hardness of the porous materials.

4.3 Results and Discussion

4.3.1 Porous carbide foam obtained by carburization

As detailed in Ref 14, the bulk porous carbide foams with tunable porous morphologies were formed by sintering compacted Cr_2O_3 powder at elevated temperatures in a carbonaceous environment containing CH_4 [14]. Figure 4-1(a) shows the surface morphology of an as-pressed Cr_2O_3 sample using micrometer-size Cr_2O_3 powders. The porosity of the as-pressed sample was about 36.9-40.7 % determined based on the dimension and mass of the pressed disc. Figure 4-1 (b) and (c) show SEM micrographs of the surface and cross-section of the sample after reactive sintering at 1100 °C for 10 hour in a reducing atmosphere (2% CH_4 +98% H_2). It can be seen that the sintering has caused a remarkable change in structure and a homogeneous porous morphology with smooth three-dimensional networks was formed. The porous sample after carburization was identified as Cr_3C_2 by X-ray diffraction analysis. The porous properties were characterized by mercury intrusion porosimetry. Test results revealed that the porosity of this carbide was about 77.8% with an average pore size around 2 μm .

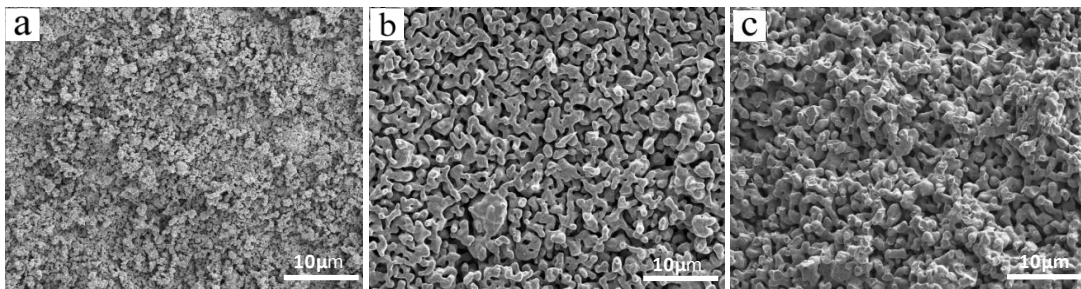
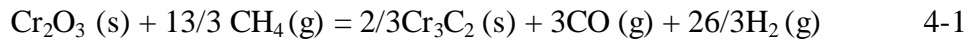


Figure 4- 1. SEM micrographs of 100% Cr_2O_3 green disk before sintering (a) and after sintering at 1100 °C in reducing atmosphere (2% CH_4 +98% H_2) for 10 hours (b) surface and (c) cross-section [14].

The carburization of chromium oxide in the current carbonaceous environment (2%CH₄+98%H₂) has been studied in details by several investigators [15-17]. Chromium oxide was formed through the following reaction:



Reaction 4-1 was confirmed by XRD analysis as well as the thermodynamic calculation [16]. The formation of the porous structure was mainly attributed to the density reduction when the oxide phase transformed to carbide, as chromium carbide has a smaller molar volume than chromium oxide.

4.3.2 Porous M(Cr, Co)₇C₃-Co Composites

4.3.2.1 Microstructure and phase analysis

Figure 4-2 shows the microstructure of the samples containing different amounts of cobalt after sintering at 1100 °C for 10 hour in the carbonaceous atmosphere (2% CH₄ +98% H₂). As shown in Figure 4-2, the cobalt-added samples exhibited appreciably uniform porous structure. The porous structure has obviously been altered by the addition of cobalt. When cobalt content increased, the struts of porous structure were thickened and the pore density was reduced. The results of the porosity volume fraction measured by Archimedes method are shown in Figure 4-3. Porous sample with a porosity of around 70 % was attained when cobalt was added to 5 wt. %. The porosity linearly decreased with the rise of the cobalt content and it was dramatically reduced when cobalt ratio increased to 45 wt. %, as shown in Figure 4-3.

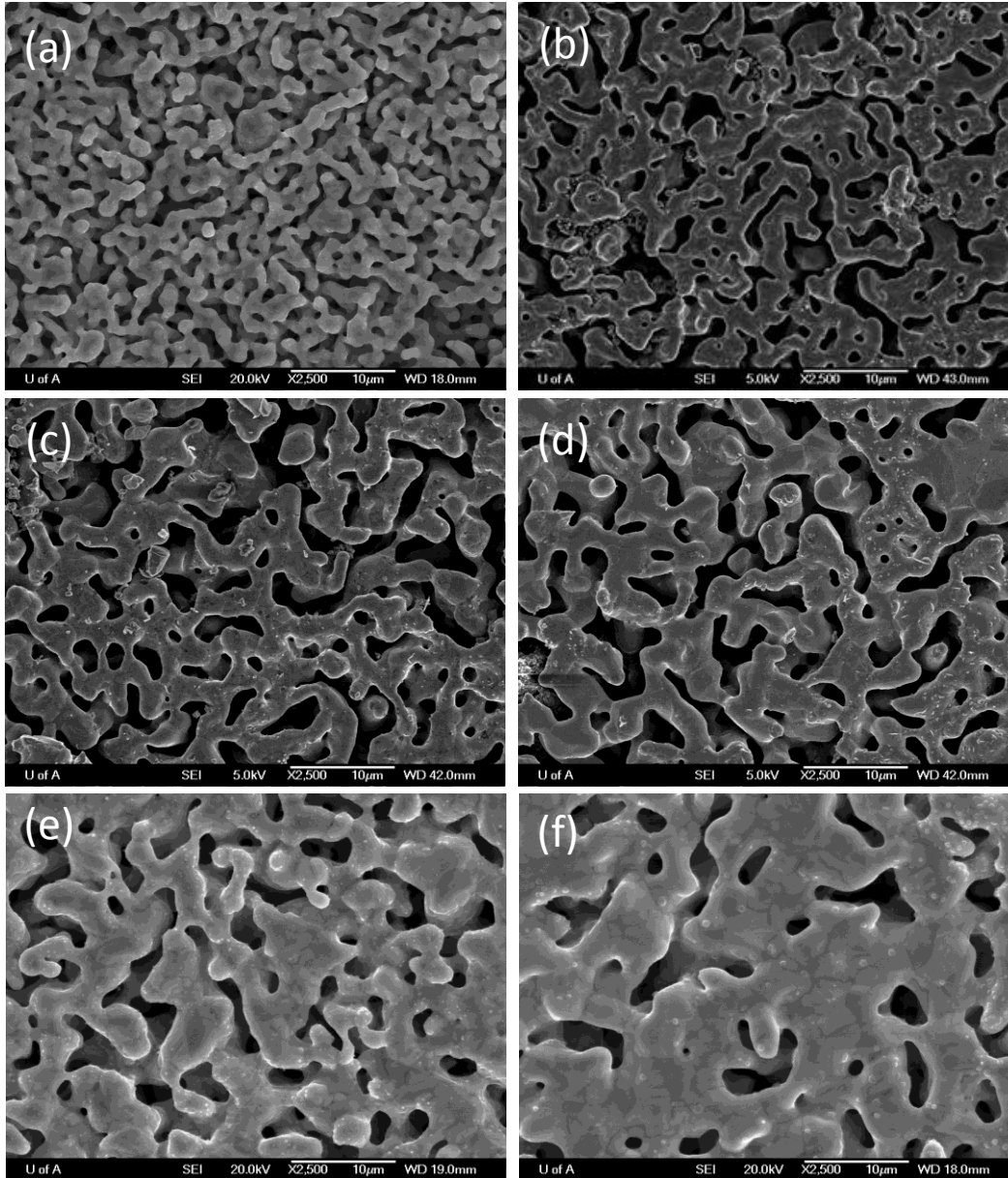


Figure 4- 2. SEM micrographs of chromium oxide sample added with various amount of cobalt after carburization at 1100°C for 10 hours: (a) 5 wt. % Co (b) 10 wt. % Co (c) 15 wt. % Co (d) 20 wt. % Co (e) 35 wt. % Co (f) 45 wt. % Co.

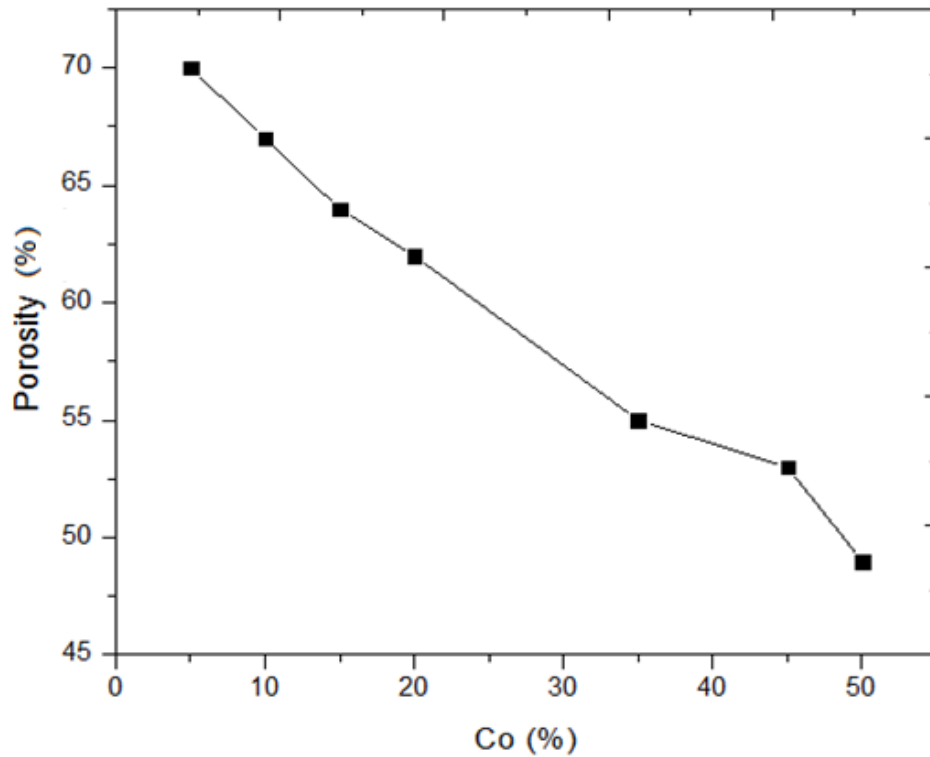


Figure 4- 3. The change of porosity with the cobalt content.

X-ray diffraction analysis were conducted to identify the phases of the porous samples obtained. The XRD patterns for the sintered samples added with various amounts of cobalt are displayed in Figure 4-4. Cr_3C_2 was found to be the only phase for the sample without cobalt addition (not shown) [14]. As cobalt was introduced to the sample, the peaks were indexed to Cr_7C_3 phase only. It can be seen that evident peaks belonging to metallic cobalt phase are also present when the amount of cobalt increased to 35 wt. %. Therefore, a portion of metallic cobalt must have been carburized and most likely dissolved into the carbide phase.

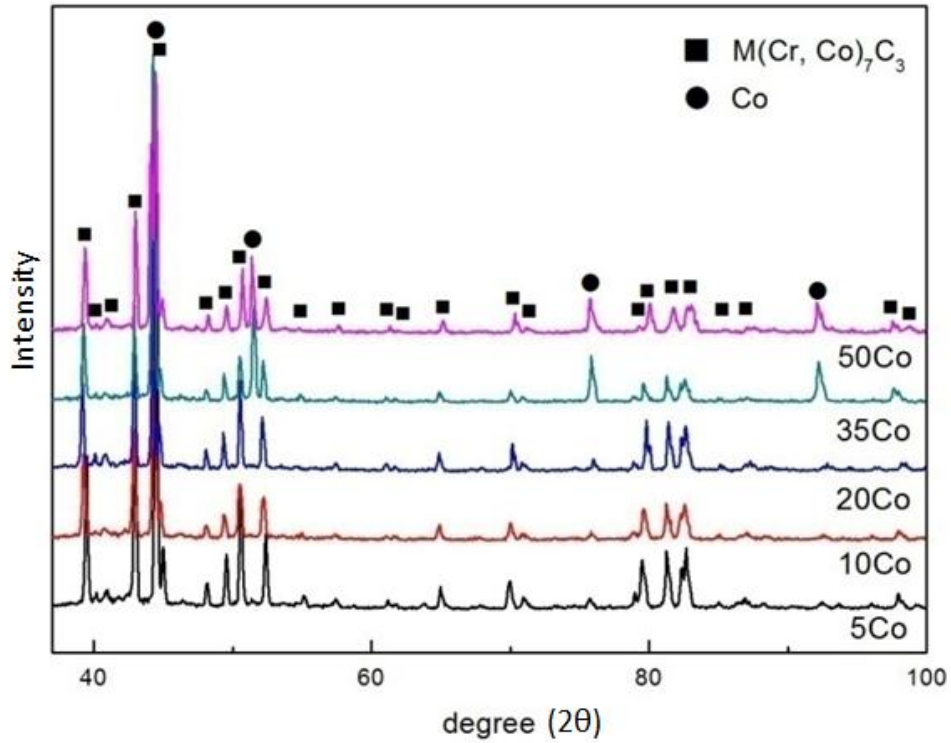


Figure 4- 4. XRD patterns of carburized samples added with various amount of cobalt.

To confirm the dissolution of cobalt in carbides, a sample with a composition of 24.4 wt. % Co + 75.6 wt. % Cr_7C_3 was prepared by mixing cobalt and carbide (Cr_7C_3) powders without any sintering process. The component ratio (24.4 wt. % Co + 75.59 wt. % Cr_7C_3) is equivalent to that of a 20 wt. % cobalt added sample after carburization, assuming that Cr_2O_3 was carburized to Cr_7C_3 and metallic cobalt was not reacted. The XRD patterns of both the mixed sample and the carburized sample are comparatively shown in Figure 4-5. It can be seen that the cobalt peaks for the mixed sample is much stronger than the carburized sample, indicating that the cobalt was involved into the reactive sintering and the (M(Co,

Cr_7C_3) phase was produced during the sintering. This will be further investigated in the following sections.

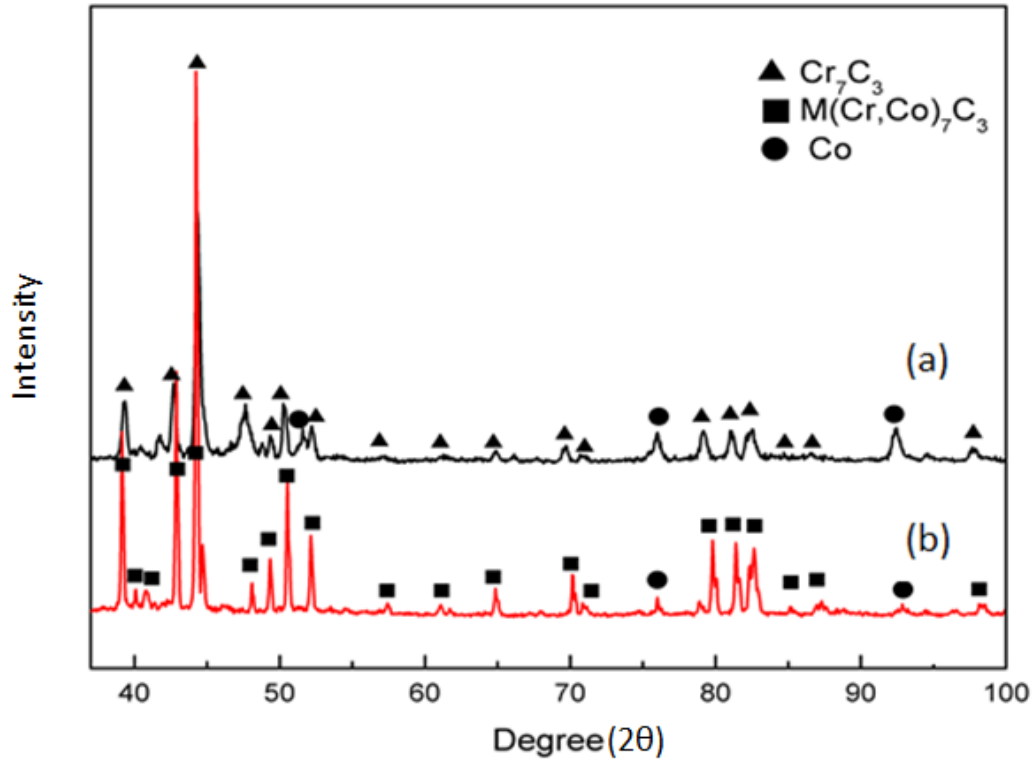


Figure 4- 5. XRD patterns of (a) mixing sample (24.4 wt. % Co + 75.59 wt. % Cr_7C_3); (b) carburized sample with 20 wt. % Co.

The elemental distribution of the samples added with cobalt was characterized by EDS mapping. Figure 4-6 shows the EDS maps of the carburized sample containing 10 wt. % cobalt. The noisy Cr signals may be induced by the porous morphology of the sample. Cobalt is seen to be quite uniformly distributed in the structure and the signal of cobalt consistently coincides with that of carbon and the porous morphology, indicating the dissolution of cobalt in the carbide phase. Figure 4-7 shows the cobalt distribution in the samples added with various

amounts of cobalt. It can be seen that the areas with high cobalt concentration appear to increase with increasing the cobalt content. Therefore, it can be hypothesized that the $M(\text{Cr}, \text{Co})_7\text{C}_3$ phase was formed as a result of cobalt dissolution into Cr carbide phase during the sintering process. When cobalt amount was higher than its solubility in $M(\text{Cr}, \text{Co})_7\text{C}_3$ phase, cobalt enriched areas where metallic cobalt or Co-Cr solid solution is most likely present are formed.

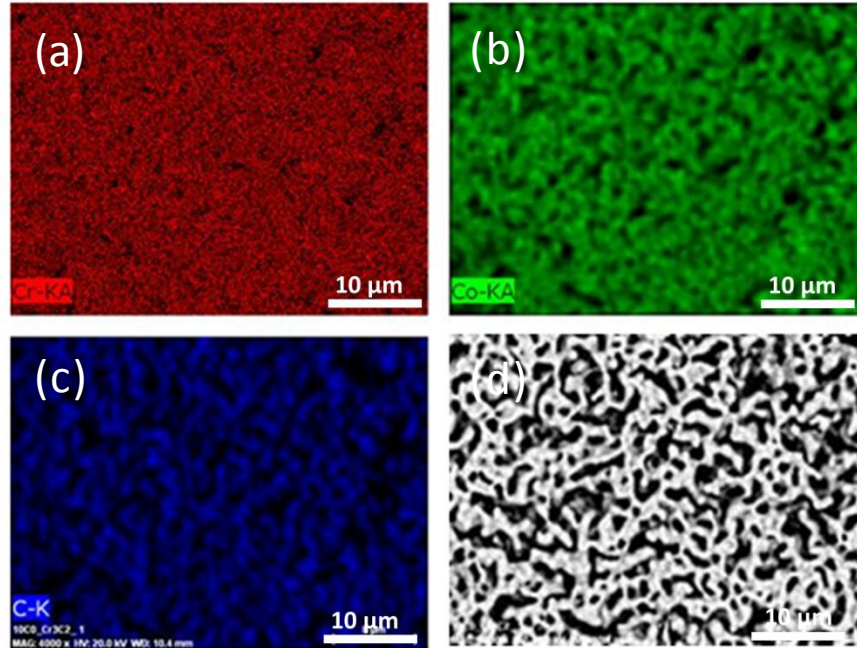


Figure 4- 6. EDS mapping results for carburized sample added with 10 wt. % cobalt: (a)(b)(c) are mapping images for Cr, Co, and C, respectively; (d) is backscatter electron image.

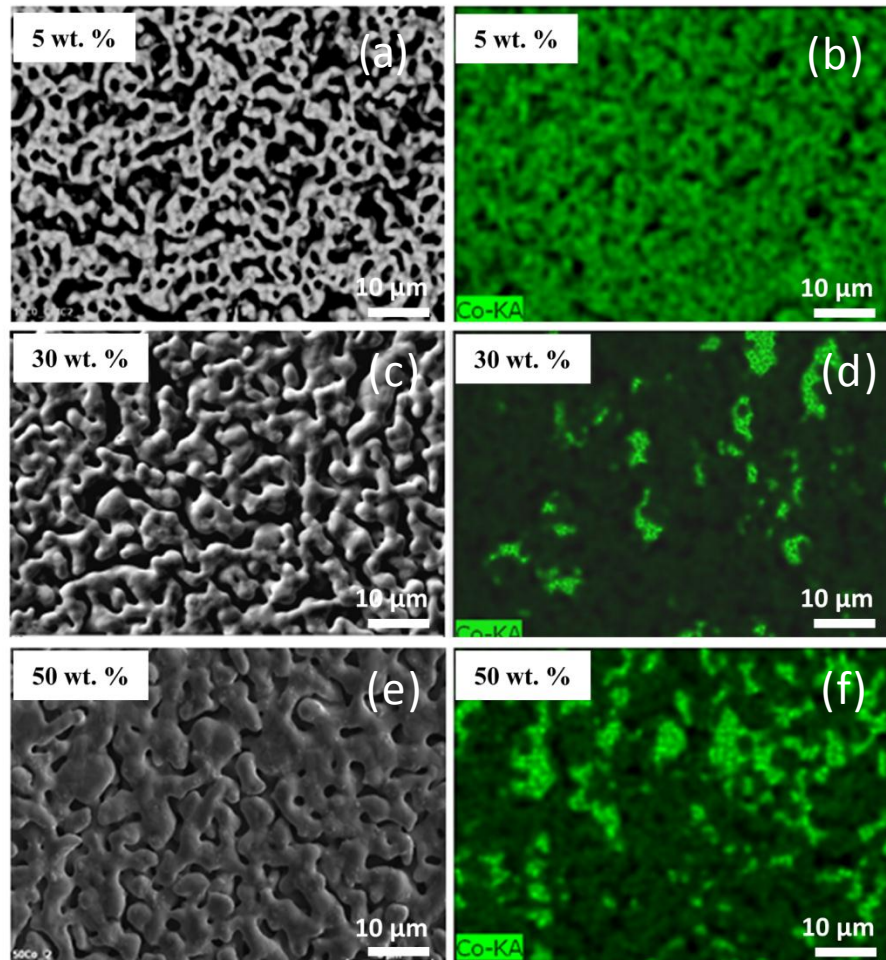


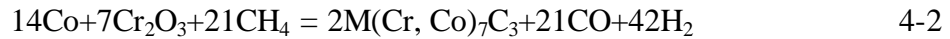
Figure 4- 7. EDS mapping results for carburized samples added with various amounts of cobalt: (a)(c)(e) are SEM images; (b)(d)(f) are mapping images for Co.

The C-Co-Cr system has been studied because of its wide applications in the hard metal industry, and determining the maximum solubility of Co in M_7C_3 phase is one of the key issues for the fabrication of Co-Cr-C hard material as the $M(Cr, Co)_7C_3$ phase is a primary phase that might precipitate during cooling after sintering of the quaternary system C-Co-Cr-W [12]. The first investigation on the ternary system Cr-Co-C was reported by Koster and Sperner in 1955 [8]. They determined that the maximum solubility of Co in the Cr_7C_3 phase was 26 wt. %

after characterizing more than 60 different C-Co-Cr compositions at 1073K. The following investigation on the solubility of cobalt in $M(\text{Cr}, \text{Co})_7\text{C}_3$ phase was conducted by Thompson [9], Sahm [10] and Kusoffsky [11]. Their results indicated that the solubility of cobalt in $M_7\text{C}_3$ -type phase was ranged between 10 wt. % and 26 wt. %. The latest study on the C-Co-Cr system was carried out by Sterneland et al. in 2006 by using both experimental and atomistic simulation method [13]. They heat-treated a mixture of Cr_7C_3 and cobalt powder for a very long time (28 days) and found that the solubility of cobalt in $M_7\text{C}_3$ was 38.66 wt. % at 1373K, which is higher than the results previously reported. The maximum solubility determined by atomistic simulation is even higher, which was 43.5 wt. % [13]. Therefore, it is reasonable to expect that a $M(\text{Cr}, \text{Co})_7\text{C}_3$ phase could be formed by dissolving cobalt into the obtained Cr_7C_3 phase in this study.

The elemental contents in the cobalt added samples were quantified by EDS analysis which are listed in Table 4-1. The results show that the cobalt content in $M_7\text{C}_3$ phase increased consistently with the amount of cobalt being added, despite the observation of cobalt metal when the cobalt content reached 30 wt. %, as indicated by EDS mapping. The highest solubility of cobalt in $M_7\text{C}_3$ phase was determined to be 41.6 wt. %, which was achieved in the sample with an addition of 50 wt. % Co. The highest solubility measured in this study is roughly consistent with the solubility limit reported by Sterneland [13, 19]. A slight higher value found in this investigation may be caused by the different experimental methods used for achieving cobalt dissolution. Some error may be caused by the

detection limit of EDS analysis and the roughness of the porous surface. However, the heat treating period of 28 days conducted by Sterneland was much longer than that of the current test (10 hours), indicating a much faster phase formation process in the current investigation. The sintering of $M(\text{Cr}, \text{Co})_7\text{C}_3$ phase in this investigation is suggested to occur through the following reaction:



Cobalt could be completely dissolved into carbide and form single phase $M(\text{Cr}, \text{Co})_7\text{C}_3$ when cobalt content was low. As cobalt content increased, more cobalt was dissolved into $M(\text{Cr}, \text{Co})_7\text{C}_3$ and some cobalt remained either due to insufficient time of reaction or due to the reach of solubility of cobalt locally.

Table 4- 1. EDS tests for samples added with various amounts of cobalt.

| Cobalt content (%) | M_7C_3 | | | Cobalt enriched phase | | |
|--------------------|----------|-------|-------|-----------------------|-------|-------|
| | Co | Cr | C | Co | Cr | C |
| 5 | 5.93 | 84.38 | 9.69 | | | |
| 10 | 12.17 | 78.47 | 9.36 | | | |
| 15 | 17.86 | 73.7 | 8.44 | | | |
| 20 | 22.49 | 69.99 | 7.52 | | | |
| 30 | 27.67 | 43.89 | 28.44 | 72.17 | 9.14 | 15.58 |
| 35 | 27.61 | 64.47 | 7.91 | 86.87 | 10.65 | 2.47 |
| 45 | 36.07 | 54 | 9.96 | 86.93 | 9.61 | 3.46 |
| 50 | 41.6 | 51.21 | 7.2 | 88.88 | 7.37 | 3.75 |

4.3.2.2 XPS analysis for the cobalt-added samples

The porous samples with the addition of cobalt of 5 wt. %, 10 wt. % and 50 wt. % were examined by X-ray photoelectron spectroscopy, which is shown in Figure 4-8. The spectra for the Co $2p_{3/2}$ region are shown in Figure 4-8(a-(1~3)). The spectrum peak located at 781.0 ± 0.2 eV and 778.5 ± 0.3 eV can be assigned to Co(III) and metallic cobalt, respectively [20-22]. It can be seen that the 5 wt. % Co-added sample consisted of not only of Co(III) indicated by the peak at 781.2 eV, but also the metallic form of cobalt, indicating that the metallic cobalt was still partially left even when the weight ratio of cobalt was low (5 wt. %), though XRD analysis failed to detect the existence of metallic cobalt. Increasing the cobalt content leads to more metallic cobalt, as shown in Figure 4-8 (a-(1~3)).

The Cr $2p_{3/2}$ peaks for the cobalt-added samples are shown in Figure 4-8 (b-(1~3)). Unlike the Cr $2p_{3/2}$ peak reported for Cr_7C_3 which shows a symmetric peak profile at BE of 574.5 ± 0.2 eV [23, 24], the Cr $2p_{3/2}$ peaks observed here were all non-symmetrically broadened on the high binding energy side. The broadened non-symmetrical peak could be resolved into two peaks, one is at 574.5 eV which can be assigned to chromium metal (Cr-Cr) or chromium carbide (Cr-C in Cr_7C_3) [23], and the other is at 576.1 eV which is consistent with the BE of Cr $2p_{3/2}$ in Cr_2O_3 [25]. However, no obvious change was observed for the Cr $2p_{3/2}$ peaks with the variation of cobalt content. The reason for the non-symmetrical broadening has not been completely clarified. It may be caused by the change of atomic bonding in $\text{M}(\text{Cr},\text{Co})_7\text{C}_3$ phase or the presence of chromium oxide phase formed during the Ar-purging stage.

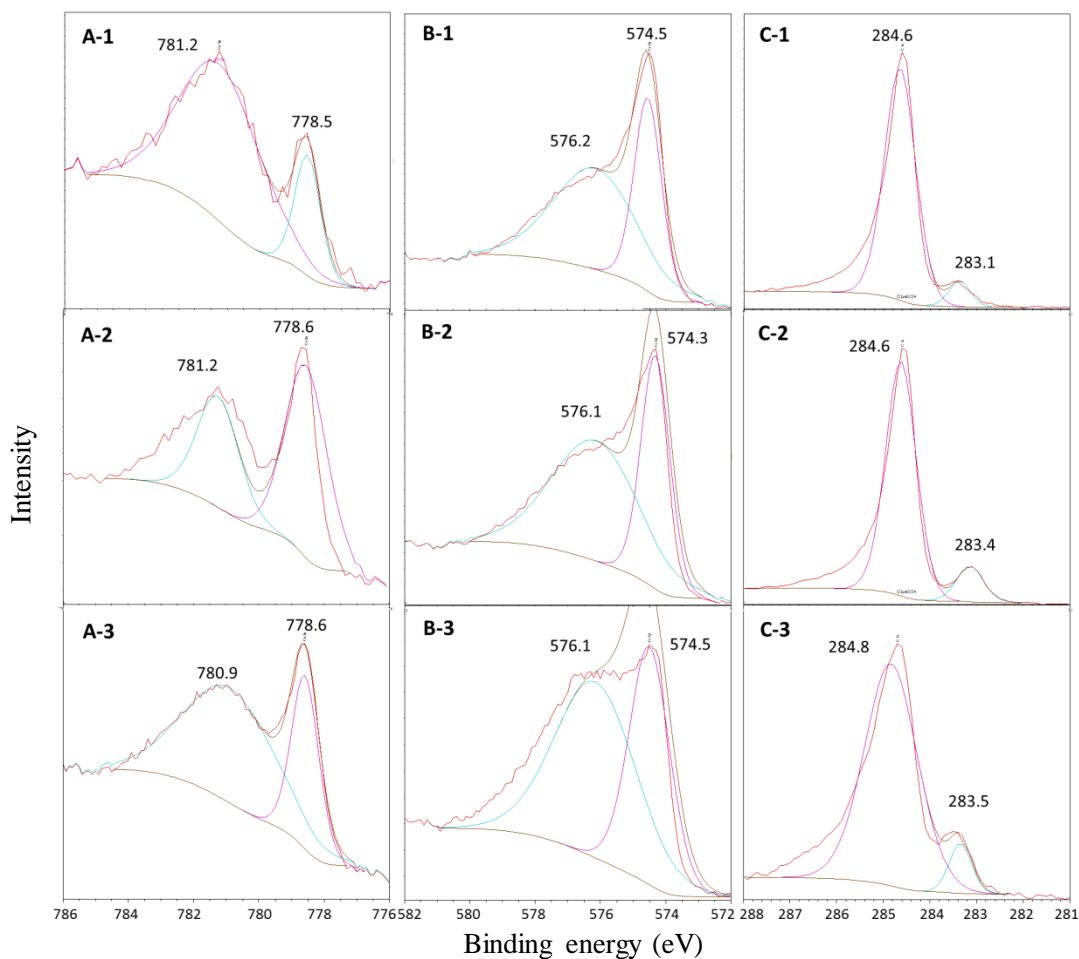


Figure 4- 8. XPS analysis for the cobalt added samples: A(1-3) - Co 2p_{3/2} peaks; B(1-3) - Cr 2p 3/2 peaks; C(1-3) - C 1s peaks; 1, 2, 3 denote the samples added with cobalt of 5, 20, and 50 wt. % respectively.

The C 1s peaks of different samples are shown in Figure 4-8(c-(1~3)). It can be seen that all the C 1s peaks can be fitted at two BE levels. The peaks at 284.6 ±0.2 eV can be assigned to the bonding energy of carbon-carbon (C-C) [26], indicating the deposition of free carbon on the surfaces of samples, resulted from the catalytic effect of metallic cobalt in the carbonaceous environment. The C 1s peak at BE of 283.1, 283.4 and 283.5 eV can be assigned to the carbide carbon

bond [27]. Detroye et al. [23] have reported that the C 1s peak has higher energy in $M(\text{Cr, Fe})_7\text{C}_3$ (283.3 eV) than that in the Cr_7C_3 (283.0 eV). The shifting of the C 1s peak to higher energy observed should be related to the formation of $M(\text{Cr, Co})_7\text{C}_3$ and the different bonding energy affected by the increase of cobalt dissolution in the carbide.

4.3.3 Hardness characterization of the porous cermets

Hardness testing is a simple way to determine the resistance of a material to plastic deformation and/or fracture. The relationship of hardness with other properties such as tensile strength, wear resistance, compressibility, toughness, elastic modulus have been investigated and reported by various researchers [5, 28-33]. Porosity is a pervasive and important microstructural factor in all materials that often exerts a significant effect on some aspects of mechanical properties. The correlation of porosity to the hardness of materials has been extensively studied. One well known model that describes the porosity dependence of hardness is the Minimum Solid Area (MSA) Model proposed by Rice [34], as expressed by

$$H_V = H_0 \exp(-bP) \quad 4-3$$

H_V —measured hardness, H_0 —hardness value of a specimen with zero porosity, b —material dependence constant, P —volume fraction of the porosity.

The measured hardness values of the porous samples with various cobalt additions are listed in Table 4-2. The hardness of the porous carbide (Cr_3C_2) with

a porosity of 77 % was around 42 (Hv). When a small amount of cobalt (5 wt. %) was added, the hardness of porous $M(\text{Cr}, \text{Co})_7\text{C}_3$ cermet with a porosity of 70 vol. % was measured to be around 26 (Hv). Although the porosity of the cobalt added sample had decreased compared with the porous Cr_3C_2 , the hardness of the sample with 5 wt. % cobalt added is lower than that of the porous Cr_3C_2 . This may be caused by the hardness difference of the two types of carbide, as the hardness of Cr_7C_3 (Hv 1620) is lower than that of Cr_3C_2 (Hv 1830) [13, 18, 19].

Table 4- 2. Porosity and hardness of the samples added with various amounts of cobalt.

| | Cr_3C_2 | M_7C_3 | | | | | | |
|----------------------------|-------------------------|------------------------|------|------|------|------|------|------|
| Cobalt ratio(wt. %) | 0 | 5 | 10 | 15 | 20 | 35 | 45 | 50 |
| Porosity | 0.77 | 0.7 | 0.67 | 0.64 | 0.62 | 0.55 | 0.53 | 0.49 |
| Hardness(HV) | 42 | 26 | 31.9 | 53 | 70.8 | 68.5 | 97 | 127 |

The hardness values of the cobalt-added samples were plotted against the porosity as shown in Figure 4-9. The reference hardness curve was drawn for the pure Cr_7C_3 based on Equation (3). The material dependence constant (b) was taken to be 5.9, which was derived by the hardness value of sample added with 5 wt. % cobalt. The reference curve represents the dependence of the hardness of porous Cr_7C_3 on the ceramic porosity according to the MSA model.

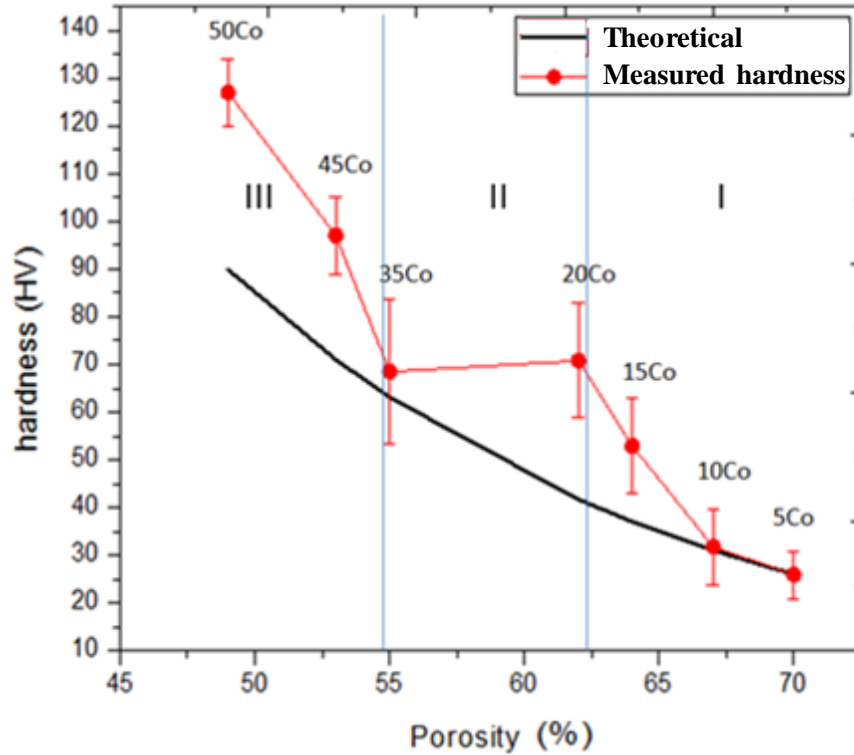


Figure 4- 9. Measured hardness values of cobalt-added samples and calculated hardness values based on MSA model.

The curve plotted using the measured hardness of the cobalt added samples can be divided into three regions. In region I, the porous samples with cobalt additions ranging from 5 wt. % to around 20 wt. % consisted mainly of the $M(Cr, Co)_7C_3$ phase. The rising of the hardness curve with the increase of the cobalt content in this region could result from a combined effect of the reduction of the porosity and the increased solid solution hardening of the $M(Cr, Co)_7C_3$. When the cobalt content additions increased from 20 wt. % to 35 wt. %, cobalt enriched areas were present in the sample, as shown in Figure 4-7 with cobalt content of 30 wt.%. The potency for the increase of the hardness was therefore reduced for region II as shown in the Fig. 4-9, because of the presence of soft metallic cobalt. For region

III in Fig. 4-9, although the hardness was found to be influenced by the increased cobalt enriched areas and the higher dissolution of cobalt in M_7C_3 phase, the effect of the reduction of the porosity on the hardness was dominant as the slope of the measured hardness curve approached that of the theoretical curve with the decrease of porosity.

To our knowledge, few reports have been published on the investigation of alloying effect on the mechanical properties of M_7C_3 type ceramics. However, hardening of metallic materials has been extensively studied and explained usually by the following hardening mechanisms: (1) grain refinement hardening, (2) solid solution hardening, (3) precipitation hardening, and (4) work hardening. The above mechanisms could also be used to rationalize the hardening effect in the ceramic materials.

Mott et al. proposed a relationship between the amount of hardening (ΔH) and the atomic concentration as shown below [35]:

$$\Delta H = A\mu\varepsilon^{4/3}C \quad 4-4$$

Where A is a constant, μ is the shear modulus, C is the atomic concentration of substitutional atom, ε is the difference of the atomic size between the solvent and solute atoms. It can be seen that the increase of hardness holds a linear relationship with the concentration of the substitutional atom as the other

parameters can be pre-determined by the alloying element. Therefore, it is reasonable to believe that the hardening of M_7C_3 carbide phase by the addition of cobalt is due to the solid solution hardening.

Inoue et al. reported the effect of alloying elements on the defect structure and hardness of $M(\text{Cr, Fe, X})_{23}C_6$ type carbides [36]. They suggested that the hardening effect by alloying the carbide could not be solely attributed to the solid solution hardening. They found that the defect structure in $(\text{Cr, Fe})_{23}C_6$ was remarkably modified by the addition of various amounts of alloying elements (Mn, W, Mo, etc). They proposed that the modification of the defects by alloying element may also be responsible for the hardness change of the carbide ceramics. Their results also show that stacking faults with some other defects (dislocations, antiphase domain boundaries) were observed when alloying elements were introduced into $(\text{Cr, Fe})_{23}C_6$. Zackrisson et al. investigated the WC-Co based cemented carbides with different amounts of Cr_3C_2 (0-12 vol%) [6]. They found a chromium-rich M_7C_3 carbide phase mainly composed of Co, Cr and C existed in the cermet. TEM/EDX analysis revealed that chromium and cobalt contents in this phase depended on the amount of Cr_3C_2 added to the starting powder. A high density of planar faults were observed in the M_7C_3 phases by TEM analysis. Therefore, the hardness increase of the $M(\text{Cr, Co})_7C_3$ phase could be caused by the dissolution of cobalt, which may result in the possible formation of planar faults in the M_7C_3 phase.

The above discussion on various attributes of the change of hardness can be further summarized as follows:

- 1) The change of porosity, which could cause a change of hardness that can be modeled by Eq. (3) (the theoretical value in Fig. 9)
- 2) The change of solubility of Co in $M(\text{Cr}, \text{Co})_7\text{C}_3$, which will result in different solid solution strengthening. Increasing cobalt content being added into the starting powder would increase the dissolved Co in $M(\text{Cr}, \text{Co})_7\text{C}_3$ after carburization.
- 3) The presence of remaining metallic Co, which would reduce the hardness with increasing metallic Co content. Increasing cobalt content being added into the starting powder will lead to more remaining metal in the form of cobalt and lower hardness of porous ceramics.

Factor 1) in the above attribute list can be eliminated by considering the difference in hardness between the measured hardness value and the theoretical hardness value (Fig. 4-9). This hardness difference is presented in Fig. 4-10 as a function of cobalt content being added. The curve in Fig. 4-10 can be roughly divided into three regions as marked in the figure, similar to that in Fig. 4-9. It can be seen in Fig. 4-10 that the hardness difference increased with cobalt content by a linear relationship in Region I and Region III, although the hardness of the sample with cobalt addition at 5 wt. % slightly deviated from the line. The increase in hardness with increasing Co content in Region I and III can be attributed to the increased solubility of Co in $M(\text{Cr}, \text{Co})_7\text{C}_3$ phase (factor 2). The

slope of the line in region III is little smaller than that of the line in region I due to the present of the cobalt enriched area in the sample, which will be further discussed later.

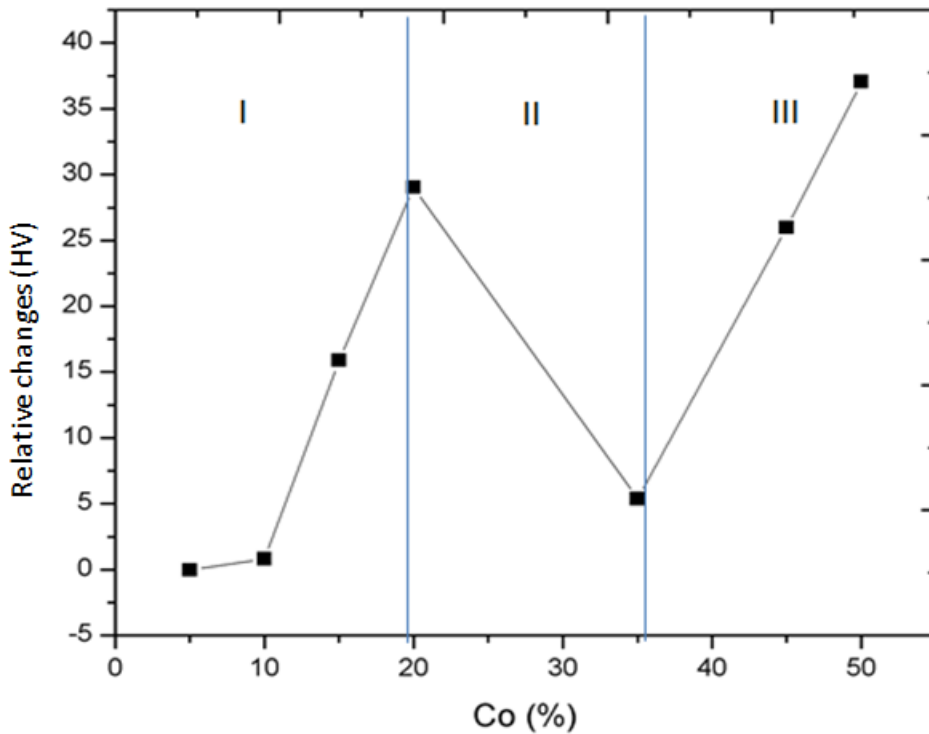


Figure 4- 10. Relative changes of the hardness derived by using the measured average value minus the theoretical value.

A large disruption in hardness curve in Region II of Fig. 4-10 was observed. This disruption could be related to the effects of Factor 2 and/or Factor 3, since the effect of Factor 1 has been eliminated. As discussed above, the change of Co dissolution in $M(\text{Cr}, \text{Co})_7\text{C}_3$ phase is accompanied with a change of hardness. The cobalt content in $M(\text{Cr}, \text{Co})_7\text{C}_3$ phase was plotted against the cobalt content being added, which was shown in Figure 4-11. It can be seen that the amount of

dissolved cobalt increased linearly with the cobalt content being initially added in the ranges of 0~20 wt. % and 40~50 wt. %. However, there exists a plateau shift between 20 wt. % and 40 wt. % as shown in Figure 4-11. This disruption may be related to the onset of cobalt enriched phase formation. It was observed that the struts of porous carbides became coarsened with increasing Co addition, as shown in Figure 4-2. This may retard the dissolution of cobalt because of longer diffusion path. In addition, the undissolved Co particles may experience coarsening as well. This would make Co less dispersed, which would further retard the diffusion and dissolution of Co-species into the carbides.

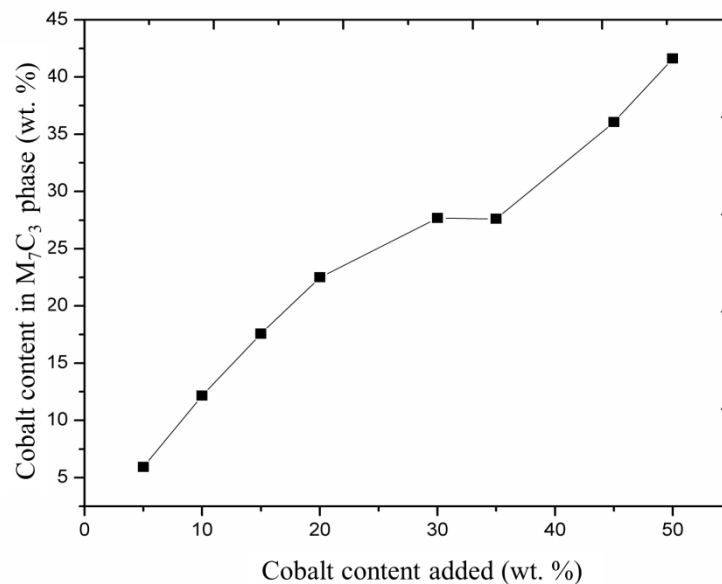


Figure 4-11. The dissolved cobalt content in M_7C_3 phase plotted against the cobalt content being added.

The large disruption in hardness observed in Figure 4-10 should not be attributed to the change of dissolution behavior of cobalt in the carbide since the dissolved Co was not reduced with increasing Co when the Co content being added was in

the range of 20~40 wt. %. Since the metallic cobalt enriched areas were observed only after the cobalt content was increased to 30 wt. %, the presence of soft Co-rich phases should be mainly responsible for the reduction of the hardness (Stage II) shown in Figure 4-10.

4.4 Concluding Remarks

Porous $M(\text{Cr}, \text{Co})_7\text{C}_3$ -Co composite materials have been successfully prepared by carburizing samples composed of chromium oxide (Cr_2O_3) mixed with various amounts (5 wt. % - 50 wt. %) of cobalt. It has determined that both the porous structure and the chemical composition of the porous composites were affected by the cobalt content added. The porosity of the composite decreased with increasing cobalt content, whereas the pore size increased. When the cobalt content was below 30 wt. %, the porous composites mainly consisted $M(\text{Cr}, \text{Co})_7\text{C}_3$ phase. When more cobalt was added, cobalt enriched phases were formed. The results show that a high solubility of cobalt in $M(\text{Cr}, \text{Co})_7\text{C}_3$ phase could be achieved by the current reactive sintering method and the increased dissolution of cobalt can strengthen the $M(\text{Cr}, \text{Co})_7\text{C}_3$ phase as indicated by the hardness evaluation.

4.5 Bibliography

- [1] P. Colombo, *Science*, 322 (2008) 381-383.
- [2] P. Colombo, *Philosophical Transactions of the Royal Society a-Mathematical Physical and Engineering Sciences*, 364 (2006) 109-124.
- [3] P. Colombo, T. Gambaryan-Roisman, M. Scheffler, P. Buhler, P. Greil, *Journal of the American Ceramic Society*, 84 (2001) 2265-2268.
- [4] A.R. Studart, U.T. Gonzenbach, E. Tervoort, L.J. Gauckler, *Journal of the American Ceramic Society*, 89 (2006) 1771-1789.
- [5] W. Schubert, H. Neumeister, G. Kinger, B. Lux, *International Journal of Refractory Metals and Hard Materials*, 16 (1998) 133-142.
- [6] J. Zackrisson, B. Jansson, G. Uphadyaya, *International Journal of Refractory Metals and Hard Materials*, 16 (1998) 417-422.
- [7] A. Petersson, J. Ågren, *International Journal of Refractory Metals and Hard Materials*, 23 (2005) 258-266.
- [8] W. Koster, F. Sperner, *Arch. Eizenhuttenuesen*, 26 (1955).
- [9] E. Thompson, F. Lemkey, *Metallurgical and Materials Transactions B*, 1 (1970) 2799-2806.
- [10] P. Sahn, D. Watts, *Metallurgical and Materials Transactions B*, 2 (1971) 1260-1261.
- [11] A. Kusoffsky, B. Jansson, *Calphad*, 21 (1997) 321-333.
- [12] J. Zackrisson, U. Rolander, G. Weinl, *International Journal of Refractory Metals and Hard Materials*, 16 (1998) 315-322.
- [13] T. Sterneland, J. Xie, N. Chen, S. Seetharaman, *Scripta materialia*, 54 (2006) 1491-1495.

- [14] T. Xing, X. Cui, W. Chen, R. Yang, *Materials Chemistry and Physics*, 128 (2011) 181-186.
- [15] H. Li, W. Chen, *Corrosion Science*, 53 2097-2105.
- [16] M. Colombo, F. Clemente, *Crocevia Di Suoni Records*, [S.I.].
- [17] H. Li, Y. Zheng, L.W. Benum, M. Oballa, W. Chen, *Corrosion Science*, 51 (2009) 2336-2341.
- [18] T. Tomita, Y. Takatani, K. Tani, Y. Harada, *JOURNAL-HIGH TEMPERATURE SOCIETY*, 26 (2000) 248-253.
- [19] T. Sterneland, A. Markström, S. Norgren, R. Aune, S. Seetharaman, *Metallurgical and Materials Transactions A*, 37 (2006) 3023-3028.
- [20] B.J. Tan, K.J. Klabunde, P.M.A. Sherwood, *Journal of the American Chemical Society*, 113 (1991) 855-861.
- [21] I. Alstrup, I. Chorkendorff, R. Candia, B.S. Clausen, H. Topsøe, *Journal of Catalysis*, 77 (1982) 397-409.
- [22] I.G. Casella, M.R. Guascito, *Journal of Electroanalytical Chemistry*, 476 (1999) 54-63.
- [23] M. Detroye, F. Reniers, C. Buess-Herman, J. Vereecken, *Applied surface science*, 144 (1999) 78-82.
- [24] M.D. Healy, D.C. Smith, R.R. Rubiano, N.E. Elliott, R.W. Springer, *Chemistry of materials*, 6 (1994) 448-453.
- [25] T. Boiadjieva, D. Kovacheva, K. Petrov, S. Hardcastle, A. Sklyarov, M. Monev, *Journal of applied electrochemistry*, 34 (2004) 315-321.

- [26] S.C. Wang, H.T. Lin, P.K. Nayak, S.Y. Chang, J.L. Huang, *Thin Solid Films*, 518 (2010) 7360-7365.
- [27] P. Smith, O. Biest, J. Corish, *Oxidation of metals*, 24 (1985) 47-83.
- [28] Y. Bao, W. Wang, Y. Zhou, *Acta materialia*, 52 (2004) 5397-5404.
- [29] Y.T. Cheng, C.M. Cheng, *Applied physics letters*, 73 (1998) 614.
- [30] G.P. Evans, J.C. Behiri, J.D. Currey, W. Bonfield, *Journal of Materials Science: Materials in Medicine*, 1 (1990) 38-43.
- [31] W.C. Oliver, G.M. Pharr, *Journal of materials research*, 7 (1992) 1564-1583.
- [32] L. Qian, X. Xiao, Q. Sun, T. Yu, *Applied physics letters*, 84 (2004) 1076-1078.
- [33] D. Tabor, *Philosophical Magazine A*, 74 (1996) 1207-1212.
- [34] R. Rice, *Journal of materials science*, 31 (1996) 102-118.
- [35] N. Mott, F. Nabarro, *Physical Society, London*, 1 (1948).
- [36] A. Inoue, S. Arakawa, T. Masumoto, *Transactions of the Japan Institute of Metals*, 20 (1979) 585-592.

Chapter 5 Corrosion Behavior of Porous Chromium Carbide in Supercritical Water

* A version of this chapter has been published. Z. Dong, W. Chen, W. Zheng, D. Guzonas, Journal of Nuclear Materials, 420 (2012) 320-327.

5.1 Introduction

The Super Critical Water-cooled Reactor (SCWR) is one of the most promising advanced reactor concepts proposed by Generation-IV International Forum (GIF), which will fulfill the criteria of economics, safety and sustainability [1]. Supercritical Water (SCW) was used as a coolant in the SCWR, offering many advantages, such as higher thermal efficiency (i.e., 45-50% versus about 30-35% efficiency for current LWR), reduced size of reactor components and simplification of the heat transport circuit, as the steam generators, steam dryers, steam separators, are eliminated [2, 3]. On the other hand, using SCW as the coolant leads to some materials challenges as SCW is a very aggressive medium, especially at higher operating temperatures and pressures with the presence of high concentration of oxidants.

Supercritical water, as the water above its thermodynamic critical point (374 °C, 22.1MPa), exists as a single phase with physical properties intermediate between that of liquid and gaseous water phases. It is a medium with high diffusivity and good heat-transport properties [4-6]. Low-density supercritical water behaves like a non-polar solvent, showing high solvency for non-polar organic compounds and gases. The coolant of the proposed Gen-IV SCWR will be operated at 25 MPa, with an inlet temperature of 350 °C and outlet temperature of up to 625 °C [3]. Currently available alloys may not be suitable for application in an SCWR under these conditions. As ceramic materials can exhibit higher stability and corrosion resistance in some critical environments as compared to metallic materials, it may be possible to use a ceramic coating on a metal to improve the corrosion

resistance. A number of ceramics have been tested to determine their stabilities under different SCW conditions. In the work conducted by Boukis et al. [7], it was observed that HIP-BN, B₄C, TiB₂, Y₂O₃ and Y-TZP disintegrated after being exposed to SCW containing 0.44 mol kg⁻¹ oxygen and 0.05 mol kg⁻¹ hydrochloric acid at a temperature of 465 °C and a pressure of 25 MPa. SiC- and Si₃N₄- based materials showed large weight losses up to 90%. Homogeneous surface attack and grain boundary diffusion were observed for the ceramic samples tested. Monolithic Al₂O₃ showed better corrosion resistance than mixed Al₂O₃ with ZrO₂. The addition of non-oxide hard particles (20 vol % TiC/TiN) reduced the corrosion resistance of Al₂O₃. Schacht et al. [8] systematically examined the corrosion resistance of alumina ceramics and zirconia toughened alumina (ZTA) ceramics in aqueous acidic solutions (HCl, H₂SO₄, H₃PO₄) under hydrothermal conditions. It was found that the dominant corrosion mechanisms for Al₂O₃ under hydrothermal conditions were intergranular attack with dissolution of Al₂O₃. The intensity of the grain boundary attack depends on the material purity, since impurities like SiO₂ and CaO or sintering aids like MgO have only a small solubility in Al₂O₃ and move to the grain boundaries during the sintering process where they segregate or form a grain boundary phase. Accordingly, high purity alumina (99.7 % Al₂O₃) generally shows the highest resistance against intergranular corrosion in SCW.

Chromium carbide (Cr₃C₂) is a ceramic material which is widely used in industry applications for its unique properties such as high hardness and Young's modulus,

medium fracture toughness, excellent high-temperature erosion and wear resistance, low density, high-temperature and chemical stability [9-11]. It is usually thermally sprayed for protecting the underlying metal surface, or used as an additive in coatings to increase their resistance to corrosion and wear. The thermal expansion coefficient of Cr_3C_2 is almost equal to that of steel, which can reduce the stress buildup at the boundary between Cr_3C_2 and the surface of steel. Kosolapova et al. conducted initial work on the stability of Cr_3C_2 in oxidizing environments at high temperatures and determined that the initial oxidation temperature of Cr_3C_2 was 700 °C [12]. However, to our knowledge, no systematic work has been conducted to characterize the corrosion behavior of Cr_3C_2 in SCW environments.

The work reported in this chapter investigated the stability of the porous chromium carbide (Cr_3C_2) in different SCW environments. The porous Cr_3C_2 was prepared by a reactive sintering process. The corrosion behavior of chromium carbide under SCW conditions was characterized by evaluating the weight and morphology changes. The mechanism of the degradation of Cr_3C_2 in high-temperature SCW was also discussed.

5.2 Experimental

Chromium (III) oxide powder (Alfa Aesar, USA, average particle size P_s of $\sim 2\ \mu\text{m}$, purity of 99%) was used as the starting material. The oxide powder was uniaxially compressed in a cylindrical mold under a pressure of 80 MPa to form disk-shaped

samples with a diameter of 16 mm and thickness of 2 mm. The disk shaped samples were put into a tube furnace (GSL1600X, MTI Corporation) and heated to 1100 °C, in a reducing gas mixture (2% CH₄+98%H₂, Praxair Canada) at a flow rate of 140 ml/min for 15 hours.

To investigate the stability of the porous carbide in SCW environments, a static reactor was built to conduct SCW tests as shown in Figure 5-1. The static reactor was made of a length of Inconel 625 tubing, with an outside diameter of 9.525 mm and a wall thickness of 1.651 mm. The ceramic coupons were cut from porous chromium carbide disk samples with a size of 10mm×4mm×2mm and cleaned by using ethanol in an ultrasonic cleaner. The ceramic coupons were then separately sealed in a tube capsule with a controlled amount of deionized water. Only one coupon was put in each tube. Air-saturated, neutral pH de-ionized water with an oxygen concentration of about 8 ppm was used in the SCW tests. Since no purge procedure was conducted, some air was present in the sealed reactor.

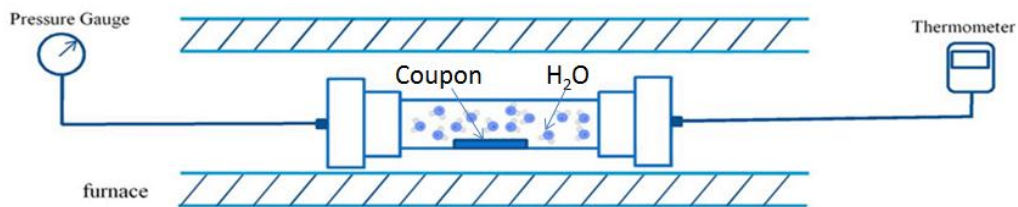


Figure 5- 1. Supercritical water test facility.

Morphologies of the ceramic samples were examined using JEOL (JSM-6301FXV) field emission scanning electron microscope and ZEISS (EVO –MA15) SEM. X-ray diffractometer (XRD) analysis was carried out using a Rigaku Geigerflex 2173 X-ray diffraction equipment. The porous properties of the as-carburized samples were characterized using a mercury intrusion porosimeter (AutoPore IV 9510). Infrared spectra were recorded by Nicolet 8700 Fourier Transform Infrared Spectrometer in KBr pellets (0.005 g sample and 0.095 g KBr).

5.3 Results

5.3.1 Porous chromium carbide ceramic

The surface morphology of an as-pressed Cr_2O_3 sample before reactive sintering is shown in Figure 5-2(a) [13]. It can be seen that the surface consists of micrometer-sized Cr_2O_3 particles compacted together, which were mainly held together by electrostatic forces across the particle interface. The porosity of the compact samples calculated from the sample dimensions and mass is about 36.9-40.7 %. Figures 5-2 (b) and (c) show SEM micrographs of the surface and cross-section for the sample obtained by reactive sintering in a reducing atmosphere (2% CH_4 +98% H_2) at a sintering temperature of 1100 °C for 10 hours. The sample after sintering exhibits a remarkably homogeneous porous morphology with a smooth three-dimensional network skeleton structure. The phase for this porous sample was identified as Cr_3C_2 by X-ray diffraction analysis. The porosity properties were characterized by mercury intrusion porosimeter. Test results

revealed that the porosity of this carbide was about 77% and the average pore size was around 1.16 μm .

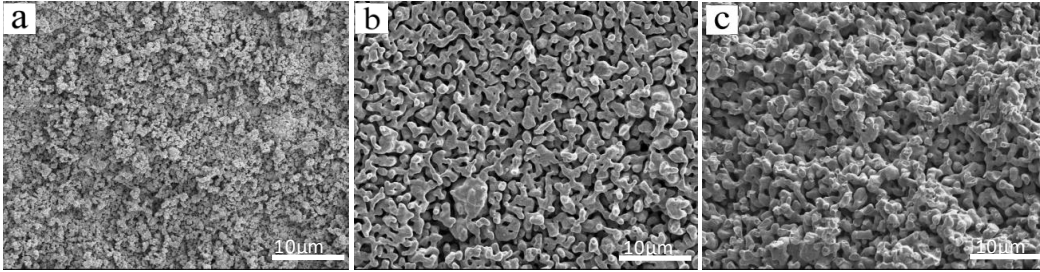


Figure 5- 2. SEM micrographs of 100% Cr_2O_3 green disk before sintering (a) and after sintering at 1100 $^\circ\text{C}$ under a reducing atmosphere (2% CH_4 +98% H_2) for 10 hours (b) surface and (c) cross-section [13].

5.3.2 Stability of porous chromium carbide in SCW

5.3.2.1 Corrosion tests of chromium carbide in SCW at different temperatures

The porous chromium carbide coupons were exposed to SCW environments at temperatures ranging from 375 $^\circ\text{C}$ to 625 $^\circ\text{C}$ under a constant pressure at 25~30 MPa. All tests were conducted for 25 hours. The weight change results after exposure are listed in Table 5-1. It can be seen that little weight gain (0.14% -0.80% of the original mass) was observed for the coupons tested in SCW at temperatures from 375 $^\circ\text{C}$ to 415 $^\circ\text{C}$. As the temperature increased to 425 $^\circ\text{C}$, a weight gain of about 10.16% was measured. When the temperature increased above 450 $^\circ\text{C}$, the integrity of the coupon was not retained after SCW exposure. The porous ceramic coupons disintegrated into powders during the SCW tests. It is interesting that there was a smell similar to that of gasoline when the capsule was opened for all the SCW tests.

Table 5- 1. Weight changes of ceramic coupons after exposure to SCW for 25 h at different temperatures.

| SCW condition | dG/G* |
|-------------------|---------------|
| 375 °C, 25~30 MPa | +0.0014 |
| 400 °C, 25~30 MPa | +0.0031 |
| 415 °C, 25~30 MPa | +0.0080 |
| 425 °C, 25~30 MPa | +0.1016 |
| 450 °C, 25~30 MPa | disintegrated |
| 625 °C, 25~30 MPa | disintegrated |

*dG-weight change after SCW test; G-initial weigh of coupon

The surface morphologies of the coupons after SCW tests were examined by high resolution field emission scanning electron microscopy. Figure 5-3 shows the surface SEM images of the coupons tested in SCW at 375 °C, 425 °C and 450 °C. The coupon exposed to SCW at 375°C didn't show obvious changes after SCW exposure, which is consistent with the small weight change. For the coupon tested in SCW at 425 °C, cracks along some preferred orientations were observed on the surface of the carbide, as shown in Figure 5-3(b). A magnified image (Figure 5-3(e)) shows that cracks roughly parallel to each other were present on the struts. Although cracks occurred during the test at 425 °C, the porous structure integrity was retained through SCW exposure. When the temperature increased to 450 °C, the porous chromium carbide coupon disintegrated. The surface morphologies of the powder produced by SCW exposure at 450 °C are shown in Figure 5-3(c) and (f). It can be seen that the uniform three dimensional porous structures have

deteriorated. The resulting powders were composed of particles with a size of 2-3 μm . Parallel cracks were observed within each particle as shown in Figure 5-3(f).

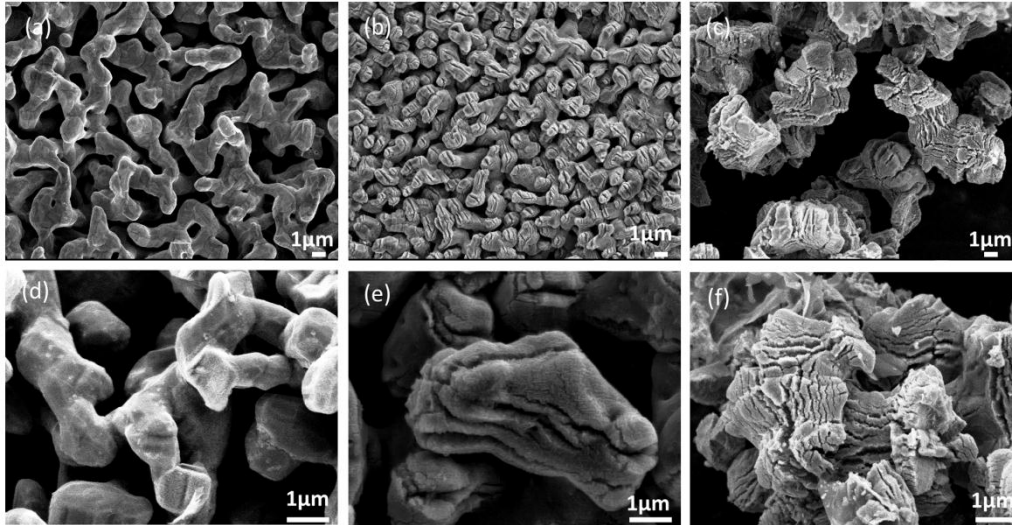


Figure 5- 3. Surface morphologies of porous carbide coupons after SCW tests at (a) 375 °C, (b) 425 °C and (d) 450 °C; (d) (e) (f) are magnified images.

Figure 5-4 shows the XRD patterns for the coupons after SCW tests at temperatures of 375 °C, 425 °C, 450 °C and 625 °C. In the pattern for coupon exposed to SCW at 375 °C, almost all intense reflections can be attributed to Cr_3C_2 phase. As the temperature increased to 425 °C, some weak peaks identified as Cr_2O_3 were present along with the Cr_3C_2 peaks. For the coupon exposed to SCW at 450 °C, broadened peaks indexed to Cr_2O_3 appeared, while the Cr_3C_2 peaks were eliminated. When the SCW temperature increased to 625 °C, the main phase in the powder that retained after the test was Cr_2O_3 as revealed by the XRD pattern. The XRD results are consistent with the results of the weight measurement and morphology observations, indicating that chemical reactions

accompanied by phase transformation may be responsible for the disintegration of chromium carbide. It also seems that a temperature of around 425 °C is the critical point for the stability of chromium carbide in SCW environments at a pressure of 25-30 MPa.

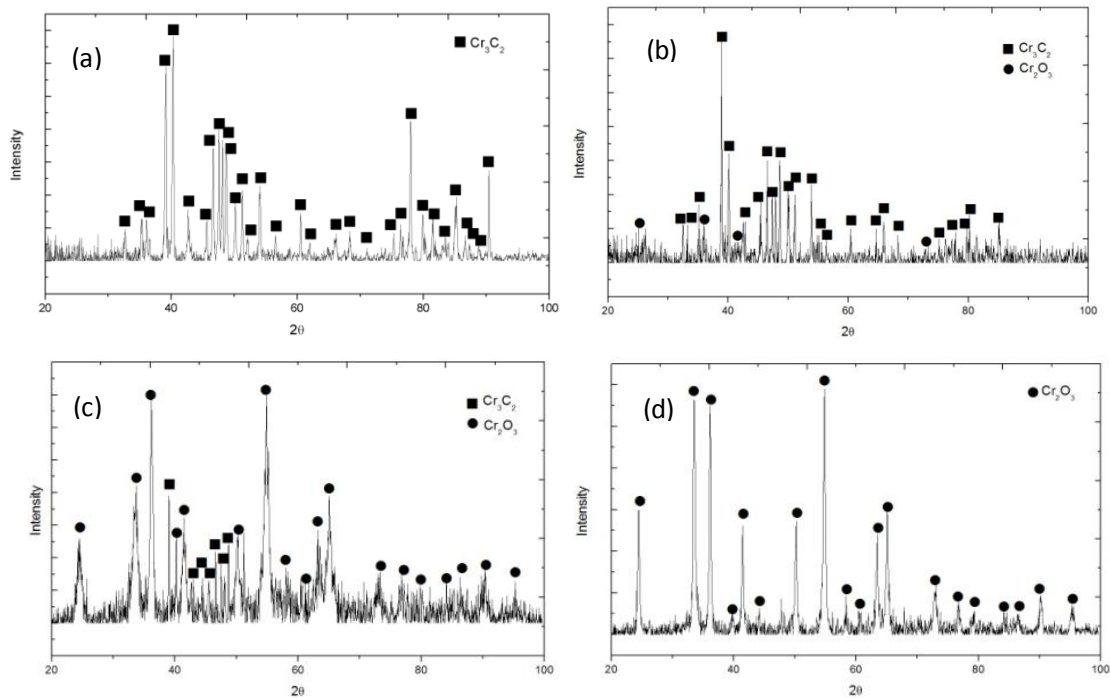


Figure 5- 4. XRD patterns of coupons after SCW tests at different temperatures: (a) 375 °C; (b) 425 °C; (c) 450 °C; (d) 625 °C.

5.3.2.2 Corrosion tests of chromium carbide in SCW at different pressures

To investigate the effect of pressure on the stability of porous carbide in SCW environments, the ceramic coupons were exposed to SCW at pressures ranging from 12~15 MPa to 47~50 MPa at constant temperatures of 400 °C and 415 °C. Table 5-2 lists the results of the weight change for the coupons after the SCW tests. No disintegration was observed for any of the coupons tested at 400 °C and

415 °C in SCW. Although it seems that the weight gain increased with the pressure, the effect of pressure on the stability of porous carbide sample was not significant at the temperatures tested. SEM images of the coupon surfaces after SCW exposures at 415 °C are shown in Figure 5-5. No obvious change in the surface morphologies of the coupons tested under different pressures was observed. XRD analysis (not shown) also showed that there was no phase change through the SCW exposures at different pressures.

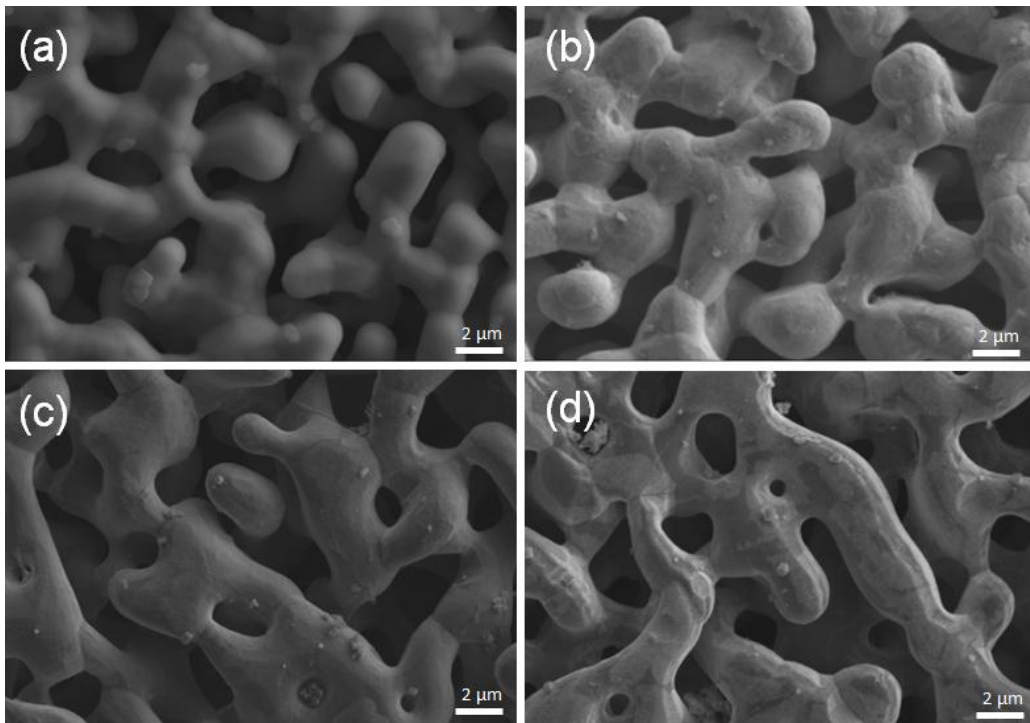


Figure 5- 5. Surface morphologies of porous chromium carbide after SCW tests at 415 °C under different pressures: (a) 12~15 MPa; (b) 25~28 MPa; (c) 33~35 MPa; (d) 47~50 MPa.

Table 5- 2. Weight changes of ceramic coupons exposed to SCW for 25 hours at different pressures

| SCW condition | dG/G |
|--------------------|---------|
| 400 °C, 12~15 MPa* | +0.0028 |
| 400 °C, 25~28 MPa | +0.0035 |
| 400 °C, 33~35 MPa | +0.0045 |
| 400 °C, 47~50 MPa | +0.0071 |
| 415 °C, 12~15 MPa* | +0.0030 |
| 415 °C, 25~28 MPa | +0.0037 |
| 415 °C, 33~35 MPa | +0.0080 |
| 415 °C, 47~50 MPa | +0.0082 |

*Water was not in supercritical region under this condition

5.4 Discussion

The carbides of transition metals (Group VI) are widely used as engineering materials. Their behavior in corrosive environments, especially in oxidizing atmospheres, has also been a subject of interest. The investigation on the corrosion behavior of chromium carbide conducted by Kosolapova et al. revealed that the initial oxidation temperature of Cr_3C_2 powder is 700 °C [12]. A massive specimen of Cr_3C_2 was stable at 800 °C to 1000 °C. It was also found that the oxidation of powdery Cr_3C_2 at 800 °C to 1000 °C obeys a parabolic rate law. Voitovich et al. investigated the oxidation behavior of the carbides Cr_3C_2 , Mo_2C , and WC over a wide temperature range (500-1200 °C) in air [14]. The oxidation

experiments were carried out using 8 mm diameter cylindrical specimens produced by hot pressing. Their results showed that chromium carbide (Cr_3C_2) has the highest oxidation resistance among the carbides investigated. A layer of nonporous and strongly adherent oxide film formed on chromium carbide at all temperatures, which effectively protect the substrate against further oxidation.

5.4.1 Exposure of porous chromium carbide in air

To compare its corrosion behavior in different corrosion environments, porous chromium carbide was exposed to air at 425 °C and 800 °C for 25 hours. Figure 5-6 shows the surface morphologies of the porous chromium carbide samples after exposure in air at these temperatures. No obvious change could be observed for the carbide sample exposed in air at 425 °C, which is different from the behavior of the carbide exposed to SCW at the same temperature. When the temperature increased to 800 °C, the surface of the chromium carbide became coarsened and small crystals identified by XRD as Cr_2O_3 formed on the surface. These results agree well with the oxidation tests reported before. The weight measurement and XRD test for the sample oxidized at 800 °C showed that the porous carbide could be oxidized completely in air within 25 hours due to the large surface area of the porous structure. No disintegration or cracking occurred for either of the samples tested in air, and no spallation was observed for the samples. It seems that the phase transformation from Cr_3C_2 to Cr_2O_3 through the oxidation process in air did not induce the occurrence of cracks or disintegration for the porous carbide ceramic. Therefore, the corrosion behavior of chromium carbide in SCW is quite

different from that in air, although the same corrosion product, that is, the transformation of Cr_3C_2 to Cr_2O_3 , has been found.

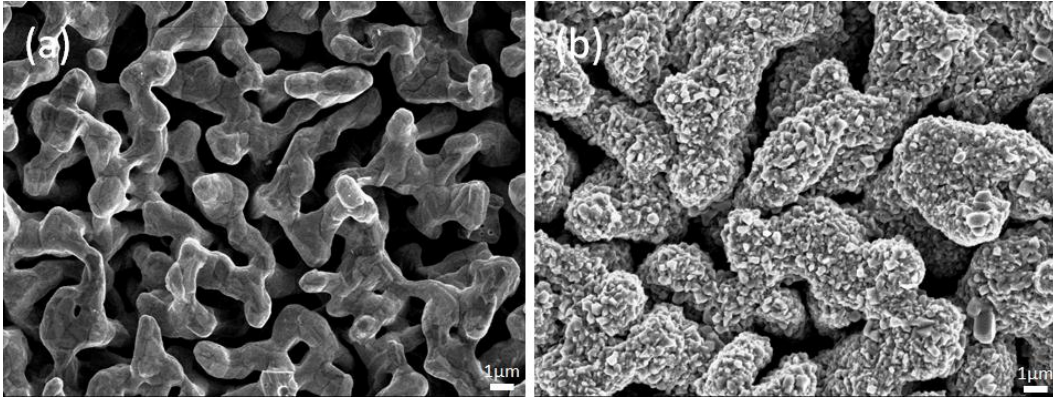


Figure 5- 6. Surface morphologies of the porous chromium carbide after exposure in air at different temperatures (a) 425 °C, (b) 800 °C.

5.4.2 Corrosion of chromium carbide in SCW

To understand the corrosion behavior of chromium carbide in SCW, a dense Cr_3C_2 sample was prepared by hot isothermal pressing. Figure 5-7 shows the surface of the sample before and after SCW exposure at 500 °C for 25 hours. It can be seen that some intergranular corrosion cracks were present on the surface of the dense sample after SCW exposure. This might be attributed to the high energy state of the atoms and the high diffusivity at grain boundaries. In addition to some intergranular corrosion, transgranular cracks also appeared on the surface, as shown in Figure 5-7(c). Figure 5-7(d) shows the cross-section of the dense Cr_3C_2 sample after the SCW test. The penetration depth of SCW corrosion is about one or two grain around 7~8 μm . EDS analysis reveals that chromium oxide corresponding to Cr_2O_3 was present in the oxide layer. Therefore, It seems that

chromium carbides exposed to SCW at high temperatures suffer both intergranular and transgranular corrosion. The disintegrated particles in Figure 5-3(c) and (f) may have been formed by intergranular corrosion while transgranular corrosion induced the observed parallel cracks within each particle. Although oxygen was present in the test capsule, the oxidation of chromium carbide directly by oxygen was not favorable at 425 °C due to the thermodynamic barrier. Therefore, the occurrence of cracks and the disintegration of the porous chromium carbide samples in SCW cannot be attributed solely to oxidation by the oxygen present in the test chamber, as discussed above. Water is likely also involved in the corrosion process, reacting with chromium carbide at elevated temperatures.

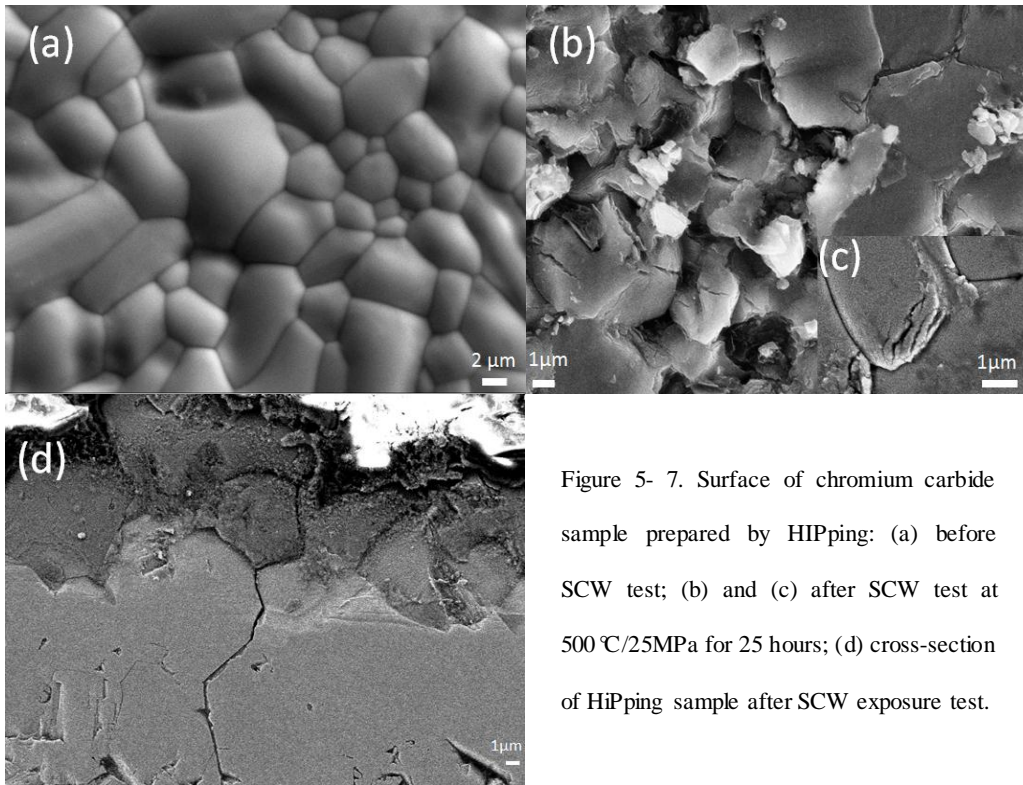
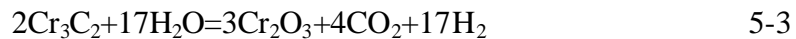
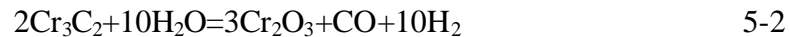
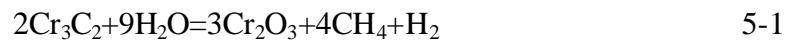


Figure 5- 7. Surface of chromium carbide sample prepared by HIPping: (a) before SCW test; (b) and (c) after SCW test at 500 °C/25MPa for 25 hours; (d) cross-section of HiPping sample after SCW exposure test.

S. Jacobson et al. studied carbon formation from carbides (SiC, TiC, TaC, NbC, WC and B₄C) under hydrothermal conditions [15]. Both thermodynamic calculations and experiments were employed in their investigation. They suggested that the corresponding metal oxides, CH₄, CO₂, CO, H₂ and carbon are the main products of hydrothermal corrosion of the carbides in the temperature range 300-1000 °C. The final corrosion products depend on the ratio between H₂O and carbides. The following reactions are postulated to occur between chromium carbide and water under hydrothermal conditions.



To predict the expected corrosion products of chromium carbide under SCW conditions, FACTSAGE software program was employed to determine the possible reactions that could occur under the SCW exposure conditions studied. Figure 5-8 shows the predicted equilibrium composition of the Cr₃C₂-steam at various temperatures; it includes H₂O, H₂, Cr₂O₃, CO₂, CO and CH₄ for a Cr₃C₂:H₂O molar ratio is 1:10. It can be seen that Cr₂O₃ is thermodynamically stable at temperatures ranging from 375 °C to 625 °C. As the temperature increases, methane becomes less stable and more hydrogen is present.

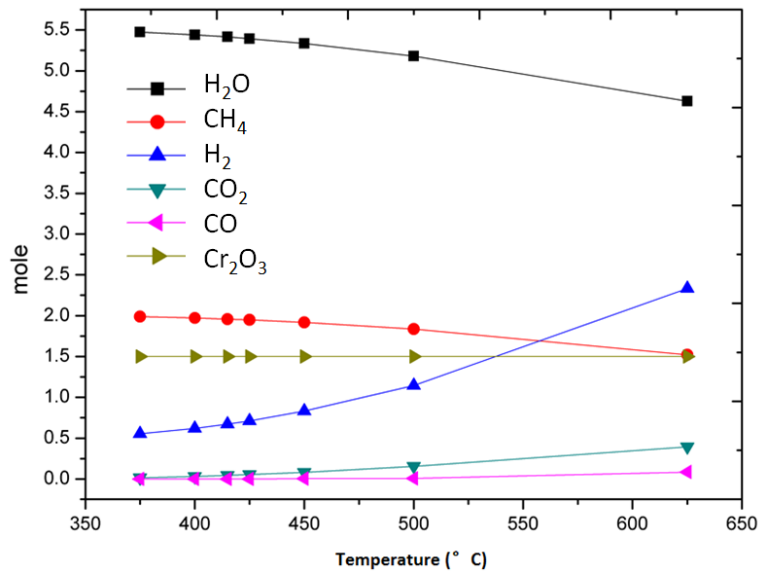


Figure 5- 8. Predicted corrosion products in equilibrium between Cr₃C₂ and H₂O.

Two questions are raised by the results of the FACTSAGE calculations: 1). Why is corrosion of the porous chromium carbide not observed in SCW at temperatures below 425 °C, as predicted by thermodynamic modeling? 2). How are the cracks (shown in Figure 5-3) formed during the corrosion exposure. For the first question, one can assume that the reaction kinetics of the corrosion process may be very slow at temperatures below 425 °C.

For the second question raised above, it is hypothesized that H₂O participated in the corrosion reaction; hydroxide or oxyhydroxide could therefore be formed in this hydrothermal process. To identify hydroxide or oxyhydroxide species, FTIR measurements were conducted for the four samples with conditions as shown in Figure 5-9. In the region 1000-2200 cm⁻¹, a band at 1627 cm⁻¹ (Figure 5-9 (b))

was assigned to the bending modes of non-dissociated water molecules or O-H stretching vibrations in OHO groups [16]. A broad band at 3405 cm^{-1} (Figure 5-9(a)) corresponds to the OH stretching vibrations of non-dissociated water molecules and the stretching of surface hydroxyls in hydrated chromium oxides [17]. A broad band in the region $1700\text{-}2100\text{ cm}^{-1}$ as shown in curves (c) and (d) is a characteristic of O-H stretching vibrations in OHO groups in crystalline CrOOH [18]. The bands present in the $500\text{-}1000\text{ cm}^{-1}$ (curve d) range were identified as characteristic of crystalline $\alpha\text{-Cr}_2\text{O}_3$ [17].

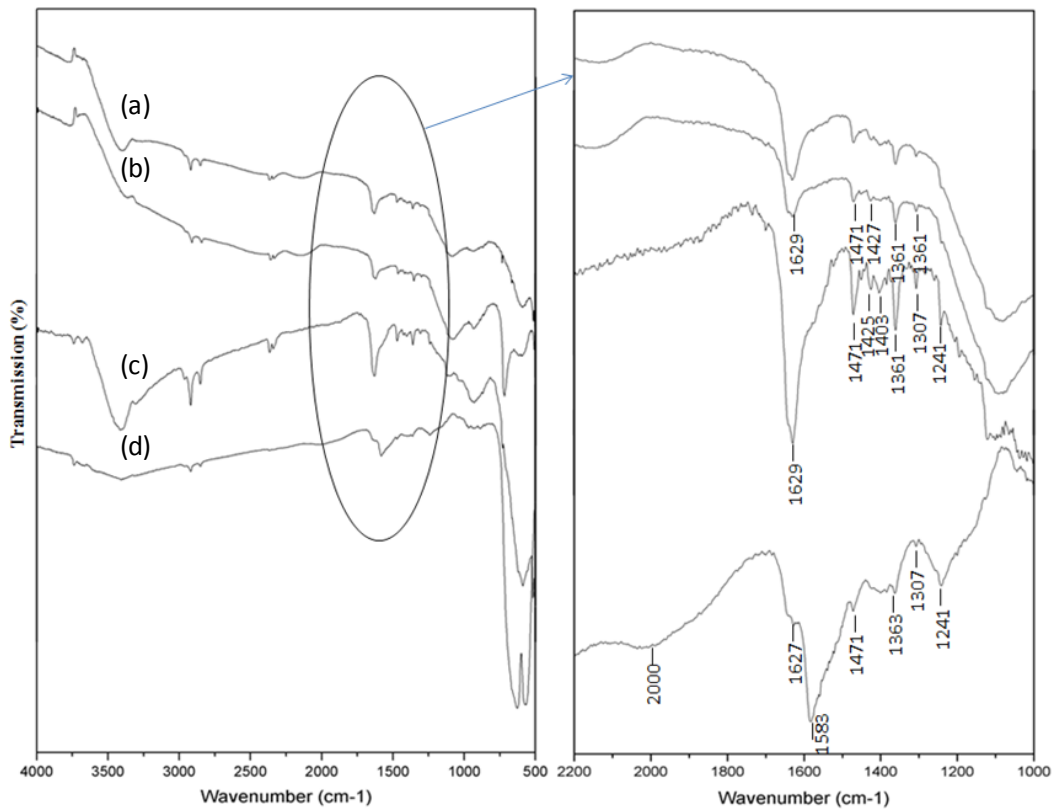


Figure 5- 9. FTIR spectra (transmission) of (a) porous Cr_3C_2 ; (b) porous Cr_3C_2 exposed in air at $425\text{ }^\circ\text{C}$; (c) porous Cr_3C_2 exposed in SCW at $400\text{ }^\circ\text{C}$; (d) porous Cr_3C_2 exposed in SCW at $450\text{ }^\circ\text{C}$.

The FTIR results can be interpreted as follow: there were no evident phase changes for the chromium carbide sample before and after exposure in air at 425 °C as shown in curve (a) and (b) in Fig. 5-9, since the temperature is below the initial oxidation temperature of Cr₃C₂. The sample exposed to SCW at 400 °C may contain coordinately bonded water molecules, which was eliminated when temperature was increased. Cr₂O₃ formed when the SCW temperature was above 425 °C. These findings are in agreement with the data from weight change, SEM, and XRD observations. One important finding is that an O-H bond corresponding to CrOOH was present after SCW exposure as a broad band in the region 1700-2100 cm⁻¹ was detected.

5.4.3 Formation of cracks in SCW environments

α-CrOOH possesses a layered crystal structure with trigonal symmetry as shown in Figure 5-10 [19]. Layers of Cr atoms perpendicular to the trigonal axis are sandwiched between two parallel sheets of oxygen atoms, which are joined by short hydrogen bonds aligned along the trigonal axis. It has been reported that α-CrOOH could be observed when a metallic chromium coupon exposed to hydrothermal conditions at temperatures above 374 °C with a pressure at 25MPa [20]. Laubengayer et al. studied the chromium(III) oxide-water system in the temperature range 145-560 °C . They found that CrOOH was formed in the hydrothermal conditions at temperatures below 419-424 °C and that it decomposed endothermically at 420-430 °C to give rhombohedral Cr₂O₃ [21]. This decomposition temperature coincides with the temperature at which cracks began to appear in the surface of porous chromium carbide (Fig 3). Since the O-H

IR band corresponding to CrOOH was observed for samples tested in SCW at 400 °C and 450 °C, it is reasonable to assume that CrOOH may be an intermediate product in the corrosion of chromium carbide exposed to SCW. When chromium carbide was exposed to SCW environments, CrOOH forms due to the reaction between Cr₃C₂ and H₂O. As CrOOH is stable at temperatures below 420-430 °C, it forms a protective layer at the surface and the corrosion process cannot proceed continuously. Therefore, no cracks or disintegration are observed when the samples tested in SCW below 420-430 °C. When the temperature is above 420-430 °C, CrOOH decomposes to Cr₂O₃ and H₂O; under these circumstances, corrosion could proceed continuously. The occurrence of parallel cracks shown in Figure 5-3 is related to the break of the layered crystal structure of α-CrOOH as shown in Figure 5-10. When CrOOH decomposes, two layers of hydrogen atoms and one layer of oxygen could combine to form H₂O. The oxygen atoms on the upper layer relocate from their original positions and re-bond with chromium atoms on the lower layer. Therefore, a contraction in the c direction during the decomposition of CrOOH may lead to the formation of the parallel cracks.

5.5 Concluding Remarks

The corrosion behaviour of high porous chromium carbide (Cr₃C₂) in different SCW environments was investigated in this study. The results show that chromium carbide is stable in SCW at temperatures below 425 °C. Cracks and disintegration occurred when carbide samples were exposed to SCW at temperatures above 425 °C. The lowest critical temperature at which chromium

carbide becomes unstable in SCW should be within 420-430 °C. Both intergranular and transgranular corrosion were observed for chromium carbide tested in SCW at elevated temperatures. The disintegration of carbide is believed to be related to the formation of the intermediate product of CrOOH and its subsequent decomposition.

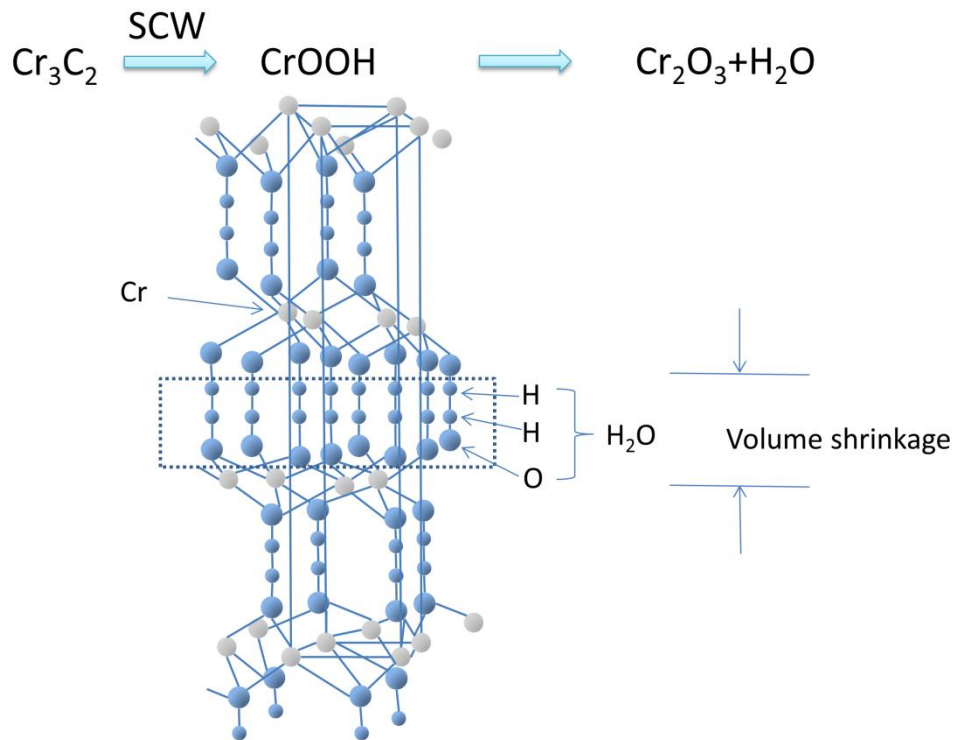


Figure 5- 10. Proposed mechanism for cracks induced by decomposition of CrOOH; the crystal structure of CrOOH was adapted from reference [18].

5.6 Bibliography

- [1] GIF-002-00, 2002 December.
- [2] R.B. Duffey, B.A. Gabaraev and Yu. N. Kuznetsov, The 14th International Conf. on Nuclear Engineering (ICONE-14), 2006, pp. Paper 89609.
- [3] C.K. Chow, H.F. Khartabil, Nuclear Engineering and Technology, 40 (2007) 139.
- [4] E.U. Franck, Berichte Der Bunsen-Gesellschaft-Physical Chemistry Chemical Physics, 88 (1984) 820-825.
- [5] E.U. Franck, Journal of Chemical Thermodynamics, 19 (1987) 225.
- [6] E.U. Franck, Supercritical water and other fluids - A historical perspective, in: E. Kiran, P.G. Debenedetti, C.J. Peters (Eds.) Supercritical Fluids - Fundamentals and Applications, Springer, Dordrecht, 2000, pp. 307-322.
- [7] N. Boukis, N. Claussen, K. Ebert, R. Janssen, M. Schacht, Journal of the European Ceramic Society, 17 (1997) 71-76.
- [8] M. Schacht, N. Boukis, E. Dinjus, Journal of Materials Science, 35 (2000) 6251-6258.
- [9] K. Juhani, J. Pirso, M. Viljus, S. Letunovits, Mater. Sci.-Medzg., 14 (2008) 341-344.
- [10] D.-Y. Wang, K.-W. Weng, C.-L. Chang, W.-Y. Ho, Surface and Coatings Technology, 120-121 (1999) 622-628.
- [11] E. Yun, S. Lee, Materials Science and Engineering: A, 405 (2005) 163-172.
- [12] T.Y. Kosolapova, G.V. Samsonov, Journal Name: Zhur. Fiz. Khim.; Journal Volume: Vol: 35; Other Information: Orig. Receipt Date: 31-DEC-61, (1961) Medium: X; Size: Pages: 363-366.

- [13] T. Xing, X. Cui, W. Chen, R. Yang, *Materials Chemistry and Physics*, 128 (2011) 181-186.
- [14] R.F. Voitovich, É.A. Pugach, *Powder Metallurgy and Metal Ceramics*, 12 (1973) 314-318.
- [15] N.S. Jacobson, Y.G. Gogotsi, M. Yoshimura, *Journal of Materials Chemistry*, 5 (1995) 595-601.
- [16] P. Ratnasamy, A.J. Leonard, *The Journal of Physical Chemistry*, 76 (1972) 1838-1843.
- [17] A. Zecchina, S. Coluccia, E. Guglielminotti, G. Ghiotti, *The Journal of Physical Chemistry*, 75 (1971) 2774-2783.
- [18] R. Douglass, *Acta Crystallographica*, 10 (1957) 423-427.
- [19] T. Fujihara, M. Ichikawa, T. Gustafsson, I. Olovsson, T. Tsuchida, *Ferroelectrics*, 259 (2001) 133 - 138.
- [20] J.E. Maslar, W.S. Hurst, W.J. Bowers, J.H. Hendricks, M.I. Aquino, I. Levin, *Applied Surface Science*, 180 (2001) 102-118.
- [21] A.W. Laubengayer, H.W. McCune, *Journal of the American Chemical Society*, 74 (1952) 2362-2364.

Chapter 6 Effect of Yttria Addition on the Stability of Porous Chromium Oxide Ceramics in Supercritical Water

6.1 Introduction

The Supercritical Water-cooled Reactor (SCWR) is a promising next generation reactor concept proposed by the Generation IV International Forum, being designed to meet the goals of improved safety, reduced waste production, low cost electricity and reduced proliferation risk [1]. SCWRs use water above its thermodynamic critical point (374 °C, 22.1 MPa) as the coolant with a direct once-through cycle. The use of supercritical water (SCW) as the coolant in a nuclear reactor can increase the thermal efficiency from about 30-35% for current generation water-cooled reactors to about 45-48% [2]. As the coolant remains one single phase from the core inlet to the high pressure turbine, the heat transport system is simplified by elimination of the steam generators, steam dryers, and steam separators [3, 4]. On the other hand, using SCW as a coolant also leads to some materials challenges, especially for the in-core components. Among the requirements for materials to be used in an SCWR core, corrosion resistance in a SCW environment is one of the most important issues.

The Canadian SCWR concept is being designed to be operated at temperatures between 350 °C at the core inlet and 625 °C at the core outlet with a constant pressure of 25 MPa [3]. The High Efficiency Channel (HEC) is a key design feature of the Canadian-SCWR concept, and is illustrated in Figure 6-1 [4]. In this concept, the SCW flows through a pressure tube that is in direct contact with the heavy water moderator operated at an average temperature of about 80 °C. The zirconium alloy pressure tube acts as the pressure boundary for the heat transport system and is thermally insulated from the hot coolant by an insulator. A metallic

liner is placed between the hot coolant and insulator to protect the insulator from being damaged by the fuel bundles and by erosion of the coolant flow. The insulator must provide an effective thermal barrier that can withstand thermal stresses and cycling and be dimensionally stable during irradiation. Unless the insulator is encapsulated, it must also have excellent corrosion resistance in SCW and this paper presents the results of an evaluation of the corrosion resistance of some porous ceramics of interest for the development of the Canadian SCWR concept.

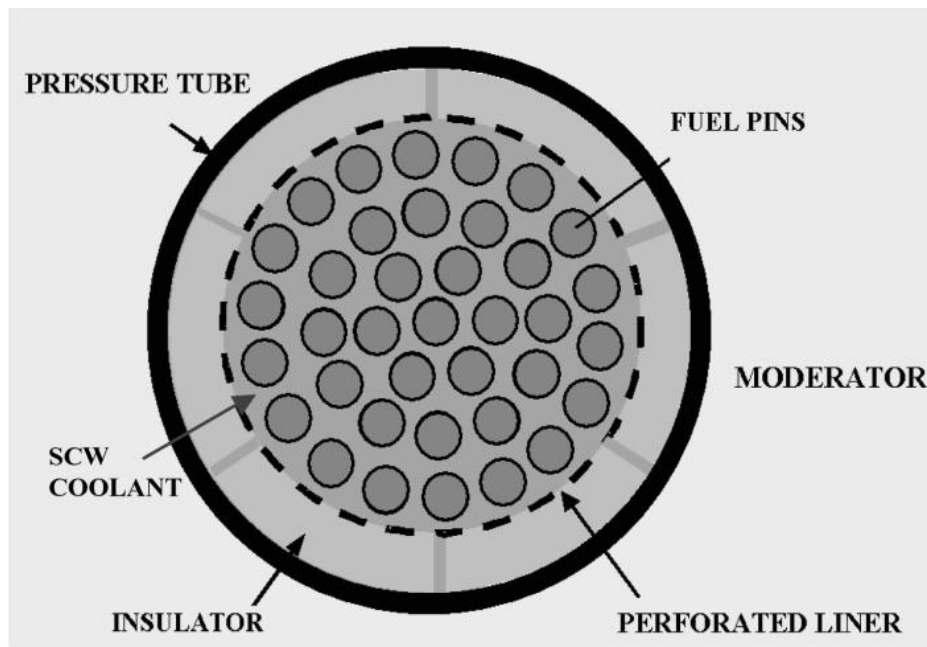


Figure 6- 1. An insulated pressure tube design of the CANDU-SCWR fuel channel [4]

Several ceramic materials have been proposed as candidate insulator materials for use in an SCWR. Porous yttria stabilized zirconia (YSZ) has been identified as a

good candidate insulator material owing to its low thermal conductivity, low neutron cross-section and high corrosion resistance in SCW [4]. Despite those advantages, there is a concern that the high oxygen ion conductivity of YSZ can potentially cause the corrosion of the Zr-alloy pressure tube, which will be in direct contact with the YSZ [5].

Chromium oxide (Cr_2O_3) is widely used in industry as a coating material that exhibits excellent corrosion and wear resistance, because of the excellent chemical inertness, high mechanical strength and hardness. It can also be used as a refractory and insulator material by virtue of its high melting temperature and low thermal conductivity [6]. It was reported that the thermal conductivity of as-pressed chromium oxide powder with an apparent density of 2.35 g/cm^3 is only $0.45 \text{ W/m} \cdot \text{K}$ at $20 \text{ }^\circ\text{C}$ [7]. The thermal conductivity of a chromium oxide block with an open porosity of 12-18% is around $3.1 \text{ W/m} \cdot \text{K}$ at $1200 \text{ }^\circ\text{C}$ which is comparable with a zirconium oxide block with an open porosity of 8% [6].

No relevant study has been published on the stability of bulk porous Cr_2O_3 in SCW environments, although extensive effort has been made to investigate the corrosion behaviour of Cr-containing alloys under various SCW conditions. The stability of those alloys depends on the formation of a stable oxide layer that consists of Cr_2O_3 and other oxides, such as iron or nickel oxides. Adschiri et al. used a revised Helgeson-Kirkham-Flowers (HKF) model to estimate the solubility

of different metal oxides under SCW conditions [8]. Their results show that the solubility of chromium oxide in SCW is lower than that of iron and nickel oxides.

This chapter presents the results of an investigation of the stability of porous chromium oxide-based ceramics in various SCW environments to explore their potential application as an insulator in the Canadian SCWR concept. The porous chromium oxide based ceramics were prepared by oxidizing highly porous chromium carbides obtained by reactive sintering in a carbonaceous atmosphere [9, 10]. The reactive element yttrium was introduced to the porous chromium oxide ceramics by adding different amounts of yttria to the starting powders prior to the reactive sintering process. The effect of adding yttria on the stability of porous chromium oxide in SCW was also investigated in this study.

6.2 Experimental

The starting material used to prepare the porous ceramics was chromium (III) oxide powder (Alfa Aesar, USA, average particle size P_s of $\sim 2 \mu\text{m}$, purity of 99%). The oxide powder was uniaxially compressed in a cylindrical mold under a pressure of 80 MPa to form disc shaped samples with a diameter of 16 mm and thickness of 2 mm. The disc shaped samples were put into a tube furnace (GSL1600X, MTI Corporation) and sintered in a carbonaceous gas mixture (2% CH_4 +98% H_2 , Praxair Canada) at temperatures ranging from 1100 °C to 1300 °C for 15 hours, to produce porous chromium carbide ceramics. The flow rate of the gas mixture was controlled at 140 ml/min. Details of sintering in carbonaceous

environments were reported in Ref [9]. Porous chromium oxide ceramics were prepared by oxidizing the porous chromium carbide at 850 °C for 50 hours in air. Yttria was added to the starting chromium oxide powder with different mass ratios of 5 %, 10 % and 20 %. The powder mixtures were mixed through ball milling for 10 hours.

To investigate the stability of the porous oxide ceramics in SCW environments, a static reactor was built to conduct SCW tests as shown in Figure 6-2. The static reactor was made of Inconel 625 tubing, with an outside diameter of 9.525 mm and a wall thickness of 1.651 mm. Only one coupon was placed in the tube for each test. Air-saturated neutral deionized water with an oxygen concentration of about 8 ppm was utilized. Some tests used hydrogen peroxide solution (30 wt. % H₂O₂) instead of de-ionized water to increase the oxygen concentration in the reactor. Air was not purged out and was present in the sealed reactors. It is important to note that, in a sealed capsule reactor such as that used in these tests, the concentrations of reactive species such as oxygen in the system will decrease with time as they are consumed by reaction with the test samples and the reactor walls. The ceramic coupons tested were cut from the porous chromium oxide disc samples with a size of 10 mm × 4 mm × 2 mm and then cleaned using ethanol in an ultrasonic cleaner. Each of the SCW exposure conditions was evaluated three times using coupons with the same composition and processing conditions. Mass changes were measured on a five-decimal balance.

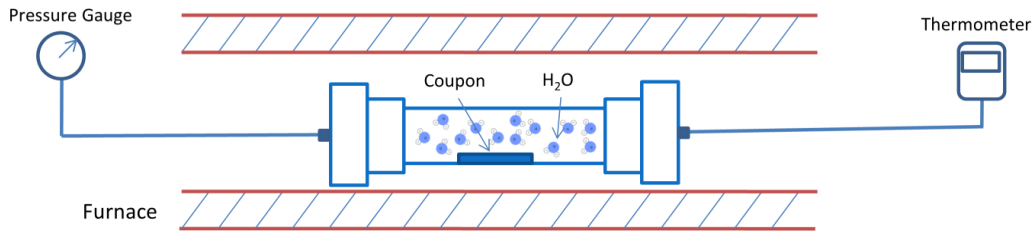


Figure 6- 2. Supercritical Water Test Facility.

The morphologies of the ceramic samples were examined by JEOL (JSM-6301FXV) field emission scanning electron microscope (FESEM) and ZEISS (EVO –MA15) SEM. X-ray diffraction (XRD) analysis was performed by using a Rigaku Geigerflex 2173 X-ray diffraction equipment. The porous properties of the as-carburized samples were characterized using a mercury intrusion porosimeter (AutoPore IV 9510). The concentrations of elements in the water liquid after SCW exposures were measured using a Perkin Elmer Elan 6000 inductively-coupled plasma mass spectrometer (ICP-MS). X-ray Photoelectron Spectroscopy (XPS) analysis was conducted using a Kratos Axis 165 X-ray Photoelectron Spectrometer. Liquid samples were frozen using a cooling holder when XPS test was conducted.

6.3 Results and Discussion

6.3.1 Porous chromium oxide based ceramics

6.3.1.1 Porous chromium oxide ceramic

Figure 6-3(a) shows the surface morphology of an as-pressed chromium oxide sample before reactive sintering. After sintering in a carbonaceous atmosphere, a

three dimensional porous structure was formed, as shown in Figure 6-3(b). The porous chromium oxide ceramic was obtained by oxidizing the highly porous chromium carbide at 850°C in air. Figure 6-3(c) shows the surface morphology of the porous chromium oxide formed. Compared to the porous carbide, the struts of re-oxidized sample are seen to be thickened slightly. XRD measurements revealed that the Cr_2O_3 was carburized to Cr_3C_2 through carburization in the high temperature carbonaceous environments and then re-oxidized to Cr_2O_3 by exposure to air at 850°C for 50 hours. Figure 6-4 shows porous Cr_2O_3 with different porous morphologies inherited from the chromium carbide carburized at different temperatures. Table 6-1 lists the porosity measured for the chromium carbide by varying sintering temperature from 1000 °C to 1300 °C. It can be seen that highly porous carbide with pore volume fraction of about 77% can be obtained when the sintering temperature was 1000 °C or 1100 °C. With increasing temperature, the porosity decreased, and was about 51% at 1300 °C. The porosity of the Cr_2O_3 ceramic was determined based on the measurement of weight and volume of the oxidized samples. The porous Cr_2O_3 was less porous than the chromium carbide, since the density of Cr_3C_2 (6.68 g/cm^3) is larger than that of Cr_2O_3 (5.22 g/cm^3) and the solid volume expansion on the transformation from carbide to oxide reduces the porosity.

Table 6- 1. Porosity of chromium carbide and chromium oxide

| Carburization Temp. | 1000 °C | 1100 °C | 1200 °C | 1300 °C |
|--|---------|---------|---------|---------|
| Porosity of Cr ₃ C ₂ | 76.01% | 77.76% | 66.68% | 51.96% |
| Porosity of Cr ₂ O ₃ | 62.78% | 64.20% | 46.23% | 26.19% |

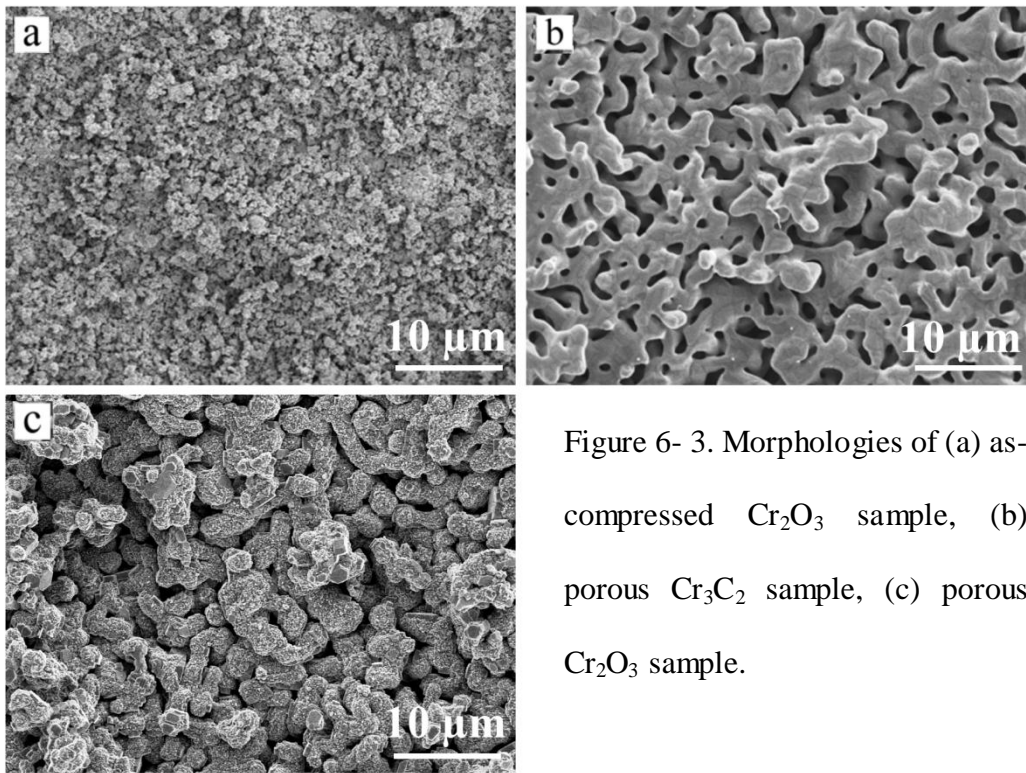


Figure 6- 3. Morphologies of (a) as-compressed Cr₂O₃ sample, (b) porous Cr₃C₂ sample, (c) porous Cr₂O₃ sample.

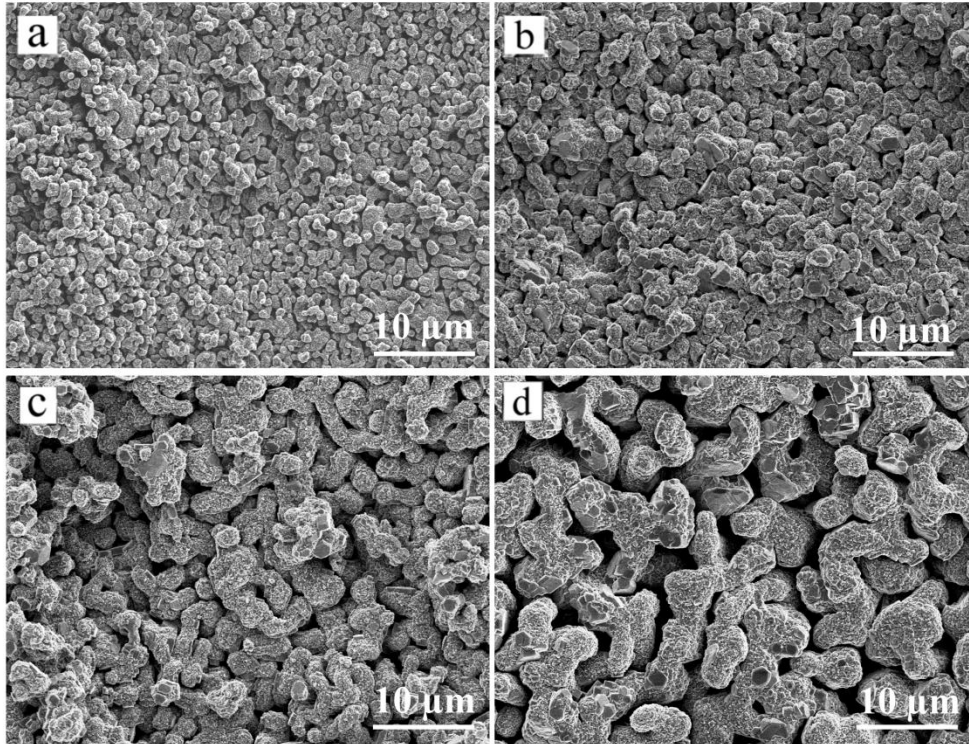


Figure 6- 4. Morphologies of porous chromium oxide obtained by oxidizing different porous chromium carbide ceramics at 850 °C for 50 hours in air; the carbide ceramics were obtained by carburizing chromium oxide at: (a) 1000 °C; (b) 1100 °C; (c) 1200 °C; (d) 1300 °C for 15 hours.

6.3.1.2 Porous Cr₂O₃ with yttria addition

Porous Cr₂O₃ ceramics with the addition of yttria were prepared by the same process described above. Figure 6-5 shows the surface morphologies of porous Cr₂O₃ ceramics with added yttria at 5, 10 and 20 wt. %, respectively. It can be seen that with the increase in yttria content, clusters consisting of small particles (in white) were increasingly observed. EDS analysis indicated that those clusters were enriched in yttrium, which could be the aggregations of yttria formed during the sintering.

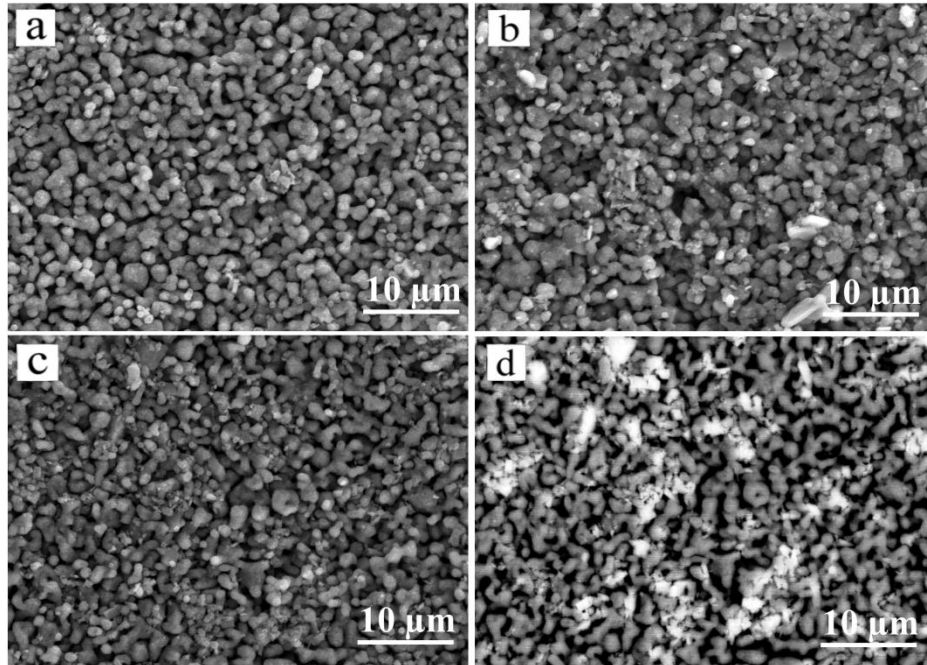


Figure 6- 5. Morphologies of the porous Cr_2O_3 added with (a) 5 wt. % Y_2O_3 , (b) 10 wt. % Y_2O_3 , (c) 20 wt. % Y_2O_3 , (d) Back scattered electron image of porous Cr_2O_3 with 20 wt. % Y_2O_3 .

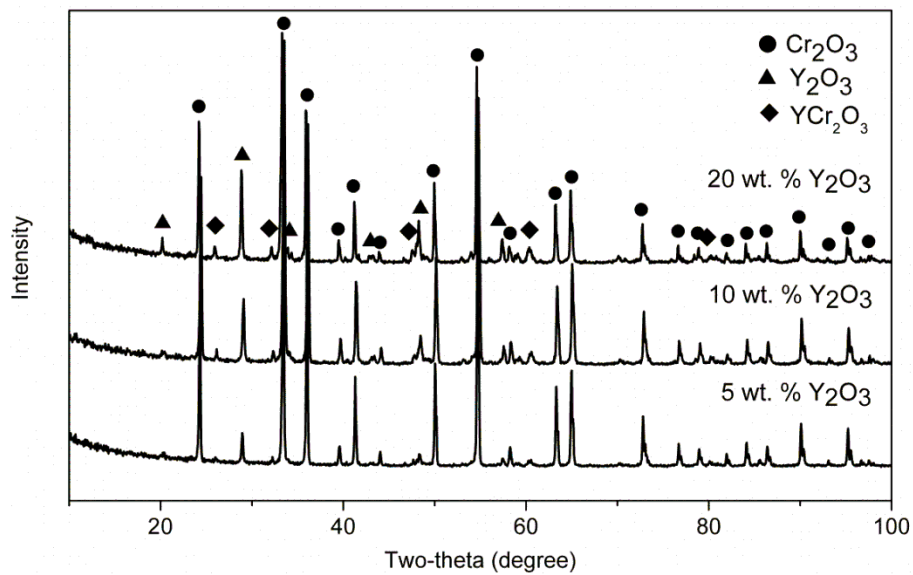


Figure 6- 6. X-ray diffraction patterns of chromium oxides added with various amounts of yttria at 5 wt. %, 10 wt. % and 20 wt. %.

The XRD analysis (Figure 6-6) showed that Cr_2O_3 and Y_2O_3 were the main phases present. Besides these two phases, an intermediate compound, YCrO_3 , was also indexed in the XRD patterns. This perovskite phase should be produced from the solid reaction between Cr_2O_3 and yttria during the oxidation process. Chevalier et al. reported the synthesis of a perovskite phase from the oxide powder mixtures at 1000 °C [11] and their results show that the transformation to the perovskite phase from a Cr_2O_3 - Y_2O_3 mixture was slower than that of other reactive elements mixed with chromia and could not be transformed completely even after reaction for 288 hours. Peck calculated the Gibb's free energy of the formation of perovskite compounds based on thermodynamic data and found that YCrO_3 was more difficult to synthesise compared to other perovskite compounds [12]. Therefore, the added yttria could be partially reacted with Cr_2O_3 to form YCrO_3 during the re-oxidizing process and the porous ceramic samples after oxidation were composed of Cr_2O_3 , Y_2O_3 , and YCrO_3 .

6.3.2 SCW testing of the porous Cr_2O_3 -based ceramics

6.3.2.1 Stability of porous Cr_2O_3 in SCW

The porous Cr_2O_3 ceramic obtained from oxidizing porous chromium carbide (carburization temperature: 1100 °C) in air at 850 °C was tested in different SCW environments with the temperatures ranging from 375 °C to 625 °C at a constant pressure of 25-30 MPa. The weight changes of the porous oxide coupons after SCW exposure up to 100 hours are shown in Figure 6-7. No measurable weight change was detected for the coupon tested at 375 °C in SCW. As the SCW temperature increased to 450 °C, a gradual weight loss was measured. However,

only a small amount of weight loss, around 0.6 %, was measured after exposure at 450 °C for 100 hours. As the SCW temperature increased to 550 °C, the coupons suffered a little more weight loss than that exposed to SCW at 450 °C. Nevertheless, there was no obvious disintegration observed for the coupons tested at temperatures below 550 °C and the weight loss increased with the exposure time.

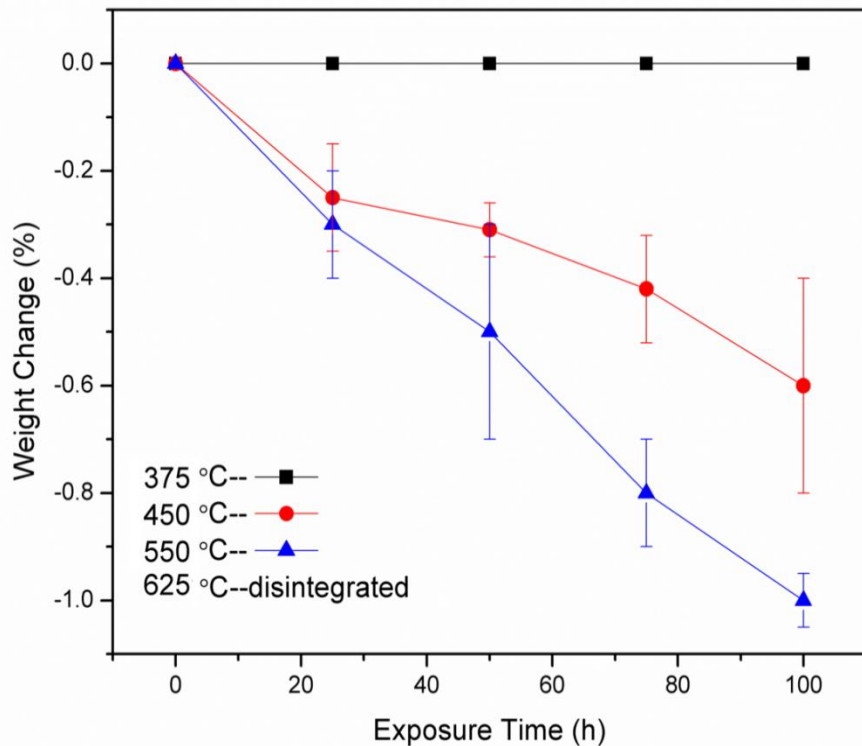


Figure 6- 7. Weight changes of porous Cr_2O_3 after exposure at different temperatures for 100 hours under a pressure of 25-30 MPa in supercritical water.

When the SCW temperature increased to 625 °C, evident disintegration was observed. Among the three repeats of porous coupons tested at 625 °C, two of

them suffered obvious partial disintegration and another one crumbled totally. Figure 6-8 shows the SEM images of the coupon which disintegrated during the SCW tests. It can be seen that part of the porous Cr_2O_3 disintegrated (Fig. 8 (a)) and some cracks and pits appeared on the surface (Fig. 8b) and c)). The high magnification image in Fig. 8 (d) shows that the cracks appeared along the grain boundaries, indicating that grain boundaries were more susceptible to corrosion in high temperature SCW; corrosion occurring at grain boundaries may lead to the cracking and disintegration of the sample.

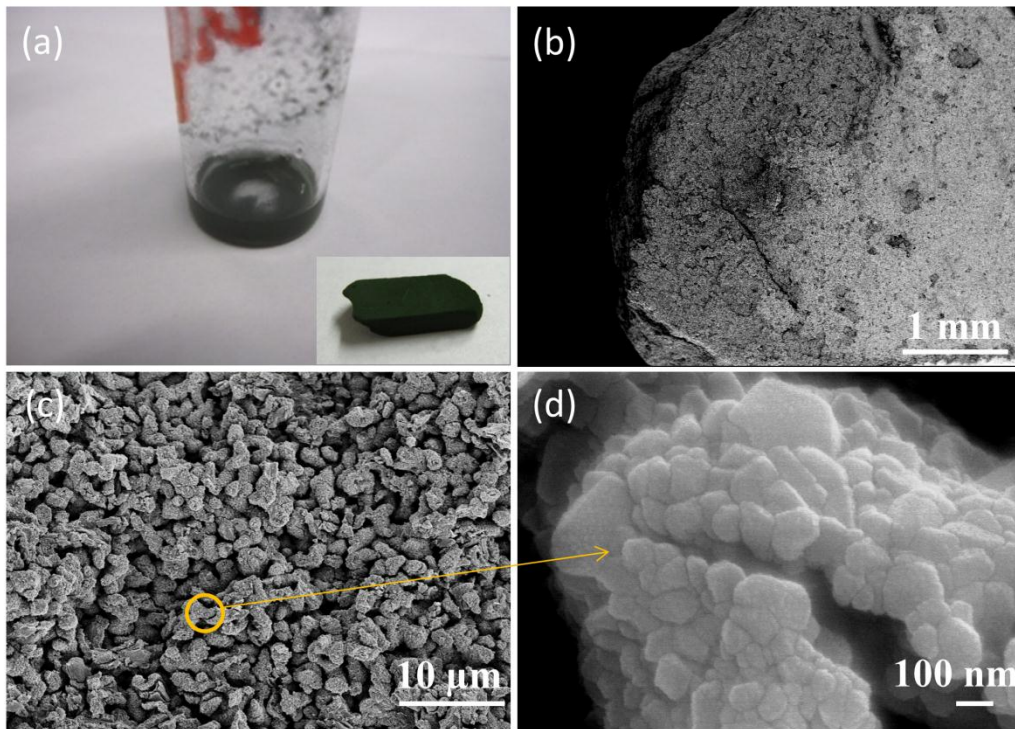


Figure 6- 8. Partial disintegration of porous chromium oxide after exposure at 625 °C for 100 hours in SCW: (a) Powders collected from the SCW capsule reactor and un-disintegrated sample remain (inset); SEM image of Cr_2O_3 sample after SCW test: (b) at low magnification; (c) Zoom in on the surface; (d) at high magnification.

Many studies have been performed on the corrosion behaviour of Cr-containing alloys under various SCW conditions. The stability of those alloys in SCW depends on the formation of a protective Cr_2O_3 layer, and therefore on the stability of Cr_2O_3 . The factors affecting the corrosion behaviour of those alloys in SCW environments include temperature, pressure, pH-value, density of SCW and oxygen concentration [13]. Watanabe et al. studied the effect of oxygen concentration on the corrosion behaviour of different alloys in SCW [10]. Their results show that the corrosion rate of Cr-containing alloy (1% Cr) increases with the increase of the oxygen concentration. In addition to the effect of oxygen concentration, they also found that an increased pressure leads to a higher corrosion rate for all the metals tested, because of the increase in solubility of metal oxides in SCW at higher pressures (SCW density). The potential-pH diagram was constructed for Cr at 25 °C/1 MPa and 625 °C/25 MPa as shown in Figure 6-9 using Factsage software (Version 6.1). While the utility of a potential-pH diagram at 625 °C is questionable [14], because the low dielectric constant at this temperature favours ion association. Since no acidic species were added to the initial de-ionized water and the water used in current study is near-neutral pH. Under these conditions the relative stability of the oxide phases predicted is identical to the stabilities predicted by Ellingham diagrams and can be considered qualitatively correct. From the diagram it can be seen that Cr_2O_3 becomes less stable at elevated temperatures and forms more soluble species such as H_2CrO_4 , HCrO_4^- , $\text{Cr}_2\text{O}_7^{2-}$ or CrO_4^{2-} in neutral pH and alkaline SCW; as the temperature increases the neutral species will be favoured over charged species. Since no inert

gas purging was conducted to exclude the air out of the tube in our tests, oxygen was present and totally miscible with SCW in the tests. The calculated oxygen concentration is around 3748 ppm assumed that the oxygen left in the tube dissolved in SCW completely. It is reasonable to consider that the oxidation reaction may be the reason of the disintegration of the porous Cr_2O_3 ceramic. The disintegration likely proceeds through the following reaction:



To determine the extent of dissolution of Cr_2O_3 in the SCW, the water after the test at 450 °C for 25 hours was examined by X-ray photoelectron spectroscopy (XPS). No obvious Cr signals were found in the XPS spectra, indicating that the concentration of Cr in the water after exposure was lower than the detection limit (2 ppm) of XPS. Therefore, the dissolution rate at 450 °C was low.

Increasing the oxygen concentration will increase the transformation to chromic acid if Cr_2O_3 is oxidized in SCW following Reaction (1). To prove the occurrence of Reaction (1), hydrogen peroxide water (30 % H_2O_2) was used instead of the de-ionized water, and the test temperature was also increased to 600 °C for 25 hours. This test temperature was lower than 625 °C to avoid the release of a large amount of Cr_2O_3 particles by disintegration of the porous ceramic, which would interfere with the analysis for dissolved Cr species in the liquid. The SCW test reactor was first preheated to 200 °C and maintained at that temperature for 2 hours to

dissociate the hydrogen peroxide to form oxygen. After the SCW test, the liquid became lightly yellowish colored. XPS analysis clearly showed Cr signals in the XPS spectrum (Figure 6-10). The binding energy of Cr $2p_{3/2}$ was around 578.6 eV which can be assigned to Cr^{6+} specie [15].

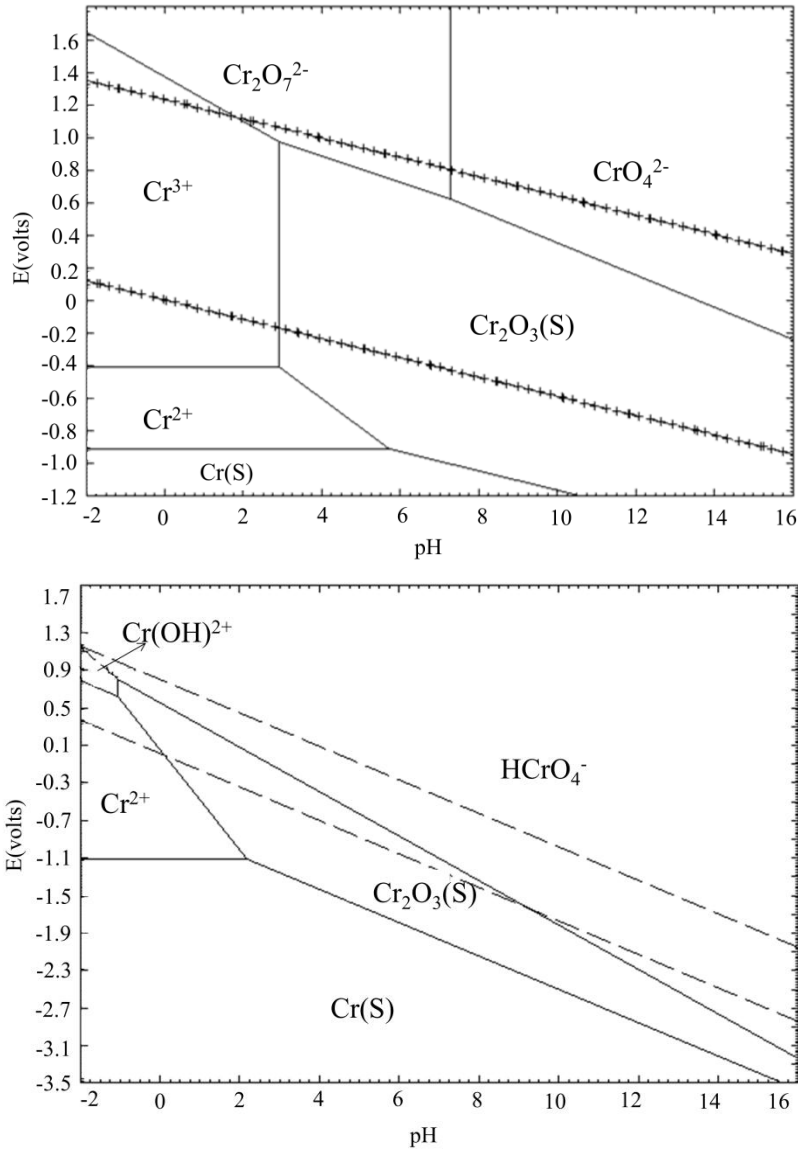


Figure 6- 9. Pourbaix diagram for Cr-H₂O system under different conditions: (a) 25 °C/1 MPa; (b) 625 °C/25 MPa.

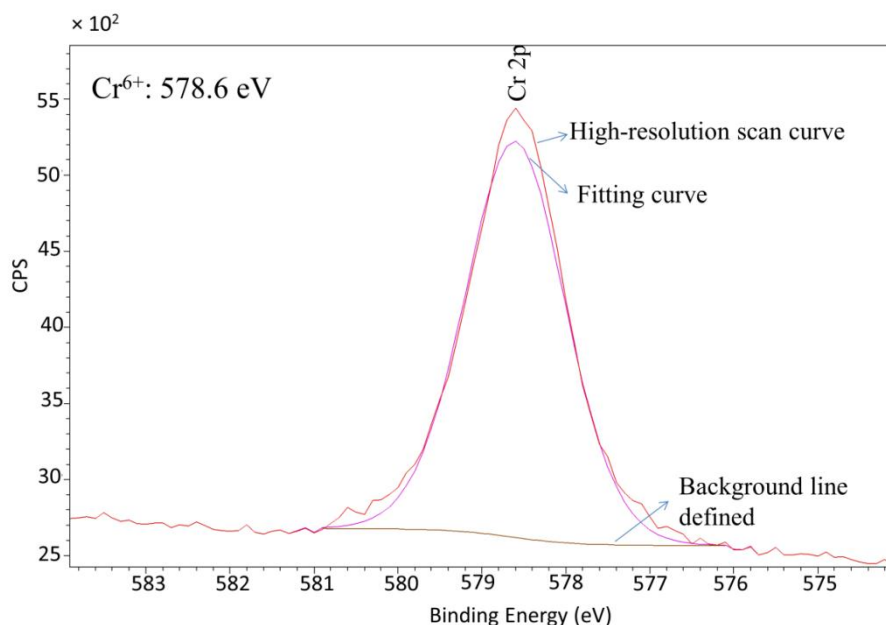


Figure 6- 10. Spectra of Cr2p_{3/2} from the high resolution XPS analysis of water after SCW test at 600 °C for 25 hours using hydrogen peroxide solution (30 wt. %).

Since the reactor tubing was made of Alloy 625 with 20-23 % Cr, it is possible that Cr⁶⁺ can also be released by oxidation of the reactor material during the test. To quantify the amount of release from the reactor, a blank run using a reactor with no tests sample loaded was filled with the same amount of hydrogen peroxide water (30% H₂O₂) and tested under the same conditions. The water in the reactor after the SCW exposure was transparent and was not discoloured. The water liquid was analyzed and no detectable Cr signals were found in XPS spectrum. Therefore, the Cr⁶⁺ detected when the Cr₂O₃ coupon was present in the reactor was mainly from oxidation of the Cr₂O₃ coupon. The results also show that, as expected from the Pourbaix diagram, the oxidation rate of Cr₂O₃ to

soluble chromate (VI) is a function of the oxygen concentration present in the SCW environment.

The oxidation of Cr_2O_3 to soluble chromate (VI) species in an oxidative SCW environment is likely responsible for the disintegration of the porous Cr_2O_3 ceramic observed at 625 °C in SCW. Because of the lattice distortion/strain existing at grain boundaries, the Cr in this area should be more reactive and more susceptible to corrosion, leading to preferential dissolution along the grain boundaries, that is, intergranular corrosion, as seen in Figure 6-8(d). In addition, grain boundaries are also short-circuit paths for the diffusion of SCW and O_2 due to the defect structure in those areas. Therefore, it is reasonable that the grain boundaries of Cr_2O_3 ceramic are more susceptible to corrosion attack in SCW, especially at high temperatures.

Other factors may also need to be considered with respect to the stability of porous Cr_2O_3 in SCW. Impurities such as SiO_2 , CaO and MgO can diffuse to the grain boundaries during sintering, making the grain boundaries more prone to attack under SCW conditions [16]. However no obvious segregation of the impurities mentioned above was detected for all the ceramic samples from either EDS or XRD analysis. The disintegration could also be caused by instability of any residual chromium carbide in the porous Cr_2O_3 ceramics due to incomplete oxidation. This possibility, however, is believed to be very low as carbide conversion to oxide would have been completed at 850 °C after 50 hours based on

previous research results, and disintegration of Cr carbide was found to occur at temperatures as low as 425 °C in SCW environments. Despite that, it is evident from this investigation that Cr₂O₃ can be oxidized to soluble chromate (VI) under oxidative SCW conditions. It should be noted that testing in 30% H₂O₂ represents a very extreme condition, and the expected concentrations of oxidants in an SCWR core will be much lower. However, it is still unclear how oxidizing the SCWR coolant will be in the core and downstream piping, as there are still major gaps in our understanding of water radiolysis about the critical point [17]. Recent radiolysis modeling of the concentrations of H₂O₂ and O₂ expected in the core of a pressure vessel-type SCWR [18] predicted very high; while this model was based on many input parameters extrapolated from lower temperatures, a procedure known to be incorrect, it nonetheless highlights the potentially highly oxidizing conditions that could exist in an SCWR core. Additional work on the stability of porous Cr₂O₃ in SCW at lower oxygen concentrations is in progress to assess the limits of stability.

6.3.2.2 Stabilities of porous Cr₂O₃ ceramics with yttria addition in SCW environments

Samples of porous Cr₂O₃ containing different amount of yttria were exposed to SCW at 625 °C under a constant pressure of around 25-30 MPa. The weight change curves of the coupons tested for up to 600 hours are shown in Figure 6-11. Among the yttria-containing materials tested, Cr₂O₃ with 5 wt. % yttria exhibited the best stability with the least weight changes over the entire period of SCW

exposure. The coupons with 10 wt. % and 20 wt. % yttria addition displayed more weight loss than the coupon with 5 wt. % yttria after exposure for 600 hours.

It is interesting that a slight increase in weight was observed for all the yttria-added coupons exposed to SCW after the first 100 hours, which was not observed for the porous Cr_2O_3 coupon without yttria addition. The observation of weight gains was confirmed by duplicate tests, and therefore was not the result of errors in weight measurements. One possible reason might be that small amounts of chromium carbide remained in the samples after re-oxidation of carbide in air prior to SCW exposure since adding yttria can improve the oxidation resistance of carbides. The residual chromium carbide could be oxidized during exposure in SCW, leading to a slight increase of sample weight during the initial stage of exposure. However, no carbide phase was identified by XRD analysis in any yttria-added samples.

As shown in Figure 6-11, the weight gains during the initial period seem to be correlated with the amount of added yttria; larger weight increases were observed for samples with higher concentrations of added yttria. Kuroda et al. have investigated the adsorption behavior of water on Y_2O_3 surfaces and found that Y_2O_3 , unlike other metal oxides, can react easily with water even at room temperature [19]. The water molecules were observed to interact strongly with the Y_2O_3 on the surface, and were incorporated into the Y_2O_3 progressively to form hydrate or hydroxide species. Therefore, the weight gains observed in this study

can be explained as follows: The dissociation of the ceramics samples in SCW was not very significant within the first 100 hours, whereas the rapid interaction of water with the Y_2O_3 phase generated an increase in weight from hydration or the formation of a hydroxide phase. Therefore, weight gains for all the yttria-bearing samples were detected in the first part of the exposure. With the increased exposure time, weight losses can be observed because of the increased corrosion. The observed correlation between weight gain and the yttria content can also be rationalized by the above hypothesis.

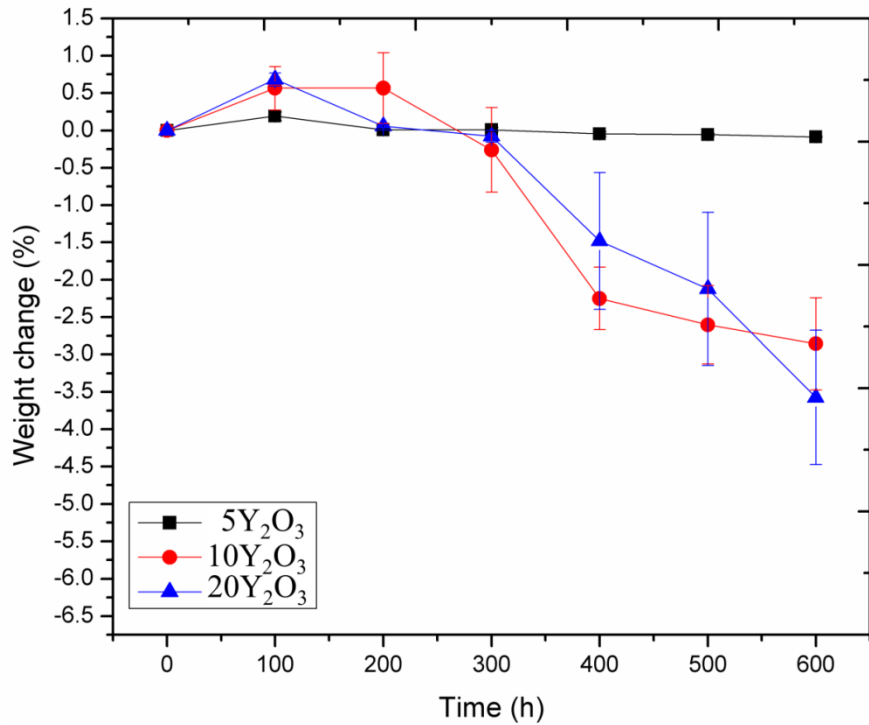


Figure 6- 11. Weight changes of chromium oxide based ceramics with yttria addition after being exposed to SCW at 625 °C under a constant pressure of around 25-30 MPa.

The surface morphologies of the coupons after the SCW tests were examined by Scanning Electron Microscopy, as shown in Figure 6-12. No obvious change of the morphology was observed for the coupon with 5 wt. % added yttria. The surface morphologies of 10 wt. % and 20 wt. % yttria-added coupons became rougher after SCW tests as shown in Figure 6-12(b) and (c). However, no disintegration was observed for any yttria-added coupons exposed to SCW at 625 °C.

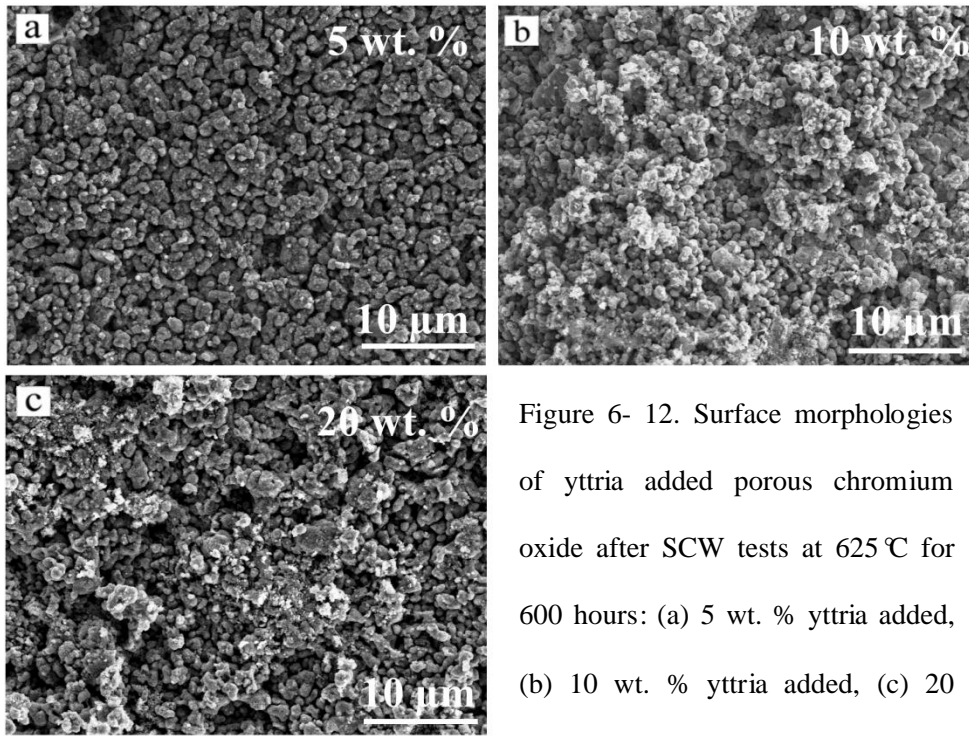


Figure 6- 12. Surface morphologies of yttria added porous chromium oxide after SCW tests at 625 °C for 600 hours: (a) 5 wt. % yttria added, (b) 10 wt. % yttria added, (c) 20 wt. % yttria added.

The water samples after SCW tests were analyzed by ICP-MS (Perkin Elmer Elan 6000). The concentrations of Cr and Y in the liquids are shown in Figure 6-13. It can be seen that the Cr concentrations in the water from tests with yttria-added samples were lower than those found with pure Cr₂O₃ sample, suggesting that the dissolution of Cr can be retarded in the presence of Y. However, it seems that the

Cr concentration increased with increasing yttria content, which seems hard to rationalize if yttria reduces Cr release. The concentration of Y in the water is consistent with the weight loss of the yttria-added coupons. It was reported that pure Y_2O_3 disintegrated after testing in SCW for 80 hours [20]. Lange et al. suggested that Y_2O_3 reacted with H_2O to form $Y(OH)_3$ in their experiments [21]. Therefore, it is reasonable to suggest that the weight loss observed for the coupons added with yttria at 10 wt. % and 20 wt. % was mainly attributed to the dissociation of Y_2O_3 in the SCW.

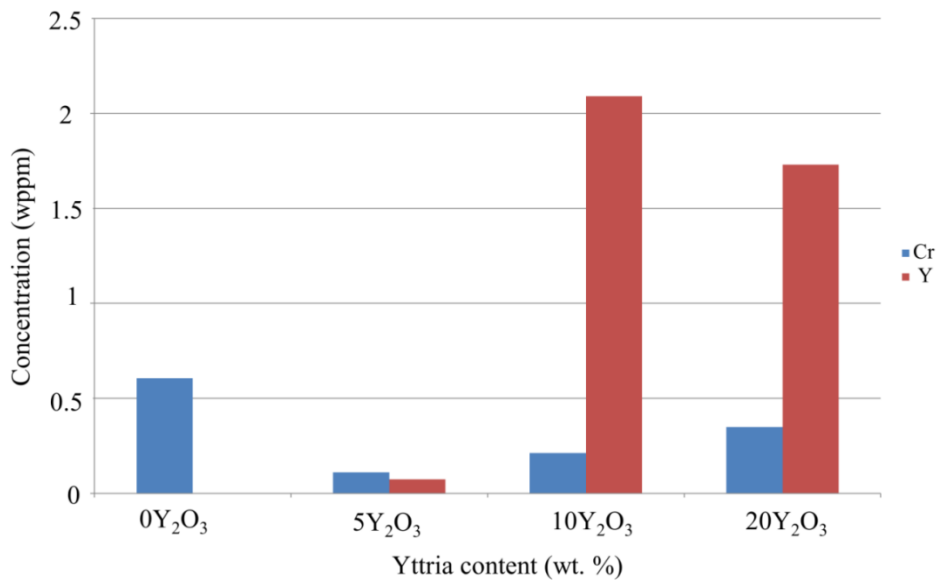


Figure 6- 13. Y and Cr concentration analyzed by mass spectra for the water liquid after SCW tests at 625 °C for 100 hours; (0Y₂O₃- Pressed pure Cr₂O₃ sample, 5Y₂O₃, 10Y₂O₃, 20Y₂O₃- Porous Cr₂O₃ ceramics added with yttria at 5 wt. %, 10 wt. %, 20 wt. %, respectively).

The above conclusion is supported by the results of the XRD analysis as shown in Figure 6-14, in which the Y_2O_3 peaks were more clearly observed before the SCW exposure. It is also obvious that peaks corresponding to the $YCrO_3$ phase became more evident after exposure in the SCW. These observations may be due to the synthesis of the $YCrO_3$ phase in the high temperature SCW environment or the formation of the perovskite phase since it was reported that $YCrO_3$ can be directly synthesized under hydrothermal conditions [22]. Nevertheless, the identification of the perovskite phase ($YCrO_3$) reveals that the high concentration of Y in the water sample after SCW exposure was not from the dissolution of $YCrO_3$, but the dissolution of Y_2O_3 phase, that is, $YCrO_3$ is more stable than Y_2O_3 in SCW. It should also be noted that all the XRD peaks have shifted to a high angle in the samples after SCW exposure. This shift was observed not only for the yttria-added samples but also for the pure Cr_2O_3 sample, suggesting a change in lattice parameter of the porous ceramics when exposed to the high temperature and high pressure SCW environment. Further studies are needed to understand the origins of the change of lattice parameter during SCW exposure. The surface roughening observed on 10 wt. % or 20 wt. % yttria-added Cr_2O_3 coupons after SCW exposure, as shown in Figure 6-12, may be caused by selective dissociation of yttria aggregation clusters (Figure 6-5), as indicated previously.

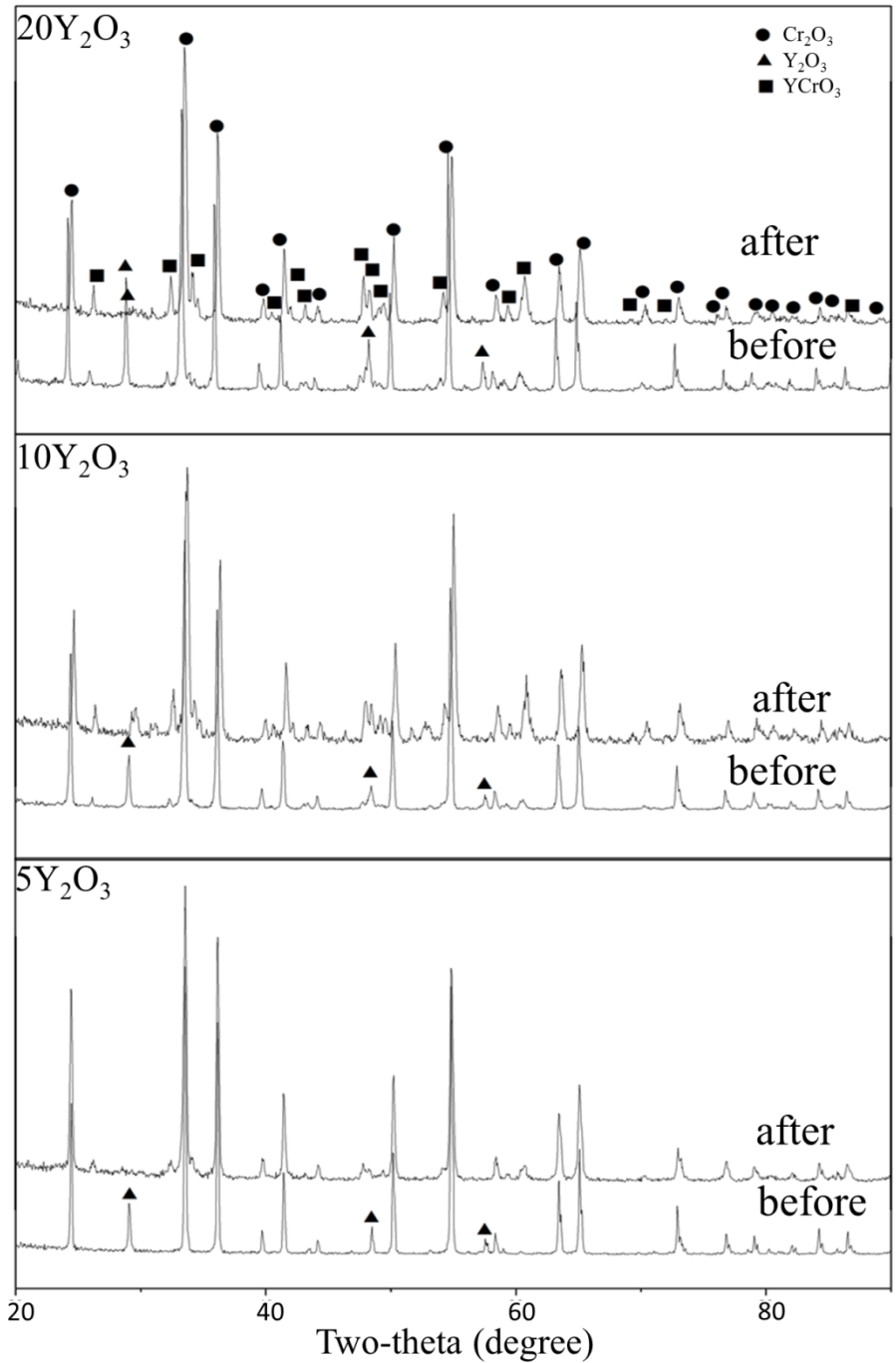


Figure 6- 14. XRD patterns recorded for samples added with various amounts of yttria before and after SCW tests at 625 °C for 600 hours.

Since the porous coupon with 5 wt. % added yttria showed the lowest weight loss, adding small amount of yttria is considered to be beneficial in terms of the stability of Cr_2O_3 in SCW environments. To further support this finding, two additional coupons were exposed to SCW at 600 °C at a pressure of 25-30 MPa. The first coupon was porous Cr_2O_3 without yttria addition. The other one was a porous Cr_2O_3 with 5 wt. % added yttria. Hydrogen peroxide solution (30% H_2O_2) was used in the two SCW tests. The SCW test reactor was first preheated to 200 °C and maintained at temperature for 2 hours to dissociate the hydrogen peroxide to oxygen to make the SCW environment more oxidizing. This is expected to lead to increased formation of soluble Cr^{6+} species through Reaction (1). A reference reactor without any Cr_2O_3 sample loaded was also exposed to the same SCW conditions. The samples of the test solution after SCW exposure were analyzed by ICP-MS. The results for the Cr concentration are shown in Figure 6-15. It can be seen that the Cr content in the reference test is much lower than that of the reactors with loaded coupons, confirming that, as noted previously, the measured Cr in the solution came mainly from the test coupons. The results also clearly show that adding yttria can lower the dissolution of Cr_2O_3 . The concentration of Cr in the water sample from the reactor with 5 wt. % yttria- Cr_2O_3 coupon is more than 50% lower than that from the test with a pure Cr_2O_3 coupon. The results agree well with the weight loss results presented before.

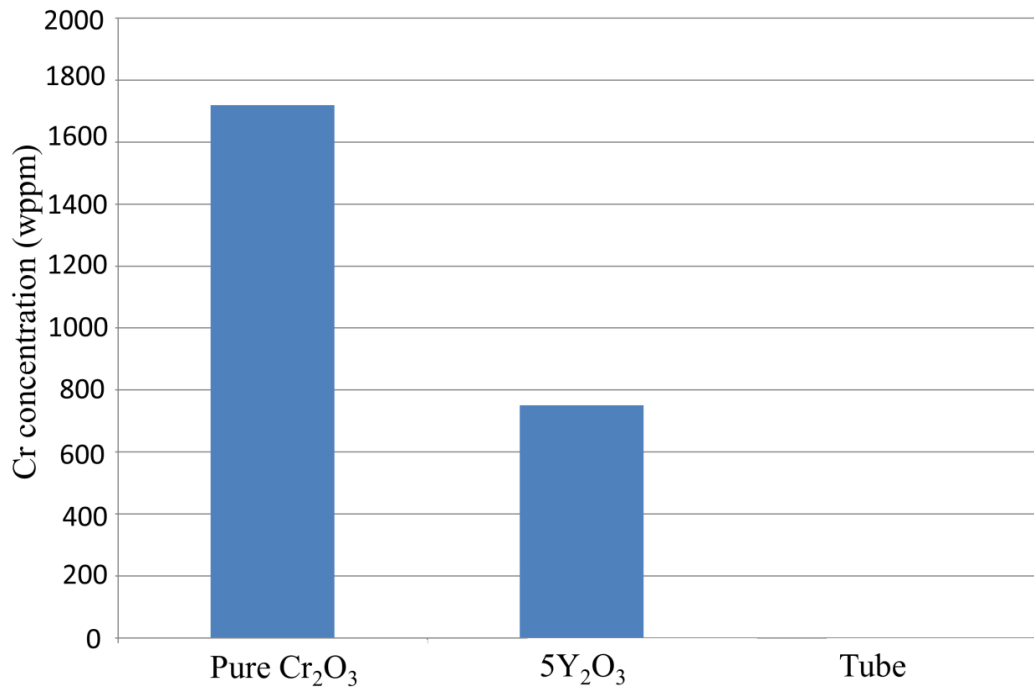


Figure 6- 15. Comparison of Cr concentration measured in the water samples from three capsule reactors after exposure at 600 °C for 100 hours. The capsule reactor was either not loaded or loaded with a pure chromium oxide coupon and a 5Y₂O₃-Chromium oxide coupon, respectively (wppm-in weight).

It has been found that adding small amounts of rare earth elements, such as Y, Ce, La, and Hf, can improve the oxidation resistance of alloys, often termed the “Reactive Element Effect” (REE) [23]. The positive effects of adding reactive elements include: improving the adherence of oxide scale; formation of a fine grained oxide layer with improved plasticity; reduction of oxide scale growth by blocking oxygen anion and metallic cation diffusion; and, reducing the segregation of harmful elements such as S at the interface [23-26].

Yttrium has been extensively studied and is commonly used to improve the oxidation resistance of high-temperature alloys containing chromium or aluminum. Yttrium is also added in the form of fine yttrium oxide particles to form oxide dispersion alloys, and can be implanted into the surface of an alloy or coated onto the surface to form a thin layer of yttrium oxide. The improvement of oxidation resistance by adding Y into Cr-containing alloys is believed to be mainly related to the segregation of Y at the grain boundaries of Cr_2O_3 scale and at the metal-scale interface, which can impede the diffusion of cations, although the diffusion flux of anions in this area was less affected [23, 27]. The strain-induced segregation of Y at Cr_2O_3 grain boundaries has been verified either through direct experimental observation [27, 28] or by theoretical simulations [29, 30]. Fang et al. calculated the interfacial and segregation energies of reactive elements in $\alpha\text{-Cr}_2\text{O}_3$ by first-principle simulation [29]. The calculations show that the larger the ionic size, the higher the tendency for the reactive elements to segregate to grain boundaries. The migration of the dopants to the grain boundaries could lower the interfacial energies at grain boundary areas, $\gamma_{\text{GB}}(\text{X})$, and therefore decrease the free energy of the system. This conclusion is consistent with the work by Cooke et al. [31] and Fabris et al. [32] who studied elemental segregation in Fe_2O_3 and Al_2O_3 . They concluded that the migration of doping elements into the interface region can release the elastic strain energy in this area.

Many studies on the stability of ceramics in harsh SCW environments have shown that intergranular corrosion was the primary mechanism of degradation [16, 20]. In

this study, for the pure Cr_2O_3 ceramic sample, the Cr at grain boundaries appears to have a higher tendency to react with SCW due to their higher energy, leading to the dissolution of Cr_2O_3 in this area as shown in Figure 6-8. The observed effects of adding yttria is consistent with the so-called reactive element effect. The large size Y atoms segregate to the grain boundaries and lower the distortion energy. Therefore the preferential dissolution of Cr at grain boundaries can be retarded and the stability of Cr_2O_3 in SCW is enhanced. The Y atom may also block diffusion of oxidizing species, which will reduce the oxidation rate and increase the corrosion resistance of Cr_2O_3 ceramics.

6.4 Concluding remarks

The stability of porous Cr_2O_3 based ceramics in various SCW environments were investigated in this study. Different amounts of yttria were introduced to the porous oxide ceramics to evaluate its effect on the stability of Cr_2O_3 in SCW environments. The following conclusions can be drawn from this study:

- 1) Cr_2O_3 is not stable in high temperature oxidizing SCW environments and can be oxidized to more soluble chromate (VI) species;
- 2) Adding yttria can improve the stability of Cr_2O_3 in SCW environments and retard the oxidation of Cr_2O_3 to chromate;

Larger amounts of yttria decrease the stability of the porous Cr_2O_3 -based ceramics because of the increased dissolution of yttria in SCW environments.

6.5 Reference

- [1] GIF-002-00, 2002 December.
- [2] R.B. Duffey, I.L. Pioro, Japan, 2005.
- [3] R.B. Duffey, I.L. Pioro, B.A. Gabaraev, Y.N. Kuznetsov, The 14th International Conf. on Nuclear Engineering (ICONE-14), 2006, pp. Paper 89609.
- [4] C.K. Chow, H.F. Khartabil, Nuclear Engineering and Technology, 40 (2007) 139.
- [5] M.R. Howlader, K. Shiiyama, C. Kinoshita, M. Kutsuwada, M. Inagaki, Journal of Nuclear Materials, 253 (1998) 149-155.
- [6] P.P. Krivoruchko, V.P. Kravchenko, B.G. Alapin, D.M. Shakhtin, E.V. Degtyareva, Y.I. Kolesov, Refractories, 22 (1981) 228-233.
- [7] T. Averbukh, P. Pavlov, Khimiya, Moscow, (1967).
- [8] T. Adschiri, K. Sue, K. Arai, Y. Watanabe, CORROSION 2001, (2001).
- [9] T. Xing, X. Cui, W. Chen, R. Yang, Materials Chemistry and Physics, 128 (2011) 181-186.
- [10] Y. Watanabe, T. Adschiri, K. Shoji, CORROSION 2002, (2002).
- [11] S. Chevalier, J.P. Larpin, Acta Materialia, 50 (2002) 3107-3116.
- [12] D.-H. Peck, M. Miller, D. Kobertz, H. Nickel, K. Hilpert, Journal of the American Ceramic Society, 79 (1996) 3266-3272.
- [13] P. Kritzer, The Journal of Supercritical Fluids, 29 (2004) 1-29.
- [14] L. Qiu, D.A. Guzonas, 3rd Canada-China Joint Workshop on Supercritical Water-Cooled Reactors, Xian, China, 2012.
- [15] A.B. Gaspar, C.A.C. Perez, L.C. Dieguez, Applied Surface Science, 252 (2005) 939-949.

- [16] M. Schacht, N. Boukis, E. Dinjus, *Journal of Materials Science*, 35 (2000) 6251-6258.
- [17] D. Guzonas, F. Brosseau, P. Tremaine, J. Meesungnoen, J. Jay-Gerin, *Nuclear Technology*, 179 (2012) 205.
- [18] T.K. Yeh, M.Y. Mang, H.M. Liu, M. Lee, *Topsafe2012*, Helsinki, Finland, 2012.
- [19] Y. Kuroda, H. Hamano, T. Mori, Y. Yoshikawa, M. Nagao, *Langmuir*, 16 (2000) 6937-6947.
- [20] N. Boukis, N. Claussen, K. Ebert, R. Janssen, M. Schacht, *Journal of the European Ceramic Society*, 17 (1997) 71-76.
- [21] F.F. Lange, G.L. Dunlop, B.I. Davis, *Journal of the American Ceramic Society*, 69 (1986) 237-240.
- [22] K. Sardar, M.R. Lees, R.J. Kashtiban, J. Sloan, R.I. Walton, *Chemistry of Materials*, 23 (2011) 48-56.
- [23] J. Stringer, *Mater. Sci. Eng. A-Struct. Mater. Prop. Microstruct. Process.*, 120 (1989) 129-137.
- [24] D.G. Lees, *Oxidation of Metals*, 27 (1987) 75-81.
- [25] D.P. Moon, *Materials Science and Technology*, 5 (1989) 754-764.
- [26] B.A. Pint, *Oxidation of Metals*, 45 (1996) 1-37.
- [27] C. Cotell, G. Yurek, R. Hussey, D. Mitchell, M. Graham, *Oxidation of Metals*, 34 (1990) 173-200.
- [28] A. Ul-Hamid, *Oxidation of Metals*, 58 (2002) 23-40.

- [29] H.Z. Fang, Y. Wang, S.L. Shang, P.D. Jablonski, Z.K. Liu, *Journal of Physics-Condensed Matter*, 24 (2012).
- [30] S. Galmarini, U. Aschauer, P. Bowen, S.C. Parker, *Journal of the American Ceramic Society*, 91 (2008) 3643-3651.
- [31] D.J. Cooke, S.E. Redfern, S.C. Parker, *Physics and Chemistry of Minerals*, 31 (2004) 507-517.
- [32] S. Fabris, C. Elsässer, *Acta Materialia*, 51 (2003) 71-86.

Chapter 7 Stability of Cr₂O₃ in Various SCW Environments

* A version of this chapter has been published. Z. Dong, W. Chen, W. Zheng, D. Guzonas, Corrosion Science, 65 (2012) 461-471.

7.1 Introduction

The Super Critical Water-cooled Reactor (SCWR) has been proposed as a promising next generation nuclear reactor concept and has attracted considerable attention because of the advantages offered by using SCW as a coolant [1]. The advantages of the SCWR over current generation water-cooled nuclear reactors include higher thermal efficiency (i.e., 45 -50% versus about 30-35% efficiency for current LWR), simplification of the reactor design (the steam generators, steam dryers and steam separators can be eliminated), and reduced size of reactor components [2, 3]. Although many SCWR design concepts have been proposed [4], one key common issue for all SCWR concepts is the identification of appropriate materials for reactor core components, as it has been found that both alloys and ceramics suffer severe degradation under SCW conditions, especially when high concentrations of oxidants are present [5-8].

Extensive investigations have been conducted to evaluate a wide range of candidate alloys for use in an SCWR, including nickel-based alloy (Alloy 625, etc.) [9, 10], iron-based alloy (ferritic-martensitic steels [11-13], austenitic stainless steels [14] and ODS steels [15, 16]), zirconium-based alloys [17, 18] and titanium-based alloys [18]. Ceramic materials have received less attention for structural applications because of their brittleness. In spite of that, ceramics are being considered for some specific applications in an SCWR, for example, as coatings or insulator materials, owing to their unique properties, including high hardness, chemical inertness, low thermal conductivity and high corrosion resistance. In addition, the performance of metallic materials under SCW

conditions is intimately related to the dissolution behaviour of the oxides or hydroxides formed on the surface when exposed to SCW environments, especially when the coolant is oxidizing, as may be the case if water radiolysis cannot be controlled [19]. Therefore, understanding the corrosion behaviour of ceramic materials in SCW environments is essential for the development of the SCWR.

The performance of some ceramics in SCW has been studied. Boukis et al. [20] conducted screening tests for various commercial ceramics in SCW containing oxygen and hydrochloric acid. The test results show that hot-isostatic-pressed BN (HIP-BN), B_4C , TiB_2 , Y_2O_3 , and yttrium-doped tetragonal zirconia (Y-TZP) disintegrated after being exposed to SCW containing 0.44 mol kg^{-1} oxygen and 0.05 mol kg^{-1} hydrochloric acid at $465 \text{ }^\circ\text{C}/25 \text{ MPa}$. A large weight loss, up to 90%, was observed when SiC - and Si_3N_4 - based materials were exposed to the SCW environment. Dense-sintered pure Al_2O_3 (99.7%) exhibited better corrosion resistance than Al_2O_3 containing other ceramic particles (20 vol % TiC/TiN). The present investigators have conducted a systematic study of the corrosion behaviour of porous chromium carbide (Cr_3C_2) in SCW environments at temperatures ranging from $375 \text{ }^\circ\text{C}$ to $625 \text{ }^\circ\text{C}$ with a constant pressure of 25-30 MPa [5], and found that Cr_3C_2 is stable in SCW at temperatures below 420-430 $^\circ\text{C}$. At temperatures above $425 \text{ }^\circ\text{C}$, cracking and disintegration occurred, and both intergranular and transgranular corrosion was observed. It was also

determined that the disintegration of Cr_3C_2 was related to the formation of an intermediate product (CrOOH) and its subsequent decomposition.

Cr_2O_3 is an important oxide which plays an important role in protecting steels from corrosion, since a protective Cr_2O_3 layer usually forms when alloys containing chromium above a certain threshold concentration are exposed to oxidizing environments. Numerous investigations have studied the kinetics of formation and loss of Cr_2O_3 scale on the surface of chromium and chromium-containing alloys in high temperature oxidizing environments. However, little work has been done to study the corrosion behaviour of bulk Cr_2O_3 ceramics under various SCW conditions.

In this chapter, bulk Cr_2O_3 ceramics with different morphologies were exposed to static or flowing SCW to investigate their corrosion behaviour under various SCW conditions. It is well known that the oxidation resistance of Cr-containing alloys can be improved by introducing the rare earth element (REE) yttrium into the alloy, either as fine yttrium oxide particles or by coating onto the surface [21, 22]. In this study, different amounts of Y_2O_3 or YSZ (YSZ- 8 mol % Y_2O_3) were added to Cr_2O_3 to study the effect on the stability of the material in a SCW environment.

7.2 Experimental

7.2.1 Preparation of Cr₂O₃ based ceramics

The compositions of the ceramics prepared for the SCW tests are listed in Table 7-1. The samples denoted A1, A2 and A3 were pure Cr₂O₃ samples with different morphologies prepared by three different sintering processes. These samples were used to investigate the influence of the processing method and resulting morphology on the stability of Cr₂O₃ ceramics in a SCW environment. The samples denoted B1, B2 and B3 were Cr₂O₃-based ceramics with Y₂O₃ added at concentrations ranging from 5 wt. % to 20 wt. %. The samples denoted C1, C2 and C3 were Cr₂O₃-based ceramics with Y₂O₃-stabilized ZrO₂ (YSZ- 8 mol % Y₂O₃) added. All the oxide powders were prepared according to the compositions listed in Table 7-1 and were mixed using a ball milling process. The mixed oxide powders were then uni-axially compressed in a cylindrical mold under a pressure of 80 MPa to form disc-shaped samples with a diameter of 16 mm and a thickness of 2 mm.

Table 7- 1. Chromium oxide based ceramics prepared for SCW test*

| Sample No. | Cr ₂ O ₃ | Y ₂ O ₃ | YSZ | ZrO ₂ | Sintering process** |
|------------|--------------------------------|-------------------------------|-----|------------------|---------------------|
| A1 | 100 | 0 | 0 | 0 | P1 |
| A2 | 100 | 0 | 0 | 0 | P2 |
| A3 | 100 | 0 | 0 | 0 | P3 |
| B1 | 95 | 5 | 0 | 0 | P3 |
| B2 | 90 | 10 | 0 | 0 | P3 |
| B3 | 80 | 20 | 0 | 0 | P3 |
| C1 | 80 | (2.75)*** | 20 | (17.25)*** | P3 |
| C2 | 50 | (6.87) | 50 | (43.13) | P3 |
| C3 | 20 | (11.00) | 80 | (69.00) | P3 |

* All values here are in weight percentage; ** P1-sintered at 1200 °C for 15 hours in air, P2-HIPped at 1650 °C/17.24 MPa for 2 hours, P3-carburized at 1100 °C followed by oxidation at 850 °C for 50 hours in air; *** calculated weight of Y₂O₃ and ZrO₂ based on the amounts of YSZ added.

Three different sintering processes (denoted P1, P2 and P3) were employed to sinter the green samples. In process P1 pressed pellets were sintered at 1200 °C for 15 hours in air. P2 was a hot isostatic pressing (HIPping) process that was conducted at 1650 °C at a pressure of 17.24 MPa. Process P3 consisted of two steps: first, the green samples were carburized in a carbonaceous environment at 1100 °C, which formed a highly porous carbide foam [23]; the carbide foams were then oxidized at 850 °C for 50 hours in air. The sintered ceramic samples were cut into coupons with a dimension of 10 mm × 4 mm × 2 mm. The coupons were cleaned in ethanol in an ultrasonic bath before SCW exposures as described in the following section.

7.2.2 SCW test facilities

An autoclave, shown in Figure 7-1, was built for static SCW tests. The static autoclave was made of Alloy 625 tubing, with an outside diameter of 9.525 mm and a wall thickness of 1.651 mm. Only one coupon was placed in the autoclave in each test. Air-saturated neutral pH deionized water with an oxygen concentration of 8 ppm was used in the static SCW tests. In some cases, H₂O₂ solution (30 wt. % H₂O₂) was used instead of the deionized water to increase the concentration of dissolved oxygen in SCW. The filling ratios of water in static reactors were around 7.85 vol. % at 550 °C, 6.76 vol. % at 625 °C, and 6.48 vol. %; the volumes were determined based on the data for water in the NIST database [24]. Figure 7-2 shows a schematic drawing of the SCW loop facility used to evaluate the stability of the ceramics in dynamic SCW environments. The oxygen concentration in the SCW loop facility was controlled by using water

liquids with different oxygen levels. The SCW fluid with a low oxygen level (around 8 ppb) was obtained by using deoxygenated water as the feeding liquid. The deoxygenation process was conducted by bubbling argon in the deionized water for three days. Air-saturated deionized water with an oxygen concentration of 8 ppm was used for the SCW loop test with a moderate oxygen level. The SCW fluid with a high oxygen level was achieved by using hydrogen peroxide solution (4 vol. % hydrogen peroxide) as the feeding liquid.

7.2.3 Characterization

The morphologies of the ceramic samples were examined using a high-resolution JEOL (JSM-6301FXV) field emission scanning electron microscopy (FESEM) and ZEISS (EVO-MA15) scanning electron microscopy (SEM). X-ray diffraction (XRD) analysis was conducted using a Rigaku X-ray diffractometer equipped with Geigerflex 2173 vertical goniometer. The concentration of elements in the water liquid after the SCW tests was measured using a Perkin Elmer Elan 6000 inductively-coupled plasma mass spectrometer (ICP-MS) with a detection limit of 0.001 ppm for Cr. X-ray Photoelectron Spectroscopy (XPS) analysis was conducted using a Kratos Axis 165 X-ray Photoelectron Spectrometer. The liquid sample was frozen using a cooling holder for the XPS measurements.

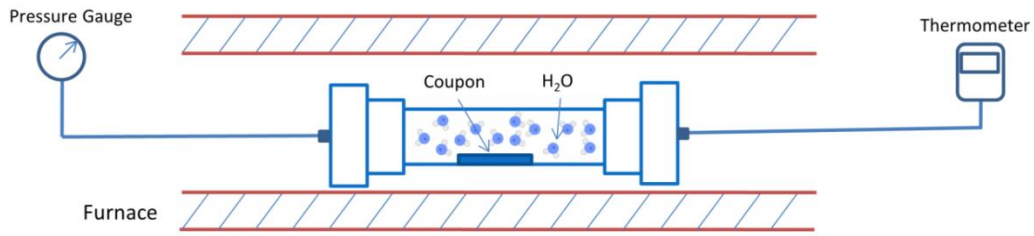


Figure 7- 1. Schematic illustration of the static SCW test autoclave adopted in the current study.

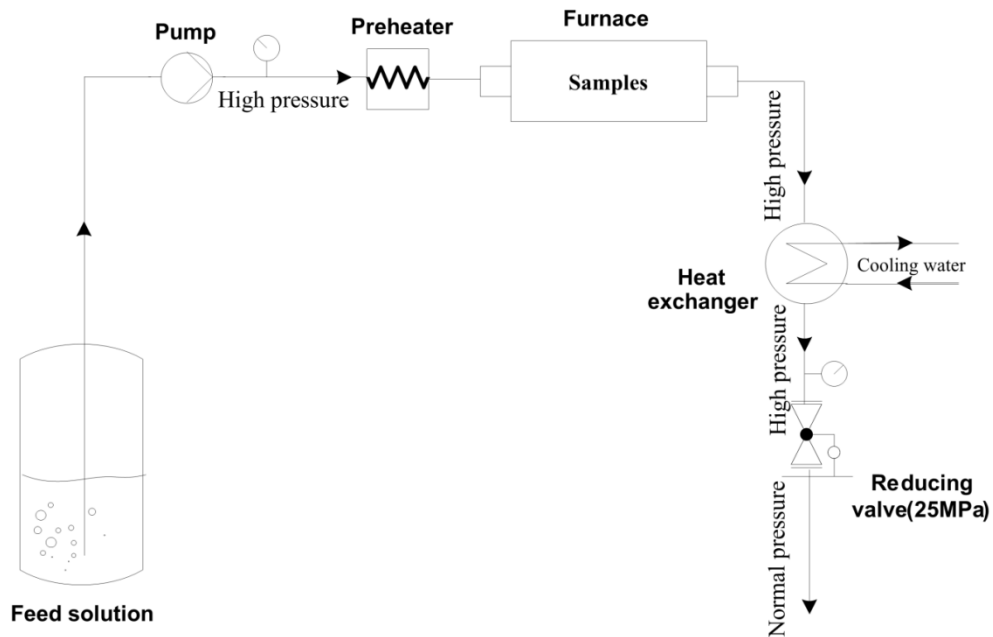


Figure 7- 2. Schematic illustration of the dynamic SCW fluid loop adopted in the current study.

7.3 Results

7.3.1 Morphology of the samples prior to SCW exposures

The morphologies of Samples A1, A2 and A3 as observed by SEM are shown in Figure 7-3(a-c). Sample A1, which was prepared by sintering the pressed pellet at 1200 °C in air, shows a porous structure consisting of oxide particles of 1-2 μm

diameter, almost the same as that of the starting Cr_2O_3 powder. This indicates that the sintering temperature ($1200\text{ }^\circ\text{C}$) was too low to cause any coarsening of the oxide powder [25-27]. Sample A2 was prepared through the HIPping process at $1650\text{ }^\circ\text{C}$ and 17.24 MPa . It can be seen that HIPping led to substantial densification and coarsening of the sample. The grain size in the sample after HIPping was measured to be around $10\text{-}20\text{ }\mu\text{m}$. Sample A3 exhibited a porous structure consisting of well-defined open pores constructed of inter-connected struts, as shown in Figure 7-3(c). Fine Cr_2O_3 crystallites with a size of $0.1\text{-}0.2\text{ }\mu\text{m}$ were seen on the struts. The microstructure of Samples B(1-3) and C(1-3) are shown in Figure 7-3(d-i).

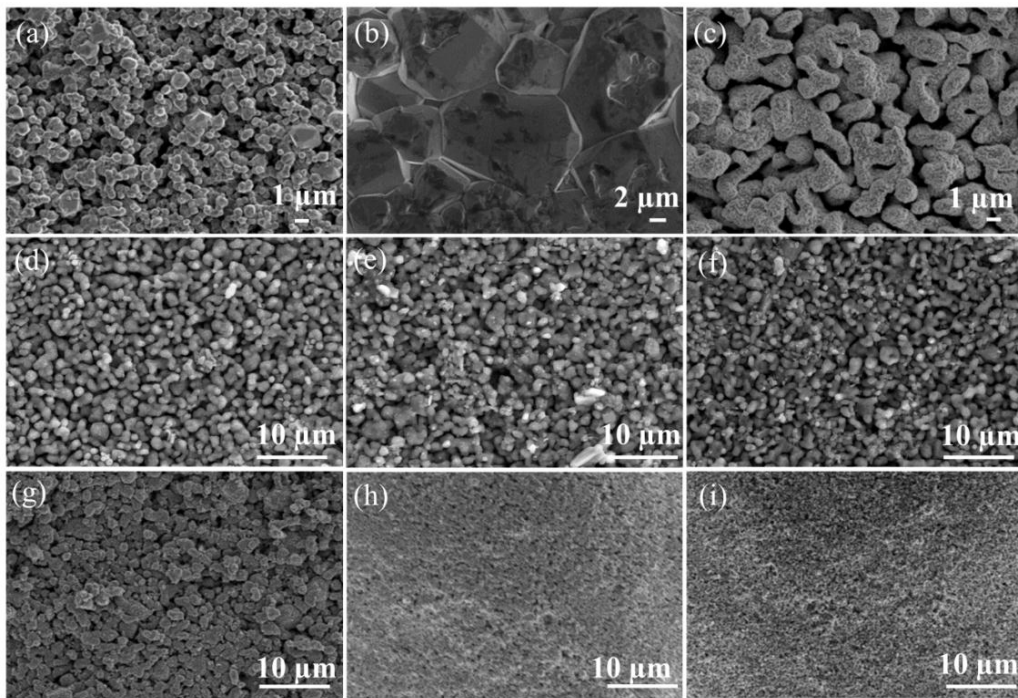


Figure 7- 3. Morphology of the as-sintered samples (a) Sample A1; (b) Sample A2; (c) Sample A3; (d) Sample B1; (e) Sample B2; (f) Sample B3; (g) Sample C1.

It can be seen that samples with added Y_2O_3 or YSZ also exhibited a porous structure that appears almost the same as the structure of the porous Cr_2O_3 sample shown in Figure 7-3(c). Clusters of fine particles were observed, particularly in the sample with higher amount of Y_2O_3 -addition, and were found to be composed of Y_2O_3 by EDS analysis. It was found that the samples with 50 wt. % YSZ and 80 wt. % YSZ added show less porosity, as shown in Figure 7-3(h, i).

7.3.2 Corrosion tests in static SCW environments

7.3.2.1 Stability of pure Cr_2O_3 ceramics in various SCW environments

(a) The effect of ceramic morphology

The pure Cr_2O_3 samples (A1, A2 and A3) were exposed to SCW at 625 °C and 25 MPa. Two concentrations of oxygen were studied: Condition I, with 8 ppm of oxygen obtained by using air-saturated deionized water as the test liquid; and, Condition II, with a much higher oxygen concentration (about 168,000 ppm), achieved by utilizing hydrogen peroxide solution (30 wt.% H_2O_2) as the test solution. Weight change data for the samples after SCW exposures for 100 hours and 200 hours are shown in Figure 7-4. It can be seen that only very minor weight loss (about 0.045%) was detected for the sintered sample (A1) after exposure in SCW under Condition I for 100 hours. The weight loss of the same sample increased with increasing exposure time as well as with increasing oxygen concentration. The HIPped sample (Sample A2) had no measurable weight change after SCW exposure under Condition I for 100 hours, and only a weight loss of only about 0.025% when the exposure time was extended to 200 hours.

Interestingly, the weight of Sample A2 slightly increased after the SCW test under Condition II. The porous sample (A3) exhibited the poorest stability under both exposure conditions, disintegrating during SCW exposures with or without H₂O₂ addition. Figure 7-5 shows the morphology of Sample A3 after SCW exposure; part of disintegrated sample crumbled into a powder as shown in Figure 7-5(a). From the SEM image shown in Fig. 7-5(b), it can be seen that the particles consisted of fine grains with a surface profile following the grain structure, indicating that corrosion occurred along the grain boundaries. It can also be seen that cracks and pits appeared on the surface of the still-intact pieces of Sample A3 (Fig. 7-5 (c)). The cracks appeared along the grain boundaries as shown in the high magnification image (Fig. 7-5 (d)), further confirming the occurrence of grain boundary attack and the high susceptibility of this material to intergranular corrosion in the SCW environments studied.

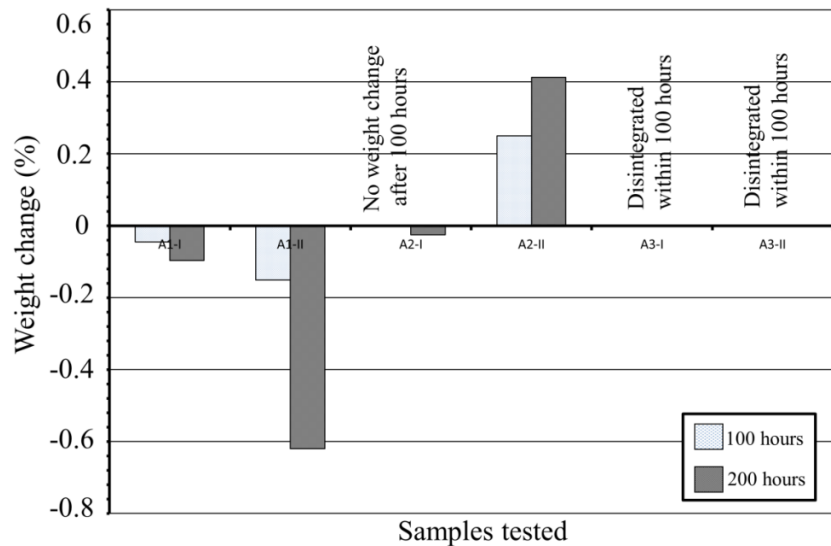


Figure 7- 4. Weight changes of Cr₂O₃ samples after exposure in SCW with different levels of oxygen at 625 °C/25 MPa: I-deionized water utilized to conduct the test; II-hydrogen peroxide solution (30 wt. % H₂O₂) utilized to conduct the test.

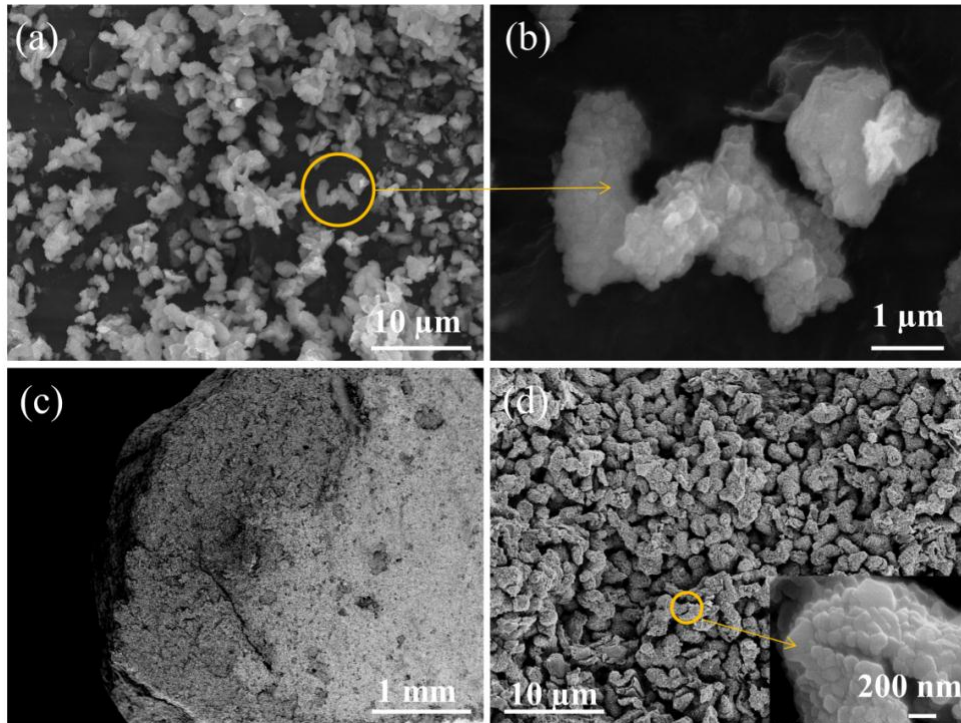


Figure 7- 5. Disintegration of porous chromium oxide sample (A2) in SCW at 625 °C/25 MPa: (a) Powders from the disintegration; (b) Magnified image of powder particles; (c) Remained part of the sample after SCW exposure; (d) Magnified image on the surface of remained part (inset: magnified image to show the cracks formed).

(b) On the dissolution of Cr₂O₃ in SCW

It is believed that the volatility of Cr_2O_3 exposed to oxygen-water mixtures at temperatures below $1000\text{ }^\circ\text{C}$ is mainly caused by the formation of soluble (volatile) $\text{CrO}_2(\text{OH})_2$, which has been confirmed in a recent study conducted by Opila et al [28]. Aki et al. examined the stability of a Cr_2O_3 catalyst in a Supercritical Water Oxidation (SCWO) environment at temperatures ranging from $390\text{ }^\circ\text{C}$ to $420\text{ }^\circ\text{C}$ and found that hexavalent chromium ion was present in the SCW effluent and its concentration was influenced by the test variables [29].

In this study, the concentration of chromium ion in the water after exposure of some selected samples under SCW conditions was analyzed using ICP-MS to determine the extent of metal release from Cr_2O_3 ceramics in SCW. Figure 7-6 shows the concentration of chromium ion presented in the water samples after Sample A1 was exposed to SCW with different concentrations of dissolved oxygen. The oxygen concentrations in SCW were calculated based on the test conditions: In the condition which air had been purged out of the autoclave, the oxygen content equals to the amount of oxygen dissolved in the deionized water; If no purging conducted, the oxygen content should be the total amount of oxygen present in the autoclave, which includes the oxygen dissolved in the deionized water and also the oxygen from the air remained in autoclave; If hydrogen peroxide solution was used, the total oxygen content also includes the amount of oxygen dissociated from hydrogen peroxide. The calculation of oxygen concentration was based on the assumption that oxygen was totally miscible with the water under SCW conditions. However, the accuracy of those values may be

compromised due to the limitation of the testing apparatus. Because chromium species may also be released into the water by corrosion of the autoclave tubing, which is made from a Cr-containing alloy, a reference blank run using a tubing specimen with no sample coupon loaded was conducted at the same high oxygen concentration, and the result is also shown in Figure 7-6. It can be seen that the Cr concentration in the water sample of the reference test is very low even at the high oxygen concentration, indicating that the chromium present in the water was mainly due to the corrosion of the Cr_2O_3 samples. It can also be noted that the concentration of chromium present increased with increasing concentration of dissolved oxygen. The concentration of chromium was around 1719 ppm in the tests that used H_2O_2 solution, much higher than that detected when deionized water was utilized, indicating that dissolution of Cr_2O_3 was much more severe in SCW under this condition. The chromium content in the water after the test was also measured after exposure of Sample A1 in SCW at 550 °C and 650 °C for various lengths of time as shown in Figure 7-7. The results show that the chromium content increased with increasing temperature as well as with exposure time. However, the increase was reduced after exposure for 100 hours, possibly because in a sealed capsule reactor such as that used in these tests, the concentrations of reactive species such as oxygen in the system will decrease with time as they are consumed by reaction with the test samples and the reactor walls.

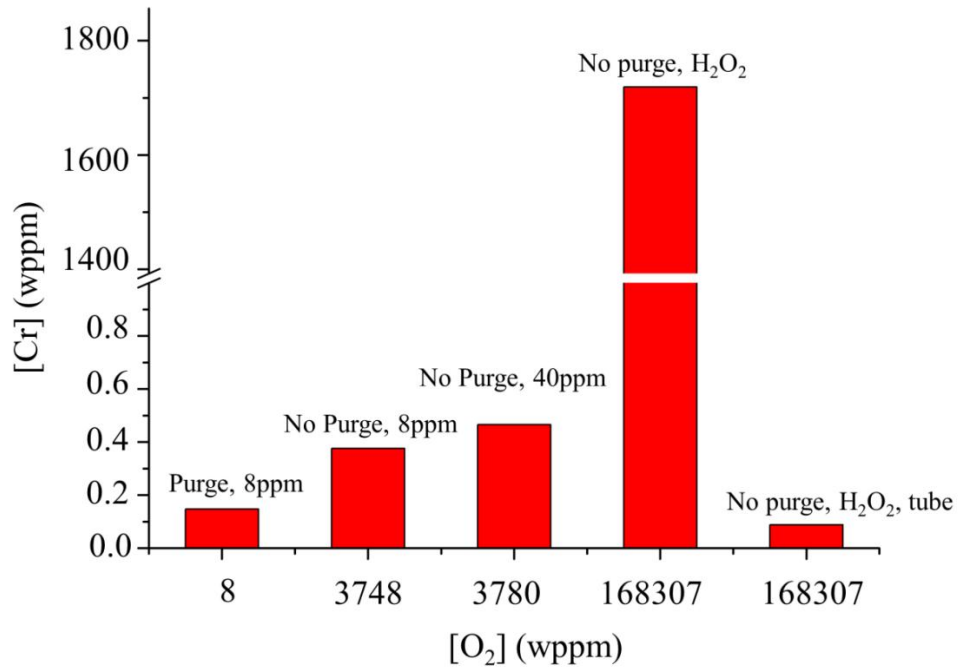


Figure 7- 6. The concentration of chromium ion present in the water liquid after the static SCW tests. ([O₂]-calculated oxygen concentration present in SCW; 8 ppm, 40 ppm-the oxygen concentration of the deionized water used; H₂O₂- 30 wt.% H₂O₂ solution was used.)

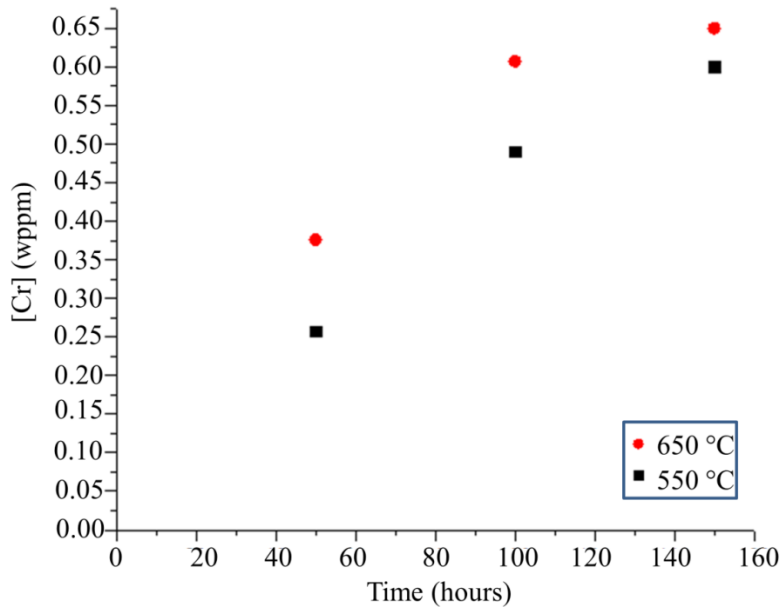


Figure 7- 7. The concentration of chromium ion present in the water solution after an exposure of Sample A1 in SCW 650 °C/25 MPa for different times. Deionized water with 8 ppm oxygen concentration was used to conduct the tests with no purge procedure.

7.3.2.2 Stability of Cr₂O₃ ceramics with added Y₂O₃ and YSZ

Different amounts of Y₂O₃ or YSZ were added to the Cr₂O₃ ceramic for the purpose of improving its stability. It has been reported that yttrium, can segregate to grain boundaries and enhance the corrosion resistance of grain boundary (GB) materials [21, 30-32]. All the coupons added with Y₂O₃ (B1, B2, and B3) and YSZ (C1, C2, and C3) were exposed to SCW at 625 °C and 25MPa for up to 500 hours. These samples were prepared by the same process as that used for Sample A3, which disintegrated within 100 hours in SCW at 625 °C and 25 MPa. The samples with added Y₂O₃ and YSZ exhibited higher stability and only suffered from minor weight loss after SCW exposure. Figure 7-8 compares the changes in weight of the coupons after SCW exposure for 500 hours. The coupon with 5 wt. % Y₂O₃ experienced the least weight variation as compared to those with higher amounts of Y₂O₃-addition, indicating that excessive Y₂O₃ addition (10 wt. % and 20 wt. %) reduced the stability of Cr₂O₃ in SCW. All the samples with added YSZ exhibited even better stability as no measurable weight change was detected after exposure.

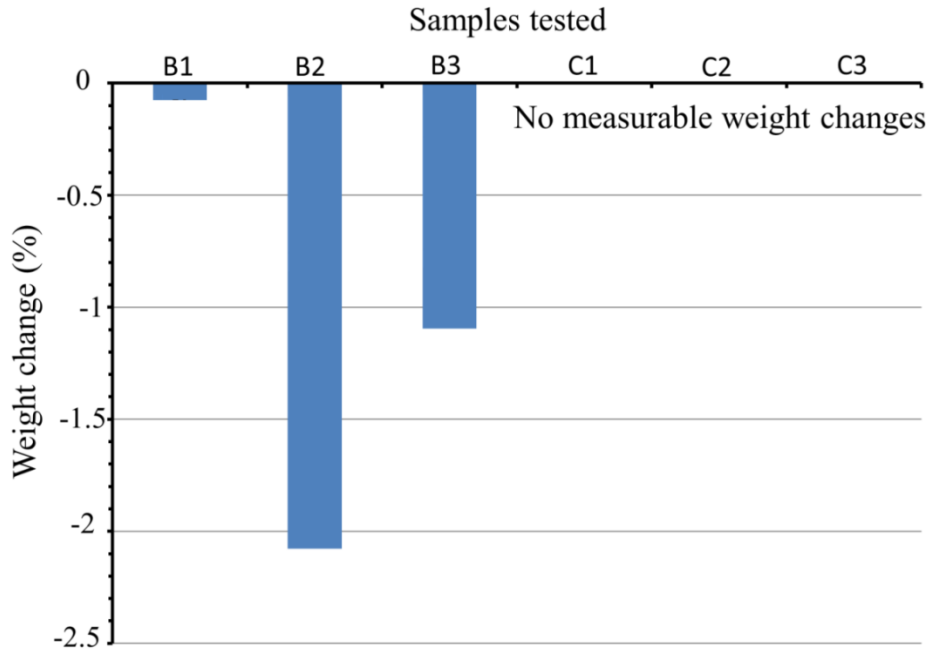


Figure 7- 8. Weight changes of sample B(1~3) and C(1~3) after static SCW tests for 500 hours. Deionized water with 8 ppm oxygen was used to conduct the tests with no nitrogen purge.

7.3.3 Corrosion tests in flowing SCW

7.3.3.1 Weight loss

To avoid possible contamination or damage to the loop facility due to the disintegration of the ceramics, only selected samples (A3, B1, B2, C1, C2, and C3) which exhibited relatively good stability during static exposure in SCW were tested in the SCW loop to further examine their stability. Figure 7-9 shows the weight changes of tested samples throughout the loop exposure. The oxygen concentration in the loop was adjusted from low (8 ppb) at the start of the test to high (4 vol. % H₂O₂ solutions) at the end. It can be seen that at 8 ppb, all the samples tested showed excellent stability, with no measurable weight change after

exposure for up to 350 hours. When the oxygen concentration was increased to a moderate concentration of 8 ppm, a small loss in weight was observed only for the HIPped pure Cr_2O_3 sample (A2). However, when the oxygen concentration was further increased by using a 4 vol. % H_2O_2 solution as the feed liquid, all the samples tested, except for Sample A2, show evident weight loss. Sample B2 (10 wt. % Y_2O_3) showed the largest weight loss (about 47 %) which is almost twice that recorded for sample B1 (5 wt. % Y_2O_3). The Cr_2O_3 sample (C1) with 20 wt. % added YSZ exhibited better stability. Sample C2, with 50 wt. % YSZ addition showed the largest weight loss of the samples with added YSZ. Little weight gain, around 5 %, was observed for the HIPped pure Cr_2O_3 sample (A3) after the SCW test at the highest oxygen concentration.

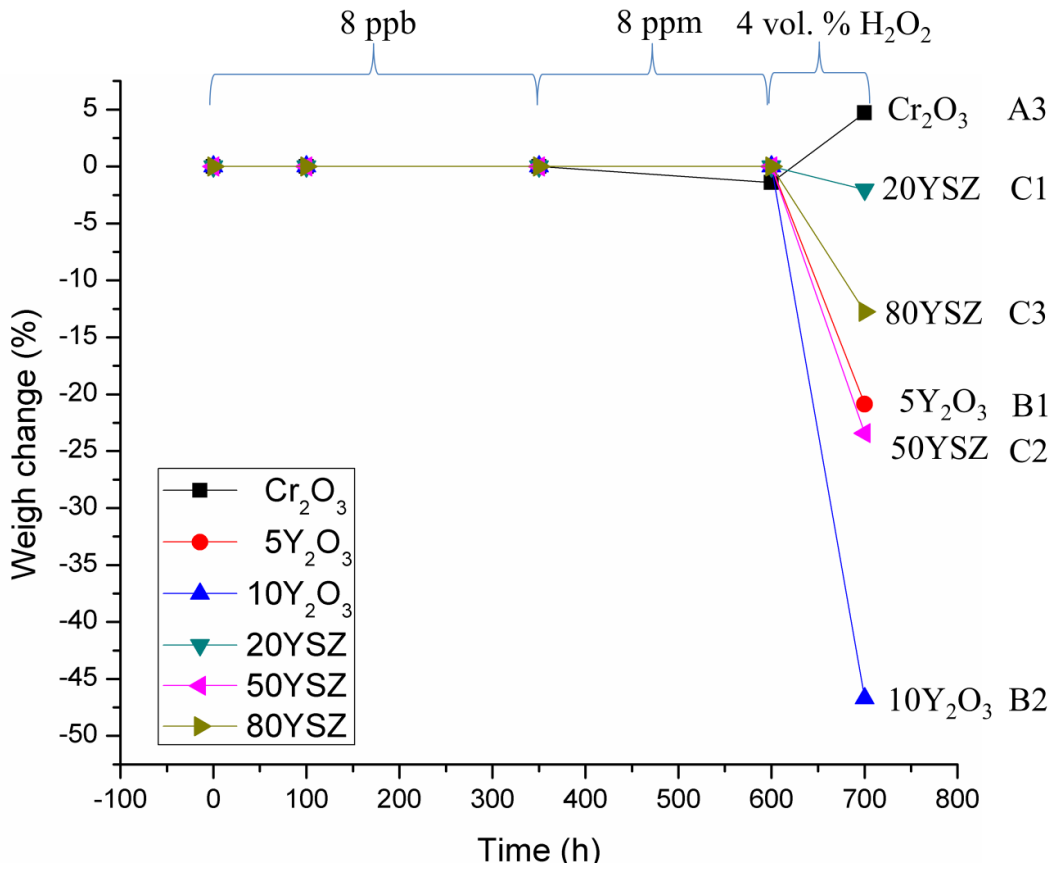


Figure 7- 9. Weight changes of Cr₂O₃ based ceramics after exposure to flowing SCW at 625 °C/25 MPa. Each sample was sequentially exposed to flowing SCW with different levels of oxygen: 8 ppb (using deionized water as the feeding liquid), 8 ppm (using deionized water with oxygen concentration of 8 ppm as the feeding liquid), H₂O₂ (4 vol. %)(using hydrogen peroxide solution containing 4 vol. % H₂O₂ as the feeding liquid).

7.3.3.2 Morphology after SCW loop exposures

The surfaces of the samples after tests in the SCW loop were examined using SEM. No obvious changes were observed on the surfaces for any samples after exposure in SCW with oxygen concentration at 8ppb and 8ppm. However,

changes in surface morphology were observed on all the samples after exposure in the SCW loop using 4 vol. % H_2O_2 solution.

HIPped Cr_2O_3 sample

Figure 7-10 shows the SEM images of the HIPped sample (A2) after loop exposure. A network of cracks appeared on the surface as shown in Figure 7-10(a). Some pits of 10-20 μm in size were observed on the surface. The Cr_2O_3 grains are seen to be faceted after the test, as shown in Figure 7-10(b).

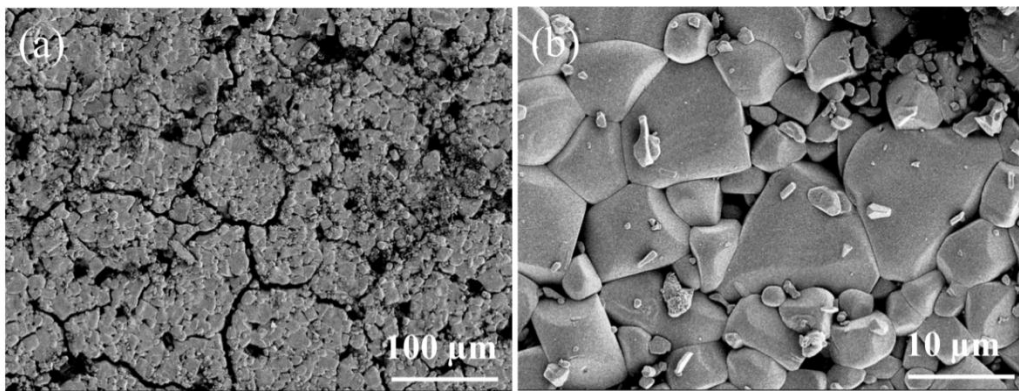


Figure 7- 10. Surface morphologies of Samples A2 after SCW loop test for 700 hours: (a) low magnification; (b) high magnification.

Y_2O_3 added samples

The surface microstructures of Samples B1 and B2 after loop tests are shown in Figure 7-11. Cracks were observed in both samples as shown in the inset images in Figure 7-11. The surfaces appeared rougher than the original surfaces after the

SCW tests, suggesting selective dissolution in SCW with a high concentration of oxygen.

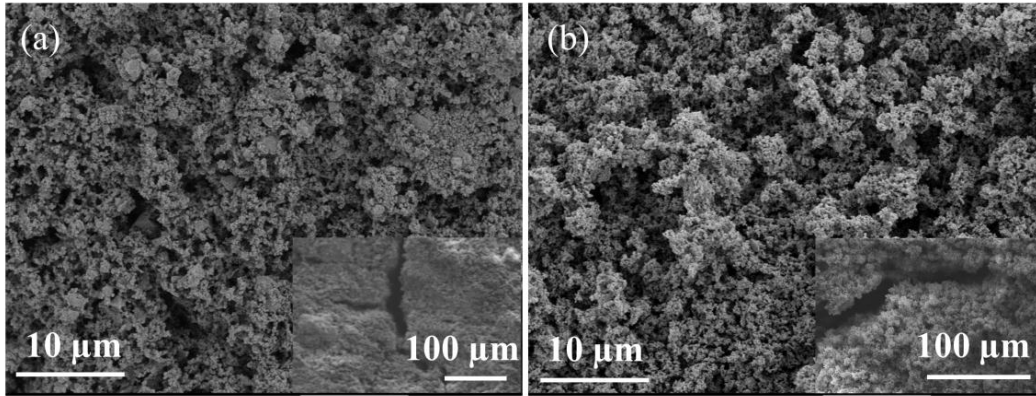


Figure 7- 11. Surface morphologies of Samples B1 (a) and B2 (b) after SCW loop test for 700 hours (insets: cracks observed).

YSZ added samples

Figure 7-12 shows the surface morphologies of YSZ-containing samples (C1, C2, and C3). Although the sample (C1) with 20 wt. % added YSZ showed the lowest weight loss among all the porous ceramic samples, the surface was also roughened after the loop test as shown in Figure 7-12 (a) and (d). Deposition of crystals was observed on the surfaces of Samples C2 and C3. EDS analysis revealed that the crystals were composed of chromium and oxygen with a mole ratio of around 0.4-0.6, which is consistent with the composition of Cr_2O_3 .

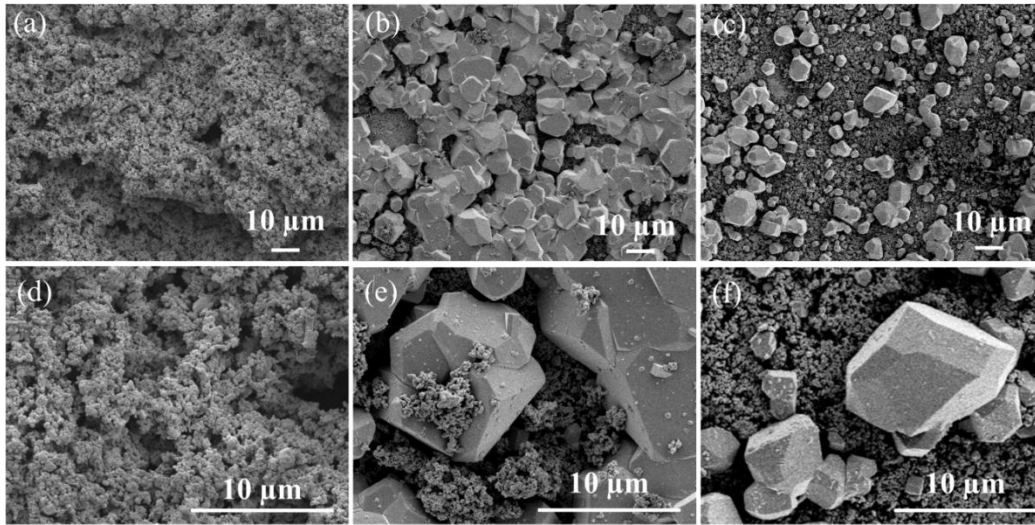


Figure 7- 12. Surface morphologies of Samples C1: (a) low mag. (d) high mag., C2: (b) low mag. (e) high mag. and C3: (c) low mag. (f) high mag. after SCW loop test for 700 hours.

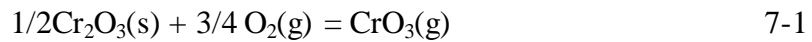
7.4 Discussion

7.4.1 Corrosion of Cr_2O_3 in SCW environments

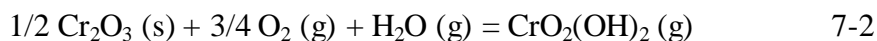
The Pourbaix diagram for chromium [33] shows that chromium can dissolve as H_2CrO_4 (transpassive dissolution), as observed in boiling water reactors operating with normal water chemistry because of the high concentrations of oxidizing species produced by water radiolysis. Similarly high concentrations of oxidants are possible in an SCWR core if water radiolysis cannot be controlled [19], as observed by Karasawa et al. [34] and Fujiwara et al. [35]. However, the validity of Pourbaix diagrams for assessing the thermodynamic stability of metals and metal oxides in SCW at temperatures above 500 °C and a pressure of 25 MPa is questionable [36], because at this pressure the density and dielectric constant of SCW are low and ion association is favoured over ion dissociation. As a result,

pH is not a useful parameter under the near-neutral water chemistry expected to be used in an SCWR [37] at temperatures above about 500 °C.

It has also been well documented that the evaporation of Cr₂O₃ in dry air or oxygen at temperatures higher than 1000 °C is mainly caused by the formation of CrO₃(g) by the following reaction [38, 39]:



The rate of evaporation of Cr₂O₃ is insignificant at temperatures below 1000 °C, but in the environments containing both O₂ and H₂O, the evaporation rate of Cr₂O₃ was found to increase even at temperatures below 1000 °C. Yamauchi et al. investigated the evaporation of Cr₂O₃ exposed to N₂-O₂-(H₂O) atmospheres at temperatures ranging from 900 °C to 1200 °C [40]. They found that the evaporation rate of Cr₂O₃ in the N₂-O₂-H₂O atmosphere was one order of magnitude higher than that when Cr₂O₃ was exposed to N₂-O₂ or N₂-H₂O atmosphere alone. The enhanced evaporation of Cr₂O₃ by water vapour in oxidising environments has also been observed at temperatures between 600 °C to 800 °C [41, 42]. This water assisted evaporation of Cr₂O₃ is believed to be caused by the formation of volatile chromium oxy-hydroxide species, such as CrO₂(OH)₂, CrOOH, Cr(OH)₂, Cr(OH)₃, and Cr(OH)₄. Recent studies revealed that CrO₂(OH)₂, formed by the following reaction, is the dominant volatile chromium species at temperatures below 1000 °C [28].



$\text{CrO}_2(\text{OH})_2$ is chemically identical to the species H_2CrO_4 which appears in the chromium Pourbaix diagram; referring to the loss of chromium at high oxygen concentrations in SCW as chromium evaporation or chromium dissolution is really a function of whether one is in low density or high density SCW [37]. The underlying chemistry involves the reaction of Cr with water to form a chemical compound whose thermodynamic stability in the fluid phase is high.

One liquid sample obtained after static autoclave exposure of sample A1 in SCW with a high dissolved oxygen concentration (using H_2O_2) was analyzed using X-ray photoelectron spectroscopy (XPS). A peak corresponding to Cr $2p^{3/2}$ at a binding energy of 578.6 eV was found, corresponding to Cr^{6+} [43] as shown in Figure 7-13. No peaks belonging to Cr^{3+} were identified in the solution sample; Cr^{3+} oxides have very low solubilities in SCW. This result is consistent with that reported by Aki et al. [29] who investigated the stability of a Cr_2O_3 catalyst under SCWO conditions and found that only Cr^{6+} was present in the effluent.

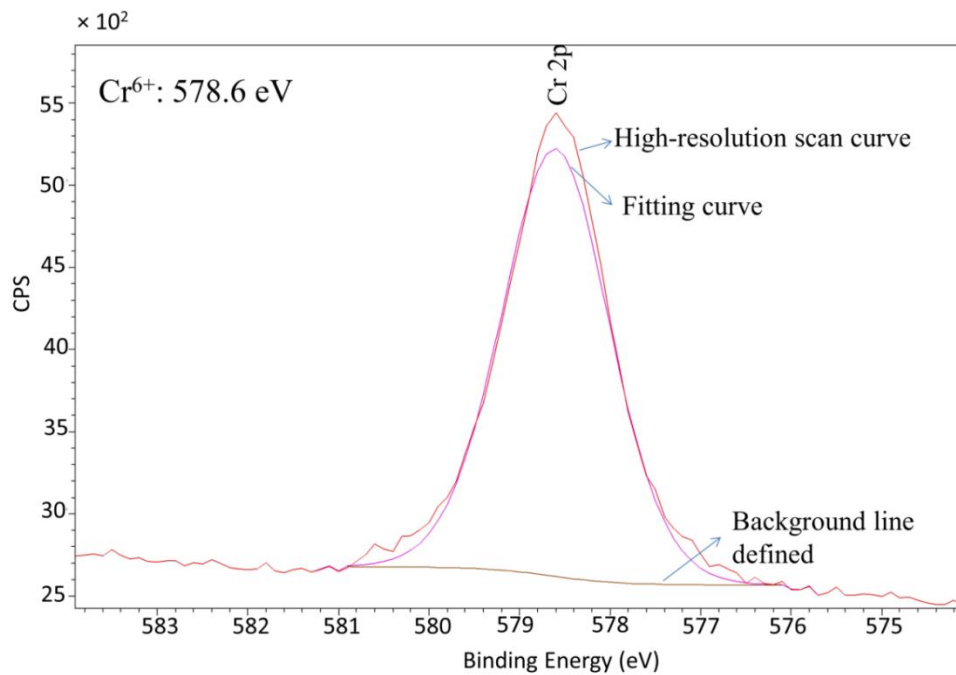


Figure 7- 13. Spectra of Cr2p3/2 from the high resolution XPS analysis of water after SCW test at 600 °C for 25 hours using hydrogen peroxide solution (30 wt. %).

Since oxygen is involved in the formation of $\text{CrO}_2(\text{OH})_2$, changes in the dissolved oxygen concentration should affect the corrosion kinetics of the Cr_2O_3 ceramics in SCW. It is obvious from Figure 7-4 that the weight loss increased when the sintered sample (A1) was exposed to SCW at the higher oxygen concentration. This tendency could not be clearly observed for Sample A3 since it suffered severe disintegration at both oxygen concentrations. The weight gain observed for the HIPped sample (A2) could be attributed to deposition of corrosion products from corrosion of the Alloy 625 reactor at high oxygen concentration, as confirmed by the observation by SEM/EDS that some crystals, identified as

molybdenum oxide (Figure 7-14), deposited on the surfaces of samples exposed to SCW and H₂O₂ solution. This is consistent with the published data showing that that molybdenum is dissolves in oxidizing SCW [8]. The molybdenum oxide crystals likely precipitated as the autoclave was cooling down. Figure 7-6 clearly shows that an increased amount of chromium was measured in the liquid samples with increasing initial oxygen concentration in SCW.

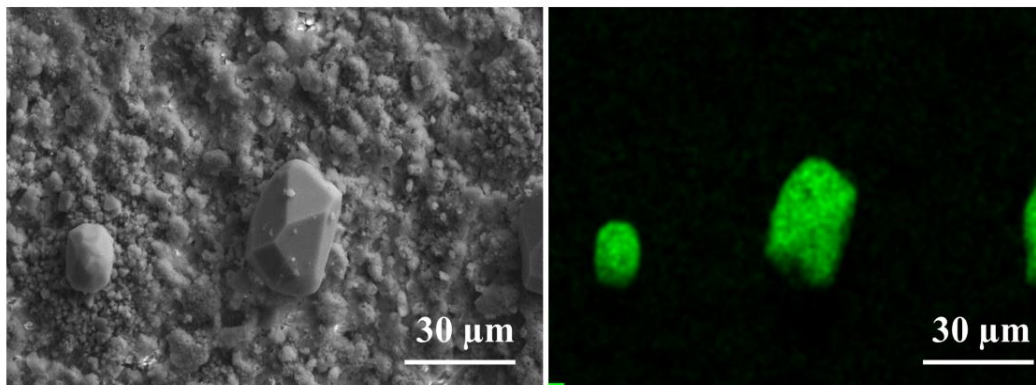


Figure 7- 14. EDS mapping of chromium oxide based ceramics after exposure at 625 °C in SCW with high oxygen level (30 % H₂O₂ solution was used) for 100 hours: (a) Secondary electron image; (b) EDS mapping for Mo.

The above experimental results can be summarized as follows: The stability of Cr₂O₃ in SCW environments is significantly affected by its morphology. Of the pure Cr₂O₃ samples tested, the sample (A2) sintered by HIPping, which consisted of large oxide grains, showed the lowest weight loss in SCW at 625 °C and 25 MPa, although some weight gain was observed in SCW at high oxygen concentrations. Intergranular corrosion was the main mechanism of degradation for this sample. The air sintered sample (A1) showed more weight loss than the

HIPped sample (A2) after the SCW tests. The porous sample (A3) suffered significant degradation and disintegrated during the SCW test. The low resistance of Sample A3 to corrosion is attributed to the extremely small grain size (around 0.2 μm , Fig. 3), much smaller than that of Sample A1 (1~2 μm) and Sample A2 (10~20 μm); the small grain size facilitates dissolution of the oxide because of the high surface area exposed to the solution. This dependence on exposed surface area also explains the observation that the porous samples A1 and A3 suffered more corrosion (as measured by weight loss) than the densified sample (A2). When the grain size in the sample is very small, for example, Sample A3, intergranular attack can result in a direct disintegration of the sample, as evidenced in Figure 7-5.

The relationship between the stability of Cr_2O_3 ceramics, exposed surface area and grain size is further illustrated in Figure 7-15. Figure 7-15(a) and (b) represent Cr_2O_3 ceramics having different grain sizes. The sample with smaller grains should exhibit a higher tendency to disintegrate because intergranular corrosion at the grain boundaries will separate the grains, even though the geometric surface area of the samples are the same. If the grain boundaries are modified to achieve higher stability by, for example, doping with a reactive element such as yttrium (Figure 7-15(c)), higher stability of the ceramic can be expected. As noted in section 2.2.1, the porous sample (A3) showed the worst stability and highest tendency to disintegrate because of its very fine grain structure. The increased stability of the porous sample with Y_2O_3 added (B1, B2, B3) compared to sample

A3 is a direct result of the increased grain boundary stability arising from segregation of the reactive element (the so-called 'reactive element effect').

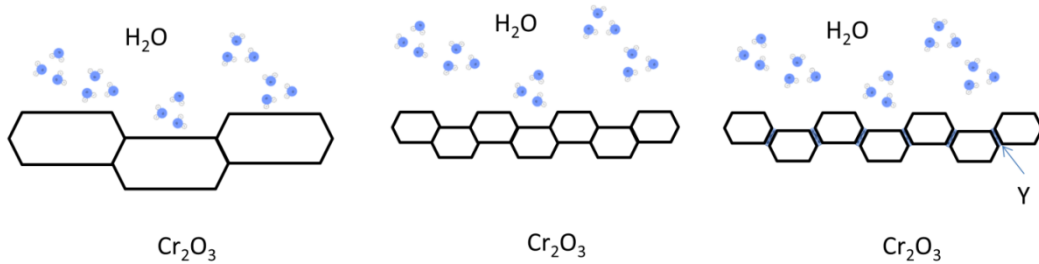


Figure 7- 15. Illustration of the roughness, grain size and grain boundaries with the stability of Cr₂O₃ ceramics in SCW environments.

Grain boundaries in polycrystalline materials are usually the preferred sites for corrosion because of the high interfacial energy and different bonding structures. Some ceramics have been reported to suffer from intergranular corrosion in SCWO environments. Barringer et al. [44] investigated the corrosion behavior of a high-purity CVD β -SiC exposed to deoxygenated supercritical water at 500 °C. Their results show that the grain boundaries of CVD SiC were preferentially corroded. Schacht et al. investigated the corrosion behaviour of alumina ceramics in SCW containing acidic species [45]. It was also found that intergranular attack was the dominant corrosion mechanism for the alumina exposed to those SCW environments. As seen in Figure 7-5, cracking along grain boundaries occurs; the HIPped sample (A2) also exhibited obvious intergranular cracking (Figure 7-10) after SCW loop exposure. The pits observed in Figure 7-10 might be formed due to the loss of one or more grains from the surface after the grain boundaries since

the size of pits was close to that of the Cr_2O_3 grains in the HIPped sample. Therefore, we conclude that the grain boundaries of Cr_2O_3 ceramics are preferentially attacked by the SCW, especially when the concentration of dissolved oxygen is high.

7.4.2 Comparison of the static autoclave and loop tests

The results obtained from the SCW loop tests are consistent with those obtained in the SCW static autoclave tests. For example, sample (B1) with 5 wt. % Y_2O_3 exhibited better stability than sample B2 with 10 wt. % Y_2O_3 , and samples with added YSZ (C1 and C3) showed even better stability. However, Sample B2 with 50 wt. % YSZ exhibited a weight loss comparable to that of Sample B1. This may be attributed partly to the corrosion of Cr_2O_3 and partly to the loss of YSZ. The latter occurs when Cr_2O_3 is leached out by dissolution and the remaining microstructural components in the ceramics are no longer intact. The more severe corrosion observed in the loop tests at high oxygen concentrations may be a flow induced corrosion phenomenon in which the corrosion products are carried away from the corrosion site by the solution; the resulting concentration gradient in the solution provides a driving force for further corrosion.

It has been reported that condensation of Cr_2O_3 from $\text{CrO}_2(\text{OH})_2$ can occur at temperatures higher than 400 °C[28], explaining the observation that Cr_2O_3 crystals were found to be deposited on the surfaces of Samples C2 and C3 (Figure 7-12). The Cr-containing species may have come from corrosion of the SCW loop or from the Cr_2O_3 sample; more Cr_2O_3 crystals were observed on the surface of

Sample C2 that has higher fraction of Cr_2O_3 than on Sample C3. The movement of Cr from loop surfaces to sample surfaces in SCW was reported by Daigo et al. [46] and Guzonas and Cook [37]. To assess the migration of Cr-containing species to the surface, cross-sections of Sample C2 and C3 were mapped by EDS (Figure 7-16). It can be clearly seen that there exists a chromium depletion zone at the surface of both the samples with added YSZ. There is also a chromium-enriched layer just under the leaching zone in Sample C2, indicating that chromium can be transported inside the ceramics when exposed to SCW at high oxygen concentrations. These observations are further illustrated in Figure 7-17. Because of the porous nature of the sample, SCW can easily penetrate into the pores of sample to react with Cr_2O_3 to form $\text{CrO}_2(\text{OH})_2$; as $\text{CrO}_2(\text{OH})_2$ builds up in the film and at the surface, the process will be limited by diffusion of $\text{CrO}_2(\text{OH})_2$ away from the surface. In a static system this may limit the rate of dissolution, while in a flowing system the SCW carries the volatile (dissolved) chromium species away from the surface and gradually create a chromium depletion zone in the oxide.

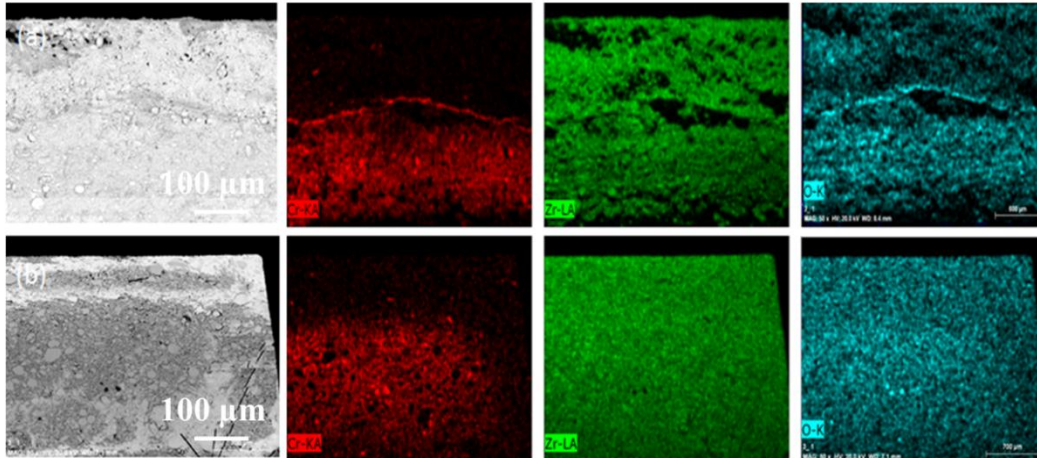


Figure 7- 16. EDS mapping of cross-section of Samples C2 and C3 after SCW loop tests.

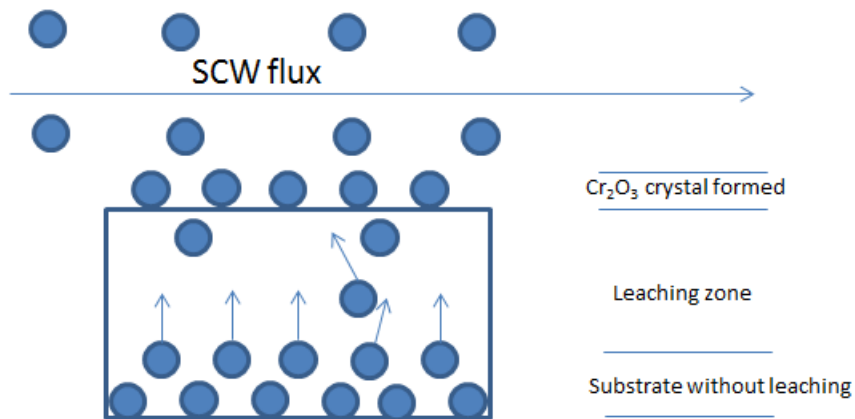


Figure 7- 17. Illustration showing the transportation of chromium species from Samples C2 and C3 during SCW loop exposure.

7.5 Concluding Remarks

The corrosion behaviour of various Cr_2O_3 -based ceramics exposed to SCW environments at $625\text{ }^\circ\text{C}$ and 25 MPa with different dissolved oxygen

concentrations has been investigated under static and flowing conditions. The experimental results show that the stability of Cr_2O_3 ceramics was affected by the morphology of the ceramic samples as well as the oxygen concentration. Of the pure Cr_2O_3 samples examined, the most porous sample exhibited the lowest stability in SCW. The stability of the porous Cr_2O_3 sample was enhanced by addition of Y_2O_3 (5 wt. %) or YSZ (20 wt. %). The disintegration of porous Cr_2O_3 is attributed to increased grain boundary attack under SCW condition, observed both in the static and loop exposures. The results show that it will be important to control the oxidant concentration in an SCWR core to prevent dissolution of the protective Cr_2O_3 films on alloy surfaces.

7.6 Bibliography

- [1] GIF-002-00, 2002 December.
- [2] R.B. Duffey, I.L. Pioro, B.A. Gabaraev, Y.N. Kuznetsov, The 14th International Conf. on Nuclear Engineering (ICONE-14), 2006, pp. Paper 89609.
- [3] C.K. Chow, H.F. Khartabil, Nuclear Engineering and Technology, 40 (2007) 139.
- [4] Y. Oka, ICAPP'02: 2002 International Congress on Advances in Nuclear Power Plants, Hollywood, FL (United States), 2002.
- [5] Z. Dong, W. Chen, W. Zheng, D. Guzonas, Journal of Nuclear Materials, 420 (2012) 320-327.
- [6] M.C. Sun, X.Q. Wu, Z.E. Zhang, E.H. Han, Journal of Supercritical Fluids, 47 (2008) 309-317.
- [7] M. Son, Y. Kurata, Y. Ikushima, CORROSION 2002, (2002).
- [8] P. Kritzer, The Journal of Supercritical Fluids, 29 (2004) 1-29.
- [9] N. Boukis, W. Habicht, G. Franz, E. Dinjus, Materials and Corrosion, 54 (2003) 326-330.
- [10] J. Konys, A. Ruck, J. Novotny, J. Hausselt, CORROSION 2001, (2001).
- [11] P. Ampornrat, C.B. Bahn, G.S. Was, in: T.R. Allen, P.J. King, L. Nelson (Eds.) 12th Int. Conf. on Environmental Degradation of Materials in Nuclear Power Systems-Water Reactors, 2005, pp. 1387-1396.
- [12] X. Ren, K. Sridharan, T. Allen, Journal of nuclear materials, 358 (2006) 227-234.
- [13] K. Yin, S. Qiu, R. Tang, Q. Zhang, L. Zhang, The Journal of Supercritical Fluids, 50 (2009) 235-239.

- [14] Y. Chen, K. Sridharan, T. Allen, CORROSION 2007, NACE International, Nashville, Tennessee, USA, 2007, pp. 14.
- [15] J. Isselin, R. Kasada, A. Kimura, Corros. Sci., 52 (2010) 3266-3270.
- [16] J.H. Lee, R. Kasada, A. Kimura, T. Okuda, M. Inoue, S. Ukai, S. Ohnuki, T. Fujisawa, F. Abe, Journal of nuclear materials, 417 (2011) 1225-1228.
- [17] Y. Jeong, J. Park, H. Kim, J. Busby, E. Gartner, M. Atzmon, G. Was, R. Comstock, M.G. da Silva, A. Motta, in: T.R. Allen, P.J. King, L. Nelson (Eds.) 12th International conference on environmental Degradation of Materials in Nuclear Power System-Water reactors, TMS, 2005, pp. 1,369-361,377.
- [18] G. Was, P. Ampornrat, G. Gupta, S. Teyseyre, E. West, T. Allen, K. Sridharan, L. Tan, Y. Chen, X. Ren, Journal of nuclear materials, 371 (2007) 176-201.
- [19] D. Guzonas, F. Brosseau, P. Tremaine, J. Meesungnoen, J.-P. Jay-Gerin, Nucl. Technol., 179 (2012) 205.
- [20] N. Boukis, N. Claussen, K. Ebert, R. Janssen, M. Schacht, Journal of the European Ceramic Society, 17 (1997) 71-76.
- [21] J. Stringer, Mater. Sci. Eng. A-Struct. Mater. Prop. Microstruct. Process., 120 (1989) 129-137.
- [22] C. Cotell, G. Yurek, R. Hussey, D. Mitchell, M. Graham, Oxid. Met., 34 (1990) 173-200.
- [23] T. Xing, X. Cui, W. Chen, R. Yang, Materials Chemistry and Physics, 128 (2011) 181-186.

- [24] E.W. Lemmon, M.O. McLinden, D.G. Friend, NIST Chemistry WebBook, NIST Standard Reference Database Number 69, Eds. P.J. Linstrom and W.G. Mallard, National Institute of Standards and Technology, Gaithersburg MD, 20899, <http://webbook.nist.gov>.
- [25] A. Yamaguchi, J. Am. Ceram. Soc., 64 (1981) 67-68.
- [26] P. Ownby, G. Jungquist, Journal of the American Ceramic Society, 55 (1972) 433-436.
- [27] W.C. Hagel, P.J. Jorgensen, D.S. Tomalin, Journal of the American Ceramic Society, 49 (1966) 23-26.
- [28] E.J. Opila, D.L. Myers, N.S. Jacobson, I.M.B. Nielsen, D.F. Johnson, J.K. Olminsky, M.D. Allendorf, Journal of Physical Chemistry A, 111 (2007) 1971-1980.
- [29] S.N.V.K. Aki, Z.-Y. Ding, M.A. Abraham, AIChE Journal, 42 (1996) 1995-2004.
- [30] D.G. Lees, Oxidation of Metals, 27 (1987) 75-81.
- [31] D.P. Moon, Materials Science and Technology, 5 (1989) 754-764.
- [32] B.A. Pint, Oxidation of Metals, 45 (1996) 1-37.
- [33] D.J. Cooke, S.E. Redfern, S.C. Parker, Physics and Chemistry of Minerals, 31 (2004) 507-517.
- [34] H. Karasawa, M. Fuse, K. Kiuchi, Y. Katsumura, 5th Int. Workshop on LWR Coolant Water Radiolysis and Electrochemistry, 2004.
- [35] K. Fujiwara, K. Watanabe, M. Domae, Y. Katsumura, (2007).

- [36] L. Qiu, D.A. Guzonas, 3rd Canada-China Joint Workshop on Supercritical Water-Cooled Reactors, Xian, China, 2012.
- [37] D.A. Guzonas, W.G. Cook, *Corros. Sci.*, in press.
- [38] C.A. Stearns, F.J. Kohl, G.C. Fryburg, *J. Electrochem. Soc.*, 121 (1974) 945-951.
- [39] J.E. Croll, G.R. Wallwork, *Oxid. Met.*, 4 (1972) 121-140.
- [40] A. Yamauchi, K. Kurokawa, H. Takahashi, *Oxidation of metals*, 59 (2003) 517-527.
- [41] H. Asteman, J.E. Svensson, M. Norell, L.G. Johansson, *Oxidation of metals*, 54 (2000) 11-26.
- [42] R. Peraldi, B.A. Pint, *Oxidation of metals*, 61 (2004) 463-483.
- [43] A.B. Gaspar, C.A.C. Perez, L.C. Dieguez, *Applied Surface Science*, 252 (2005) 939-949.
- [44] E. Barringer, Z. Faiztompkins, H. Feinroth, T. Allen, M. Lance, H. Meyer, L. Walker, E. Lara-Curzio, *Journal of the American Ceramic Society*, 90 (2007) 315-318.
- [45] M. Schacht, N. Boukis, E. Dinjus, *Journal of Materials Science*, 35 (2000) 6251-6258.
- [46] Y. Daigo, Y. Watanabe, K. Sue, *Corrosion*, 63 (2007) 277-284.

Chapter 8 Infiltration of Porous Cr_3C_2 with Molten Cu

8.1 Introduction

A great deal of attention has been given to the development of metal matrix composites (MMCs), which exhibit unique physical, mechanical and thermal properties, such as specific strength and modulus, elevated temperature stability, thermal conductivity and controlled coefficient of thermal expansion. Because of the unique properties, MMCs have found applications in many industrial areas, such as aerospace, automotive, electronic, thermal management and wear [1-4]. MMCs are usually fabricated using metals (e.g., Al, Mg, Cu, Ti) strengthened with some reinforcement materials including carbides (e.g., SiC, B₄C, Cr₃C₂), nitride (e.g., Si₃N₄, AlN), oxides (e.g., Al₂O₃, SiO₂), as well as elemental materials (e.g., C, Si), that may be in the form of continuous fibres, chopped fibres, whisker, platelets, or particulate [5, 6]. By combining metallic properties (e.g., ductility and toughness) with ceramic properties (e.g., high strength and high modulus), some specific properties such as low density, high specific strength, high specific modulus, high thermal conductivity, good fatigue response, controlled thermal expansion and high abrasion and wear resistance are obtained [6-11].

Early studies on MMCs mainly focus on developing continuous fibre reinforced high performance hybrid materials to achieve high specific stiffness and improved properties for high temperature applications [12, 13]. Nevertheless, this kind of MMCs is restricted by the possible degradation of reinforced fibre caused by an interfacial reaction between the fibre and the matrix when the composites are processed and serviced at elevated temperatures. Another family of MMCs is the

metal matrix reinforced by discontinuous fibres or whiskers that has attracted considerable attention attributed to: (a) availability of various types of reinforcement, (b) the successful development of manufacturing processes to produce MMCs with reproducible structures and properties, and (c) the availability of standard or near standard metal working methods [10, 14]. It has been demonstrated that MMCs reinforced with discontinuous fibre provide essentially isotropic properties with substantial improvements in strength and stiffness, compared to unreinforced materials. However, the properties of this kind of MMCs are influenced and restricted by the morphology of the discontinuous fibres.

Recently, many efforts have been made in developing some MMCs or CMCs (Ceramic Matrix Composites) by infiltrating desired metals into porous preforms in which both the matrix and reinforcement phases are continuous and tri-dimensionally interpenetrating throughout the microstructure [15, 16]. Most of the research on developing these composites are inspired by the fantastic microstructures and fabulous properties exhibited by many natural structural materials like bone, wood, bamboo, nacre etc [17-20]. These kinds of composites that mimic the natural structural materials possess interpenetration phase network (IPN) and exhibit multifunctional characteristics with each phase contributing its own properties, as one phase (ceramic) provides strength or wear resistance while the other (metal or polymer) provides ductility or toughness. Compared to conventional composites reinforced with particulates or fibres, composites with

interpenetration phase network have isotropic microstructures and improved mechanical properties.

In this chapter, a novel copper based MMC reinforced by tri-dimensional chromium carbide (Cr_3C_2) was prepared by infiltrating molten copper into preformed porous chromium carbide foam. To our knowledge, little research has ever been conducted to study composites having the range of pore sizes used in this study due the difficulty in fabrication[21]. The microstructures of the composites were characterized and mechanical properties (hardness and elastic property) were evaluated in this study.

8.2 Experimental

8.2.1 Preparation of carbide foam

Chromium (III) oxide powder (Alfa Aesar, USA, average particle size P_s of ~ 10 μm , purity of 99%) was used as starting material to prepare the carbide foam. The oxide powder was uniaxially compressed in a cylindrical mold under a pressure of 80 MPa to form disk shaped samples. Then the disk shaped samples were put into a tube furnace (GSL1600X, MTI Corporation) and heated to 1100 $^\circ\text{C}$, in a carbonaceous gas mixture (2% CH_4 +98% H_2 , Praxair Canada) at a flow rate of 140ml/min for 15 hours.

8.2.2 Preparation of composite

The preformed ceramic foam was put into an alumina crucible with a bulk copper placed on it. The crucible was covered with an alumina plate and then was heated in a tube furnace. The tube furnace used hydrogen gas to form a protective environment that inhibited the oxidation of copper metal. The temperature of the furnace increased from ambient temperature to 1250 °C with a heating speed at 5 °C/min and was kept at 1250 °C for 10 hours, then cooled down with a cooling speed also at 5 °C/min.

8.2.3 Sample characterization

The morphologies of samples were examined by JEOL (JSM-6301FXV) field emission scanning electron microscope and ZEISS (EVO –MA15) SEM. X-ray diffraction (XRD) analysis was carried out by using a Rigaku Geigerflex 2173 X-ray diffraction equipment. The porous properties of the as-carburized samples were characterized by mercury intrusion porosimetry (AutoPore IV 9510). Hardness of composite was measured by a micro indentation hardness tester (Buehler, USA, IndentaMet 1100 Series) with a load of 1 kg. A dynamic mechanical analyzer (Perkin-Elmer, USA, DMA 8000) testing apparatus was used to determine the elastic property of the composite.

8.3 Results and Discussion

8.3.1 Porous chromium carbide foam prepared [22]

The porous carbide foam with a high density of pores was obtained by reactive sintering a Cr_2O_3 powder compact in a carbonaceous environment. The gas mixture containing 2% $\text{CH}_4+98\%\text{H}_2$ was used as carbon resource as the carbon activity for current environment was calculated to be 3.1 that is high enough to carburize Cr_2O_3 . Figure 8-1(a) shows the surface morphology of as pressed Cr_2O_3 sample, in which the micrometer size Cr_2O_3 particles were mainly compacted together. The porosity of the compact samples before carburization calculated from the sample dimensions and mass was about 36.9-40.7 %. Figure 8-1 (b) and (c) show SEM micrographs of the surface and cross-section for the sample after reactive sintering in a reducing atmosphere (2% $\text{CH}_4+98\%\text{H}_2$) at a temperature of 1100 °C for 10 hours. It can be seen that the sample after sintering exhibits a remarkable structure change and represent a homogeneous porous morphology with a smooth three-dimensional network skeleton structure. The porous sample after carburization was identified as Cr_3C_2 by X-ray diffraction analysis.

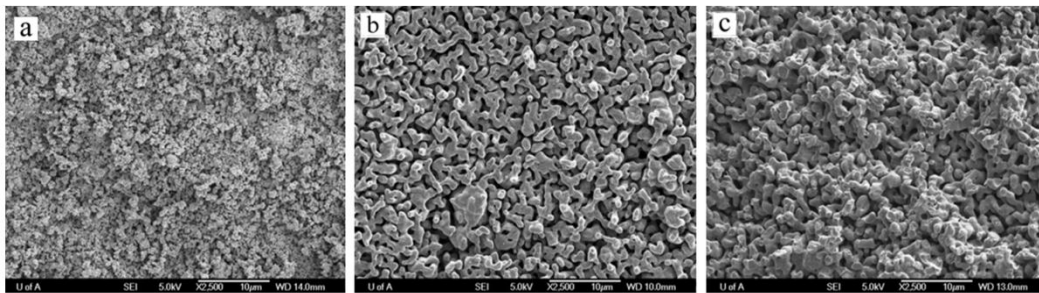


Figure 8- 1. SEM micrographs of 100% Cr_2O_3 green disk before sintering (a) and after sintering at 1100 °C in reducing atmosphere (2% $\text{CH}_4+98\%\text{H}_2$) for 10 hours (b) surface and (c) cross-section [22].

8.3.2 Cu-Cr₃C₂ composite fabricated by infiltration

8.3.2.1 Microstructure of Cu+Cr₃C₂ composite

The microstructure of the composite prepared by infiltrating the carbide foam with copper is shown in Figure 8-2. It can be seen that the copper metal has interpenetrated almost all the pore spaces of the carbide foam which forms a bi-continuous structure composite material. Since the infiltration process was performed under ambient pressure, the high uniformity of infiltration achieved can be attributed to the good wet-ability between copper and chromium carbide (Cr₃C₂), as the contact angle of the copper with the carbide (Cr₃C₂) was reported to be 47° at 1100 °C [23]. The obtained Cu-Cr₃C₂ composite exhibits a homogeneous and continuous bi-phase microstructure in which the metal (Cu) and the carbide (Cr₃C₂) networks are mutually interpenetrated. The magnified image (Figure 8-2(d)) shows a good interfacial bonding between the copper and carbide. However, voids were occasionally observed in the composite, as shown in Figure 8-2, which may result from either the insufficient infiltration of some closed pores (void A) in the composite or the volume shrinkage of the copper metal during solidification (void B and gap C). The XRD patterns of the composite material are shown in Figure 8-3, in which only copper and chromium carbide (Cr₃C₂) phases were detected.

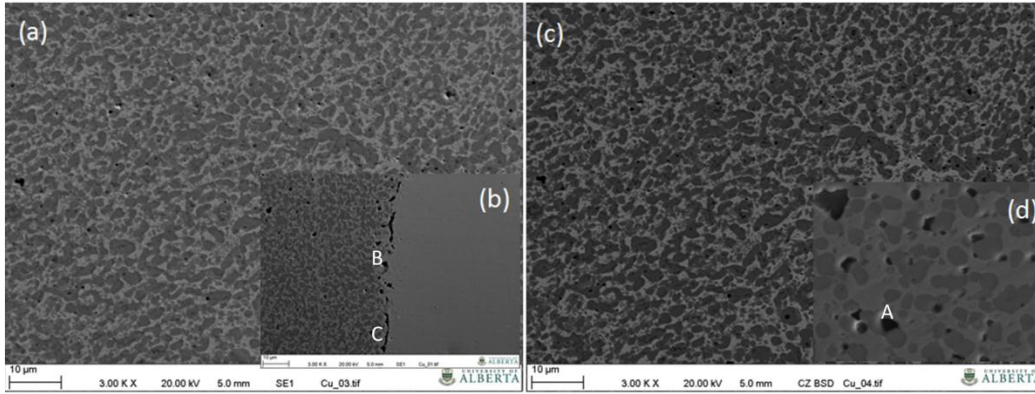


Figure 8- 2. (a) and (c): SE and BE SEM images of obtained composite; (b): Interface between the composite and copper; (d): magnified microstructure image of composite. (A: closed pore; B, C: voids and gaps formed may be due to the shrinkage of copper during solidification).

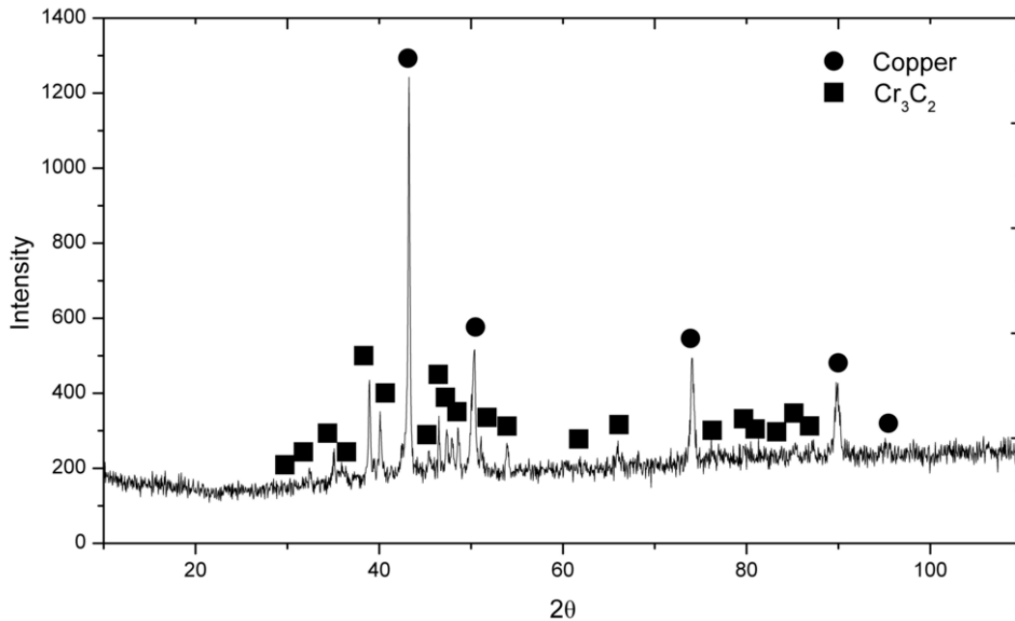


Figure 8- 3. XRD patterns of the composite obtained.

To further characterize the interfacial bonding, the composite sample was fractured and examined as shown in Figure 8-4. The fractured surface exhibits a typical ductile fracture mode with equiaxed dimples surrounding the carbides. It can be seen that fractured carbide was located within each dimple as shown in Figure 8-4 (b), (c) and (d). Because of ductile copper matrix, it is natural that the ductile fracture occurred. The fact that the carbide phase is seen to be located in the bottom of each dimple suggests that voids may be mainly initiated from the cracking of the carbide phase under deformation. This is consistent with the observation of cracks appeared in carbide phase and arrested at the phase interfaces as shown in Figure 8-4 (b). Because of poor ductility of carbide phase, fracture of carbide should occur prior to the formation of ductile dimples and may have facilitated their formation.

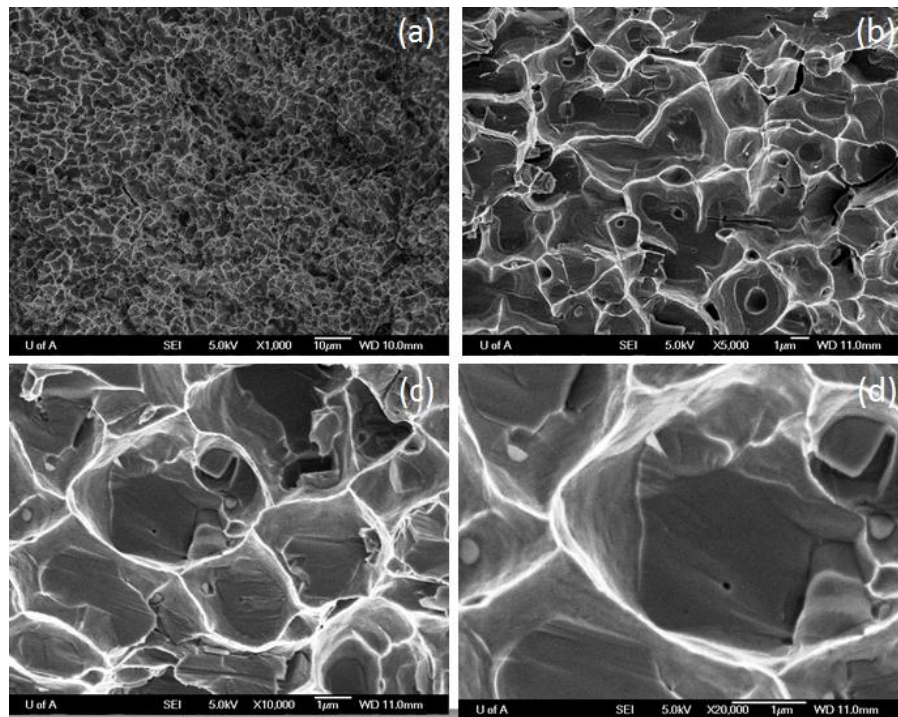


Figure 8- 4. Fracture surface of the composite at different magnification.

8.3.2.2 Mechanical properties of the composite material

a. The hardness

The simplest way to determine the resistance of a material to plastic deformation is through a hardness test. The correlations of some mechanical properties such as tensile strength, wear resistance, compressibility, toughness, and elastic modulus with the value of hardness have been investigated and reported by many researchers [24-30]. The indentation hardness test was performed to measure the hardness of the obtained composite material. The measured Vickers hardness (HV) of the composite sample was around 2716 MPa. The standard deviation of the measured hardness value was small, which was around 2.8 %, indicating a homogeneous structure of the obtained composite. The hardness of the composite sample was about three times higher than that of pure copper, as a result of carbide reinforcement. However, the measured hardness value is lower than the hardness value (7174 MPa) calculated based on the volumetric rule of mixtures given below:

$$H_c = H_m V_m + H_r V_r \quad 8-1$$

Where H is hardness, V is volume fraction and the subscripts c , m and r refer to the composite, matrix and reinforcement, respectively.

Equation (1) provides an approximate estimate of the hardness value of a composite and is usually referred to as the upper bound of the “rule of mixtures”

[31]. And it works reasonably well for composites with directional structure configurations such as aligned fibres. It was obvious that there exists an evident discrepancy between the measured hardness value and the theoretical value of the upper bound of the “rule of mixtures”, although the hardness of the carbide reinforced copper sample increased significantly compared to pure copper. In spite of that, the measured hardness of the composite is still higher than the value (995 MPa) calculated based on equation (2) which is usually referred to as the lower bound of the “rule of mixtures”.

$$H_c = \frac{H_r H_m}{V_r H_m + V_m H_r} \quad 8-2$$

The discrepancy between the measured hardness and the upper bound of the “rule of mixtures” may be attributed to a number of reasons. One might be the presence of voids or holes in the sample, as shown in Figure 8-2 and Figure 8-6. However, the volume fraction of the voids in the current system is extremely low and should be insignificant in terms of its effect on the hardness value. There may be some other reasons for the discrepancy observed. Regarding to porous materials, the mechanical properties depend on not only the density of porosity but also the pore-geometry, including the shape, size, and distribution (continuity and connectivity) of the pore. As it is known, hardness is an extremely structure-sensitive property of materials. Therefore, the pore-geometry of carbide network in the pre-prepared carbide foam which is also inversely related to the geometry of the copper network after infiltration should be considered. Extensive work has

been conducted and numerous publications are available on the effect of pore shape on the mechanical properties of porous materials [32-38]. As summarized by Kelly et al., three main approaches have been established for the determination of mechanical dependence of porous structure, which are composite theory, cellular solids and minimum solid area [39]. Among them, minimum solid area has been shown to be more accurate than other models and has been used over many years for various porous structures. Sprigg first proposed a simple equation that can be considered as the earliest work for developing the minimum solid area models which can be represented by the following equation:

$$A_v = A_0 \exp(-bP) \quad 8-3$$

A_v —Measured mechanical properties, A_0 —Mechanical properties of a specimen with zero porosity, b — parameter determined by the geometry of pore, P — Volume fraction of the porosity.

Many researchers have used this model for analyzing their experimental results. In the beginning, parameter b was empirically related to the nature of porosity characteristic of the fabrication method used for making the ceramic. Later, Brown et al. derived different values of b for different pore geometries and orientations [40]. Rice also determined a similar range of empirically derived values for b related to pore geometry [41]. All of those results suggested that the geometry of pore can affect the mechanical properties of the porous materials.

Nielsen [42] proposed another model to determine the elasticity of porous materials derived from their work on civil engineering composite in the form of:

$$E = E_0 \frac{(1-P)^2}{1 + \left\{ \left(\frac{1}{\rho} - 1 \right) \right\}^P} \quad 8-4$$

The pore-shape factor ρ appearing in this equation is determined based on pore's geometry. As addressed by Nielsen, when sharply edged pore network forms, porous material has a low shape factor, for which the solid phase joined only at small areas of contact tends to be cleaved into particles. This typical porous system can be best illustrated by a material made of a compaction of spherical particles where links are formed due to agglomeration only at small areas between particles. The extreme case ($\rho=0$) for this kind of porous structure is that the pores are totally surrounded by solid particles where the solid phase is extremely inefficient in transferring loads as shown in Figure 8-6(A). It is reasonable to consider that the reduction of the measured hardness as compared to the upper bound value of the "rule of mixture" can be attributed to the geometry of the pore in the pre-prepared carbide foam as well as the resultant geometry of the copper phase in the infiltrated composite.

Recently, Ji, et al. [43] proposed a revised formula for the "rule of mixture" which was named as the "generalized mixture rule (GMR)" expressed as:

$$P_c^J = \sum_{i=1}^N (V_i P_i^J) \quad 8-5$$

Where P is a specific property, V is the volume fraction of component, *i* and c represent the *i*th phase and the composite consisting of N phases. J is considered as a fractal parameter, which is decided by the shape, size distribution, and distribution of the phases.

For a two-phase composite as the sample in this study, Equation 4 can be simplified:

$$P_c^J = (1 - V_m)P_s^J + V_mP_m^J \quad 8-6$$

When porous materials are considered, Equation (5) can be written as

$$\frac{P_c}{P_s} = (1 - p)^{1/J} \quad 8-7$$

For the porous chromium carbide foam prepared by carburization at 1100 °C, the hardness was measured to be around 420 MPa. Therefore, the fractal parameter J can be determined by Equation 8-6, which was calculated to be 0.263. The predicted hardness value according the GRM model can be determined by Equation 8-5 which is 3176 MPa. The comparison of the hardness values are shown in Figure 8-5. It is obvious that the predicted value according to the GRM model is closer to the actual measured hardness of the obtained composite as the geometry of the phases was considered in this model.

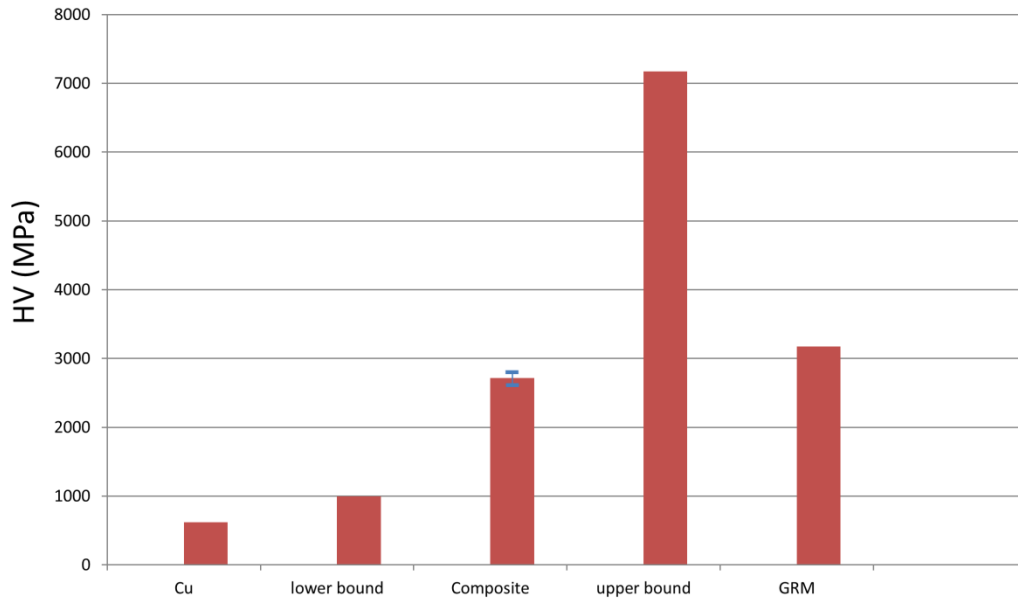


Figure 8- 5. Comparison of hardness values of pure copper, composite, “lower bound” and “upper bound” determined by the “rule of mixture” and calculated value according “GRM” model.

As addressed by Ji [43], J is a parameter that depends on the geometrical shape, spatial arrangement, orientation and size distribution of pores. When porous materials containing long cylindrical or hexagonal pores which align parallel to the stress direction, the parameter J equals 1, in that case the GRM formula is simplified to Equation 8-1 which is the upper bond of the “rule of mixtures”. J equals to 0 represents that the property of a porous material will vanish. It was also noted that a lower J value will be produced by intergranular, continuous, channel pores cavities. And a higher J value can be caused by intragranular, isolated and rounded pores. The materials with open pores usually exhibit a lower J value and thus more pronounced effects on the effective mechanical properties than the closed pores. Through carefully examining the detailed morphology of

the infiltrated sample (Figure 8-6(b)), it can be seen that the contours of most of the carbide phase are close to the shape of a circle or several circles after coalescence, as shown in Figure 8-6 (b), indicating that the carbide phase may mainly behave as spherical particles due to the aggregation effect at the high temperature, and therefore a low pore shape factor was caused. It is reasonable that a spherical contour with smooth surface is formed in the current carbide foam because pore formation took place at high temperatures where diffusion achieving a surface with minimum surface area is possible.

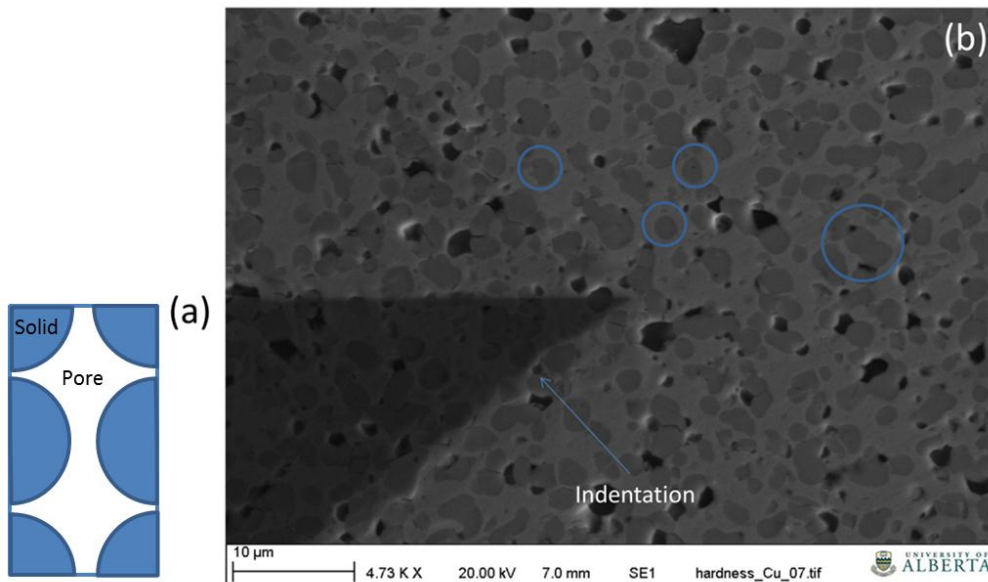


Figure 8- 6. (a) diagram representing the extreme case ($\rho=0$) for porous structure that the pores totally surround solid particles; (b) Part of the indentation after the hardness test for the composite.

Therefore, the reactive sintering of the porous chromium carbide can be divided into two related processes. One process is the chemical reaction by which chromium oxide was carburized to chromium carbide. This process could

contribute to the increase of the porosity. The other process is the aggregation of the ceramic particles under the high temperature condition, which could affect the pore-geometry of the obtained sample and hence determine the J value of this ceramic.

The J-values of the carbide foam obtained from this research as well as those from published data are listed in Table 1. The data are consistent and imply that for porous ceramics consisting of aggregated particles, the shape factor J will be low and lay in between 0.2 to 0.3, which is close to the situation of the Nielsen's model as shown in Figure 8-6(A). Ceramics with lower shape factor will suffer higher stress concentration, lower ability of stress transfer and higher tendency of cracking. In such an instance, the solid phase (Cr_3C_2) tends to be cleaved by high stress concentration at carbide struts with the smallest cross sections. This should be responsible for the occurrence of carbide cracking as shown in Figure 8-6 (b), resulting in the reduced hardness measured. Nevertheless, no obvious cracks were found at the tip of the indentation (Figure 8-6(b)), and only small cracks appeared within the carbide phase and arrested by surrounding copper phase, which indicates that the composite may possess high toughness.

Table 8- 1. Comparison of the J factor: Cr₃C₂-carbide foam for this study, P=63%. Al₂O₃-1: Porous polycrystalline aggregates, P≤30% [43, 44]; Al₂O₃-2: porous, P≤40% [43, 45]; MgO: aggregates, P≤40% [43, 46] ; SiC: aggregates, P≤42% [43]; MgAl₂O₄: aggregates [43, 47].

| Porous ceramics | Cr ₃ C ₂ | Al ₂ O ₃ -1 [43, 44] | Al ₂ O ₃ -2[43, 45] | MgO[43, 46] | SiC[43] | MgAl ₂ O ₄ [43, 47] |
|-----------------|--------------------------------|--|---|-------------|---------|---|
| J | 0.263 | 0.284 | 0.263 | 0.241 | 0.27 | 0.270/0.280 |

b) Elastic property of the composite

The measured elastic modulus (Young's modulus) of the carbide foam was about 8.89 GPa. According to Equation 6, the shape factor J was calculated to be 0.266 which is consistent with the derived value (0.263) based on the measured hardness value. The results seem pertinent and reasonable. Using the J value (0.266), the Young's modulus of the composite was predicted to be 187.53 GPa. Nevertheless, the elastic modulus of the obtained composite was measured to be around 205 GPa that is higher than the value predicted by the GMR model and close to the upper bond value calculated by the rule of mixture. This result also suggests that a composite possesses a relative higher elastic modulus has been obtained since most of the composites reported have Young's moduli which are significantly lower than the upper bond values calculated by the rule of mixture. Considering the density of the composite material, the stiffness value is around

25.30 GN m⁻²/Mg m⁻³. Muscat et al. investigated Al/TiC composites prepared by infiltrating pre-formed TiC with molten Al [48]. Their results show that the elastic moduli of the composites fell down to the lower bound values of the “role of mixtures”

Peng et al. [49] examined bi-continuous metal matrix composites prepared by infiltrating an alumina preform which had the structure of a reticulated ceramic foam. The elastic moduli of the composites they measured were lower than the maximum theoretical values as given by the rule of mixtures and dropped down to the values that can be represented by a model developed by Tuchinskii [50] as expressed below:

$$E_c = E_m(1 - t)^2 + E_r t^2 + \frac{2E_r t(1-t)}{t + (E_r/E_m)(1-t)} \quad 8-8$$

Where the parameter t is related to the volume fraction V_r through

$$V_r = (3 - 2t)t^2 \quad 8-9$$

A comparison of the elastic modulus of the obtained composite with some theoretically calculated values is made in Figure 8-7. It can be seen that the elastic modulus of the composite is higher than the values given by the GRM model and the Tuchinskii model. The ceramic foam used in this study features a finer porous structure (pore size: 1~2 μm) as compared with the ceramic foams (pore size:

150~215 μm) studied by Peng. The relatively higher elastic modulus of this composite in this study was believed to be attributed to the more homogeneous microstructure composed of the finer carbide reinforcement network and the much better connectivity of the carbide reinforce phase as shown in Figure 8-3 as well as the good interfacial bonding between the copper and carbide phases.

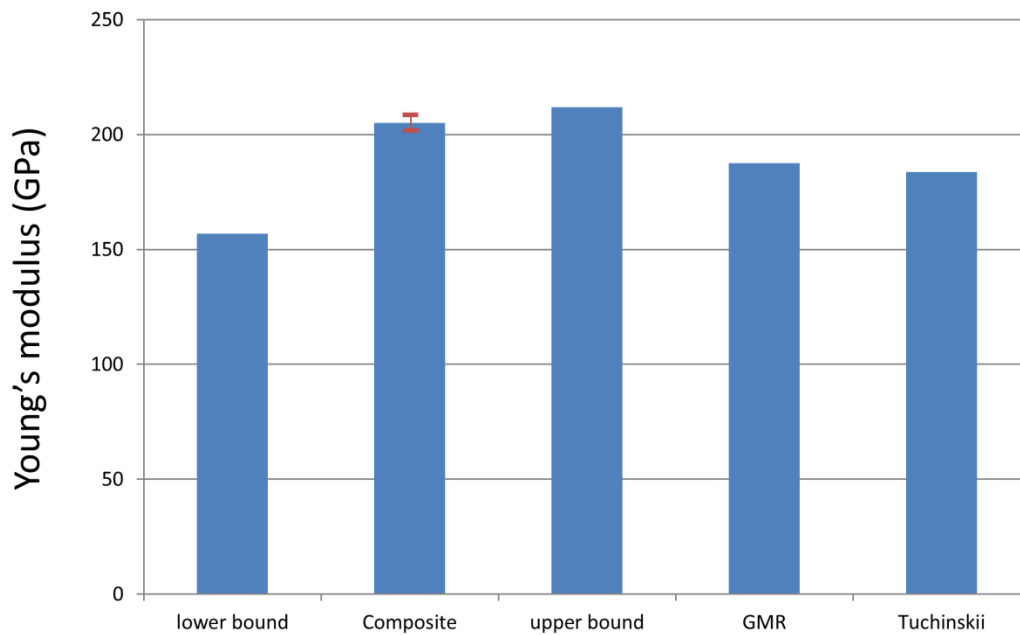


Figure 8- 7. Comparison of Young's modulus values of composite with calculated values predicted: "lower bound" and "upper bound" determined by the "rule of mixture" and calculated value according "GRM" model and "Tuchinskii" model (lower bound).

8.4 Concluding Remarks

A new bi-continuous metal matrix composite was produced by infiltrating green pre-prepared chromium carbide foam with molten copper. Compared to some other impregnated composites, the obtained copper matrix composite possesses

excellent homogeneous structure with fine reinforcement network. The mechanical properties (hardness, elastic modulus) of the composite were evaluated in this study. This composite exhibited good elastic property which is believed to be related to the feature of the structure and the good interfacial bonding between the matrix phase and the reinforce phase. Hardness values measured were a little lower than that calculated using the rule of mixtures. This was attributed to the shape factor of the porous structure characteristic of the method used for fabricating the porous foams.

8.5 Bibliography

- [1] A. Mortensen, J. Llorca, *Annual Review of Materials Research*, 40 (2010) 243-270.
- [2] M. Nofar, H. Madaah Hosseini, N. Kolagar-Daroonkolaie, *Materials & Design*, 30 (2009) 280-286.
- [3] M. Vetterli, R. Tavangar, L. Weber, A. Kelly, *Scripta materialia*, 64 (2011) 153-156.
- [4] J. Hemanth, *Materials & Design*, 30 (2009) 323-329.
- [5] D.D.L. Chung, *Composite materials: science and applications*, Springer Verlag, 2010.
- [6] R. Thiraviam, T. Sornakumar, A. Senthil Kumar, *International Journal of Materials and Product Technology*, 31 (2008) 305-313.
- [7] K.K. Chawla, N. Chawla, *Metal • Matrix Composites*, Wiley Online Library, 2004.
- [8] Y. Han, D. Gallant, X.G. Chen, *Corrosion*, 67 (2011) 115005-115005-115011.
- [9] P. Joyce, L. Brown, A. Lazzaro, 2010.
- [10] O. Akalin, K.V. Ezirmik, M. Urgan, G.M. Newaz, *Journal of Tribology*, 132 (2010) 041603.
- [11] P. Gudlur, A. Forness, J. Lentz, M. Radovic, A. Muliana, *Materials science & engineering. A, Structural materials: properties, microstructure and processing*, 531 (2012) 18-27.
- [12] V. Tvergaard, *Acta Metallurgica et Materialia*, 38 (1990) 185-194.
- [13] H. Rack, *Materials and Manufacturing Processes*, 3 (1988) 327-358.

- [14] I.A. Ibrahim, F.A. Mohamed, E.J. Lavernia, *Journal of Materials Science*, 26 (1991) 1137-1156.
- [15] Y. Sun, H. Zhang, A. Wang, H. Fu, Z. Hu, C. Wen, P. Hodgson, *Applied Physics Letters*, 95 (2009) 171910.
- [16] L.J. Huang, S. Wang, Y.S. Dong, Y.Z. Zhang, F. Pan, L. Geng, H.X. Peng, *Materials Science and Engineering: A*.
- [17] B. Francois, *Bioinspiration & Biomimetics*, 5 (2010) 035001.
- [18] H.D. Espinosa, J.E. Rim, F. Barthelat, M.J. Buehler, *Progress in Materials Science*, 54 (2009) 1059-1100.
- [19] M.E. Launey, E. Munch, D.H. Alsem, H.B. Barth, E. Saiz, A.P. Tomsia, R.O. Ritchie, *Acta Materialia*, 57 (2009) 2919-2932.
- [20] R. Weinkamer, P. Fratzl, *Materials Science and Engineering: C*, 31 (2010) 1164-1173.
- [21] A.R. Studart, U.T. Gonzenbach, E. Tervoort, L.J. Gauckler, *Journal of the American Ceramic Society*, 89 (2006) 1771-1789.
- [22] T. Xing, X. Cui, W. Chen, R. Yang, *Materials Chemistry and Physics*, 128 (2011) 181-186.
- [23] A.R. Kennedy, J.D. Wood, B.M. Weager, *Journal of Materials Science*, 35 (2000) 2909-2912.
- [24] Y. Bao, W. Wang, Y. Zhou, *Acta materialia*, 52 (2004) 5397-5404.
- [25] Y.T. Cheng, C.M. Cheng, *Applied physics letters*, 73 (1998) 614.
- [26] G.P. Evans, J.C. Behiri, J.D. Currey, W. Bonfield, *Journal of Materials Science: Materials in Medicine*, 1 (1990) 38-43.

- [27] W.C. Oliver, G.M. Pharr, *Journal of materials research*, 7 (1992) 1564-1583.
- [28] L. Qian, X. Xiao, Q. Sun, T. Yu, *Applied physics letters*, 84 (2004) 1076-1078.
- [29] W. Schubert, H. Neumeister, G. Kinger, B. Lux, *International Journal of Refractory Metals and Hard Materials*, 16 (1998) 133-142.
- [30] D. Tabor, *Philosophical Magazine A*, 74 (1996) 1207-1212.
- [31] W. Liu, U. Koster, *Materials Science and Engineering A*, 210 (1996) 1-7.
- [32] J.A. Hudson, E. Liu, S. Crampin, *Geophysical Journal International*, 124 (1996) 105-112.
- [33] D.-M. Liu, *Journal of materials science letters*, 15 (1996) 419-421.
- [34] T. Nakamura, G. Qian, C.C. Berndt, *Journal of the American Ceramic Society*, 83 (2000) 578-584.
- [35] R. Rice, *Journal of materials science*, 32 (1997) 4731-4736.
- [36] R.W. Rice, *Journal of materials science*, 28 (1993) 2187-2190.
- [37] P. Sepulveda, F.S. Ortega, M.D.M. Innocentini, V.C. Pandolfelli, *Journal of the American Ceramic Society*, 83 (2000) 3021-3024.
- [38] Y. Xu, L. Zhang, L. Cheng, D. Yan, *Carbon*, 36 (1998) 1051-1056.
- [39] K.U. O'Kelly, A.J. Carr, B.A.O. McCormack, *Journal of Materials Science: Materials in Medicine*, 14 (2003) 379-384.
- [40] S.D. Brown, R.B. Biddulph, P.D. Wilcox, *Journal of the American Ceramic Society*, 47 (1964) 320-322.
- [41] R. Rice, *Journal of materials science*, 31 (1996) 102-118.
- [42] N. Lauge Fuglsang, *Materials Science and Engineering*, 52 (1982) 39-62.

- [43] S. Ji, Q. Gu, B. Xia, *Journal of materials science*, 41 (2006) 1757-1768.
- [44] F.P. Knudsen, *Journal of the American Ceramic Society*, 45 (1962) 94-95.
- [45] R.M. Spriggs, *Journal of the American Ceramic Society*, 44 (1961) 628-629.
- [46] C. Reynaud, F. Thevenot, T. Chartier, J.L. Besson, *Journal of the European Ceramic Society*, 25 (2005) 589-597.
- [47] D.F. Porter, J.S. Reed, D. Lewis, *Journal of the American Ceramic Society*, 60 (1977) 345-349.
- [48] D. Muscat, K. Shanker, R.A.L. Drew, *Materials science and technology*, 8 (1992) 971-976.
- [49] H.X. Peng, Z. Fan, J.R.G. Evans, *Materials Science and Engineering: A*, 303 (2001) 37-45.
- [50] L. Tuchinskii, *Powder Metallurgy and Metal Ceramics*, 22 (1983) 588-595.

Chapter 9 Concluding Remarks and Future Work

9.1 Concluding Remarks

This research aims to develop bulk porous ceramics as well as ceramic-metal composites that can be used as thermal insulation materials in the SCWR. The study consisted of two main aspects: 1. developing and engineering the porous structure materials; 2. evaluating corrosion resistance of the porous materials in SCW environments. Chapter 3 and Chapter 4 reported the fabrication of porous carbide and porous carbide-metal composite. The evaluation of the stability of porous Cr_3C_2 and Cr_2O_3 in SCW environments was covered in Chapter 5-7. Chapter 8 presents the work of the fabrication and evaluation of a carbide-copper composite material. Some concluding remarks of this study are summarized below.

9.1.1 Fabrication of ceramics and composites

Reactive sintering was used as the primary route to fabricate porous Cr_3C_2 ceramics with high densities of interconnected pores [1]. To further increase the porosity and to optimize the porous structure, we developed a new process that incorporated the freeze casting method with the reactive sintering process. By using this new process, porous Cr_3C_2 ceramics with a high porosity around 80 - 90 % were obtained. The carbide materials consisted of multi-sized pores that could be altered by changing the casting parameter.

Cobalt was introduced to the reactive sintering process for the purpose of modifying the porous structure and achieve better mechanical properties (Chapter 2). It was concluded that cobalt can be dissolved into the carbide during the

reactive sintering to form $M(\text{Cr},\text{Co})_7\text{C}_3$ phase. Cobalt metal enriched phase could be formed when the cobalt content was higher than 30 wt. %. This would lead to the formation of porous $M(\text{Cr}, \text{Co})_7\text{C}_3$ -Co composites. The porosity and pore size of the porous composites can also be altered by adding different amounts of cobalt. It was determined that the $M(\text{Cr}, \text{Co})_7\text{C}_3$ phase can be strengthened by solid solution of cobalt in the carbide phase.

9.1.2 Evaluation in SCW environments

The porous carbide prepared through reactive sintering was evaluated in SCW to examine its stability (Chapter 5). It was determined that Cr_3C_2 can be stable in SCW at temperatures below 420 - 430 °C. However, when the temperature of SCW increased above 425 °C, the disintegration of Cr_3C_2 occurred due to both intergranular and transgranular corrosion attacks. It was also identified that the disintegration of Cr_3C_2 was related to the formation of the intermediate product of CrOOH that could be subsequently decomposed. Therefore, Cr_3C_2 ceramic can be used under SCW condition at temperatures lower than 425 °C.

The corrosion behavior of porous oxide ceramics was investigated under various SCW conditions (Chapter 6, 7). It has been identified that the corrosion of Cr_2O_3 in SCW was affected by the morphology of the ceramics and the test condition of SCW. It was determined that the Cr_2O_3 generally exhibited higher corrosion resistance than Cr_3C_2 in high-temperature SCW. The stability of Cr_2O_3 in SCW is also dependent on its surface morphology and grain size. Highly porous Cr_2O_3 ceramic exhibited lower corrosion resistance because of larger exposed surface

and grain boundary areas. The disintegration of porous Cr_2O_3 observed in the static and loop exposures can be attributed to the increased grain boundary attack under SCW condition. The Cr_2O_3 ceramics with smaller grains exhibited a higher tendency of disintegration because of more separation of grains resulted from the intergranular attacks. Doping ceramic oxides with proper amounts of reactive elements or oxides such as 5 wt. % of Y_2O_3 can effectively increase the stability of porous Cr_2O_3 in SCW. However, addition of larger amounts of yttria (10~20 wt. %) decreased the stability of the porous Cr_2O_3 -based ceramics because of the increased dissolution of yttria in SCW environments.

The operation condition of SCW significantly affected the corrosion behavior of Cr_2O_3 in SCW. The Cr_2O_3 ceramics suffered from increased degree of degradation when exposed to SCW with higher temperatures. The increase of oxygen concentration in SCW can also enhance the corrosion of Cr_2O_3 . The SCW loop test confirms that Cr_2O_3 is stable in SCW with a low (8ppb) and moderate (8ppm) dissolved oxygen concentration in SCW at 650 °C, indicating that it will be important to control the oxidant concentration in SCWR core to prevent the dissolution of Cr_2O_3 . Therefore, Cr_2O_3 based ceramics, especially doped with yttrium are able to be used in high-temperature SCW environment if the oxidants can be controlled under a critical level.

Chapter 8 reported the fabrication of a Cr_3C_2 -Cu composite by immersing porous Cr_3C_2 into molten copper and solidifying them together after the infiltration. It has

been proved that an excellent homogeneous structure with fine reinforcement network could be obtained through the above process. The bi-continuous composite exhibited good elastic properties, which is attributed to the unique structure of the composite and the good interfacial bonding between the matrix phase and the reinforced phase.

9.2 Future Work

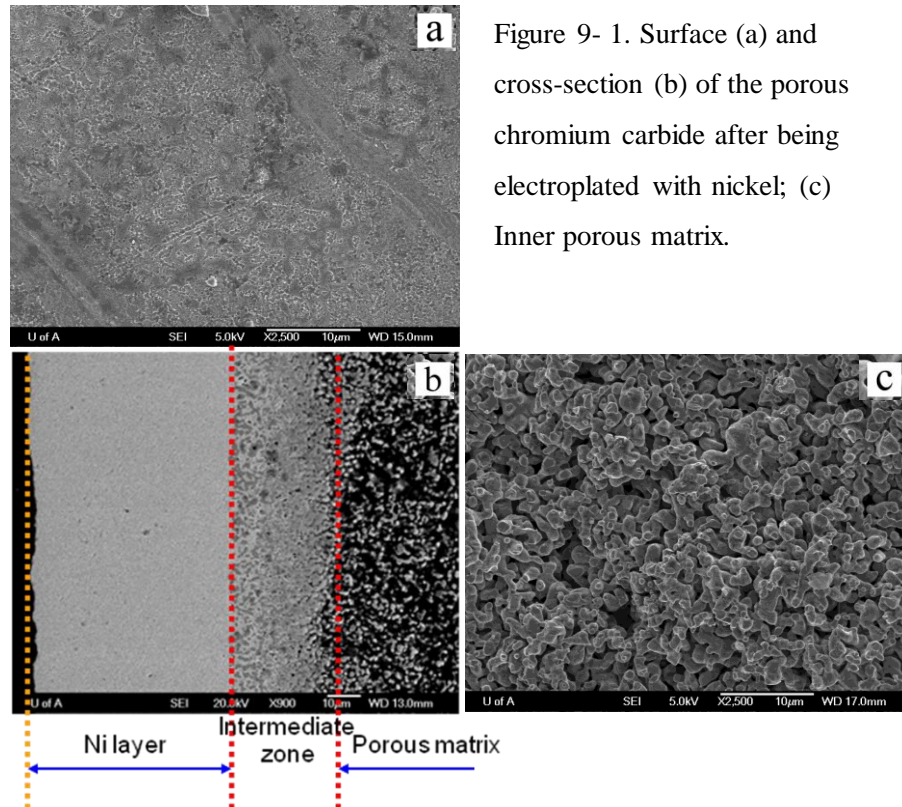
9.2.1 Evaluation of the performance of composite materials in SCW

The current SCW corrosion investigation has been mainly focused on the bulk porous Cr_3C_2 and Cr_2O_3 . The stability of the $\text{M}(\text{Cr}, \text{Co})_7\text{C}_3\text{-Co}$ and the $\text{Cr}_3\text{C}_2\text{-Cu}$ composite needs to be assessed under SCW condition. It has been reported that the high temperature oxidation and hot corrosion resistance of Cr_3C_2 can be improved by alloying Cr_3C_2 with some metallic element, such as Al, to form Cr_2AlC [2]. It was found that Cr_2AlC had a higher starting temperature (800 °C) for oxidation and displayed excellent oxidation resistance with very low parabolic rate constants at 800 and 1300 °C. Exploring the effect of alloying on the stability of carbide in the SCWR is recommended.

9.2.2 Engineering the surface of Cr_3C_2 to improve its stability in SCW

Although Cr_3C_2 was not stable in high-temperature SCW, it could be surface engineered to achieve better corrosion resistance, for example, by forming a metal layer using electroplating. Figure 9-1 shows the morphology of porous carbide

after being electroplated with Ni on its surface. Future research is needed to evaluate its stability in SCW environments.



9.2.3 The stability of other reactive element/oxides -Cr₂O₃ systems

It was found that yttria could improve the corrosion resistance of Cr₂O₃ in SCW environments. The effect of other reactive element/oxides on the stability of Cr₂O₃ in SCW environments might be worth exploring.

Bibliography

- [1] T. Xing, X. Cui, W. Chen, R. Yang, *Materials Chemistry and Physics*, 128 (2011) 181-186.
- [2] Z.J. Lin, M.S. Li, J.Y. Wang, Y.C. Zhou, *Acta Materialia*, 55 (2007) 6182-6191.